UNIVERSITAT DE BARCELONA

Compartmentalised microfluidic culture systems for *in vitro* modelling of neurological and neuromuscular microenvironments

Maider Badiola Mateos

Tesis doctoral

Compartmentalised microfluidic culture systems for *in vitro* modelling of neurological and neuromuscular microenvironments

Maider Badiola Mateos

UNIVERSITAT DE BARCELONA

Firma autora:

Maider Badiola Mateos

Firma director y tutor:

Josep Samitier Martí

Compartmentalised microfluidic culture systems for *in vitro* modelling of neurological and neuromuscular microenvironments

Memoria presentada para optar al grado de Doctora por la Universitat de Barcelona

Programa de Doctorado en Biomedicina

Autora: **Maider Badiola Mateos**

Director y tutor: **Josep Samitier Martí**

Institute for Bioengineering of Catalonia (IBEC)
Universitat de Barcelona (UB), Facultad de Física, Departamento de Ingeniería Electrónica y Biomédica

Barcelona, 2020

UNIVERSITAT DE BARCELONA

To my parents, sister and nephews,

for your eternal love, support and inspiration

DECLARACIÓ DEL DOCTORAND DE CODIS ÈTICS I BONES PRÀCTIQUES

Jo, Maider Badiola Mateos, matriculat al programa de Doctorat en Biomedicina de la Universitat de Barcelona, declaro que la tesi titulada "Compartmentalised microfluidic culture systems for in vitro modelling of neurological and neuromuscular microenvironments" és original, que la investigació que vaig realitzar compleix els codis ètics i les bones pràctiques i que la tesi no inclou plagi. Soc conscient i accepto per escrit que la meva tesi se sotmetrà al procés adequat per provar l'originalitat dels meus resultats.

(data i signatura)

DECLARACIÓ DEL DIRECTOR COMPLIMENT DE CODIS ÈTICS I BONES PRÀCTIQUES

Declaro que la tesi titulada "Compartmentalised microfluidic culture systems for in vitro modelling of neurological and neuromuscular microenvironments" presentada per la Sra. Maider Badiola Mateos, sota la meva supervisió, compleix els codis ètics i les bones pràctiques i que la tesi no inclou plagi.

Nom i cognoms: Josep Samitier Martí

(data i signatura)

ACKNOWLEDGEMENTS

First and foremost, I would like to express my gratitude to my thesis supervisor, Prof. Josep Samitier, for giving me the opportunity to work in his lab; for his patience, guidance and constructive critiques; for allowing me to explore new ideas and techniques; for arranging collaborations for my project; and for guiding my growth as a scientist researcher. I count myself lucky to have given the chance to pitch ideas, and develop them, while having his feedback and support all these years. I have had a great mentor on my side keeping a perfect balance between cheering me up, pushing me, and holding me up. I sincerely thank him for all that.

Overall, all IBEC members have been extremely welcoming and have created a very inspiring environment. In particular, I would like to thank Dr. Mª José López for her constant motivation, encouragement and constructive feedback; for her guidance, patience and support; for being a great collaborator and a better friend. Thanks to Dr. Roberto Paoli, for being like a brother for me in the lab during our PhD years, for being helpful and supportive in the professional and personal matters. Thanks to Andrea Esteban, for choosing me to guide her project for two years, for her enthusiasm, and for being not only a fantastic student, but also a good friend. I also want to thank particularly to the teammates who welcomed me in the group when I started the PhD; and to all postdocs and seniors of my group who, in one way or another, have given me feedback, have shared scientific discussions and lessons, especially to Dr. Joan Montero, and Dr. Loris Rizzello. My thanks are extended to all the members of the Nanobioengineering lab, both past and present, who have been very supportive and encouraging throughout years, and who I have had the chance to share day to day life with in the lab.

For the time I spent in Boston at MIT, I want to express my gratitude as well to my host supervisor, Prof. Roger D. Kamm, to my collaborator, Dr. Tatsuya Osaki, and to all my host group members at the Mechanobiology lab, for their support, encouraging atmosphere and feedback. I want to thank especially Dr. Kristina Haase, Dr. Clare Ko, Dr. Giovanni Offeddu, Dr. Yoojin Shin, Jean Carlos Serrano, Cynthia Hajal, Lina Ibrahim, Anya Burkart

Roberts, Tiankun Liu, and Denis Ortega Ioni for their personal support and countless ups and downs shared. I am happy to call you my friends.

When I arrived to IBEC I had the chance to collaborate with the Molecular and Cellular Neurobiotechnology lab, to knock on their door every time I needed something, and ask them thousand questions about Neurobiology, a field that I was not familiar with. I had the chance to collaborate closely with Prof. Jose Antonio del Río, Dr. Arnau Hervera and Miriam Segura. They gave me feedback in all neurobiology-related matters, and were always willing to help. To all the team, thank you for welcoming me in your lab as one of your own.

Through the PhD, I had also the chance to collaborate with Prof. Eugenio Martinelli and Dr. Davide Di Giuseppe, from the Sensors group at Università degli Studi di Roma "Tor Vergata". For the time shared, and for letting me participate in such a thrilling project, thank you.

To all IBEC members from core facilities, administration, finances, communications, IT; and to all members from technological platforms employed (IBEC MicroFabSpace and Microscopy Characterisation Facility, IRB Advanced Microscopy Facilities, CCiTUB Cytometry and Genomic Unit, CCiTUB Cryomiscroscopy Electronic Unit, CCiTUB mechanical workshop, Parc Cientific de Barcelona common facilities, and Koch Institute for Integrative Cancer Research), thank you.

This thesis was been funded by IBEC-Severo Ochoa program. My stay at MIT was funded by Severo Ochoa Triple-I program for predoctoral researchers from IBEC and MISTI Global Seed Funds from La Caixa foundation and MISTI (MIT international science and technology initiatives). To my funding organisations, thanks for making possible to do this project.

But this thesis would have been impossible to do without my supportive network of family and friends. Thanks to my mother and father, Valentina and Eduardo, and sister, Andrea, who have always believed in me more than myself; have encouraged me to pursue my crazy dreams, constantly reminding me that I could reach my goals; have always been close despite the distance; and have been there in the worst and the best moments. For that, I cannot thank you enough.

Thanks to my nephews, Lur and Ziad, for inspiring me and teaching me so much. Thank you to all my family members, Wassim Khateeb, Mª Ángeles Camáñez, Carol Flower and Ravinder Dhillon, for being a supportive and caring family.

Thanks to Itxaso Abaigar and Andrea de Diego, for sharing all our ups and downs and a life of friendship, and for always bringing out the best in me. To all my friend from Bilbao, IBEC, PhD committee, colleagues from lindy hop lessons, yoga teammates, and friends from over the globe, thank you, specially to: Andrea Ochoa, Carla Sánchez, Maryna Malevich, Adrián Pérez, Gorka García, Sandra Gómez, Jon Ander Muriel, Cuong Nguyen, Anna Bohigas, Marta Rifà, Raúl Ortíz, Gizem Altay, Marc Van der Hofstadt, Claudia Navarro, Martí Checa, Gerard Rubí, Agata Nyga, Harishankar Balakrishnan, María Blancas, Carlos Ruiz Wills, Sefora Conti, and Davia Prischich. I wish we could meet more often.

Finally, I want to thank to all the people I have met along my journey and helped me find my path, specially to Leonor, and to my group from Drala.

I would not be here today if it was not because of all of you. Thank you very much, muchas gracias, moltes gràcies, merci beaucoup, vielen Dank, grazie mille, eskerrik asko!

Maider

TABLE OF CONTENTS

LIST OF ABBREVIATIONS

8-Br-cAMP	8-bromoadenosine-3',5'-cyclic monophosphate
AA	ascorbic acid
AC	alternate current
ACh	acetylcholine
AChR	acetylcholine receptors
ACTB	β-actin
AJ	adherens junctions
ALS	amyotrophic lateral sclerosis
AraC	cytosine β-D-arabinofuranoside hydrochloride
ASW	annulospiral wrapping
B3GAT1	beta-1,3-glucuronyltransferase 1
BBB	blood-brain barrier
BBBO	transient BBB opening
BCSFB	blood-cerebrospinal fluid barrier
BDNF	brain-derived neurotrophic factor
BF	bright field
bFGF	basic fibroblast growth factor
BLB	blood-labyrinth barrier
BNB	blood-nerve barrier
BRB	blood-retinal barrier
BRN3A	brain-specific homeobox/POU domain protein 3A
BSA	bovine serum albumin
BSCB	blood-spinal cord barrier
cμFCS	compartmentalised microfluidic culture systems
C9ORF72	chromosome 9 open reading frame 72
CCiTUB	Centres Científics i Tecnològics Universitat de Barcelona
ChR2	channelrhodopsine-2
CLSM	confocal laser scanning microscopy
CNS	central nervous system
CNTF	ciliary neurotrophic factor
COP	cyclic olefin polymers
DC	direct current
ddiff	days of differentiation

DIV	days *in vitro*
DMEM	Dulbecco's Modified Eagle Medium
DMSO	dimethyl sulfoxide
DoC	day of confluency
DPBS	Dulbecco's phosphate buffered saline
DRG	dorsal root ganglia
DRG-CM	dorsal root ganglia conditioned medium
DRGn	dorsal root ganglia neurons
E.coli	*Escherichia coli*
EC	endothelial cells
ECM	extracellular matrix
EGF	epidermal growth factor
EIS	electrical impedance spectroscopy
ELA	esclerosis lateral amiotrófica
ENM	enfermedades neuromusculares
ETV1	ETS variant 1
FACS	fluorescence activated cell sorting
fALS	familiar amyotrophic lateral sclerosis
FBS	foetal bovine serum
FC	flow cytometry
FGF	fibroblast growth factor
FSE	flower spray ending
FUS	FUS RNA binding protein
GAPDH	glyceraldehyde 3-phosphate dehydrogenase
GDNF	glial cell line-derived neurotrophic factor
GFAP	glial fibrillary acidic protein
GFP	green fluorescent protein
GSK3	glycogen synthase kinase 3
hESC	human embryonic stem cell
hiPSC	human induced pluripotent stem cells
HLXB9	homeobox HB9
HNK1	human natural killer-1
hNP	human neural progenitors
hNSC	Human neural stem cells
HS	horse serum
hSkMb	human skeletal myoblasts
hSkMc	human skeletal myocytes
IBEC	Institute of Bioengineering of Catalonia

IGF-I	insulin like growth factor type I
iPSC	induced pluripotent stem cells
LDA	linear discriminant analysis
LY	lucifer yellow
MBP	myelin basic protein
MEM	minimum essential medium
MHC	myosin heavy chain
MMP	matrix metalloproteinases
MN	motor-neurons or motoneurons
MNX1	motor neuron and pancreas homebox 1
mRNA	messenger ribonucleic acid
N/A	not applicable
NCSC	neural crest stem cells
NGF	nerve growth factor
NMD	neuromuscular diseases
NMJ	neuromuscular junction
NT-3	neurotrophin-3
NTRK1	neurotrophic tyrosine kinase receptor type 1
NTRK2	neurotrophic tyrosine kinase receptor type 2
NTRK3	neurotrophic tyrosine kinase receptor type 3
NVU	neurovascular unit
P/S	penicillin-streptomycin
P75TNFR	p75 tumour necrosis factor receptor
PAMPA	parallel artificial membrane permeability assays
PBS	phosphate buffer saline
PCB	Parc Cientific de Barcelona
PDMS	poly-dimethylsiloxane
PFA	paraformaldehyde
PMMA	poly(methyl methacrylate)
PNS	peripheral nervous system
POU4F1	POU domain, class 4, transcription factor 1
PRPH	peripherin
PS	polystyrene
pSN	proprioceptive sensory neurons or sensorimotor afferents
PVALB	parvalbumin
PVDF	polyvinylidene difluoride
qPCR	quantitative polymerase chain reaction
RPS18	ribosomal protein S18

RUNX3	Runt-related transcription factor 3
sALS	sporadic amyotrophic lateral sclerosis
SC	Schwann cells
SEM	scanning electron microscopy
SFS	sequential feature selection
Shh	Sonic Hedgehog
SkM	skeletal muscle
SkMb	skeletal myoblasts
SkMc	skeletal myocytes
SLC17A7	solute carrier family 17 member 7
SN	sensory neurons
SOD1	superoxide dismutase 1
SPP1	secreted phosphoprotein 1
STL	standard tessellation language
TARDBP	TAR DNA-binding protein
TEER	trans-epithelial electrical resistance
TEM	transmission electron microscopy
TJ	tight junctions
TNFSF1B	tumour necrosis factor receptor superfamily member 1B
TP	timepoint
Trk	tropomyosin receptor kinase
TrkA	Tropomyosin receptor kinase A
TrkB	Tropomyosin receptor kinase B
TrkC	Tropomyosin receptor kinase C
TUBB3	Class III β-tubulin
TUJ1	beta III tubulin
UNF	unified national fine
UV	ultraviolet
VE-cadherin	vascular endothelial cadherin
VEGF	vascular endothelial growth factor
VGluT1	vesicular glutamate transport 1
YFP	yellow fluorescent protein
ZIF	zero injection force
ZO-1	zonula occludens 1

LIST OF BOXES

ABSTRACT

Movement of skeletal-muscle fibres is generated by the locomotion circuit, in which many cells play a different role. Failures in any part of the circuit can cause or define the severity of neuromuscular diseases (NMD), such as amyotrophic lateral sclerosis (ALS).

Conventional *in vitro* study models are based on cocultures of motoneurons and skeletal muscle cells from animal origin in 2D. These models have proved to be quite limited for the understanding of neuromuscular connection and NMD. They do not consider that: i) neural somas and muscles or peripheral glia are physically separated *in vivo* and have different microenvironment requirements; ii) both sensory and motor neurons can be altered in particular NMD; iii) glial cells are also affected and involved in several neuromuscular pathologies; iv) 2D cultures do not mimic physiological conditions; v) rodent models offer limited benefit translated into clinic research, as they do not carry human genetic background.

Later progresses in neuromuscular-mimicking *in vitro* systems, have been achieved incorporating increasingly evolving technologies, such as 3D cell-culture techniques, human induced pluripotent stem cells (hiPSC) and compartmentalised microfluidic culture systems (cμFCS). The later ones are microfluidic devices for 2D or 3D cell-cultures, with several interconnected compartments, each mimicking different microenvironments or functional units in organ or tissue level. 3D cell culture techniques make cells acquire more *in vivo* like phenotype and genotype patterns. And finally, hiPSC serve to create study models that mimic the human physiology in both healthy and pathological conditions.

This thesis, entitled **"Compartmentalised microfluidic culture systems for *in vitro* modelling of neurological and neuromuscular microenvironments"**, aims to study the neuromuscular context *in vitro* through cμFCS and to create physiologically relevant models. It offers an evolving prospective of *in vitro* models, moving from mice to human cells, from 2D to 3D cell cultures, from primary cells to hiPSC, and analysing both healthy and diseased cells.

Chapter 1 reviews the state of the art in the neuromuscular circuit, amyotrophic lateral sclerosis, and the evolution of *in vitro* techniques available for their study. ***Chapter 2*** presents the first approach of the neuromuscular *in vitro* connection model on a chip, showing the relevance of myelin in the peripheral nervous system and in the neuromuscular circuit. ***Chapter 3*** moves to study the proprioception, the differentiation of human neural stem cells to proprioceptive sensory neurons, and their role in ALS. These concepts, together with the ones introduced in *Chapter 2*, are integrated in ***Chapter 4***, presenting the development of a physiological human neuromuscular circuit on a microfluidic device, that integrates neuromuscular motor and sensory pathways in a 3D cell culture system. Lastly, in a context of neuromuscular vascularisation, ***Chapter 5*** studies the blood-brain barrier and the techniques to monitor its permeability, known to be affected in some NMD such as ALS.

This thesis presents the use of several cμFCS for different purposes, incorporating the study of several neuromuscular key role players and obtaining the following results. Myelination induction was successfully incorporated in a designed and fabricated compartmentalised microfluidic culture system (a PDMS device with two compartments connected

through microchannels). This system was capable of a simplified mimicking of both peripheral nervous system and neuromuscular afferent or efferent pathways. To move onto human models, first proprioceptive sensory neuron (pSN) differentiation protocol was established. Genetic comparative analysis between healthy and ALS diseased samples revealed differences among pSN related genetic patterns and those involved in the communication between pSN and motoneurons (MN). Human pSN differentiation was combined with skeletal muscle cells to create sensorimotor units in a two-compartment commercial microfluidic device, showing for the first time the formation of synaptic bouton like structures in the contact points of an annulospiral wrapping. Then, a human neuromuscular circuit model was created, integrating for the first time human motor and sensory pathways in 3D cultures in tailored microfluidic devices. Finally, the blood-brain barrier was studied as an example of neural vascularisation, within the framework of potentially affected components in NMD. To that end, a new technology for the *in vitro* monitorisation of blood-brain barrier permeability was created and implemented in a device previously developed in the lab. This system could easily be translated for blood-spinal cord barrier studies.

This thesis gathers many technological innovations from a Bioengineering point of view, paving the way for future studies in the neuromuscular field. It shows that the integration of the entire neuromuscular circuit components in the developed *in vitro* systems provides a wider view of the neuromuscular physiology and the pathological processes. These results show first steps towards future 3D physiological neuromuscular circuit models on a chip for NMD studies.

RESUMEN

El movimiento de las fibras musculoesqueléticas está generado por el circuito locomotor, en el que toman parte diversos tipos celulares. Los fallos en cualquier parte de dicho circuito pueden originar la aparición de enfermedades neuromusculares (ENM) o determinar su gravedad, como por ejemplo en el caso de la esclerosis lateral amiotrófica (ELA).

Los modelos de estudio *in vitro* convencionales están basados en los cocultivos de motoneuronas con células de músculo esquelético de origen animal en 2D. Estos modelos han demostrado una eficacia limitada a la hora de comprender la conexión neuromuscular y las ENM. No tienen en cuenta que: i) los somas neurales están físicamente separados *in vivo* del músculo y de la glía periférica, y tienen diferentes requerimientos microambientales; ii) tanto las neuronas motoras como las sensoriales pueden estar alteradas en ciertas ENM; iii) las células gliales también están afectadas e involucradas en diversas patologías neuromusculares; iv) los cultivos 2D no imitan las condiciones fisiológicas; v) los modelos de roedor ofrecen un beneficio limitado a la hora de trasladarlos a la investigación clínica, dado que no tienen una dotación genética humana.

Los últimos progresos realizados en sistemas *in vitro* de modelado neuromuscular, se han conseguido incorporando tecnologías punteras en constante evolución, como el cultivo celular en 3D, las células madre humanas pluripotentes inducidas (hiPSC), y los sistemas microfluídicos de cultivo compartimentado (cμFCS). Estos últimos son dispositivos microfluídicos para el cultivo celular en 2D o 3D, con varios compartimentos interconectados, cada uno de ellos capaz de imitar diferentes microentornos o unidades funcionales a nivel de órgano o

tejido. Las técnicas de cultivo celular en 3D permiten a las células desarrollar patrones de fenotipo y genotipo más parecidos a los encontrados *in vivo*. Y finalmente, las hiPSC ayudan a crear modelos de estudio capaces de imitar la fisiología humana tanto en condiciones sanas como enfermas.

Esta tesis, titulada "Sistemas microfluídicos de cultivo compartimentados para el modelaje de microentornos neurológicos y neuromusculares" (título original: "**Compartmentalised microfluidic culture systems for *in vitro* modelling of neurological and neuromuscular microenvironments**"), tiene como objetivo estudiar el contexto neuromuscular *in vitro* a través de cμFCS, y crear modelos de estudio fisiológicamente relevantes. Ofrece una perspectiva evolutiva de modelos *in vitro*, pasando de células murinas a humanas, de cultivos celulares 2D a 3D, de células primarias a hiPSC, y analizando tanto células sanas como enfermas.

El ***Capítulo 1*** hace una revisión bibliográfica del estado del arte en el circuito neuromuscular, la esclerosis lateral amiotrófica, y la evolución de las técnicas *in vitro* disponibles para su estudio. El ***Capítulo 2*** presenta la optimización inicial del modelo de conexión neuromuscular *in vitro* en un chip, junto con el estudio de la relevancia de la mielina en el sistema nervioso periférico y en el circuito neuromuscular. El ***Capítulo 3*** pasa a estudiar la propiocepción, la diferenciación de células madre neurales humanas a neuronas sensoriales propioceptivas, y su papel en el desarrollo de la ELA. Estos conceptos, junto con los introducidos en el *Capítulo 2*, se integran en el ***Capítulo 4***, presentando el desarrollo de un circuito neuromuscular humano fisiológico en un dispositivo microfluídico,

que integra las vías sensoriales y motoras neuromusculares en un sistema de cultivo celular en 3D. Finalmente, en el contexto de la vascularización neuromuscular, el ***Capítulo 5*** estudia la barrera hematoencefálica y las técnicas para monitorizar su permeabilidad, afectada en ciertas ENM como la ELA.

Esta tesis presenta el uso de varios cμFCS con diferentes fines, incorporando el estudio de diversos actores neuromusculares principales y obteniendo los resultados que se explican a continuación. La inducción de la mielinización se incorporó con éxito en los dispositivos microfluídicos compartimentados previamente diseñados y fabricados (dispositivos de PDMS con dos compartimentos conectados por medio de microcanales, cada uno conectado a diferentes reservorios con medio de cultivo celular específico). Este sistema fue capaz de imitar de forma simplificada tanto el sistema nervioso periférico como la conexión neuromuscular eferente o aferente. Para pasar a modelos humanos, primero se estableció un protocolo de diferenciación de neuronas sensoriales propioceptivas (pSN). El análisis genético comparativo entre muestras sanas y enfermas de ELA mostró diferencias en los patrones genéticos relacionados con pSN y en aquellos involucrados en la comunicación entre pSN y motoneuronas (MN). Las pSN humanas se combinaron con miocitos esqueléticos humanos para crear unidades sensorimotoras en dispositivos microfluídicos comerciales con dos compartimentos, en los que se observó por primera vez la formación de estructuras similares a botones sinápticos en los puntos de contacto de una envoltura anuloespiral. Posteriormente, se creó un modelo de circuito neuromuscular humano, integrando por primera vez las vías motora y sensorial en cultivos 3D en dispositivos microfluídicos diseñados y fabricados en el laboratorio. Finalmente, se

estudió la barrera hematoencefálica como ejemplo de la vascularización neural, dentro del marco de componentes potencialmente afectados en ENM. Para ello, se creó un nuevo método para la monitorización *in vitro* de la permeabilidad de la barrera hematoencefálica, que podría adaptarse fácilmente para estudios de la barrera sangre – médula espinal.

Esta tesis recoge muchas innovaciones tecnológicas desde el punto de vista de la Bioingeniería, abriendo nuevas puertas para futuros estudios en el campo neuromuscular. Muestra que la integración de todos los componentes del circuito neuromuscular en los sistemas *in vitro* aquí desarrollados aporta una visión más amplia de la fisiología neuromuscular y los procesos patológicos. Estos resultados representan un primer paso hacia los futuros modelos 3D de circuitos neuromusculares fisiológicos en un chip para estudios de enfermedades neuromusculares.

General objectives

The global aim of this thesis, entitled **"Compartmentalised microfluidic culture systems for in vitro modelling of neurological and neuromuscular microenvironments"**, is to study the neuromuscular context through compartmentalised microfluidic culture systems and to create physiologically relevant *in vitro* study models.

For that purpose, thesis key objectives were the following ones:

1. To develop a platform for *in vitro* neuromuscular cell culture.
2. To identify key components of the neuromuscular circuit (i.e. glia, myelination, sensory neurons and vascularisation) and implement them in the *in vitro* system.
3. To stablish the methodology for culturing neuromuscular mouse cells in 2D and 3D inside a microfluidic device.
4. To establish a protocol to obtain proprioceptive sensory neurons (pSN) from human neural stem cells.
5. To evaluate the role of proprioceptive sensory neurons (pSN) in ALS using different medium components.
6. To adapt the platform for human neuromuscular studies integrating the sensorial and motor neuromuscular pathways in a complete neuromuscular 3D culture circuit model.
7. To study the Central Nervous System – Blood barrier for neuromuscular disease treatment approach.
8. To create *in vitro* models that could be translated for ALS disease studies.

To that end, the specific objectives of each chapter were the following ones:

1. To study the neuromuscular context (addressed in *Chapter 1*).

- **1.1.** To explain the neuromuscular circuit physiology and the interaction among cells involved.
- **1.2.** To review neuromuscular study models *in vitro*.
- **1.3.** To explain amyotrophic lateral sclerosis pathology, as a neuromuscular disease example, related to myelination, proprioception and neurovascular failures.

2. To stablish the methodology for 2D and 3D neuromuscular cell culture of a mouse model in a microfluidic device (addressed in *Chapter 2*).

- **2.1.** To compare the best procedure to promote myelination in Schwann cells through different medium components.
- **2.2.** To design and fabricate a two-compartment microfluidic device suitable for the 2D neuronal culture.
- **2.3.** To mimic a simplified preliminary version of myelinating peripheral nervous system on a chip.
- **2.4.** To find an optimal Matrigel-based composite suitable for the 3D cell culture of all cells required for a neuromuscular circuit model.
- **2.5.** To mimic a simplified preliminary version of neuromuscular efferent and afferent connection on a chip.

3. To obtain sensory neurons from human neural stem cells and analyse the role of proprioceptive sensory neurons in ALS (addressed in *Chapter 3*).

- **3.1.** To optimise proprioceptive sensory neuron differentiation protocol from human neural stem cell, valid for healthy and ALS cells.
- **3.2.** To assess proprioceptive sensory neuron marker differences between healthy and ALS cells when exposed to different media conditions.

4. To stablish the basis to create a human neuromuscular circuit on a microfluidic device in 3D culture (addressed in *Chapter 4*).

- **4.1.** To differentiate neural stem cells to motoneurons and proprioceptive sensory neurons independently and assess their morphological differences.
- **4.2.** To differentiate human skeletal myoblast to myocytes.
- **4.3.** To perform compartmentalised coculture of proprioceptive sensory neurons and skeletal muscle in 2D, adapting commercial Xona microfluidic devices.
- **4.4.** To design and fabricate a compartmentalised device suitable for the 3D culture of motoneurons, skeletal myocytes and sensory neurons embedded in a hydrogel.
- **4.5.** To perform compartmentalised coculture of proprioceptive sensory neurons, skeletal muscle and motoneurons in 3D, embedding cells in Matrigel and seeding them in MINDS devices.

5. To create a microfluidic healthy blood-brain barrier (BBB) mimicking system, modulate barrier integrity and monitor it (addressed in *Chapter 5*).

- **5.1.** To adapt a two-compartment microfluidic device for a blood-brain barrier on a chip *in vitro* model.
- **5.2.** To mimic a simplified healthy BBB model, coculturing endothelial cells and pericytes on the fabricated compartmentalised microdevice
- **5.3.** To promote BBB formation, disruption after hyperosmotic treatment and recovery.
- **5.4.** To design a system to analyse barrier integrity assembled in the microfluidic device.
- **5.5.** To assess barrier status at different timepoints correlating results obtained through immunostaining with barrier integrity measurement techniques (with dyes and electrical impedance spectroscopy).

Chapter 1

General introduction

Summary

This chapter provides background information regarding the neuromuscular circuit, amyotrophic lateral sclerosis (a neuromuscular disease), and the evolution of *in vitro* techniques available for their study.

Movement of skeletal-muscle fibres is generated by the coordinated action of several cells taking part within the locomotion circuit. Failures in any part of this circuit could impede or hinder coordinated muscle movement and cause or determine the severity of neuromuscular diseases (NMD), such as amyotrophic lateral sclerosis (ALS). Studying fragments of the circuit cannot provide a comprehensive and complete view of the pathological process. This chapter reviews the historic developments of studies focused on *in vitro* modelling of the spinal-locomotion circuit and how bioengineered innovative technologies (such as compartmentalised microfluidic culture systems, human induced pluripotent stem cells and 3D cell-cultures) show advantages for an accurate mimicking of physiological conditions of spinal-locomotion circuit. It finally addresses limitations and main challenges of current neuromuscular *in vitro* study models. Overcoming these challenges would significantly facilitate understanding the events taking place in NMD and accelerate the process of finding new therapies.

Published content, contributions and acknowledgements

The work presented here is an adaptation of these paper, including some more information regarding ALS.

Challenges and Future Prospects on 3D in-vitro Modelling of the Neuromuscular Circuit

M. Badiola-Mateos[1,2], A. Hervera[1,3,4,5], J. A. del Río[1,3,4,5], J. Samitier[1,2,6]

[1] Institute for Bioengineering of Catalonia (IBEC) - Barcelona Institute of Science and Technology, Barcelona, Spain.
[2] Department of Electronics and Biomedical Engineering, Faculty of Physics, Universitat de Barcelona, Barcelona, Spain.
[3] Department of Cell Biology, Physiology and Immunology, Faculty of Biology, Universitat de Barcelona, Barcelona, Spain.
[4] Centro de Investigación Biomédica en Red sobre Enfermedades Neurodegenerativas, Barcelona, Spain.
[5] Institut de Neurociències de la Universitat de Barcelona, Barcelona, Spain.
[6] Centro de Investigación Biomédica en Red en Bioingeniería, Biomateriales y Nanomedicina, Madrid, Spain.

Published in Frontiers in Bioengineering and Biotechnology (2018).

The review cited above was achieved in collaboration with some members from the Molecular and Cellular Neurobiotechnology group at IBEC: Dr. Arnau Hervera and Prof. Jose Antonio del Río, who guided me, gave me feedback and support in Neurobiology related matters.

1.1. Locomotion circuit and neuromuscular diseases

From the physiological and anatomical points of view, the mechanosensory-motor circuit is complex, involving several cell-types with specific natural environments. Traditionally, it has been studied coculturing different cell-types on the same platform from animal origin in 2D,[1–3] and 3D,[4–6] or from human origin,[7,8] or mixed species.[9,10] These models provide valuable information in understanding some of the mechanisms underlying the system; but to the date they have not been able to replicate the exact human complexity of physiological functional-units formed by the connection of different cell-types, arising from separated microenvironments. Compartmentalised microfluidic culture systems (cμFCS)[11] represent an alternative to overcome those problems and, combined with 3D-culture techniques and the use of human induced pluripotent stem cells, they could help recreating neuromuscular physiology of humans *in vitro.*

Locomotion circuit, also known as mechanosensory-motor circuit or reflex-arc circuit, is responsible for executing voluntary and reflex skeletal-muscle movement, alternating flexion and extension of the muscle.[12–14] The coordinated-action of cells taking part within is what generates movement: **i)** motor-neurons (MN), located in the ventral area of the spinal cord, are in charge of carrying information

from the central nervous system to the muscle;[15] **ii)** sensory-neurons (SN), located in the dorsal root ganglia (DRG), carry information from the periphery of the body (the muscle in this case) to the central nervous system;[15] **iii)** interneurons, innervate motoneurons and are linked to their pattern of sensory input;[16] **iv)** Schwann cells (SC) are small cells that form a myelin-sheath around MN and SN axons that insulates them and enhances signal conduction;[15] **v)** astrocytes maintain synapses, modulate the transmission of the signal, regulate blood flow, and availability of oxygen, nutrients and survival factors onto neurons [17]; **vi)** microglia are phagocytic and immunocompetent cells within the central nervous system, able to induce MN cell-death;[18,19] **vii)** skeletal-muscle cells are multinucleated and elongated cells, with sarcomeric striations that form muscle-fibres distributed in fascicle fashion and are the last executors of voluntary and reflex skeletal-muscle movement.[20,21]

The events that take part within the neuromuscular circuit to guide the movement in mammals could be resumed as follows. Once the brain takes the decision of initiating a movement, the signal is transmitted from neocortical projecting neurons through the spinal-cord. Then the spinal-locomotion circuit (see FIGURE 1-1) takes part of guiding the voluntary and reflex skeletal-muscle movement [13,15,20]: **1)** somatic α-motoneurons (α-MN) arising from the ventral-horns of spinal-cord, send the input to the synaptic end-bulbs, triggering calcium flows inwards and the release of the

neurotransmitter acetylcholine (ACh) in the neuromuscular junction (NMJ) between the motoneuron and the motor-end plate of extrafusal muscle-fibres; **2)** ACh binds specifically to the skeletal-muscle motor-end plates' ACh-receptors (AChR), inducing contraction of sarcolemma, releasing calcium into the sarcoplasm, that binds to troponin on the thin filaments, facilitating myosin-actin binding and triggering muscle contraction; **3)** intrafusal muscle fibres, located interspersed parallel to extrafusal fibres, change in length as the whole muscle changes; **4)** proprioceptive sensory-neurons (pSN) sense muscle fibre elongation through muscle-spindle — formed by SN nerve endings wrapped around central areas of intrafusal fibres — , and contraction through Golgi tendon organ — formed by encapsulated structures of collagen fibres located at the joint between muscle fibres and tendons that compress innervating a single SN axon — propagating an impulse signal back to the spinal-cord where is modulated by local interneurons and; **5)** γ-motoneurons modulate excitatory input adjusting the contractibility of the muscle-spindle by stimulating intrafusal fibres adapting them to an appropriate length; **6)** the integration of both afferent signals from the muscle-spindle and the Golgi tendon organ travels through the spinal-cord to the brain to have awareness of the position of the muscle and movement (muscle extension-flexion state), coordinating movements.

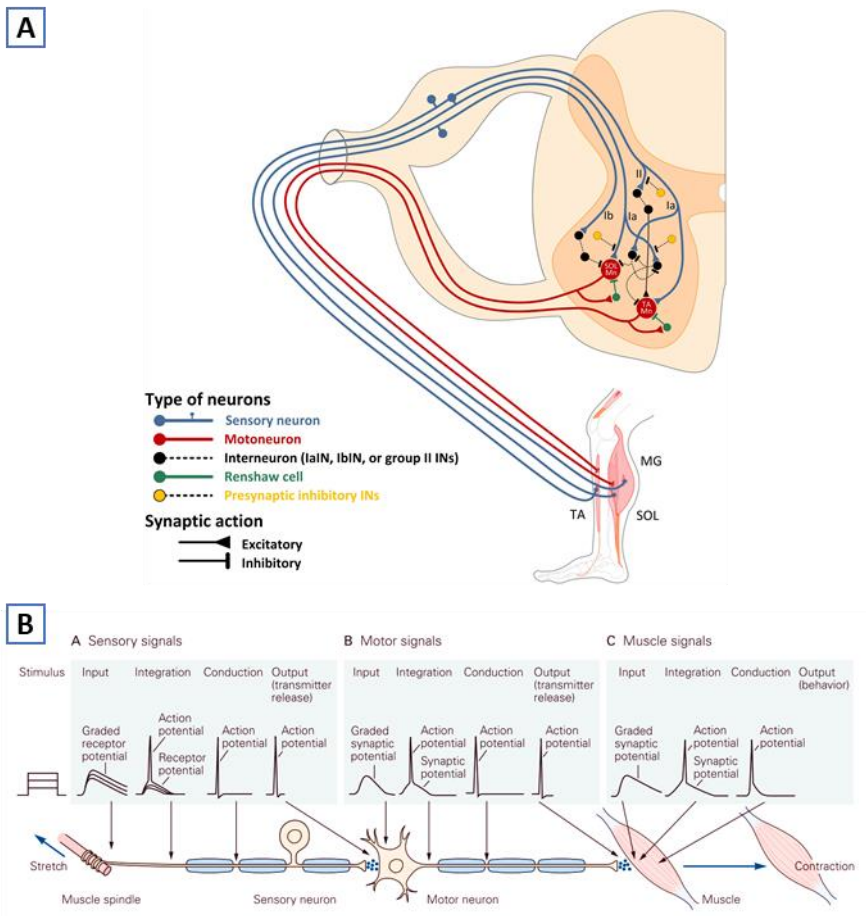

Figure 1-1. *Reflex-arc circuit.* ***A)*** *Spinal neuromuscular interneuronal circuits. Intraspinal circuits show excitatory and inhibitory signals of interneurons and Renshaw cells on motoneurons and sensory neurons to obtain coordinated movements on flexor and extensor muscles on the leg: tibial anterioris (TA), soleus (SOL) and medial gastrocnemius (MG). Image reproduced from Côté et al.*[16] ***B)*** *Myotatic reflex sequence of signals. When a muscle is stretched, the muscle spindle transmits that information through a receptor potential on sensory neurons. The signal propagates along SN axons to axon terminals, where a neurotransmitter is released initiating a synaptic potential onto motoneurons, that spreads to the MN axons where an action potential is initiated that propagates to the terminal, triggering synaptic potential in the muscle and finally leading to its contraction. Image reproduced with permission from Kandel et al.*[15]

Failures in any part of this circuit can hamper coordinated muscle movement and be the cause of neuromuscular diseases (NMD) or

be the consequence that defines their severity.[22] The term of NMD comprises several diseases with different origins and affectations (such as muscular dystrophy, amyotrophic lateral sclerosis, myasthenia gravis or spinal muscular atrophy). The effects of NMD are reflected in the mechanosensory-motor circuit at different cellular levels — including sensory and motor neurons,[22,23] Schwann cells,[1,24,25] astrocytes,[17] microglia,[19,26] muscle[27,28] —, as well as in the connexions among them — neuromuscular junction,[28–30] muscle spindle[31,32] —, or intraspinal circuits. However, they all share symptoms such as: peripheral hypotonia, muscle weakness and orthopaedic deformities, among others.[33–35] These symptoms impoverish patient's life-quality.[33] There is still no treatment for them. Current study models are far from mimicking physiology and therefore are limited on helping to find cures. The technologies reviewed in this chapter and employed along the thesis (FIGURE 1-2) aim to help on that direction.

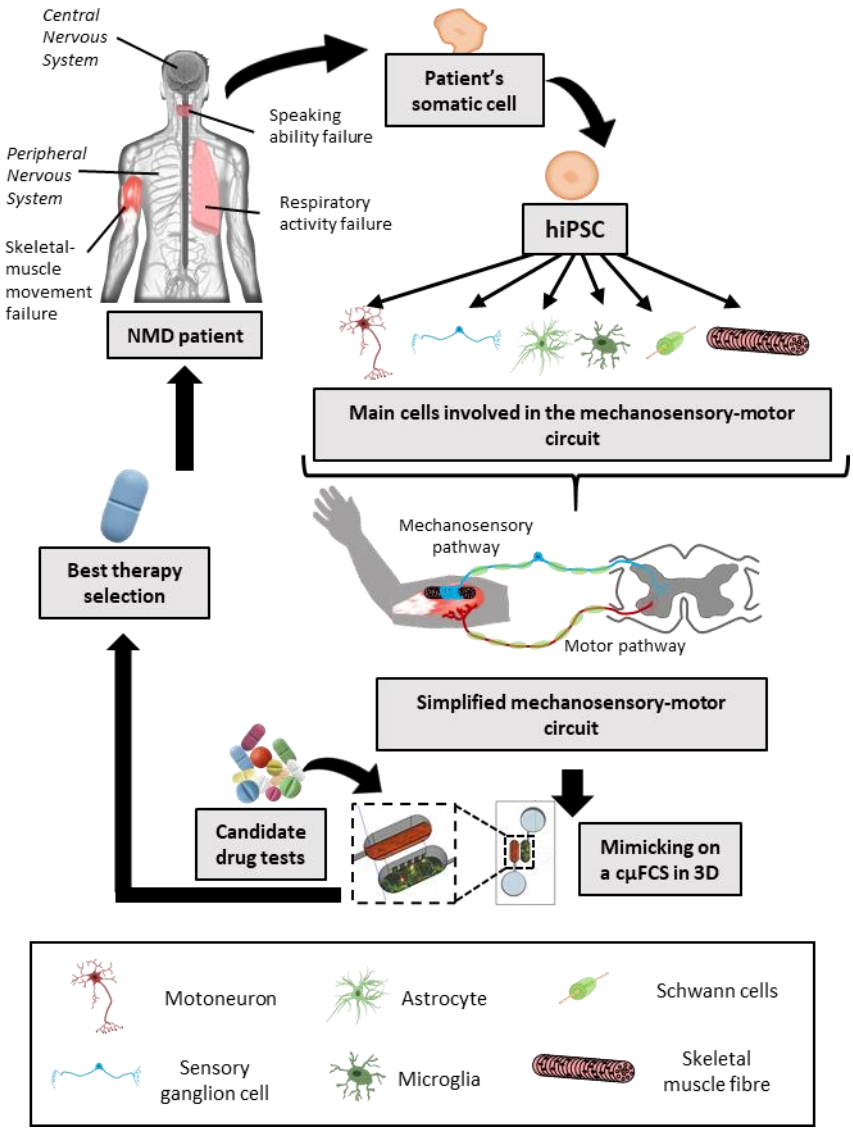

Figure 1-2. *Future prospects on in vitro neuromuscular disease modelling. The implementation and combination of later innovative technologies (hiPSC, cμFCS, 3D cell-culture) would facilitate the recreation of patient's physiological conditions with their own disease-carrying cells mimicking the mechanosensory-motor circuit in 3D inside a microfluidic compartmentalised device. And finally, it would serve to find specific treatments for each NMD. Image reproduced from Badiola-Mateos et al.*[36]

1.2. State of the art: *in vitro* study models

1.2.1. Cell source and cell culture techniques

NMD and NMJ *in vitro* models have gone through a long evolution history[37]: the use of primary cells, cell lines and stem cells; animal-animal cocultures, human-human cocultures, xeno-cocultures; and disease-specific studies. But as reported, most of the research has been done until now by coculturing healthy and diseased cells; primary cells or cell lines with stem cells; and mostly on rodent models or xeno-cultures (human-animal models). However, rodent models offer limited benefit translated into clinic as they do not carry human genetic background. Therefore, personalised medicine needs patient-specific isogenic disease models. In this regard, human induced pluripotent stem cells (hiPSC) offer the possibility of obtaining different isogenic cell-types from patient's somatic cells, by overexpressing some transcription factors,[38] later reviewed.[39] They can serve both for creating study models that mimic the physiopathology of the patient, with the further development of future therapeutic transplantation strategies.[40]

The use of induced pluripotent stem cells for disease-modelling, drug-screening and regenerative therapies of NMD has widely evolved in the last years.[41] Nevertheless, few studies have cultured hiPSC-derived motoneurons with hiPSC-derived skeletal-muscle

cells *in vitro.*[8,42–44] Puttonen *et al.* reported a method for the simultaneous differentiation of motoneurons and myotubes from patient-specific hiPSC, obtaining neuronal differentiation, multinucleated spontaneously contracting myotubes and functional NMJs on a 2D monolayer.[42] In contrast, Demestre *et al*. used hiPSC from healthy donors differentiated separately to motoneurons and myotubes, and subsequently cocultured in 2D. They observed AChR formation in the muscle and neurites outgrowing from motoneurons within the first weeks; but AChR aggregation, maturation of muscle cells and NMJ formation was not detected until 3 weeks of monolayer cocultures.[8]

The advantages and disadvantages between 2D and 3D hiPSC cultures for neurodegenerative disease studies were recently reviewed.[45] Briefly, the main outstanding contributions of 3D cultures on NMD are that: **i)** it has been proved that 2D monolayers present in some cases altered gene expression whereas 3D cultures display a genotype more relevant to *in vivo*;[45,46] **ii)** cells cultured in 3D acquire more *in vivo* like phenotype (lower proliferation rate, areas with different levels of oxygen distribution, higher cell-to-cell and cell-extracellular matrix interactions, increased viability, proliferation, differentiation and response to stimuli of other cells);[45,47,48] **iii)** some higher-order processes, such as angiogenesis, occur inherently in 3D.[45,49] But so far, only two studies have been able to mimic the NMJ in 3D using hiPSC-derived motoneurons and skeletal-muscle cells *in vitro.*[43,44] Maffioletti *et al.* used somatic cells

from muscular dystrophy patients to create hiPSC-derived isogenic multilineages (skeletal-muscle cells, vascular endothelial cells, pericytes and motoneurons), subsequently cocultured embedded in fibrin hydrogels.[43] Osaki *et al.* created an ALS microphysiological 3D model culturing ALS-hiPSC-derived neural stem cells with hiPSC-derived skeletal-myoblasts embedded in collagen-Matrigel composites.[44]

However, there are still no studies utilising hiPSC-derived sensory-neurons and hiPSC-derived muscle-cells to mimic the sensory pathway of the spinal reflex-arc circuit. The latest advances on this respect were published by the group of J.J. Hickman using sensory-neurons derived from human neural progenitor cells and intrafusal fibres generated from human skeletal-muscle stem cells, cocultured on a 2D monolayer.[32]

1.2.2. Compartmentalised microfluidic neuromuscular culture systems

The broad range of study models used for biomedical applications includes animal models of human diseases, *in vitro* models (cell culture, bacteria, viruses and yeast) in Petri dishes or modelling and simulation systems.[50] Traditional coculture methods, such as Petri dishes, do not consider: **i)** the different microenvironment requirements of muscle, nerves and neurons; **ii)** the distal connexions as they are physically separated *in vivo*. Furthermore,

finding a medium composition compatible for the long-term coculture of both cell-types could be challenging, as several medium components ideal for MN are incompatible with long-term maintenance of skeletal-muscle cells.[37,51] Hence, a coculture system between neurons and muscle offers limited benefits on mimicking the pathophysiology of NMD.

Compartmentalised microfluidic culture systems (cμFCS)[11,36] are microfluidic 2D or 3D cell-culture devices with several compartments interconnected, each mimicking different microenvironment of functional units in organ or tissue level: multicellular architecture, tissue-tissue interfaces (flows and barriers), physicochemical microenvironments (chemical gradients, mechanical strain and electrical stimulation) and pathophysiology.

Their use is increasingly growing for neurobiology studies due to the advantages offered compared to classical coculture systems, reviewed in Box 1. Most relevantly, they enable independent culture conditions for neurons and muscle cells, each supplied by its own microenvironment requirements in different interconnected but fluidically isolated compartments, whilst axons can still go through microgrooves connecting cells of both compartments.

Box 1. Top 10 advantages of compartmentalised microfluidic culture systems (cμFCS) compared to traditional coculture systems for mimicking spinal-locomotion circuit *in vitro*.

1. **Fluidic control.** Compartmentalisation enables to control de fluidic environment and provide each cell-type required nutrients to efficiently mature, facilitating survival, functionality and long-term coculture.[51,52]
2. **Experiment feasibility.** Ease to study, enhance, control and monitor some processes (cell proliferation, differentiation, directional growth, migration, and media diffusion from one compartment to the other).[50,53]
3. **Microenvironment spatiotemporal control and monitoring.** Independent manipulation of each compartment cells or extracellular matrix hydrogels could be a critical point to assess some processes. Compartmentalised platforms make possible to dissect molecular and cellular events occurring in somal versus axonal compartments (effect of compounds, drug-sensitivitiy test, etc.);[54–56] to track individual axons through microchannels;[57] and to assess axon-specific molecules through immunostaining, protein lisate isolation and mRNA isolation.[56,58]
4. **Customisability of cμFCS designs.** Control over microchannel geometry and dimensions (and therefore sifting of cells or compounds that can pass from one compartment to the other), number of compartments (and therefore number or different microenvironments, if required), compartment division tool (micochannels, microgrooves, membranes), distance between compartments, possibility to include reservoirs, covered or opened compartments, scalability, and device size.[30,55,59,60]
5. **Customisable engineering features.** Possibility to integrate and take control over parameters: shear-stress flows;[61,62] mechanical,[57] optical[63,64] and electrical stimuli;[65] topographical cues or micropatterns;[66] chemical gradients;[67] and sensory systems.[68,69]
6. **Cost-effectiveness.** Low volume of cells and reagents are required.[70]
7. **Control over the polarity of neural development.** Culturing somas on one compartment makes possible to take control over axon and dendrite polarity during the development, and hence, to mimic axon injuries and study post-injury regeneration easily.[71–73]
8. **Possibility to mimic neural distal connexions.** Neurons growing on one compartment can extend their axons to interact with the other compartment cells, mimicking distal connexions.[28,55,56]
9. **Possibility to integrate control over the polarity of myocyte differentiation.** Skeletal-muscle cells usually adopt randomised distribution *in vitro*, whereas the presence of aligned micropatterns for 2D culture, cantilevers for 3D culture, or some stimuli methods (mechanical, electrical or optical) integrated on the cμFCS can enhance its appropriate differentiation and functionality.[30,74–76]
10. **Better mimicking of physiological conditions and possibility to connect with other microfluidic platforms.** This facilitates the study interactions between different physiological functional-units,[77] as well as to integrate blood-flow effects,[78] or in a future, to mimic a full human-on-a-chip,[53,79] enhancing the development of therapies or diagnostic tools.[50,53,80]

First compartmentalised microfluidic culture system (cμFCS) for neurobiology studies on neurotrophic effects of dorsal rood ganglion cells,[81] used Teflon-made open compartments, silicone-glue and microchannels shattered in glass. Since then, and after soft-lithography fabrication improvements, cμFCS have widely evolved in the last 10 years for spinal-locomotion circuit studies (TABLE 1-1). Most compartmentalised cocultures are nowadays performed onto polydimethylsiloxane (PDMS)-based platforms with two cellular compartments separated through microchannels or, as described in the only two publications found using a 3D cell coculture, through a gel region.[30,44] Different cell sources are used for MN (predominantly mouse embryonic primary cells) and muscle-cells (using equally rodent hind limb primary skeletal-muscle cells and C2C12 cell-line).

Besides, there are progressively more commercial cμFCS on the market,[82] available for neuromuscular and other neurobiology studies in 2D or 3D, connecting two compartments through microchannels, microposts or membranes, from the following companies: **i)** Xona neuron devices (Xona Microfluidics, California), used in some neuromuscular studies;[83,84] **ii)** ANANDA Neuro-Device and Coculture-Device (Advanced Nano Design Applications Devices, Canada) employed by Magdesian *et al.* combined with AFM measurements to study neuronal growth;[85] **iii)** OrganoPlates for 3D culture (Mimetas BV, Netherlands) used to differentiate stem cells into neurons in 3D,[86] or for high-throughput evaluation of

compounds in glia and neuronal 3D culture;[87] **iv)** AIM 3D culture chips (AimBiotech, Singapore), employed mostly in cancer-research,[88] although with a great potential to be used in neuromuscular studies, as performed by Uzel *et al.* with a similar custom made device;[30] **v)** Neural Diode (MicroBrain Biotech, France) to reconstruct oriented neural network monolayer cultures;[72,89] **vi)** Idealised coculture chips (Synvivo, USA), with different options of radial slits or pillars utilised in many cases to mimic the BBB,[90] or linear slits for compartmentalization purposes.

However, and despite the advantages offered by both hiPSC and cμFCS technologies, at the moment only two studies have attempted to mimic the spinal-locomotion circuit combining both technologies.[29,44] Santhanam *et al.* seeded healthy donor's hiPSC-derived MN and human skeletal-muscle fibres in 2D, for dose-evaluation study of toxins affecting the NMJ.[29] Osaki *et al*. created an ALS microphysiological 3D *in vitro* study-model and compared it with a healthy model (muscle contraction, recovery, and response to drugs administered via endothelial cell barrier).[44,91]

Table 1-1. *Summary of the last 10 years evolution of publications using compartmentalised microfluidic culture systems (cμFCS) for the study of spinal-locomotion circuit. This review is limited to publications employing motoneurons or sensory neurons and skeletal muscle, from rodent or human origin. All papers shown are related to motor pathway studies, as no publication has been found using cμFCS for the study of the mechanosensory pathway.*
Ref.= literature reference. No publications were found utilising cμFCS to study the mechanosensory pathway. H/H = healthy neurons and healthy muscle cells utilised in the study. LxWxH = length x width x height.

Neuron cell source	Muscle cell source	Culture	Disease	cμFCS fabrication and compartment separation method	Ref.
embryonic rat (E15) primary MN	postnatal rat (P2) hind limb primary skeletal-muscle cells	2D	H/H	Xona microfluidics commercial device	83
mouse ESC-derived embryoid bodies differentiated to MN	mouse myoblast C2C12 cell line	2D	H/H	Custom made PDMS device. Microchannel dimensions (LxWxH): 500 μm x 10 μm x 2.5 μm	92
mouse embryonic (E13.5) MN	mouse myoblast C2C12 cell line	2D	H/H	Custom made PDMS device. Microchannel dimensions (LxWxH): 1mm x 10μm x 2.7μm	51
mouse embryonic (E13.5) MN	mouse myoblast C2C12 cell line	2D	H/H	Xona microfluidics commercial device	84
mouse embryonic (E11-E12) MN	adult mice hind limb primary skeletal-muscle cells	2D	H/H	Custom made PDMS device. Microchannel dimensions (LxWxH): 400 μm x 15 μm x 5 μm	56
mouse embryonic (E11.5-E12.5) MN	adult (>P30) mice hind limb primary skeletal-muscle cells	2D	H/H	Custom made PDMS device. Microchannel dimensions (LxWxH): 400 μm x 15 μm x 5 μm	93
mouse embryonic stem cell line HBG3	mouse myoblast C2C12 cell line	3D	H/H	Custom made PDMS device.	30

differentiated into light activatable MN				A gel region separates both compartments 1mm.	
hiPSC-derived MN	human skeletal muscle myoblastas cell line	2D	H/H	Custom made PDMS device. Microchannel dimensions (LxWxH): 400 µm x 10 µm x 3.5 µm	29
mouse embryonic (E12.5) MN	adult (P60) mice hind limb primary skeletal-muscle cells	2D	H/H	Custom made PDMS device. Microchannel dimensions (LxWxH): 400 µm x 15 µm x 5 µm.	28
SOD1G93A or HB9::GFP mouse embryonic (E11.5) ventral horn explants	adult (P60) SOD1G93A mice hind limb primary skeletal-muscle cells		ALS		
MN spheroids formed from human embryonic stem cell–derived neural stem cells	hiPSC-derived skeletal myoblasts	3D	H/H	Custom made PDMS device. A gel region separates both compartments 700 µm.	44,91
MN spheroids formed from ALS-patient hiPSC-derived neural stem cells			ALS		

1.3. Limitations of current study models and main challenges

1.3.1. Combination of hiPSC, cμFCS, and 3D-cell culture technologies

The three innovative technologies offer advantages (FIGURE 1-2), but the novelty itself comes with the challenge of developing, tuning and implementing them together in a unique and biologically reproducible functional platform. As previously described, there is one single research group combining 3D culture, hiPSC and cμFCS as NMD models.[44,91]

1.3.2. Consideration of main actors and roles from the spinal-locomotion circuit

The co-culture of main cell-types participating in the spinal-locomotion circuit is mandatory to provide a native microenvironment, including the inherent release of growth-factors, as well as to support the viability and maturation of both muscle and neurons, and axon elongation of MN.[94] For instance, spinal MN cannot achieve proper maturation even after long-term maintenance, unless cultured with muscle-cells and Schwann cells, as previously reviewed.[95]

The spinal neuromuscular circuit and NMD have been thoroughly studied for years paying special attention to the α-motoneuron and its connection with skeletal muscle (SkM) cells.[36] However, it comprises other cells whose role in NMD has been underestimated: Schwann cells,[1,24,25,96,97] astrocytes,[17] microglia,[19,26] oligodendrocytes,[98,99] SkM cells,[27,28] interneurons[100] (including Renshaw cells, inhibitory interneurons in the ventral horn that are innervated and inhibit α-MN, intermediating their auto inhibition), γ-MN,[101] and pSN (including type Ia, type II and type Ib afferents), and their functional interactions.[102] Both SN and MN could be altered in particular NMD,[23,31,32] but not being many available studies focused on the muscle spindle,[31,32,103–106] challenges the task of mimicking and characterising the mechanosensory spinal-locomotion circuit. Additionally, glial cells are also affected and involved in several neuromuscular pathologies.[1,95,107] And functional neurovascular barriers, required to protect the nervous system and regulate its homeostasis, have altered permeability in ALS.[108,109] Yet, most publications do not consider them in the context of NMD.

Most *in vitro* NMD studies are focused on the α-MN-muscle connexion (TABLE 1-1), very few on the γ-MN-muscle connexion,[110] some on the SN-muscle connexion,[31,32,103–106,111] some on the SC-NMJ interaction,[97] fewer on the internal SN-MN connexion,[112] and even less in the role of neurovascular barriers in NMD.[109,113] But there is still very little known about what happens beyond those

connexions, to what extent cell-strategies for synaptic-specificity contribute on the formation of a functional connexion.[28,114]

Studying parts of the circuit cannot provide a comprehensive and complete view of the pathological process and functional alterations occurring within it. The big challenge that remains out there on NMD studies is the modelling of the whole spinal-locomotion circuit with all cell-types involved, and the evaluation of independent and interdependent roles of each part of the circuit on the development of a particular NMD.

1.3.3. Modelling neurodegeneration in NMD

In a broad sense, neurodegeneration is a process characterised by the progressive functional loss of a population of neurons by intrinsic cell death or the loss of support cells (i.e. oligodendrocytes or astrocytes). Most NMD are characterised by this devastating phenomenon (i.e. motoneuron diseases: amyotrophic lateral sclerosis, or spinal muscular atrophy, etc.).

Indeed, studying only functional changes in MN cannot give a comprehensive and complete picture of the process as it is also regulated by non-neuronal cells.[28,95,107] For instance, a recent study performed by Maimon *et al.* demonstrated that axon degeneration only occurred with both MN and muscle cells carrying the genetic mutation indicative of the disorder.[28] Furthermore, the morphology

of spinal MN axons *in vitro* differs from the one presented *in vivo*: contrary to *in vivo*, axonal terminals *in vitro* manifest growth-cones and are prone to regenerate and lengthen in response to neurotrophic factors required for the *in vitro* maintenance of the culture.[95] On top of that, another caveat is the fact that extrapolating effects of short-term studies to longer-term disease processes is often not correlated. Therefore, mimicking neurodegeneration response *in vitro* as it occurs *in vivo* endures to this day as a challenge. And consequently, there is no effective treatment for neurodegenerative NMD to promote axonal regeneration yet.

1.4. Amyotrophic Lateral Sclerosis, a neuromuscular disease

Amyotrophic lateral sclerosis (ALS) is a neuromuscular neurodegenerative disease that causes the progressive paralysis and is usually fatal within 2-5 years from its diagnosis.[115] Its incidence is around 2-3 people per 100.000 population in Europe,[116] with a mortality rate of 30.000 patients per year.[117] Although it has been studied for more than hundred years, its pathology is still poorly understood.[117] ALS is known to be characterised by the progressive degeneration of motoneurons that result in the loss of synaptic connectivity with muscles and atrophy of the muscles of the tongue, oropharynx, and limbs, affecting also at the late stages muscles from the bladder and eyes.[118] And although ALS has long been thought to be just a motoneuron disease, it is currently known to be influenced by other cells and phenomena (such as inflammation,[119] oxidative stress[120]). The motoneuron degeneration comes together with neuro inflammatory processes driven by the proliferation of astroglia, microglia, and oligodendroglia,[121,122] and demyelinating processes by oligodendrocytes and Schwann cells.[96,97,123] Furthermore, recent studies have shown that proprioceptive sensory neurons are also impaired and go through degeneration.[124–126] And the blood-neural barriers have altered permeability, turning ALS also in a neurovascular disease.[109,113,127] Finding a treatment for such a complex disease involves

understanding all the cellular and biomolecular parameters involved in the pathology and modulating the status of blood-neural barriers.

1.4.1. ALS: a demyelinating disease

Glial cells are non-neuronal cells that provide support to neurons. Glial cells of the CNS include oligodendrocytes, astrocytes, microglia, pericytes, and ependymal cells. The PNS glia includes Schwann cells (SC), and satellite cells. The functions of glial cells comprise: to provide support and protection for neurons; to form a scaffold in the nervous system; to maintain homeostasis, supply nutrients, trophic factors and oxygen to neurons; to destroy pathogens and remove dead neurons or glial cells; to facilitate neurotransmission insulating electrically neurons in myelin sheaths; and to facilitate synaptic connections. Oligodendrocytes and SC are of special importance as they are the ones responsible for myelinating the CNS and PNS respectively. Oligodendrocytes wrap around many neural axons forming in them fragments of myelin sheath through a process of surveying the neuron, anchoring, wrapping and expanding.[128] In the PSN however, each SC wraps around a single axon, being each axon covered by many myelinating or unmyelinated SC that support neural survival and speed up the conduction of neural transmission. Demyelination, — the improper development of myelin or its loss — occurs in many neurological

diseases, such as multiple sclerosis and ALS, causing a disruption in electrical impulse conductivity and neural damages.

ALS is characterised by distal motor axonopathy. Peripheral axons are lost through a degeneration process of fragmentation, the disintegration of the axonal cytoskeleton, myelin degradation, and immune cell infiltration.[129] After axons are lost, SC become denervated, switch to an undifferentiated phenotype and upregulate the production of cytokines, chemokines and trophic factors.[130] In peripheral nerve injuries, SC facilitate repair and axonal growth by a phenotypic remodeling.[131,132] However, a recent publication has shown that in ALS, contrary to nerve injury cases, SC could orchestrate focal nerve inflammation by recruiting specific subsets of macrophages that amplify the disease expressing CSF1 and IL-34.[96]

Moreover, perisynaptic SC or terminal SC, located at the NMJ, play a dynamic role in the NMJ function: they detect and modulate synaptic transmission; they change their properties according to the state of innervation in the NMJ; they release gliotransmitters; they regulate stability and repair of the NMJ by promoting effective re-innervation processes.[97] Selective ablation of them induces a decrease in neurotransmitter release and motor nerve terminal retraction,[133] suggesting that they can influence synaptic activity and NMJ stability.[97] In healthy conditions, perisynaptic SC act on denervated NMJ by: **i)** rapidly extending processes towards

innervated NMJ and initiating the sprouting or formation of nerve terminal sprouts towards the denervated NMJ; and **ii)** by switching from maintenance mode to a repair mode in a denervated NMJ to proceed with phagocytosis of axonal debris, remodelling of the post-synaptic receptors and stabilising the newly re-innervated NMJ.[97] However in ALS, there is a progressive failure of adaptive sprouting — suggesting a failure in the decoding ability of perisynaptic SC that permits them to evaluate the innervation state of NMJ —, and debris clearance and re-innervation processes fail.[97] In ALS it seems that perisynaptic SC lose their ability to adapt to a given synaptic environment,[134] and have an altered production of gliotransmitters. Glial over-activation occurring in ALS leads to increased intracellular Ca^{2+} levels,[134] and could enhance free radical production, mitochondrial overload, redox process alterations and cell membrane damages, leading up to oxidative stress,[97] correlating with perturbations observed in MN.[135]

But apart from SC, oligodendrocytes, responsible for the myelination in the CNS, have been related to the disease progression of a certain type of genetic ALS pathology characterised by the mutation of superoxide dismutase 1 (SOD1) .[98,123] A recent study published by Kim *et al.*,[123] found that the mutation of SOD1 t ALS pathologies, contributes to the degeneration of mature oligodendrocytes by myelin sheath disruption and downregulation of monocarboxylate transporter 1 (MCT1), consequently inducing MN degeneration, anxiety-related behavioural abnormalities,

learning impairments, and motor defects. They suggested that mature oligodendrocyte disfunction induced by the mutation of SOD1 is sufficient to induce MN degeneration.[123]

ALS pathology is characterised as well by the manifestation of psychiatric disorders, such as anxiety and depression, before motor impairment symptoms.[136,137] These symptoms in ALS patients, occurring similarly in multiple sclerosis and other CNS demyelinating diseases,[136,137] have been reproduced in SOD1 mutant ALS models of mice,[138] and zebrafish,[123] suggesting a strong association between SOD1 mutation, ALS pathology and myelin defects.

Studying myelinating cells is a key to understand healthy and ALS diseased neuromuscular circuit functioning and the implications of myelin in the neurodegeneration, re-innervation and restoration of the neural transmission.

The relevance of myelin in the peripheral nervous system and in the neuromuscular circuit is further studied in *Chapter 2* in healthy mice models *in vitro*.

1.4.2. ALS: a proprioceptive sensory neuron disease

Proprioception is the sense of relative spatial positioning of one's body and its movement or force executed on the environment.[139] Muscle spindles, Golgi tendon organs and joint receptors are the

sensorimotor proprioceptive organs known in humans.[140] In the stretch-reflex circuit, proprioception feedback modulates MN activity.

In ALS, α-MN forming the fast-fatigable motor units go first under degeneration, followed by fast fatigue resistant MN, whereas neighbouring slow α-MN, γ-MN, ocular MN and anal sphincter NMJ remain resistant to degeneration.[101,141,142] The lack of stretch-reflex in the eye, external urethral and anal sphincters, and the lack of direct excitatory input from pSN (type Ia) onto γ-MN — both cases with resistance mechanisms to ALS — suggest together that stretch sensitivity of spindles and pSN feedback could be related to the development and progression of ALS.[101,143] The ablation of the spindle has been related to a decrease in MN death in ALS,[101] relating muscle spindle afferents to ALS early triggers of MN degeneration.[144] It is thought that α-MN and pSN may have similar molecular mechanisms involved in the failure, maintenance and repair occurring in ALS.[126] The degeneration occurring in pSN in ALS models is different in each mutation,[126] although it is not well understood yet what drives the different response.

Recent studies have shown proprioceptive sensory neuron degeneration, SN altered morphology, signal transmission and spindle malfunctions in ALS mice models ($SOD1^{\mathrm{G93A}}$, $TDP43^{\mathrm{A315T}}$ and FUS^{P525L}), human stem cell derived neuromuscular models, and human ALS patients.[101,124–126,145] Even before the symptomatic

phase of the disease, there are alterations Ia/II proprioceptive nerve endings in muscle spindles.[125] In the early disease process, stretch-reflex fails generating impaired and arrhythmic action potentials, that could be responsible for initiating fasciculations.[124] In later steps of the disease, DRG pSN have been found to suffer degeneration that involves the inflammatory recruitment of macrophagic cells.[145] The proprioceptor feedback has been found to increase α-MN loss.[101] And eliminating γ-MN — decreasing stretch sensitivity of the spindle and pSN response —, delays the progression of the disease.[101] On top of that, there are few clinical studies published in which they have found evidence of proprioception alterations in ALS patients.[146,147]

Despite all the evidences supporting the idea of an important role of pSN in early ALS development, most of the studies are still exclusively focused in the motoneuron and its connexion with skeletal muscle cells.

Proprioception and its role in the neuromuscular circuit is further explained and studied in *Chapters 3 and 4* in healthy and ALS human models *in vitro*.

1.4.3. ALS: a neurovascular disease

Blood-neural barriers are the biological barriers protecting the nervous system from blood flow. They have the function of limiting

tissue compartments and microenvironments. They regulate medium supply and waste secretion, maintain ion balance, protect the neural tissue from toxins and blood flow, filtrate fluids, etc. There are six types of blood-neural barriers, each with its specialised structure and function: blood-brain barrier (BBB), blood-cerebrospinal fluid barrier (BCSFB), blood-nerve barrier (BNB), blood-retinal barrier (BRB), blood-spinal cord barrier (BSCB), and blood-labyrinth barrier in the inner ear (BLB).[148] They are formed by a protecting layer of endothelial, epithelial, ependymal, endoneurial or perineurial cells, among other structures. Their correct performance is essential to maintain the body homeostasis and prevent serious health complications. When any of these barriers has a structural and functional alteration, with an altered permeability, it causes neurovascular diseases.

The BBB (FIGURE 1-3) is a physical dynamic barrier constituted by a single layer of non-fenestrated endothelial cells, surrounded by a basal membrane, the end-feet of perivascular cells (astrocytes and pericytes or smooth muscle in the case of larger vessels), microglia and neurons, that collectively form the neurovascular unit (NVU).[149] The BBB permeability is controlled by the junctional complexes: tight junctions (TJ), adherens junctions (AJ), and gap junctions.[150,151] Those complexes are intertwined nets of proteins that have a role in controlling the passage of substances. The major transmembrane AJ protein is vascular endothelial cadherin (VE-cadherin).[152]

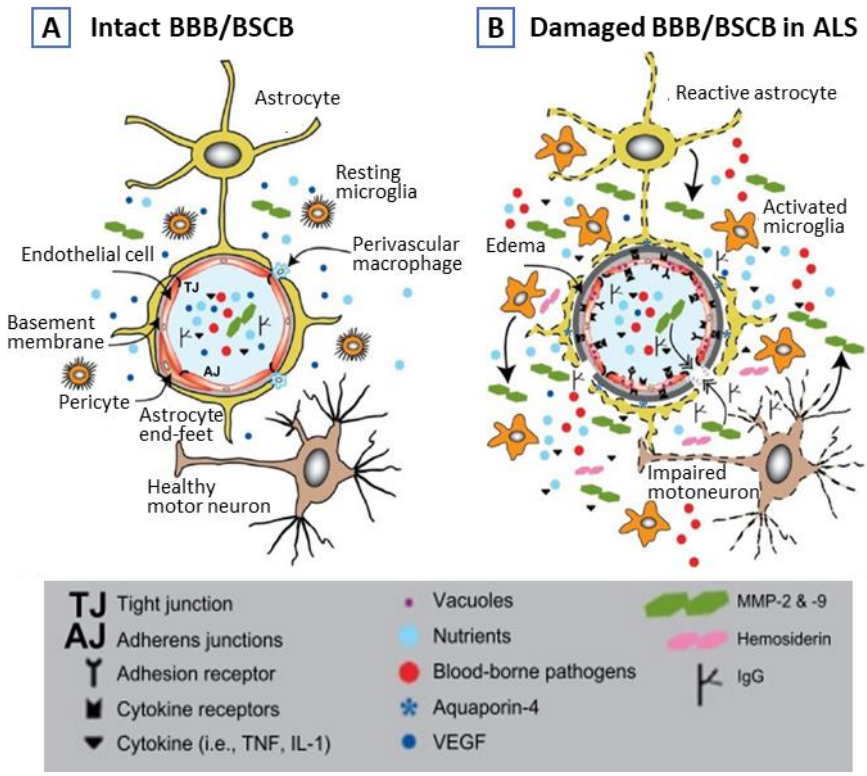

Figure 1-3. *Comparison of healthy versus ALS impaired BBB.* ***A)*** *Healthy BBB regulates brain nutrient supply, waste efflux and paracellular diffusion through specialised junctional complexes (TJ and AJ). In this way, it protects the central nervous system from paracellular diffusion of blood-borne pathogens, cytokines and matrix metalloproteinases (MMP) flowing into the blood, maintaining adequate homeostasis in the neural tissue. Brain endothelial cells (EC) compose the walls of blood vessel. Pericytes are distributed discontinuously along the BBB. Both EC and pericytes are enclosed by the basement membrane. End-feet of astrocytes are in contact with the external basement membrane. Microglia and axonal projections are located in the peripheral neural tissue. All together, they contribute on forming TJ and AJ sealing the aqueous paracellular diffusion pathway.* ***B)*** *In ALS, several modifications occur in basement membrane composition, junctional complexes and transporter system impairment, downregulation of VEGF, activation of MMP-2 and MMP-9 matrix metalloproteinases, serum protein leakage, hemosiderin deposits, and extracellular oedema. On a cellular level, ALS is characterised by the following events: EC degenerate, pericyte population is reduced, astrocyte end-feet degenerate and become reactive and together with activated microglia release cytokines that affect the vascular endothelium and influence neuron impairment. Image reproduced with permission from Rodrigues et al., 2012.*[109]

VE-cadherin based AJ are regulated by zonula occludens 1 (ZO-1), one of the main components of the TJ, essential for an efficient endothelial barrier formation.[153]

Although the main structure between the BBB and the BSCB is the same, there are some differences.[154] An outstanding distinction is that the BSCB is known to have less pericytes, lower levels of certain tight junction (TJ) proteins, such as zonula occludens 1 (ZO-1), and increased capillary permeability compared to the BBB.[155]

Both barriers (BBB and BSCB) are known to be have an altered permeability in ALS pathology, and thus ALS has recently being classified as a neuromuscular and a neurovascular disease.[108,109] Initial evidences of altered blood-neural barrier from 1984 showed blood-borne factors found in the motor cortex and spinal-cord of ALS patients,[156] and altered levels of certain antibodies and complement components in the cerebrospinal fluid, spinal cord and motor cortex of ALS patients.[157] BBB and BSCB impairment have later been demonstrated on ALS mice models and humans. First publications of BBB and BSCB studies on ALS showed in mice worsening of the barrier structure and functionality with disease progression in early stages,[127,158] and altered permeability, TJ protein levels and blood-flow.[158] These results were later correlated on ALS patients with autopsied tissue[113,159] and blood-flow analysis.[160] BBB and BSCB impairment in ALS occurs mainly via endothelial cell (EC) degeneration. However, this alteration is a

product of several events summarised in FIGURE 1-3-B. For instance, ZO-1 proteins levels are known to be reduced both from animal[158] and post-mortem ALS patient studies.[113] As most of these event occur prior to motoneuron damage, it is still arguable whether blood-neural barrier is the initial event and driving factor that causes sporadic ALS.[158,161]

Neurovascular *in vitro* models are required to monitor permeability changes occurring in ALS. The relevance of BBB permeability monitoring techniques is further studied in *Chapter 5* in a healthy *in vitro* model.

1.5. Conclusions

Locomotion circuit is a very complex circuit in which many cells, frequently underestimated, play a role in the movement conduction cascade of events. Failures in any part of the circuit can cause NMD or define their severity. Therefore, it is essential to understand the role of each part of the circuit. Conventional *in vitro* study models coculturing MN and SkM from animal origin in 2D have proved to be quite limited for the understanding of neuromuscular connection and NMD treatment studies, as they do not mimic physiological conditions and are not human-based.

Reproducing the complete spinal-locomotion (reflex-arc) circuit microphysiological conditions *in vitro* is very complex. Later progresses in neuromuscular-mimicking *in vitro* systems, have been achieved incorporating increasingly evolving technologies of hiPSC, cμFCS, and 3D cell-culture techniques here reviewed. The combination of novel technologies in the proper manner has proved to result in the acquisition of more reliable results.[29,30,43,44] But there is still room for improvement. Future studies should focus on addressing unsolved questions related to: mimicking the whole spinal-locomotion circuit (including all cell-types involved, as well as evaluating the independent and interdependent roles of each one), defining the specific role of the factors that determine the NMD and their severity; mimicking neurodegeneration processes; and above all, finding treatments for NMD.

This thesis approaches neuromuscular study models *in vitro* implementing novel techniques such as the use of cμFCS (*Chapters 2, 4* and *5*), 3D cultures (*Chapters 2* and *4*), and hiPSC as neuromuscular cell source (*Chapters 3* and *4*). Furthermore, some aspects frequently disregarded in neuromuscular studies are addressed: glia and myelination (*Chapter 2*); sensory neurons and proprioception (*Chapters 3* and *4*); and vascularisation (*Chapter 5*). Finally, the role of proprioception is evaluated for ALS, as an example of NMD (*Chapter 3*).

1.6. References

1. Vilmont, V., Cadot, B., Ouanounou, G. & Gomes, E. R. A system for studying mechanisms of neuromuscular junction development and maintenance. *Development* **143**, 2464–2477 (2016).
2. Happe, C. L., Tenerelli, K. P., Gromova, A. K., Kolb, F. & Engler, A. J. Mechanically patterned neuromuscular junctions-in-a-dish have improved functional maturation. *Mol. Biol. Cell* **28**, 1950–1958 (2017).
3. Charoensook, S. N., Williams, D. J., Chakraborty, S., Leong, K. W. & Vunjak-Novakovic, G. Bioreactor model of neuromuscular junction with electrical stimulation for pharmacological potency testing. *Integr. Biol.* **9**, 956–967 (2017).
4. Morimoto, Y., Kato-Negishi, M., Onoe, H. & Takeuchi, S. Three-dimensional neuron–muscle constructs with neuromuscular junctions. *Biomaterials* **34**, 9413–9419 (2013).
5. Martin, N. R. W. *et al.* Neuromuscular junction formation in tissue-engineered skeletal muscle augments contractile function and improves cytoskeletal organization. *Tissue Eng. Part A* **21**, 2595–2604 (2015).
6. Smith, A. S. T. *et al.* Creating interactions between tissue-engineered skeletal muscle and the peripheral nervous system. *Cells Tissues Organs* **202**, 143–158 (2016).
7. Guo, X., Gonzalez, M., Stancescu, M., Vandenburgh, H. H. & Hickman, J. J. Neuromuscular junction formation between human stem cell-derived motoneurons and human skeletal muscle in a defined system. *Biomaterials* **32**, 9602–9611 (2011).
8. Demestre, M. *et al.* Formation and characterisation of neuromuscular junctions between hiPSC derived motoneurons and myotubes. *Stem Cell Res.* **15**, 328–336 (2015).
9. Prpar Mihevc, S. *et al.* Modelling FUS mislocalisation in an in vitro model of innervated human muscle. *J. Mol. Neurosci.* **62**, 318–328 (2017).
10. Yoshida, M. *et al.* Modeling the early phenotype at the neuromuscular junction of spinal muscular atrophy using patient-derived iPSCs. *Stem Cell Reports* **4**, 561–568 (2015).
11. Bhatia, S. N. & Ingber, D. E. Microfluidic organs-on-chips. *Nat. Biotechnol.* **32**, 760–772 (2014).
12. Kiehn, O. & Dougherty, K. Locomotion: circuits and physiology. in *Neuroscience in the 21st Century* (ed. Pfaff, D. W.) 1209–1236 (Springer New York, 2013). doi:10.1007/978-1-4614-1997-6_42.
13. *Neuroscience*. (Sinauer Associates, Inc., 2004).

14. McCrea, D. A. Spinal circuitry of sensorimotor control of locomotion. *J. Physiol.* **533**, 41–50 (2001).

15. *Principles of neural science*. (Mc Graw Hill Medical, 2013).

16. Côté, M.-P., Murray, L. M. & Knikou, M. Spinal control of locomotion: individual neurons, their circuits and functions. *Front. Physiol.* **9**, 784 (2018).

17. Rindt, H. *et al.* Astrocytes influence the severity of spinal muscular atrophy. *Hum. Mol. Genet.* **24**, 4094–4102 (2015).

18. Sargsyan, S. A., Monk, P. N. & Shaw, P. J. Microglia as potential contributors to motor neuron injury in amyotrophic lateral sclerosis. *Glia* **51**, 241–253 (2005).

19. Frakes, A. E. *et al.* Microglia induce motor neuron death via the classical NF-κB pathway in amyotrophic lateral sclerosis. *Neuron* **81**, 1009–1023 (2014).

20. *Principles of Anatomy and Physiology*. (John Wiley & Sons, Inc., 2017).

21. *Essentials of human anatomy & physiology*. (Pearson Education, 2015).

22. Gogliotti, R. G. *et al.* Motor neuron rescue in spinal muscular atrophy mice demonstrates that sensory-motor defects are a consequence, not a cause, of motor neuron dysfunction. *J. Neurosci.* **32**, 3818–3829 (2012).

23. Jablonka, S. *et al.* Distinct and overlapping alterations in motor and sensory neurons in a mouse model of spinal muscular atrophy. *Hum. Mol. Genet.* **15**, 511–518 (2006).

24. Hunter, G. *et al.* Restoration of SMN in Schwann cells reverses myelination defects and improves neuromuscular function in spinal muscular atrophy. *Hum. Mol. Genet.* **25**, 2853–2861 (2016).

25. Santosa, K. B., Keane, A. M., Jablonka-Shariff, A., Vannucci, B. & Snyder-Warwick, A. K. Clinical relevance of terminal Schwann cells: An overlooked component of the neuromuscular junction. *J. Neurosci. Res.* **96**, 1125–1135 (2018).

26. Cooper-Knock, J. *et al.* A data-driven approach links microglia to pathology and prognosis in amyotrophic lateral sclerosis. *Acta Neuropathol. Commun.* **5**, 23 (2017).

27. Martínez-Hernández, R., Bernal, S., Alias, L. & Tizzano, E. F. Abnormalities in early markers of muscle involvement support a delay in myogenesis in spinal muscular atrophy. *J. Neuropathol. Exp. Neurol.* **73**, 559–567 (2014).

28. Maimon, R. *et al.* miR126-5p downregulation facilitates axon degeneration and NMJ disruption via a non–cell-autonomous mechanism in ALS. *J. Neurosci.* **38**, 5478–5494 (2018).

29. Santhanam, N. *et al.* Stem cell derived phenotypic human neuromuscular

junction model for dose response evaluation of therapeutics. *Biomaterials* **166**, 64–78 (2018).

30. Uzel, S. G. M. *et al.* Microfluidic device for the formation of optically excitable, three-dimensional, compartmentalized motor units. *Sci. Adv.* **2**, e1501429 (2016).

31. Rumsey, J. W., Das, M., Bhalkikar, A., Stancescu, M. & Hickman, J. J. Tissue engineering the mechanosensory circuit of the stretch reflex arc: Sensory neuron innervation of intrafusal muscle fibers. *Biomaterials* **31**, 8218–8227 (2010).

32. Guo, X. *et al.* Tissue engineering the mechanosensory circuit of the stretch reflex arc with human stem cells: Sensory neuron innervation of intrafusal muscle fibers. *Biomaterials* **122**, 179–187 (2017).

33. Mary, P., Servais, L. & Vialle, R. Neuromuscular diseases: Diagnosis and management. *Orthop. Traumatol. Surg. Res.* **104**, S89–S95 (2018).

34. Morrison, B. Neuromuscular diseases. *Semin. Neurol.* **36**, 409–418 (2016).

35. Bhatt, J. M. The epidemiology of neuromuscular diseases. *Neurol. Clin.* **34**, 999–1021 (2016).

36. Badiola-Mateos, M., Hervera, A., del Río, J. A. & Samitier, J. Challenges and future prospects on 3D in-vitro modeling of the neuromuscular circuit. *Front. Bioeng. Biotechnol.* **6**, 194 (2018).

37. Thomson, S. R., Wishart, T. M., Patani, R., Chandran, S. & Gillingwater, T. H. Using induced pluripotent stem cells (iPSC) to model human neuromuscular connectivity: promise or reality? *J. Anat.* **220**, 122–130 (2012).

38. Takahashi, K. & Yamanaka, S. Induction of pluripotent stem cells from mouse embryonic and adult fibroblast cultures by defined factors. *Cell* **126**, 663–676 (2006).

39. Amabile, G. & Meissner, A. Induced pluripotent stem cells: current progress and potential for regenerative medicine. *Trends Mol. Med.* **15**, 59–68 (2009).

40. Su, H. *et al.* Transplanted motoneurons derived from human induced pluripotent stem cells form functional connections with target muscle. *Stem Cell Res.* **11**, 529–539 (2013).

41. Selvaraj, S. & Perlingeiro, R. C. R. Induced pluripotent stem cells for neuromuscular diseases: potential for disease modeling, drug screening, and regenerative medicine. in *Reference Module in Biomedical Sciences* (eds. McQueen, C. A. et al.) 471–481 (Elsevier, 2018). doi:10.1016/B978-0-12-801238-3.65504-6.

42. Puttonen, K. A. *et al.* Generation of functional neuromuscular junctions from human pluripotent stem cell lines. *Front. Cell. Neurosci.* **9**, 473

(2015).

43. Maffioletti, S. M. *et al.* Three-dimensional human iPSC-derived artificial skeletal muscles model muscular dystrophies and enable multilineage tissue engineering. *Cell Rep.* **23**, 899–908 (2018).

44. Osaki, T., Uzel, S. G. M. & Kamm, R. D. Microphysiological 3D model of amyotrophic lateral sclerosis (ALS) from human iPS-derived muscle cells and optogenetic motor neurons. *Sci. Adv.* **4**, eaat5847 (2018).

45. Centeno, E. G. Z., Cimarosti, H. & Bithell, A. 2D versus 3D human induced pluripotent stem cell-derived cultures for neurodegenerative disease modelling. *Mol. Neurodegener.* **13**, 27 (2018).

46. Smith, S. J. *et al.* Recapitulation of tumor heterogeneity and molecular signatures in a 3D brain cancer model with decreased sensitivity to histone deacetylase inhibition. *PLoS One* **7**, e52335 (2012).

47. Antoni, D., Burckel, H., Josset, E. & Noel, G. Three-dimensional cell culture: a breakthrough in vivo. *Int. J. Mol. Sci.* **16**, 5517–5527 (2015).

48. LaPlaca, M. C., Vernekar, V. N., Shoemaker, J. T. & Cullen, D. K. Three-dimensional neuronal cultures. in *Methods in Bioengineering: 3D Tissue Engineering* (eds. Berthiaume, F. & Morgan, J. R.) 187–204 (Artech House Publishers, 2010).

49. Baker, B. M. & Chen, C. S. Deconstructing the third dimension – how 3D culture microenvironments alter cellular cues. *J. Cell Sci.* **125**, 3015–3024 (2012).

50. Esch, E. W., Bahinski, A. & Huh, D. Organs-on-chips at the frontiers of drug discovery. *Nat. Rev. Drug Discov.* **14**, 248–260 (2015).

51. Tong, Z. *et al.* Engineering a functional neuro-muscular junction model in a chip. *RSC Adv.* **4**, 54788–54797 (2014).

52. Park, J. W., Vahidi, B., Taylor, A. M., Rhee, S. W. & Jeon, N. L. Microfluidic culture platform for neuroscience research. *Nat. Protoc.* **1**, 2128–2136 (2006).

53. Kamm, R. D. & Bashir, R. Creating living cellular machines. *Ann. Biomed. Eng.* **42**, 445–459 (2014).

54. Hur, E. M. *et al.* Engineering neuronal growth cones to promote axon regeneration over inhibitory molecules. *Proc. Natl. Acad. Sci.* **108**, 5057–5062 (2011).

55. Yang, I. H., Siddique, R., Hosmane, S., Thakor, N. & Höke, A. Compartmentalized microfluidic culture platform to study mechanism of paclitaxel-induced axonal degeneration. *Exp. Neurol.* **218**, 124–128 (2009).

56. Zahavi, E. E. *et al.* A compartmentalized microfluidic neuromuscular co-

culture system reveals spatial aspects of GDNF functions. *J. Cell Sci.* **128**, 1241–1252 (2015).

57. Hosmane, S. *et al.* Valve-based microfluidic compression platform: single axon injury and regrowth. *Lab Chip* **11**, 3888–3895 (2011).

58. Saal, L., Briese, M., Kneitz, S., Glinka, M. & Sendtner, M. Subcellular transcriptome alterations in a cell culture model of spinal muscular atrophy point to widespread defects in axonal growth and presynaptic differentiation. *RNA* **20**, 1789–1802 (2014).

59. Park, J., Koito, H., Li, J. & Han, A. Microfluidic compartmentalized co-culture platform for CNS axon myelination research. *Biomed. Microdevices* **11**, 1145–1153 (2009).

60. Hosmane, S., Yang, I. H., Ruffin, A., Thakor, N. & Venkatesan, A. Circular compartmentalized microfluidic platform: Study of axon–glia interactions. *Lab Chip* **10**, 741 (2010).

61. Shin, H. S. Shear stress effect on transfection of neurons cultured in microfluidic devices. *J. Nanosci. Nanotechnol.* **9**, 7330–7335 (2009).

62. Wang, C. J. *et al.* A microfluidics-based turning assay reveals complex growth cone responses to integrated gradients of substrate-bound ECM molecules and diffusible guidance cues. *Lab Chip* **8**, 227–237 (2008).

63. Renault, R. *et al.* Combining microfluidics, optogenetics and calcium imaging to study neuronal communication in vitro. *PLoS One* **10**, e0120680 (2015).

64. Jang, J. M., Lee, J., Kim, H., Jeon, N. L. & Jung, W. One-photon and two-photon stimulation of neurons in a microfluidic culture system. *Lab Chip* **16**, 1684–1690 (2016).

65. Hallfors, N., Khan, A., Dickey, M. D. & Taylor, A. M. Integration of pre-aligned liquid metal electrodes for neural stimulation within a user-friendly microfluidic platform. *Lab Chip* **13**, 522–526 (2013).

66. Hoffman-Kim, D., Mitchel, J. A. & Bellamkonda, R. V. Topography, cell response, and nerve regeneration. *Annu. Rev. Biomed. Eng.* **12**, 203–231 (2010).

67. Uzel, S. G. M. *et al.* Simultaneous or sequential orthogonal gradient formation in a 3D cell culture microfluidic platform. *Small* **12**, 612–622 (2016).

68. Shen, N. Y., Liu, Z., Jacquot, B. C., Minch, B. A. & Kan, E. C. Integration of chemical sensing and electrowetting actuation on chemoreceptive neuron MOS (CvMOS) transistors. *Sensors Actuators B Chem.* **102**, 35–43 (2004).

69. Jeong, S. *et al.* A three-dimensional arrayed microfluidic blood–brain barrier model with integrated electrical sensor array. *IEEE Trans. Biomed.*

Eng. **65**, 431–439 (2018).

70. Millet, L. J., Stewart, M. E., Sweedler, J. V, Nuzzo, R. G. & Gillette, M. U. Microfluidic devices for culturing primary mammalian neurons at low densities. *Lab Chip* **7**, 987–994 (2007).

71. Renault, R., Durand, J. B., Viovy, J. L. & Villard, C. Asymmetric axonal edge guidance: a new paradigm for building oriented neuronal networks. *Lab Chip* **16**, 2188–2191 (2016).

72. Peyrin, J.-M. *et al.* Axon diodes for the reconstruction of oriented neuronal networks in microfluidic chambers. *Lab Chip* **11**, 3663–3673 (2011).

73. Tong, Z. *et al.* A microfluidic neuronal platform for neuron axotomy and controlled regenerative studies. *RSC Adv.* **5**, 73457–73466 (2015).

74. Hume, S. L. *et al.* Alignment of multi-layered muscle cells within three-dimensional hydrogel macrochannels. *Acta Biomater.* **8**, 2193–2202 (2012).

75. Tourovskaia, A., Li, N. & Folch, A. Localized acetylcholine receptor clustering dynamics in response to microfluidic focal stimulation with agrin. *Biophys. J.* **95**, 3009–3016 (2008).

76. Uzel, S. G. M., Pavesi, A. & Kamm, R. D. Microfabrication and microfluidics for muscle tissue models. *Prog. Biophys. Mol. Biol.* **115**, 279–293 (2014).

77. Maschmeyer, I. *et al.* A four-organ-chip for interconnected long-term co-culture of human intestine, liver, skin and kidney equivalents. *Lab Chip* **15**, 2688–2699 (2015).

78. Maoz, B. M. *et al.* A linked organ-on-chip model of the human neurovascular unit reveals the metabolic coupling of endothelial and neuronal cells. *Nat. Biotechnol.* **36**, 865–874 (2018).

79. Williamson, A., Singh, S., Fernekorn, U. & Schober, A. The future of the patient-specific Body-on-a-chip. *Lab Chip* **13**, 3471–3480 (2013).

80. Esch, M. B. *et al.* How multi-organ microdevices can help foster drug development. *Adv. Drug Deliv. Rev.* **69**–**70**, 158–169 (2014).

81. Campenot, R. B. Local control of neurite development by nerve growth factor (chemotaxis/culture methods/retrograde transport/sympathetic ganglia). *Cell Biol.* **74**, 4516–4519 (1977).

82. Zhang, B. & Radisic, M. Organ-on-a-chip devices advance to market. *Lab Chip* **17**, 2395–2420 (2017).

83. Southam, K. A., King, A. E., Blizzard, C. A., McCormack, G. H. & Dickson, T. C. Microfluidic primary culture model of the lower motor neuron–neuromuscular junction circuit. *J. Neurosci. Methods* **218**, 164–169 (2013).

84. Blizzard, C. A. *et al.* Identifying the primary site of pathogenesis in amyotrophic lateral sclerosis - vulnerability of lower motor neurons to proximal excitotoxicity. *Dis. Model. Mech.* **8**, 215–224 (2015).

85. Magdesian, M. H. *et al.* Rapid mechanically controlled rewiring of neuronal circuits. *J. Neurosci.* **36**, 979–987 (2016).

86. Moreno, E. L. *et al.* Differentiation of neuroepithelial stem cells into functional dopaminergic neurons in 3D microfluidic cell culture. *Lab Chip* **15**, 2419–2428 (2015).

87. Wevers, N. R. *et al.* High-throughput compound evaluation on 3D networks of neurons and glia in a microfluidic platform. *Sci. Rep.* **6**, 38856 (2016).

88. Jenkins, R. W. *et al.* Ex vivo profiling of PD-1 blockade using organotypic tumor spheroids. *Cancer Discov.* **8**, 196–215 (2018).

89. Deleglise, B. *et al.* β-amyloid induces a dying-back process and remote trans-synaptic alterations in a microfluidic-based reconstructed neuronal network. *Acta Neuropathol. Commun.* **2**, 145 (2014).

90. Prabhakarpandian, B. *et al.* SyM-BBB: a microfluidic blood brain barrier model. *Lab Chip* **13**, 1093–1101 (2013).

91. Osaki, T., Uzel, S. G. M. & Kamm, R. D. On-chip 3D neuromuscular model for drug screening and precision medicine in neuromuscular disease. *Nat. Protoc.* **15**, 421–449 (2020).

92. Park, H. S., Liu, S., McDonald, J., Thakor, N. & Yang, I. H. Neuromuscular junction in a microfluidic device. in *2013 35th Annual International Conference of the IEEE Engineering in Medicine and Biology Society (EMBC)* 2833–2835 (IEEE, 2013). doi:10.1109/EMBC.2013.6610130.

93. Ionescu, A., Zahavi, E. E., Gradus, T., Ben-Yaakov, K. & Perlson, E. Compartmental microfluidic system for studying muscle–neuron communication and neuromuscular junction maintenance. *Eur. J. Cell Biol.* **95**, 69–88 (2016).

94. Gingras, M., Beaulieu, M. M., Gagnon, V., Durham, H. D. & Berthod, F. In vitro study of axonal migration and myelination of motor neurons in a three-dimensional tissue-engineered model. *Glia* **56**, 354–364 (2008).

95. Bucchia, M., Merwin, S. J., Re, D. B. & Kariya, S. Limitations and challenges in modeling diseases involving spinal motor neuron degeneration in vitro. *Front. Cell. Neurosci.* **12**, 61 (2018).

96. Trias, E. *et al.* Schwann cells orchestrate peripheral nerve inflammation through the expression of CSF1, IL-34, and SCF in amyotrophic lateral sclerosis. *Glia* **68**, 1165–1181 (2020).

97. Arbour, D., Vande Velde, C. & Robitaille, R. New perspectives on amyotrophic lateral sclerosis: the role of glial cells at the neuromuscular

junction. *J. Physiol.* **595**, 647–661 (2017).

98. Kang, S. H. *et al.* Degeneration and impaired regeneration of gray matter oligodendrocytes in amyotrophic lateral sclerosis. *Nat. Neurosci.* **16**, 571–579 (2013).

99. Philips, T. *et al.* Oligodendrocyte dysfunction in the pathogenesis of amyotrophic lateral sclerosis. *Brain* **136**, 471–482 (2013).

100. Turner, M. R. & Kiernan, M. C. Does interneuronal dysfunction contribute to neurodegeneration in amyotrophic lateral sclerosis? *Amyotroph. Lateral Scler.* **13**, 245–250 (2012).

101. Lalancette-Hebert, M., Sharma, A., Lyashchenko, A. K. & Shneider, N. A. Gamma motor neurons survive and exacerbate alpha motor neuron degeneration in ALS. *Proc. Natl. Acad. Sci.* **113**, E8316–E8325 (2016).

102. Chand, K. K. *et al.* Defects in synaptic transmission at the neuromuscular junction precede motor deficits in a TDP-43 Q331K transgenic mouse model of amyotrophic lateral sclerosis. *FASEB J.* **32**, 2676–2689 (2018).

103. Bewick, G. S. & Banks, R. W. Mechanotransduction in the muscle spindle. *Pflügers Arch. - Eur. J. Physiol.* **467**, 175–190 (2015).

104. Dagberg, B. & Alstermark, B. Improved organotypic cell culture model for analysis of the neuronal circuit involved in the monosynaptic stretch reflex. *J. Neurosci. Res.* **84**, 460–469 (2006).

105. Matthews, P. B. C. Where Anatomy led, Physiology followed: a survey of our developing understanding of the muscle spindle, what it does and how it works. *J. Anat.* **227**, 104–114 (2015).

106. Taylor, M. D., Holdeman, A. S., Weltmer, S. G., Ryals, J. M. & Wright, D. E. Modulation of muscle spindle innervation by neurotrophin-3 following nerve injury. *Exp. Neurol.* **191**, 211–222 (2005).

107. Lobsiger, C. S. & Cleveland, D. W. Glial cells as intrinsic components of non-cell-autonomous neurodegenerative disease. *Nat. Neurosci.* **10**, 1355–1360 (2007).

108. Garbuzova-Davis, S. *et al.* Amyotrophic lateral sclerosis: A neurovascular disease. *Brain Res.* **1398**, 113–125 (2011).

109. Rodrigues, M. C. O. *et al.* Neurovascular aspects of amyotrophic lateral sclerosis. in *International Review of Neurobiology* vol. 102 91–106 (Elsevier, 2012).

110. Colón, A., Guo, X., Akanda, N., Cai, Y. & Hickman, J. J. Functional analysis of human intrafusal fiber innervation by human γ-motoneurons. *Sci. Rep.* **7**, 17202 (2017).

111. Levin, E., Andreadaki, A., Gobrecht, P., Bosse, F. & Fischer, D. Nociceptive DRG neurons express muscle lim protein upon axonal injury. *Sci. Rep.* **7**,

643 (2017).

112. Schwab, A. J. & Ebert, A. D. Sensory neurons do not induce motor neuron loss in a human stem cell model of spinal muscular atrophy. *PLoS One* **9**, e103112 (2014).

113. Garbuzova-Davis, S. *et al.* Impaired blood–brain/spinal cord barrier in ALS patients. *Brain Res.* **1469**, 114–128 (2012).

114. Fukuhara, K. *et al.* Specificity of monosynaptic sensory-motor connections imposed by repellent Sema3E-PlexinD1 signaling. *Cell Rep.* **5**, 748–758 (2013).

115. Van den Berg, L. H. Therapy of amyotrophic lateral sclerosis remains a challenge. *Lancet Neurol.* **13**, 1062–1063 (2014).

116. Hardiman, O. *et al.* Amyotrophic lateral sclerosis. *Nat. Rev. Dis. Prim.* **3**, 17071 (2017).

117. Petrov, D., Mansfield, C., Moussy, A. & Hermine, O. ALS clinical trials review: 20 years of failure. Are we any closer to registering a new treatment? *Front. Aging Neurosci.* **9**, 68 (2017).

118. Brown, R. H. & Al-Chalabi, A. Amyotrophic lateral sclerosis. *N. Engl. J. Med.* **377**, 162–172 (2017).

119. Rothstein, J. D. Current hypotheses for the underlying biology of amyotrophic lateral sclerosis. *Ann. Neurol.* **65**, S3–S9 (2009).

120. Robberecht, W. Oxidative stress in amyotrophic lateral sclerosis. *J. Neurol.* **247**, I1–I6 (2000).

121. Van Rheenen, W. *et al.* Genome-wide association analyses identify new risk variants and the genetic architecture of amyotrophic lateral sclerosis. *Nat. Genet.* **48**, 1043–1048 (2016).

122. Ferraiuolo, L. *et al.* Oligodendrocytes contribute to motor neuron death in ALS via SOD1-dependent mechanism. *Proc. Natl. Acad. Sci.* **113**, E6496–E6505 (2016).

123. Kim, S. *et al.* Myelin degeneration induced by mutant superoxide dismutase 1 accumulation promotes amyotrophic lateral sclerosis. *Glia* **67**, 1910–1921 (2019).

124. Seki, S. *et al.* Circuit-specific early impairment of proprioceptive sensory neurons in the SOD1 G93A mouse model for ALS. *J. Neurosci.* **39**, 8798–8815 (2019).

125. Vaughan, S. K., Kemp, Z., Hatzipetros, T., Vieira, F. & Valdez, G. Degeneration of proprioceptive sensory nerve endings in mice harboring amyotrophic lateral sclerosis-causing mutations. *J. Comp. Neurol.* **523**, 2477–2494 (2015).

126. Vaughan, S. K. *et al.* The ALS-inducing factors, TDP43A315T and

SOD1G93A, directly affect and sensitize sensory neurons to stress. *Sci. Rep.* **8**, 16582 (2018).

127. Garbuzova-Davis, S. *et al.* Evidence of compromised blood-spinal cord barrier in early and late symptomatic SOD1 mice modeling ALS. *PLoS One* **2**, e1205 (2007).

128. Kerman, B. E. *et al.* In vitro myelin formation using embryonic stem cells. *Development* **142**, 2213–2225 (2015).

129. Fischer, L. R. & Glass, J. D. Axonal degeneration in motor neuron disease. *Neurodegener. Dis.* **4**, 431–442 (2007).

130. Jessen, K. R. & Mirsky, R. The repair Schwann cell and its function in regenerating nerves. *J. Physiol.* **594**, 3521–3531 (2016).

131. Gomez-Sanchez, J. A. *et al.* After nerve injury, lineage tracing shows that myelin and remak Schwann cells elongate extensively and branch to form repair Schwann cells, which shorten radically on remyelination. *J. Neurosci.* **37**, 9086–9099 (2017).

132. Jessen, K. R. & Arthur-Farraj, P. Repair Schwann cell update: Adaptive reprogramming, EMT, and stemness in regenerating nerves. *Glia* **67**, 421–437 (2019).

133. Reddy, L. V., Koirala, S., Sugiura, Y., Herrera, A. A. & Ko, C.-P. Glial cells maintain synaptic structure and function and promote development of the neuromuscular junction in vivo. *Neuron* **40**, 563–580 (2003).

134. Arbour, D., Tremblay, E., Martineau, É., Julien, J.-P. & Robitaille, R. Early and persistent abnormal decoding by glial cells at the neuromuscular junction in an ALS model. *J. Neurosci.* **35**, 688–706 (2015).

135. Ilieva, H., Polymenidou, M. & Cleveland, D. W. Non–cell autonomous toxicity in neurodegenerative disorders: ALS and beyond. *J. Cell Biol.* **187**, 761–772 (2009).

136. Mioshi, E. *et al.* Neuropsychiatric changes precede classic motor symptoms in ALS and do not affect survival. *Neurology* **82**, 149–155 (2014).

137. Turner, M. R., Goldacre, R., Talbot, K. & Goldacre, M. J. Psychiatric disorders prior to amyotrophic lateral sclerosis. *Ann. Neurol.* **80**, 935–938 (2016).

138. Quarta, E., Bravi, R., Scambi, I., Mariotti, R. & Minciacchi, D. Increased anxiety-like behavior and selective learning impairments are concomitant to loss of hippocampal interneurons in the presymptomatic SOD1(G93A) ALS mouse model. *J. Comp. Neurol.* **523**, 1622–1638 (2015).

139. Proske, U. & Gandevia, S. C. The proprioceptive senses: their roles in signaling body shape, body position and movement, and muscle force. *Physiol. Rev.* **92**, 1651–1697 (2012).

140. Tuthill, J. C. & Azim, E. Proprioception. *Curr. Biol.* **28**, R194–R203 (2018).

141. Hegedus, J., Putman, C. T., Tyreman, N. & Gordon, T. Preferential motor unit loss in the SOD1 G93A transgenic mouse model of amyotrophic lateral sclerosis. *J. Physiol.* **586**, 3337–3351 (2008).

142. Valdez, G., Tapia, J. C., Lichtman, J. W., Fox, M. A. & Sanes, J. R. Shared resistance to aging and ALS in neuromuscular junctions of specific muscles. *PLoS One* **7**, e34640 (2012).

143. Keller, E. L. & Robinson, D. A. Absence of a stretch reflex in extraocular muscles of the monkey. *J. Neurophysiol.* **34**, 908–919 (1971).

144. Held, A. *et al.* Circuit dysfunction in SOD1-ALS model first detected in sensory feedback prior to motor neuron degeneration is alleviated by BMP signaling. *J. Neurosci.* **39**, 2347–2364 (2019).

145. Sábado, J. *et al.* Accumulation of misfolded SOD1 in dorsal root ganglion degenerating proprioceptive sensory neurons of transgenic mice with amyotrophic lateral sclerosis. *Biomed Res. Int.* **2014**, 1–13 (2014).

146. Simon, N. G. *et al.* Segmental motoneuronal dysfunction is a feature of amyotrophic lateral sclerosis. *Clin. Neurophysiol.* **126**, 828–836 (2015).

147. Sangari, S. *et al.* Impairment of sensory-motor integration at spinal level in amyotrophic lateral sclerosis. *Clin. Neurophysiol.* **127**, 1968–1977 (2016).

148. Choi, Y.-K. & Kim, K.-W. Blood-neural barrier: its diversity and coordinated cell-to-cell communication. *BMB Rep.* **41**, 345–352 (2008).

149. Abbott, N. J., Patabendige, A. A. K., Dolman, D. E. M., Yusof, S. R. & Begley, D. J. Structure and function of the blood–brain barrier. *Neurobiol. Dis.* **37**, 13–25 (2010).

150. Stamatovic, S. M., Johnson, A. M., Keep, R. F. & Andjelkovic, A. V. Junctional proteins of the blood-brain barrier: New insights into function and dysfunction. *Tissue Barriers* **4**, e1154641 (2016).

151. Keep, R. F. *et al.* Brain endothelial cell junctions after cerebral hemorrhage: changes, mechanisms and therapeutic targets. *J. Cereb. Blood Flow Metab.* **38**, 1255–1275 (2018).

152. Li, W., Chen, Z., Chin, I., Chen, Z. & Dai, H. The Role of VE-cadherin in Blood-brain Barrier Integrity Under Central Nervous System Pathological Conditions. *Curr. Neuropharmacol.* **16**, 1375–1384 (2018).

153. Tornavaca, O. *et al.* ZO-1 controls endothelial adherens junctions, cell–cell tension, angiogenesis, and barrier formation. *J. Cell Biol.* **208**, 821–838 (2015).

154. Bartanusz, V., Jezova, D., Alajajian, B. & Digicaylioglu, M. The blood-spinal cord barrier: morphology and clinical implications. *Ann. Neurol.* **70**, 194–

206 (2011).

155. Winkler, E. A., Sengillo, J. D., Bell, R. D., Wang, J. & Zlokovic, B. V. Blood–spinal cord barrier pericyte reductions contribute to increased capillary permeability. *J. Cereb. Blood Flow Metab.* **32**, 1841–1852 (2012).

156. Donnenfeld, H., Kascsak, R. J. & Bartfeld, H. Deposits of IgG and C3 in the spinal cord and motor cortex of ALS patients. *J. Neuroimmunol.* **6**, 51–57 (1984).

157. Leonardi, A., Abbruzzese, G., Arata, L., Cocito, L. & Vische, M. Cerebrospinal fluid (CSF) findings in amyotrophic lateral sclerosis. *J. Neurol.* **231**, 75–78 (1984).

158. Zhong, Z. *et al.* ALS-causing SOD1 mutants generate vascular changes prior to motor neuron degeneration. *Nat. Neurosci.* **11**, 420–422 (2008).

159. Henkel, J. S., Beers, D. R., Wen, S., Bowser, R. & Appel, S. H. Decreased mRNA expression of tight junction proteins in lumbar spinal cords of patients with ALS. *Neurology* **72**, 1614–1616 (2009).

160. Rule, R. R., Schuff, N., Miller, R. G. & Weiner, M. W. Gray matter perfusion correlates with disease severity in ALS. *Neurology* **74**, 821–827 (2010).

161. Kakaroubas, N., Brennan, S., Keon, M. & Saksena, N. K. Pathomechanisms of blood-brain barrier disruption in ALS. *Neurosci. J.* **2019**, 1–16 (2019).

Chapter 2

Mouse neuromuscular compartmentalised coculture on a chip

Summary

This chapter presents the initial optimisation of the neuromuscular *in vitro* connection model on a chip. Mice primary motoneurons (MN), dorsal root ganglia neurons (DRGn), SW10 Schwann cell (SC) line, and C2C12 skeletal muscle cells (SkM) were utilised for the study. The viability of SC when exposed to the media required for the primary culture of MN or DRGn was first studied. SC were also exposed to different biochemical stimuli to induce faster myelination, obtaining horse serum as a key component in the culture medium. A two-compartment tailored PDMS microfluidic device, named NeSUr8 device, was designed, fabricated and utilised to mimic the peripheral nervous system (PNS) efferent and afferent pathways, seeding in different compartments SC with pro-myelinating medium with either primary MN or DRGn respectively. The afferent pathway of the PNS was successfully mimicked culturing DRGn with SC. However, regarding the efferent pathway (MN with SC), MN long term culture in 2D represented initially a problem. To increase long term viability of cells and to create more physiological environment, 3D cultures of Matrigel-based composites were tested. Matrigel 100% resulted in a successful way to create a 3D environment for MN, DRGn and SkM cells. Finally, a neuromuscular *in vitro* model was created seeding MN with SkM, or DRGn with SkM embedded in Matrigel in NeSUr8 devices.

Published content, contributions and acknowledgements

Part of the work presented in this chapter has been adapted from the publication cited below:

In-vitro Peripheral Nervous System on a chip

M. Badiola Mateos[1,2], A. Hervera Abad[1,2,3,4], M. J. López Martínez[1,2,3], M. Segura Feliu[1,2,3,4], J. A. del Río Fernández[1,2,3,4], J. Samitier Martí[1,2,3]

[1] Institute for Bioengineering of Catalonia (IBEC) - Barcelona Institute of Science and Technology, Barcelona, Spain.
[2] University of Barcelona, Barcelona, Spain.
[3] Centre for Networked Biomedical Research (CIBER-BBN and CIBER-NED), Madrid, Spain.
[4] Institute of Neuroscience, University of Barcelona, Barcelona, Spain.

Published in Libro de Actas, XXXV Congreso Anual de La Sociedad Española de Ingeniería Biomédica (2017).

This work was achieved in collaboration with some members from the Molecular and Cellular Neurobiotechnology group at IBEC: Dr. Arnau Hervera, performed the dissections and guided me on neural cell culture and Neurobiology concepts; Miriam Segura, provided technical support on the neuron culture and dissection, and Prof. Jose Antonio del Río, collaborated in the dissection process and guided me in neural experimental design and applications. From Nanobioengineering group at IBEC, Dr. Maria José López guided me through the microdevice design, microfabrication process, flow and diffusion analysis.

2.1. Introduction

Neurological disorders affecting muscles and/or their control through nervous system, known as neuromuscular diseases (NMD), comprise several diseases with a different anatomical origin.[1] The prevalence range of 24 of these diseases is a total of 160/100.000 population (ranging from 0.1/100.000 to 60/100.000), reaching similar prevalence values to Parkinson's disease worldwide.[1] Conventionally these diseases have been studied *in vitro* coculturing skeletal muscle cells and neurons on the same dish,[2,3] culturing tissue slices,[4] or culturing neurospheres onto muscle fibres.[5] However, these models do not consider that: i) neural somas and muscles or peripheral glia are physically separated *in vivo* in and have different microenvironment requirements; ii) both sensory and motor neurons can be altered in particular NMD;[6] iii) glial cells are also affected and involved in several neuromuscular pathologies.[2,7] Compartmentalised microfluidic culture systems represent an alternative approach to overcome these problems.

2.1.1. Compartmentalised microfluidic culture systems

In vitro models are fundamental for the discovery of new treatments, a time consuming and expensive process. There is a decline in the number of new approved drugs per money spent in

research and development, described by Eroom's law.[8] This scenario highlights the need of new accurate, economic and relevant study models able to mimic and predict human physiological response reducing the use of experimental animals and costly unsuccessful clinical trials.[9] In this context, microfluidics application to lab-on-chip and organ-on-chip technologies emerges as a promising solution.

Microfluidics is the science and the technology of manipulating fluids in small volumes (within the range of microlitres and femtolitres) using microchannels (1-100 μm size channels).[10] Fluids at the microscale have typically a low Reynolds number, and therefore, laminar flow. This means that layers of liquid move parallel to the surface and fluids mix through diffusion. Lab-on-a-chip technologies integrate these microchannels in miniaturised platforms (between millimetres and centimetres) to accomplish one or several laboratory functions, reducing sample volume, reaction cost and time.[11] Organ-on-a-chip technologies combine microfluidics with *in vitro* cell culture in a physiologically relevant microenvironment, creating advanced platforms in which cells are cultured in micrometre size chambers and aim to mimic minimal functional units that recapitulate tissue- and organ-level functions.[12] Organ-on-a-chip technologies offer the advantage of culturing cells in 2D or 3D onto chemical gradients, applying flow, mechanical strain, electrical stimulation or integrating sensors.

For instance, previous muscle-on-a-chip models (both skeletal muscle and cardiac muscle) often take advantage of the possibility to incorporate mechanical strain[13–16] or electrical stimulation.[17]

The term "compartmentalised microfluidic culture systems" (cμFCS)[18] refers to organ-on-chip microfluidic 2D or 3D cell-culture devices with two or more cell-seeding interconnected compartments, each mimicking different microenvironment of functional units in organ or tissue level. These technologies are frequently used to reproduce interfaces of two interconnected but separated microenvironments, such as the following examples: placental vascularisation,[19] angiogenesis occurring on a vascularised tumour model,[20] human lung alveolar capillary interface[21] and small airway,[22] kidney glomerulus[23,24] and proximal-tubule,[25] female reproductive tract during menstrual cycle,[26] intestine incorporating peristaltic-like motions and flow,[27] liver tissue with vascular and biliary flow,[28] the blood-brain barrier,[29–31] and neuromuscular connection.[18] Some researchers have even attempted to mimic multiple organ-on-a-chip interconnected for drug toxicity analysis.[32–36]

Microfluidic devices used for laboratory research are typically fabricated in poly-dimethylsiloxane (PDMS) by standard photolithography and soft lithography techniques[37,38] (such as the example from Park *et al.*[37] described in FIGURE 2-1), and more recently also through 3D printing[39] and stereolithograpy.[40]

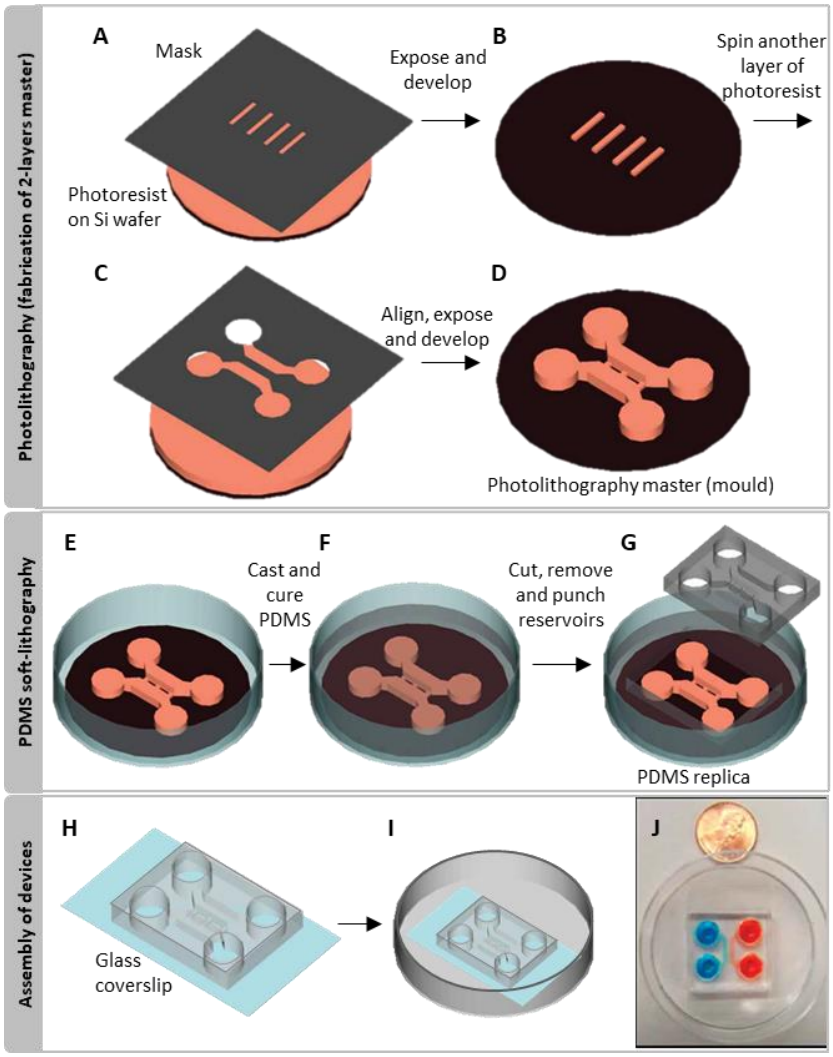

Figure 2-1. *Standard fabrication of microfluidic devices for neuroscience research. To create the photolithography mask, a thin photoresist layer is deposited onto a silicon wafer and exposed with a mask* ***(A)****, obtaining patterned microgrooves* ***(B)*** *that will serve to separate axonal and somal compartment in neural cultures. Bigger motifs for cells seeding compartment and reservoirs are achieved by exposing a thicker photoresist layer on top* ***(C, D)****. Once masters are ready to use, the master is placed inside a Petri dish* ***(E)*** *and previously degassed PDMS is poured on top and cured* ***(F)****. The PDMS replica is demoulded and cut or punched wherever is required (reservoirs and/or seeding chambers typically)* ***(G)****. The PDMS replica is then assembled with a glass through reversible or irreversible bonding* ***(H)****. The device must be placed inside a Petri dish to ensure sterile conditions* ***(I)****. Image of Xona microfluidic device shows fluidic restriction* ***(J)****. Image adapted with permissions from Park et al.*[37]

Photolithography masters are typically fabricated in SU-8, an epoxy-based negative photoresist. This means that the photoresist becomes cross-linked only on areas exposed to UV light, remaining the rest soluble. Masters are usually replica-moulded in thermoplastics or elastomers. PDMS is an optically transparent, hydrophobic, gas- and vapour-permeable elastomer. It is relatively cheap, it can be bonded reversibly or irreversibly to various materials and it can be converted to hydrophilic form by means of plasma treatment.[10,41]

2.1.2. Myelination in the neuromuscular circuit

In the neuromuscular circuit, motoneurons (MN), arising from the CNS spinal cord, innervate skeletal muscle cells connecting through neuromuscular junction ("efferent pathway"), and dorsal root ganglia sensory neurons (DRGn) form a muscle spindle that senses muscle contraction and send the signal back to the spinal cord ("afferent pathway"). Neural axons are frequently wrapped by glial cells (Schwann cells in the PNS or oligodendrocytes in the CNS), creating a discontinuous myelin cover of the axon named myelin sheath. Locomotion of the nervous system requires rapid propagation of neural impulses, facilitated in vertebrates by the electrochemical insulation of axons with myelin (a multilayered glial membrane with high lipid to protein ratio). Myelin is responsible for

the fast saltatory impulse propagation originated when the action potential is restricted to the nodes of Ranvier (unmyelinated axonal segments), consequently accelerating nerve conduction up to 100 times.[42] Myelinating cells, in addition, provide trophic axonal support, enabling long term integrity of longer axons (which can be up to meters away from neural somas but in close contact to glial cells).[43] They are also a key to stabilise and maintain neuromuscular junctions.[44–46] A failure in myelin development or its loss, named demyelination process, occurs in many neurological diseases, such as multiple sclerosis and ALS, causing neural damages and disruptions in electrical impulse conductivity.[43]

Myelin is formed in the PNS when tyrosine kinase receptors of SC sense neuregulin-1 on the axonal surface, in amounts proportional to at least 1 µm diameter axons, functioning as a trigger for SC to induce the differentiation of their plasma membrane.[42] Myelin biogenesis in the PNS has been enhanced *in vitro* by several components: brain-derived neurotrophic factor,[47] progesterone,[48] N-cadherin,[49] integrin β1,[50] Schwann cell-derived leucine rich glioma-inactivated 4 protein,[51] ascorbic acid,[52–56] or pituitary extract with N2 supplement and forskolin with 5% horse serum.[52] However some publications report as well the use of high concentrations of horse serum, up to 40%, to induce myelination.[57]

Most microfluidic devices employed to mimic nerve injury and perform nerve regeneration studies,[58,59] together with microfluidic

systems for stem-cell based neural tissue engineering,[60,61] are typically designed with two compartments connected through microchannels. Few of them suggest the use of a third chamber for myelination and synapsis assessment,[62] and even fewer a 3D cell-culture.[55,63,64] Therefore, we decided to analyse the influence of some of these components in myelin formation.

2.1.3. Extracellular matrix in 3D cultures

In vitro 2D cell cultures have been the gold-standard cell culturing technique for years. Nevertheless, they are far from mimicking physiological conditions. Therefore, 3D cell cultures have risen as a new technique with two main outstanding contributions: cells acquire more *in vivo* like phenotype and genotype patterns,[65,66] and they could potentially mimic some higher-order processes that occur inherently in 3D.[67] Both 2D and 3D culture have advantages and limitations, reviewed in TABLE 2-1.

3D cell culture techniques take into consideration the interactions among cells in the space, and between cells and the extracellular matrix (ECM). The ECM is the non-cellular component present within all tissues and organs, that provides physical scaffolding for the cells, and biochemical and biomechanical cues that cells need for the homeostasis, morphogenesis, and differentiation.[70] This biological matrix has tissue-specific composition consisting on:

water, proteoglycans and fibrous proteins (collagens, fibronectin, tenascin, elastins or laminin).[70]

Table 2-1. *Advantages and limitations of 2D and 3D cell cultures. Information is taken from previous publications.*[65,67–69]

	2D cell culture	3D cell culture
Advantages	○ Lot of literature available. ○ Easier environmental control. ○ Easier cell manipulation. ○ Easier cell observation	○ More *in vivo* like genotype and phenotype patterns. ○ Higher cell viability, proliferation, differentiation, and response to stimuli of cells. ○ Higher cell-to-cell communication in all directions. ○ Scaffolds protect cells from environmental disturbances.
Limitations	○ Cells have different genotype and phenotype patterns (differentiation, cell shape, motility, drug susceptibility, mechanotransduction, growth, adhesion, morphogenesis, etc.). ○ Cells are more exposed and have increased sensitivity to factors diffused in the medium (e.g. drugs). ○ Some higher-order cell processes are inherently in 3D (metastasis, chondrogenesis, angiogenesis). ○ Less compatible with *in vivo* systems.	○ High number of cells required. ○ Limitations in the diffusional transport (oxygen and nutrients may not reach all cells, and waste products may remain accumulated within the scaffold). ○ Difficulties to control cell culture condition in the whole scaffold (temperature, pH, nutrients and oxygen availability). ○ Difficulties in the reproducibility among batches of biomimetic scaffolds. ○ Difficult assessment of the result (incompatible with many high-throughput screening instruments and difficulties in the imaging will depend on the scaffold size, material transparency and microscope depth).

In vitro 3D cell culture models include[71]: organotypic explants, cellular spheroids (further studied in *Chapters 3* and *4*), polarised epithelial cell cultures, tissue-engineered models using scaffolds or matrices (studied in this chapter), and microcarrier cultures.

Several scaffolds and matrices have been extensively used *in vitro* to engineer tissues including: hydrogels, metals, ceramics, bioactive glasses, and carbon nanotubes (reviewed by Ravi *et al*)[69]. Hydrogels, solid porous polymers, fibrous materials and decellularised tissues are specially indicated for neural cell culture, in some cases even incorporating them in microfluidic devices.[72] Hydrogels are the most extensively used scaffolds. They differ in their source (natural, synthetic or hybrid), in the crosslinking process (e.g. thermal, ionic), and design features (stiffness, elasticity, cell adhesion, porosity, degradability and cell-specific bioactivity).[73] Among the commercial natural hydrogels used for neural cell culture (reviewed by LaPlaca *et al*)[65], the most popular one is Matrigel®. This composite is a reconstituted basement membrane preparation consisting of 60% laminin, 30% collagen IV and 8% entactin, derived from Engelbreth-Holm-Swarm mouse sarcoma, a tumour rich in ECM proteins. Matrigel has shown to be biologically active for neural cells, to promote neurite outgrowth and cytokine-related interactions.[74–76] Though, its naturally derived composition makes it prone to degradation. In some cases, it has been used as well in combination with collagen type I, due to its gelation and mechanical properties.[77]

In this chapter Matrigel and collagen type-I based composites are assessed on neuromuscular circuit cells for 3D cell cultures.

2.2. Specific objectives of the chapter

The global aim of this chapter was to stablish the techniques for 2D and 3D neuromuscular cell culture of a mouse model in a microfluidic device. For that purpose, the specific objectives of the chapter were:

- To design and fabricate a two-compartment microfluidic device suitable for the 2D neuronal culture.
- To compare the best procedure to promote myelination in Schwann cells through different medium components.
- To mimic a simplified preliminary version of myelinating peripheral nervous system on a chip.
- To find an optimal Matrigel-based composite suitable for the 3D cell culture of all cells required for a neuromuscular circuit model.
- To mimic a simplified preliminary version of neuromuscular efferent and afferent connection on a chip.

2.3. Materials and methods

2.3.1. Facilities

All cell-culture experiments were performed in between the Nanobioengineering lab and the cell culture lab of the Molecular and Cellular Neurobiotechnology group, Institute of Bioengineering of Catalonia (IBEC), Barcelona, Spain. Cell transduction process was performed in Parc Cientific de Barcelona (PCB) common facilities, in a cell culture room reserved for handling viruses. Cell sorting was carried in the Cytometry and Genomic Unit (Centres Científics i Tecnològics Universitat de Barcelona, CCiTUB). Transmission electron microscopy (TEM) imaging was carried out in the Cryomiscroscopy Electronic Unit (CCiTUB). Confocal microscopy imaging was performed at the Advanced Microscopy Facilities of Institute for Research in Biomedicine (IRB), Barcelona, Spain. Spectrometry analysis was performed in IBEC Core facilities. The microfluidic devices fabrication and Scanning Electron Microscopy (SEM) imaging was carried in the MicroFabSpace and Microscopy Characterization Facility, unit 7 of ICTS (Infraestructuras Científicas y Técnicas Singulares) NANOBIOSIS from CIBER-BBN at IBEC. The customised punch was fabricated by the mechanical workshop (CCiTUB).

2.3.2. Microfabrication and characterisation of the microdevice "NeSUr8"

2.3.2.1. Design

Microfluidic devices were designed with the features indicated in FIGURE 2-2. The design includes two chambers, connected through microchannels, and supplied by a medium reservoir. Cells were directly seeded in *chamber-1* and *chamber-2* and the medium changes were made from *reservoir-1* (*R1*) and *reservoir-2* (*R2*). Microchannels connecting both chambers limit the medium diffusion between *side-1* (neural seeding side) and *side-2* (used to seed Schwann cells mimicking the peripheral nervous system, or skeletal muscle cells), while permitting axons to grow towards *chamber-2*.

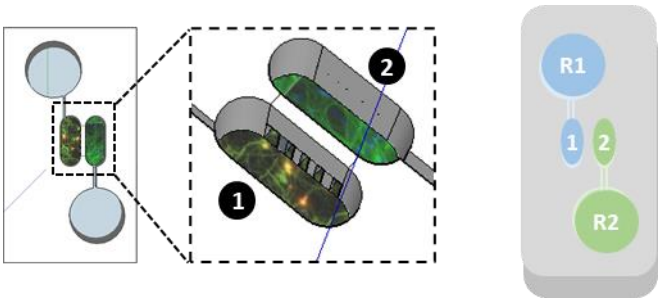

Figure 2-2. *NeSUr8 general microdevice design. It includes two seeding chambers (indicated as ① and ②) connected through microchannels, each supplied by its own medium reservoir (indicated as R1 and R2). Microchannels separate fluidically side-1 (blue) from side-2 (green).*

Devices were fabricated in poly-dimethylsiloxane (PDMS) by standard photolithography and soft lithography techniques as previously described.[37] Acetate photomasks for microchannels

(FIGURE 2-3-A), and for chambers and reservoirs (FIGURE 2-3-D), were designed in AutoCAD and printed by CAD/Art Services Inc (Oregon, U.S.).

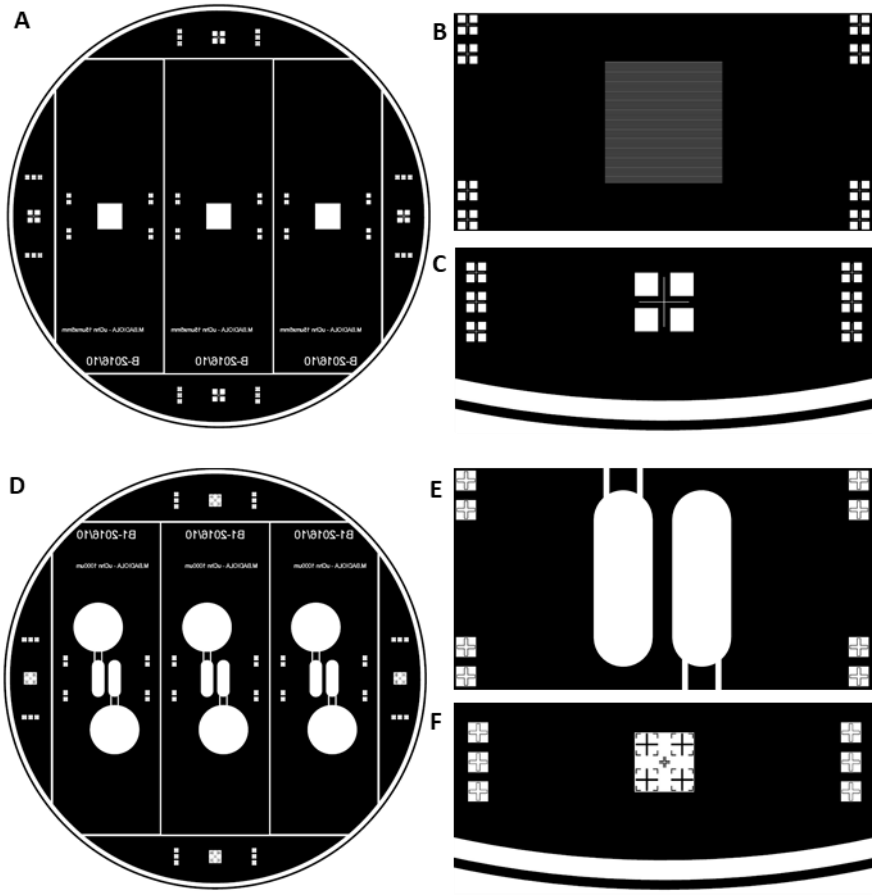

Figure 2-3. *Acetate masks for the fabrication of NeSUr8-vB2.2 masters on a 4'' silicon wafer. Mask for the first layer* ***(A)*** *with detailed image of microchannels* ***(B)*** *and alignment motifs* ***(C)****. Mask for the second layer* ***(D)*** *with detailed image of chambers separated 1 mm* ***(E)*** *and alignment motifs* ***(F)****.*

Different versions of the NeSUr8 devices (neural culturing devices with masters fabricated in SU-8) were fabricated varying microchannels dimensions and space between seeding chambers to facilitate the microfabrication manual steps, increase device

reproducibility and minimise diffusion between chambers. Initially, NeSUr8-vB2.1 devices (15 µm width and 15 µm high microchannels spaced 35 µm, and chambers separated 500 µm) were fabricated and used for certain microfabrication characterisation steps. However, the space between chambers was increased making NeSUr8-vB2.2 devices (chambers separated 1000 µm), to facilitate the manual punching steps of the fabrication, reproducibility of devices and isolate axons (that grow more than dendrites). In all cases, seeding chambers (oval shape opened chambers of 9 mm long and 3 mm width) are connected to reservoirs (12 mm diameter opened cavities) by two microchannels (300 µm width, 3 mm long and 200 µm high). All cell culture experiments presented here were done in NeSUr8-vB2.2 devices.

2.3.2.2. Fabrication of microdevices

Master microfabrication through photolithography

Photolithography processes were carried in the MicroFabSpace (IBEC), in a clean room environment. The microfabrication process was based in previous publications of our lab on a similar work,[59,78] and optimised for the desired design.

Briefly, silicon 4'' wafers were utilised as substrates. They were cleaned applying 20 min of low frequency oxygen plasma (20 min, 7.2 W, 0.2 Torr) using a plasma cleaner (Harrick Plasma, #PDC-002-CE) with pressure and gas flow controlled through Harrick PlasmaFlow.

The microfabrication process was performed in two steps, including two layers of different heights. For the photolithography of the first layer (microchannels), the previously cleaned substrates were coated on a spin coater (Laurell Technologies, #WS-400A 6TFM/LITE) with a 15 µm layer of SU-8 2010 photoresist (5 s, 500 rpm, acceleration 100; 30 s, 1500 rpm, acceleration 300), soft-baked (65 °C, 1 min; 95 °C, 3 min; cool down) in a hot plate (P Selecta, #Plactronic) and exposed with an energy of 170 $mJ \cdot cm^{-2}$ in a manual mask aligner (SÜSS Microtec, #MJB4) using the acetate mask corresponding to microchannels (FIGURE 2-3-A). After post-exposure bake (65 °C, 1 min; 95 °C, 4 min; cool down), the second layer was fabricated.

For the second layer (chambers and reservoirs), the substrate was spin-coated with a 200 µm layer of SU-8 2100 photoresist (5 s, 500 rpm, acceleration 100; 30 s, 1500 rpm, acceleration 300), soft-baked (65 °C, 6 min; 95 °C, 45 min; cool down), and exposed with an energy of 450 $mJ \cdot cm^{-2}$ using the acetate mask corresponding to chambers (FIGURE 2-3-D), previously aligned manually to the motifs visible from the first layer. After post-exposure bake (65 °C, 5 min; 95 °C, 15 min; cool down), both SU-8 layers were developed in SU-8 developer for 15 min, rinsed in isopropanol, dried with nitrogen gas stream, and developed for additional 2 min in clean SU-8 developer. After rinsing in isopropanol, and drying with nitrogen gas stream, the master was ready for hard-bake process (65 °C, 5 min; 95 °C, 5

min; 150 °C, 30 min; 95 °C, 5 min; 65 °C, 5 min; cool down at room temperature).

Finally, silanisation was carried out in the Nanobioengineering lab, exposing masters to trichloro(1H,1H,2H,2H-perfluorooctyl)silane (Sigma Aldrich, #448931) vapour for 30 min under vacuum in a desiccator connected to a vacuum pump at room temperature, and then drying for 30 min at 65 °C in the oven. Once cooled down, masters were ready to use.

PDMS soft lithography, demoulding and assembly of devices

PDMS replicas were made by pouring degassed 10:1 mixture of PDMS base:crosslinker (Dow Chemical, SYLGARD™ 184 Silicone Elastomer Kit) on the masters and curing overnight at 65-85 °C. The rest of the demoulding and bonding process was carried in the clean room.

Coverslips of 24x60 mm (Fisher Scientific, #11778691) were cleaned by washing with water and soap, rinsing in water, drying with nitrogen gas stream and then using three subsequent solvent baths of acetone, ethanol and isopropanol.

PDMS replicas were demoulded from the SU-8 masters, cut to rectangle shape using a scalpel. The reservoirs were punched using a biopsy tool (Harris Uni-core, 12 mm diameter) and seeding chambers were opened using a custom-made aluminium punch

with the measures of the seeding chambers (FIGURE 2-4). PDMS replicas were washed in ethanol and dried for 10 min at 95 °C.

Then glasses were permanently bonded to the PDMS replicas exposing both to 30 seconds of high frequency oxygen plasma, then putting both pieces together and sealing the bonding with 10 min dehydration in a hot plate at 95 °C. At this point, devices could be stored for the beginning of the experiment.

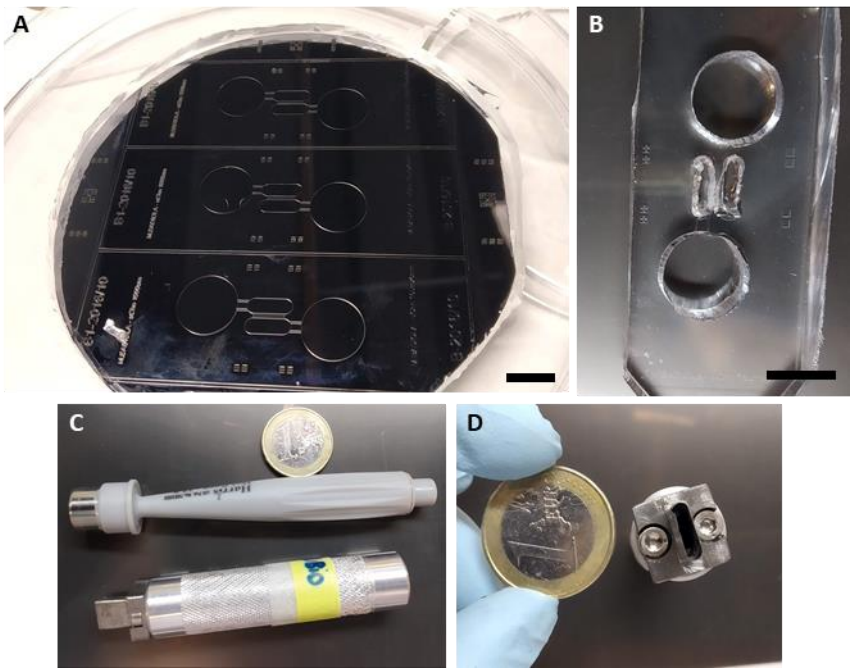

Figure 2-4. *NeSUr8-vB2.2 device fabrication.* ***A)*** *Fabrication master on a silicon wafer.* ***B)*** *A PDMS device.* ***C)*** *Side view of the punches used to open the PDMS showing the commercial one of 12 mm and the custom made one.* ***D)*** *Top view of the custom-made punch fabricated to open the seeding chambers. Scale bars are 1 cm.*

Activation and sterilisation of microdevices

Washing and activation process to make the device hydrophilic was carried out in the cleanroom, and sterilisation in the cell culture

room. Microdevices were washed in ethanol for 10 min, dried with nitrogen air and in a hot plate for 10 min at 96 °C. After cooling down for 5 min in the bench, devices were activated exposing to 5 min of medium frequency oxygen plasma. Subsequently they were filled with Milli-Q sterile water (putting 450 µL on one side and 250 µL on the other side 5 min later). Once activated and filled with water, they were sterilised with ultraviolet (UV) radiation for 15 min in the cell culture hood. From this moment devices were kept with water in sterile conditions until the seeding of cells.

2.3.2.3. Characterisation of microdevices

Lithography masters were characterised using a surface profilometer (Veeco Instruments, #Dektak6M), an upright microscope (Olympus, #BX51RF) and scanning electron microscopy (SEM, FEI™, #NOVA NanoSEM 230).

The fluidic connectivity and leakage of PDMS devices was tested with fluorescein. For this analysis, the water of activated microdevices was aspirated, and 450 µL of 0.01 M of fluorescein (Fluka, #46955) filtered-sterilised (0.22 µm filter) were added in *side-1*, with 250 µL of Milli-Q water in *side-2*. Once volumes were balanced, images were taken with an inverted fluorescent microscope (Olympus, #IX71).

Finally, the diffusion between chambers on NeSUr8-vB2.2 (the devices used later for cell culture) was assessed through

spectrometry. First of all, absorbance spectrum of supplemented medium and each of the different medium components was measured, based on a previous publication[79]: 4.5 $g \cdot L^{-1}$ of D-glucose (Sigma Aldrich, #G8270) in water filtered-sterilised, 1 $mg \cdot mL^{-1}$ of phenol red (Sigma Aldrich, #P3532), foetal bovine serum (FBS, Gibco, #10270-106), DMEM (Gibco, #41965-039), *SC medium* (see composition later on in TABLE 2-4) as an example of a supplemented medium, and Milli-Q water. A 1:5 dilution of all components in water was measured in a spectrophotometer (Tecan, Infinite M200 Pro) reading absorbance from 230 to 1000 nm (see APPENDIX, FIGURE 2-18). Peaks at 560 nm were observed in all samples containing phenol red (i.e. phenol red dilution, DMEM and SC medium), as previously reported[79]. To test the diffusion on chips, 450 µL of *SC medium* were added on *side-1* of activated microdevices, and 450 µL of PBS on *side-2*. Three devices were prepared for each timepoint. Devices were placed in a CO_2 incubator at 37 °C and 95% humidity and samples of *side-1* and *side-2* were collected every 24 h for three days (the maximum time without changing the medium according to cell culture protocols). The absorbance of collected samples was measured at 560 nm, and *SC medium* percentage on each device side and timepoint was calculated based on a previously made calibration curve with serial dilutions. Results were plotted to assess the evolution of diffusion in time.

2.3.3. Cell culture protocols

In the experiments described below, primary motoneurons (MN), primary dorsal root ganglia neurons (DRGn), an established mouse green fluorescent protein (GFP) positive Schwann cells (SC), and yellow fluorescent protein (YFP) positive mouse skeletal muscle (SkM) cell line were utilised. All cells were handled in sterile conditions and maintained in a CO_2 incubator at 37 °C and 95% humidity (Thermo Fisher Scientific).

Primary MN were harvested from the ventral area of the spinal cord of E12.5 mice (i.e. 12.5 days embryos of a CD1 type pregnant mouse). Mice were obtained from Charles River Laboratories (France). All experiments were performed under the guidelines and protocols of the Ethical Committee for Animal Experimentation (CEEA) of the University of Barcelona. For 2D cultures, they were plated at a density of around $5 \cdot 10^4\ cells \cdot cm^{-2}$ on surfaces previously coated with poly-L-ornithine and laminin. This coating was made by incubating surfaces for 1 h at 37 °C with poly-L-ornithine (Sigma Aldrich, #P4957), followed by aspiration and overnight incubation at 37 °C with a 2 $\mu g \cdot mL^{-1}$ solution of laminin from Engelbreth-Holm-Swarm murine sarcoma basement membrane (Sigma Aldrich, #L2020). MN were cultured on *MN medium* (TABLE 2-2), changing it every 2 or 3 days, by removing half volume of the old medium and adding the new one with growth factors at double concentration.

Table 2-2. *Composition of the primary mice MN maintenance medium. GDNF = glial cell line-derived neurotrophic factor; CNTF = ciliary neurotrophic factor; AraC = cytosine β-D-arabinofuranoside hydrochloride. (*) = added fresh in the medium every day the medium is changed.*

Medium	Components and final concentration	Commercial reference
MN medium	Neurobasal medium	(Gibco, #21103-049)
	2% horse serum	(Gibco, #26050-088)
	1X final concentration of B-27™ supplement	(Gibco, #17504-044)
	50 mM of L-glutamine	(Gibco, #25030-081)
	1% penicillin-streptomycin	(Gibco, #15140-122)
	(*) 0.01 $\mu g \cdot \mu L^{-1}$ of GDNF	(Peprotech, #450-44)
	(*) 0.01 $\mu g \cdot \mu L^{-1}$ of CNTF	(Peprotech, #450-50)
	(*) 5µM of AraC	(Sigma, #C6645)

Primary DRGn were harvested from 6-8 weeks old adult mice. Mice were obtained from Charles River Laboratories (France). All experiments were performed under the guidelines and protocols of the Ethical Committee for Animal Experimentation (CEEA) of the University of Barcelona. For 2D cultures, they were plated at a density of $2.5 \cdot 10^4\ cells \cdot cm^{-2}$ on surfaces previously coated with poly-D-lysine and laminin. This coating was made by incubating surfaces for 1 h at 37 °C with a 0.01% solution of poly-D-lysine (Sigma Aldrich, #P6407), followed by the aspiration and overnight incubation at 37 °C with a 2 $\mu g \cdot mL^{-1}$ solution of laminin (Sigma Aldrich, #L2020). DRGn were cultured on *DRG medium* (TABLE 2-3), changing it every 2 or 3 days.

Table 2-3. *Composition of the primary mice DRGn maintenance medium.*

Medium	Components and final concentration	Commercial reference
DRG medium	DMEM/F-12	(Gibco, #11320074)
	1X final concentration of B-27™ supplement	(Gibco, #17504-044)
	1% penicillin-streptomycin	(Gibco, #15140-122)

In the case of Schwann cells, mouse SW10 cells (ATCC, #CRL-2766) were transduced with an eGFP positive lentivirus (pLenti-CMV-MCS-GFP-SV-puro plasmid, Addgene, #73582) and were purified through Fluorescence Activated Cell Sorting (FACS) using BD FACSAria™ Fusion Cell Sorter, obtaining a cell line of GFP positive Schwann cells (SW10-GFP+), named in this chapter as SC. They were maintained in *SC medium* (TABLE 2-4), changing it every 2 or 3 days. Once they reached confluency, cells were washed with sterile phosphate buffer saline (PBS, Gibco, #21600-010), detached with Trypsin-EDTA (0.25%) (Gibco, #25200-072), counted with a haemocytometer and transferred in the desired density to new surfaces or frozen in culture medium of the cell line with 5% dimethyl sulfoxide (DMSO, #D2650) for stock.

Table 2-4. *Composition of the SC medium.*

Medium	Components and final concentration	Commercial reference
SC medium	DMEM with high glucose	(Gibco, #41965-039)
	10% foetal bovine serum	(Gibco, #10270-106)
	1 mM of sodium pyruvate	(Gibco, #11360-039)
	1% penicillin-streptomycin	(Gibco, #15140-122)

Finally, mouse myoblast C2C12 cell line (ATCC, #CRL-1772) were transduced with channelrhodopsine-2 — ChR2, a light-activated cation selective membrane channel that can be used in skeletal muscle cells to induce contraction through optical stimulation[80,81] — positive lentivirus containing YFP sequence as a reporter (pLenti-EF1a-hChR2(H134R)-EYFP-WPRE, Addgene, #20942).[82–84] Cells were purified through FACS as for SW10-GFP+ cells, obtaining C2C12-

ChR2+YFP+ cell line, named in this chapter as SkM cells. Cells were cultured by plating at a density of $2.5 \cdot 10^3\ cells \cdot cm^{-2}$. They were maintained in *C2C12 proliferation medium*, changing it every 2 or 3 days, and once around 90% confluency was reached, they were differentiated to myocytes by changing to *C2C12 differentiation medium* (TABLE 2-5), or trypsinised to passage cells or frozen for stock in *C2C12 proliferation medium* with 5% DMSO.

Table 2-5. *Composition of the medium utilised to maintain and differentiate C2C12 myoblasts into myocytes.*

Medium	Components and final concentration	Commercial reference
C2C12 proliferation medium	DMEM with high glucose	(Gibco, #41965-039)
	10% foetal bovine serum	(Gibco, #10270-106)
	1 mM of sodium pyruvate	(Gibco, #11360-039)
	1% penicillin-streptomycin	(Gibco, #15140-122)
C2C12 differentiation medium	DMEM with high glucose	(Gibco, #41965-039)
	5% horse serum	(Gibco, #26050-088)
	2 mM of L-glutamine	(Gibco, #25030-024)
	25 mM of HEPES	(Gibco, #15630-056)
	1% penicillin-streptomycin	(Gibco, #15140-122)

2.3.4. Promoting myelination in the PNS

2.3.4.1. Glia viability assay

To assess the viability of SC after *MN medium* diffusion, SC were seeded at a density of 3.000 $cell \cdot cm^2$ on *SC medium*. Two days later, the medium was changed to *MN medium*. A Propidium Iodide viability test was performed on Schwann cells as previously reported,[85] together with a morphology analysis for a period of 5 days, using as control SC cultured with *SC medium*.

In order to verify the viability of Schwann cells with *DRG medium*, a morphology analysis was performed, with SC, followed by a viability assay through morphology analysis with *DRG medium* plus different nutrients to find out the essential medium requirements of SC: 1% *SC medium*, 1% sodium pyruvate, 4.5 $mg \cdot mL^{-1}$ of glucose (Sigma Aldrich, #68270), or 10% foetal bovine serum (FBS).

2.3.4.2. Myelin protein production analysis

To find a pro-myelinating medium, different media components and combinations were tested on Schwann cells: *SC medium, DRG medium* and *DRG conditioned medium* (DRG-CM) as base medium, combined in some cases with FBS (Gibco, #26140079), horse serum (HS, Gibco, #26050-088), AraC (Sigma Aldrich, #C6645) and ascorbic acid (AA, Sigma Aldrich, #A2218). The conditions tested are specified on TABLE 2-6. DRG-CM was prepared from the *DRG medium* with the secretome of DRGn obtained over 24 h culture and filtered at 0.2 µm.

SC were plated at a density of 500 $cell \cdot cm^{-1}$ onto 12 well plates with *SC medium* and 4 h after plating, they were changed to the experimental medium. Cells were incubated at 37 °C changing the medium every two days, and they were lysed at 1-4-7 days *in vitro* (DIV). Protein lysates were analysed through western blot.

Table 2-6. *Media conditions tested to induce myelination on Schwann cells. N/A = not applicable; HS = horse serum; FBS = foetal bovine serum; AraC = cytosine β-D-arabinofuranoside hydrochloride; AA = ascorbic acid.*

Condition	Base medium	Additional supplements and final concentration
C1	SC medium	N/A
C2	SC medium	10% HS
C3	SC medium	25% HS
C4	SC medium	1.5 µM of AraC
C5	SC medium	25% HS, 1.5 µM of AraC
C6	SC medium	50 µg · mL^{-1} of AA
C7	SC medium	50 µg · mL^{-1} of AA, 10% HS
C8	DRG medium + 1% FBS	N/A
C9	DRG medium + 1% FBS	10% HS
C10	DRG medium + 1% FBS	25% HS
C11	DRG medium + 1% FBS	1.5 µM of AraC
C12	DRG medium + 1% FBS	25% HS, 1.5 µM of AraC
C13	DRG medium + 1% FBS	50 µg · mL^{-1} of AA
C14	DRG medium + 1% FBS	50 µg · mL^{-1} of AA, 10% HS
C15	DRG-CM + 1% FBS	N/A
C16	DRG-CM + 1% FBS	1.5 µM of AraC

Cell lysis

After removing the medium and washing cells with PBS, each well was scratched with scrappers (Biologix, #70-1250), were used to detach cells. Cells were gently resuspended with the micropipette and transferred to an Eppendorf tube to spin (2.000 g, 5 min, 4 °C). From this moment, samples were always kept cold. After the centrifugation, supernatants were discarded, and pellets were incubated with RIPA lysis buffer (see composition in APPENDIX, TABLE 2-9) in a rotatory shaker at 4 °C for 30 min. Then samples were centrifuged (13.200 rpm, 25 min, 4 °C). The supernatant was transferred to a new tube and stored at -80 °C for a later analysis.

Protein quantification

Protein amount of lysates was quantified using pierce BCA protein assay kit (Thermo Scientific, #23227), in accordance to the manufacturer's protocol and reading absorbance of samples in a spectrophotometer (Tecan, Infinite M200 Pro) at 562 nm. The protein quantification results obtained were utilised to prepare samples for western blot (WB) analysis.

Western blot

Electrophoresis gels were prepared with the components indicated in APPENDIX, TABLE 2-11 onto assembled Mini-PROTEAN Tetra Cell casting frame and casting stand (Bio-Rad, #1658051) placing Mini-PROTEAN spacer plates with 1.5 mm integrated spacers (Bio-Rad, #1653312) with Mini-PROTEAN short plates (Bio-Rad, #1653308). The resolving gel mix was first prepared, poured onto the casting frame with isopropanol (PanReac, #131090.1212) on top and polymerised for about 30 min at room temperature. Then, after removing the isopropanol, the stacking gel mix was added on top placing the comb (Bio-Rad, #1653365) and polymerised for 30 min at room temperature.

Samples were prepared mixing them with loading buffer (see APPENDIX TABLE 2-12 for composition) and Milli-Q water as indicated in equations below. The amounts prepared (50 µg of protein for each experimental sample, and 10 µg of protein for the positive control, a lysate of a sciatic nerve or an adult mouse) were

calculated according to the previous protein quantification. Samples were boiled for 10 min at 96 °C, cooled down and spun down. The molecular weight marker (Bio-Rad, #1610385) was also mixed with the loading buffer.

$$Loading\ buffer\ (LB)\ volume = \frac{desired\ total\ volume}{3} \quad (2\text{-}1)$$

$$Sample\ volume = \frac{desired\ \mu g\ of\ sample}{original\ concentration} \quad (2\text{-}2)$$

$$Water\ volume = desired\ total\ volume - sample\ volume - LB\ volume \quad (2\text{-}3)$$

After mounting the Mini-PROTEAN Electrophoresis System (Bio-Rad, #1658004), placing the gels, adding the running buffer (see APPENDIX, TABLE 2-12 for composition) and removing the combs, samples were loaded in the gels and the electrophoresis was conducted running the samples at room temperature for around 90 min at constant amperage of 20 mA per gel with a PowerPac™ Basic Power Supply (Bio-Rad, #1645050).

Then polyvinylidene difluoride (PVDF) membranes with 0.45 µm pore size (Bio-Rad, #1620177) were cut to the size of the gel, peeled, and hydrated by placing 1 min in methanol (Sigma Aldrich, #179337) 1 min in Milli-Q water and leaving them in transfer buffer (see composition in the APPENDIX, TABLE 2-12). From this moment membranes were always kept humidified. Each electrophoresis gel was placed on the anode side with a membrane in contact in the cathode side, a blotting paper (Bio-Rad, #1703932) on each side, and a foam pads on each side onto the transfer cassette of Mini Trans-

Blot Electrophoretic Transfer Cell (Bio-Rad, #1703930). The transfer cassettes were placed onto the holder with transfer buffer and the transference of proteins from the gel to the membranes was conducted running samples for 1 h with a constant voltage of 100 V at 4 °C with a PowerPac™ Basic Power Supply (Bio-Rad, #1645050).

After the transference was completed, membranes were stained with Ponceau solution (Sigma Aldrich, #P7170), and cut onto the 37 kDa band. The top of each membrane was kept to stain actin and the bottom for myelin. Membranes were washed with transfer buffer.

All the immunoblotting incubations with different buffers and solutions were performed in shaking conditions at room temperature unless stated otherwise. Membranes were washed for 5 min with TPBS and blocked incubating with a blocking solution for 1 h (see composition of both buffers in the APPENDIX, TABLE 2-13). Membranes were then washed with TPBS for 7 min and incubated with the primary antibody solution overnight at 4 °C in shaking conditions. For the membranes corresponding to the top of the gel, the primary antibody solution was: 0.02% sodium azide (Sigma Aldrich, #71290), and 1:10.000 dilution of mouse anti-actin antibody (Chemicon, #MAB1501) in TPBS. For the membranes corresponding to the bottom of the gel, the primary antibody solution was: 0.02% sodium azide, and 1:500 dilution of mouse anti-MBP antibody, also known as myelin basic protein (Abcam, #ab62631) in TPBS.

The day after, membranes were washed with TPBS: one wash of 10 s, 4 washes of 5 min, and 1 wash of 10 min. Then membranes were incubated for 1 h protected from light with the secondary antibody solution (see composition in the APPENDIX, TABLE 2-13). From this moment, membranes were always kept protected from light. Membranes were then washed with TPBS in the same way. Then, the excess of liquid was drained, and membranes were transported to a dark room. Membranes were incubated with Clarity™ Western ECL Substrate kit (Bio-Rad, #1705060) placing in contact X-ray films.

The bands obtained in X-ray films were quantified through ImageJ software[86] utilising the tool to analyse mean grey value of plot lanes areas on gels. Results were normalised as in the following equation for each sample:

$$Normalised\ MBP\ expression = \frac{mean\ grey\ area\ of\ MBP}{mean\ grey\ area\ of\ actin} \qquad (2\text{-}4)$$

The average and standard error for every three replicas was calculated and plotted.

2.3.4.3. Myelinating peripheral nervous system

To analyse the myelin ultrastructure, DRGn were cocultured with SC on top of Aclar® surfaces with PDMS moulds. To analyse myelin production in the peripheral nervous system (PNS), DRGn or MN were cultured in *chamber-1* of NeSUr8-vB2.2 microdevices with SC in *chamber-2* (FIGURE 2-2).

Cell culture

Aclar® (a thermoformable film with plastic and anti-adherent properties) facilitates the inclusion of cells on epoxy resins and PDMS moulds concentrate and localise the neural somas leaving a bigger area with only axons exposed for analysis. Aclar surfaces (Ted Pella Inc., #10501-25) were cut to the desired size and sterilised by washing three times with ethanol 70%, rinsing with sterile Milli-Q water, and irradiating with UV light for 15 min in the cell culture hood. Once dried, they were placed in sterile Petri dishes. PDMS moulds were prepared by polymerising a 5 mm layer of PDMS and making a 5 mm diameter hole with a biopsy punch inside a 6 mm side square cut made with a punch. To sterilize them, they were left for 1 h in 70% ethanol inside the cell culture hood, rinsed 3 times with sterile Milli-Q water, placed in thermoresistant Petri dishes, and dehydrated for 2 h on a hotplate at 90 °C. Once dried, they were carefully placed on top of Aclar surfaces in a corner of rectangle shape Aclar pieces by pressing against them. Microdevices were sterilised and activated as previously described (SECTION 2.3.2.2).

All culture surfaces (microdevices, Petri dishes and Aclar surfaces) were coated with PDL for a coculture of DRGn with SC, or with poly-ornithine and laminin for a coculture of MN with SC, according to the previously described protocols (SECTION 2.3.3). In the case of microdevices, the incubation of each solution was made by placing a total of 400 µL on *side-1*, and 250 µL on *side-2* to create a

difference of volumes and facilitate the coating of microchannels connecting *chamber-1* with *chamber-2*.

DRGn and MN were seeded at a density of $2 \cdot 10^4\ cell \cdot cm^{-2}$ and $1 \cdot 10^5\ cell \cdot cm^{-2}$ respectively in microdevices, Aclar covers and Petri dishes. In the case of microdevices, the cell suspension obtained from dissections of DRGn or MN was concentrated to a maximum volume of 45 µL, and inserted in *chamber-1*, followed by the addition of up to 450 µL of medium (*DRG medium* or *MN medium* without AraC) in *R1* and 350 µL of same medium in *R2*. In the case of Aclar surfaces, 3.800 cells obtained from the DRG dissection were concentrated to a volume of 44 µL, and inserted in the PDMS mould, incubated for 1 h at 37 °C to let cells adhere slightly to the surface, before removing the mould and adding the volume of *DRG medium*.

Cells were cultured with *DRG medium* or *MN medium*, changing it every day after. In both cases, once neurons crossed the microchannels, after 12 days *in vitro* (DIV), SC were seeded at a density of $1.5 \cdot 10^3\ cell \cdot cm^{-2}$. In the case of cocultures of SC on top of DRGn or MN (on Aclar and Petri dish controls), the medium was replaced by *PM medium* or *MNPM medium* (see composition in TABLE 2-7) respectively before adding Schwann cell suspension. In the case of microdevices, SC were seeded in *chamber-2* with *PM medium* in *R2* maintaining *DRG medium* or *MN medium* in *R1*.

Table 2-7. *Composition of promyelinating medium utilised for the coculture of motoneurons with Schwann cells (MNPM medium) and for the coculture of DRG with Schwann cells (PM medium).*
GDNF = glial cell line-derived neurotrophic factor; CNTF = ciliary neurotrophic factor; MNPM medium = motoneuron promyelinating medium; PM medium = promyelinating medium. (*) = added fresh in the medium every day the medium is changed.

Medium	Components and final concentration	Commercial reference
Motoneuron promyelinating medium (MNPM medium)	Neurobasal medium	(Gibco, #21103-049)
	1X final concentration of B-27™ supplement	(Gibco, #17504-044)
	1% of foetal bovine serum	(Gibco, #25030-081)
	1% penicillin-streptomycin	(Gibco, #15140-122)
	25% horse serum	(Gibco, #26050-088)
	(*) 0.01 $\mu g \cdot \mu L^{-1}$ of GDNF	(Peprotech, #450-44)
	(*) 0.01 $\mu g \cdot \mu L^{-1}$ of CNTF	(Peprotech, #450-50)
Promyelinating medium (PM medium)	DMEM/F-12	(Gibco, #11320074)
	1X final concentration of B-27™ supplement	(Gibco, #17504-044)
	1% penicillin-streptomycin	(Gibco, #15140-122)
	1% foetal bovine serum	(Gibco, #10270-106)
	25% horse serum	(Gibco, #26050-088)

Fixation

Cells cultured on Aclar surfaces were fixed after 17 DIV (5 days of coculture) by incubating for 1h at room temperature in a 2.5% glutaraldehyde solution in phosphate buffer (PB) 0.1 M. Samples were then washed in a 0.1 M PB solution four times, 10 min each time. After the fixation, samples were transferred to the Cryomiscroscopy Electronic Unit (CCiTUB) to perform the inclusion in a resin, cutting and prepare the sample for transmission electron microscopy (TEM) observation. Samples were observed in a Jeol J1010 80 kV transmission electron microscope with CCD Orius camera.

The rest of the samples (microdevices and Petri dish controls) were fixed after 2, 5 or 7 days of coculture (total of 14, 17 and 19 DIV for the primary culture). Samples were first incubated for 10 min with 2% paraformaldehyde removing half of the medium and adding half volume of 4% paraformaldehyde (PFA, Sigma Aldrich, #P6148). Then, they were incubated for 1 h at 4 °C in 4% PFA. Samples were gently washed three times in PBS, 10 min each time, and stored at 4 °C in a solution of 0.02% azide (Sigma Aldrich, #71290) in PBS until the immunostaining was performed.

Immunostaining

Immunostaining against TUJ1 and MBP proteins was performed on microdevices. In the case of microdevices, the aspiration and addition of all solutions was performed from the reservoirs, adding more volume in *side-1* than *side-2* to facilitate diffusion through microchannels promoted by volume balancing as in cell cultures.

Samples were washed with PBS, three times 10 min each, permeabilised washing twice with 0.1% triton (Sigma Aldrich, #T8787) in PBS, 10 min each, and incubated 2 h at room temperature with the blocking solution containing: 0.1% triton and 10% FBS in PBS. Samples were then washed three times with PBS-0.1% triton, 10 min per wash, and incubated with the primary antibody solution overnight at 4 °C, containing: 0.1% triton, 5% FBS, 0.01% sodium azide, 1:500 dilution of mouse anti-MBP antibody

(Abcam, #ab62631), and 1:1000 dilution of rabbit anti-TUJ1 (anti-beta III tubulin, Abcam, #ab18207) in PBS.

Then, samples were washed four times with PBS-0.1% triton, 10 min per wash, and they were incubated overnight at 4 °C with the secondary antibody solution containing: 0.1% triton, 5% FBS, 0.01% sodium azide, 1:1000 dilution of goat anti-rabbit biotin (Abcam, #ab6720), and 1:1000 dilution of Alexa Fluor 568 donkey anti-mouse (Invitrogen, #A10037) in PBS. From this moment, samples were kept protected from light throughout the whole process.

Samples were washed seven times with PBS-0.1% triton, 10 min per wash, and they were incubated overnight at 4 °C with AMCA solution, containing: 0.01% sodium azide, and 1:500 dilution of AMCA Avidin-D (Vectorlabs, #A-2008) in 1 M HEPES (Gibco, #15630-056).

Finally, samples were washed four times with PBS, 10 min each, and after aspirating it, they were mounted with Fluoromount™ aqueous mounting medium (Sigma Aldrich, #F4680). Images were acquired using inverted confocal Leica SP5 microscope and were processed with ImageJ software.[86]

2.3.5. 3D cell culture

2.3.5.1. ECM viability test

To optimise the seeding density in 3D cultures and ECM composition of SC, SkM cells, MN and DRGn, different seeding densities and Matrigel-based ECM compositions were tested: 100% Matrigel (Corning, #356237), 75% Matrigel diluted in culture medium, 50% Matrigel diluted in culture medium, and 1:1 mixture of Matrigel and collagen type I (Corning, #354236).

Cell culture

Matrigel was thawed the day before plating cells overnight on ice at 4 °C according to manufacturer's protocol and was always handled on ice to avoid polymerisation. Collagen neutralised solution was prepared right before resuspending cells on it by mixing collagen type I with filter-sterilised 10X Minimum Essential Medium (MEM, Gibco, #11012-044) and 7.5% (wt/vol) sodium bicarbonate ($NaHCO_3$, Sigma Aldrich, #S5761) according to a previously published protocol.[87] Briefly, the mentioned components were handled on ice and mixed in the following order and volumetric proportion: 10.86% $NaHCO_3$, 2.17% MEM, and 86.97% collagen.

DRGn and MN were obtained from a dissection, whereas SC and SkM cells were obtained from the trypsinization of a passage of cells. In all cases, after counting cells from the cell suspension, the required volume corresponding to the density needed for every three replica, was centrifuged 5 min at different speeds (13.200 rpm

for SC and SkM cells, 850 rpm for MN, and 1.200 rpm for DRGn). After aspirating the supernatant, the pellet was resuspended in the corresponding ECM composite solution. A drop of 30 µL containing cells resuspended in ECM composite was placed in the middle of a well of a 24 well plate, avoiding the formation of bubbles. Samples were left in the incubator for 10 min at 37 °C in the case of the ones with collagen and for 30 min the rest to polymerise the ECM before covering gently each sample in 500 µL of the corresponding culture medium. Cells were incubated at 37 °C changing the medium every day after.

Table 2-8. *ECM viability test seeding densities and experimental endpoint for each cell type assessed.*

Cell type	Culture medium	Seeding densities tested	Experimental endpoint
SkM cells	C2C12 proliferation medium	$1 \cdot 10^6\ cell \cdot mL^{-1}$ $5 \cdot 10^6\ cell \cdot mL^{-1}$ $1 \cdot 10^7\ cell \cdot mL^{-1}$	10 DIV
SC	SC medium	$5 \cdot 10^5\ cell \cdot mL^{-1}$ $1 \cdot 10^6\ cell \cdot mL^{-1}$ $5 \cdot 10^6\ cell \cdot mL^{-1}$	5 DIV
MN	MN medium	$1 \cdot 10^6\ cell \cdot mL^{-1}$ $2.5 \cdot 10^6\ cell \cdot mL^{-1}$ $6.25 \cdot 10^6\ cell \cdot mL^{-1}$	7 DIV
DRGn	DRG medium	$0.5 \cdot 10^6\ cell \cdot mL^{-1}$ $1 \cdot 10^6\ cell \cdot mL^{-1}$ $2 \cdot 10^6\ cell \cdot mL^{-1}$	12 DIV

Viability test

Cell death of samples was observed every 2 days incubating a replica with 30 µM of propidium iodide (PI, Sigma Aldrich, #P4170). At the experimental endpoint (different for each cell type, stablished according to the time length required for a coculture on future

experiments and the death observed), 30 µM of PI were incubated for 15 min and 1 µM of Hoechst (Invitrogen, #H3570) were incubated for 30 min. Then SkM cells and SC images were taken in an inverted fluorescence microscope (Olympus, #IX71), observing PI and Hoechst staining together with phase contrast. MN and DRGn samples were fixed in 4% PFA to prepare for an immunostaining.

Immunostaining of DRGn and MN was performed as indicated in SECTION 2.3.4.3, to distinguish neurons from glial cells. Samples were incubated with primary antibody solution containing 1:1000 dilution of rabbit anti-TUJ1 antibody (Abcam, #ab18207); and secondary antibody solution containing 1:1000 dilution of Alexa Fluor 488 donkey anti-rabbit (Invitrogen, #A21206). Images of SkM cells cultured in all ECM composites tested and only in Matrigel 100% for the rest of the cells were acquired using an inverted fluorescence microscope (Olympus, #IX71) and were processed with ImageJ software.[86]

Viability percentage was calculated for SkM samples according to the equation below and average and standard deviation for every three samples was plotted on a graph.

$$\%\, Viability = 100 - \left(\frac{death\ colocalising\ nuclei}{total\ nuclei}\right) \qquad (2\text{-}5)$$

2.3.5.2. Neural 3D cell cultures in Matrigel-collagen

To test the viability of Matrigel-collagen ECM, neural 3D cell cultures were made similarly to SECTION 2.3.5.1 and myelination was induced as in SECTION 2.3.4.3.

On one side, $1 \cdot 10^6\ cell \cdot mL^{-1}$ DRGn were embedded in a drop made of 15 µL Matrigel and 15 µL previously neutralised collagen. DRGn were maintained in *DRG medium* for 12 DIV. Then a 30 µL drop of $1 \cdot 10^6\ cell \cdot mL^{-1}$ SC embedded in Matrigel-collagen 1:1 was placed on top. Cells were maintained in coculture with *PM medium* for 4 DIV.

Similarly, $2.5 \cdot 10^6\ cell \cdot mL^{-1}$ MN were embedded in Matrigel-collagen 1:1 mixture and maintained in MN medium for 12 DIV. Then, $1 \cdot 10^6\ cell \cdot mL^{-1}$ of SC in Matrigel-collagen 1:1 were added on top. Cells were maintained in coculture with *MNPM medium* for 7 DIV.

Immunostaining of TUJ1 and MBP was performed as in SECTION 2.3.4.3. Images were acquired using inverted confocal Leica SP5 microscope and were processed with ImageJ software.[86]

2.3.5.3. Preliminary neuromuscular culture on a chip in 3D

To mimic the motor pathway of the neuromuscular circuit on a chip, SkM cells were seeded in a density of $8 \cdot 10^{\ 6}\ cell \cdot mL^{-1}$ in 30 µL of Matrigel in *chamber-2* of microdevices, polymerising for 45 min at

37 °C before adding *C2C12 proliferation medium* in both sides of the device from reservoirs. The medium was changed every two days. After 4 DIV, SkM cells medium was replaced with *C2C12 differentiation medium,* and MN and DRGn were harvested and seeded in *chamber-1* in 30 µL of Matrigel with *MN medium* or *DRG medium*. Some devices containing SkM cells, were seeded with MN in a density of $5.4 \cdot 10^{6}\ cell \cdot mL^{-1}$ and some others with DRGn in a density of $1 \cdot 10^{6}\ cell \cdot mL^{-1}$. After polymerising at 37 °C for 45 min, *DRG medium* or *MN medium* was added in reservoir *R1*. The medium was changed in all cases every two days. Cells were maintained in compartmentalised coculture for additional 9 DIV, until spontaneous contraction was observed in SkM cells, and samples were fixed in 4% PFA as previously described (SECTION 2.3.4.3).

Then the immunostaining was performed as previously described (SECTION 2.3.4.3) changing the composition of antibody solutions to incubate with. For some samples a primary antibody solution containing 1:1000 dilution of rabbit anti-TUJ1 (Abcam, #ab18207) antibody was incubated overnight at 4 °C; secondary antibody solution containing 1:1000 dilution of Alexa Fluor 568 goat anti-rabbit (Invitrogen, #A11010) was incubated overnight at 4 °C; followed by final incubation with 5 µM of Hoechst for 1 h at 4 °C. Some other samples were incubated first with a primary antibody solution containing 1:1000 dilution of rabbit anti-TUJ1, 1:500 dilution of mouse anti-myosin 4, also known as myosin heavy chain

(MHC, Invitrogen, #14650382) overnight at 4 °C; then with a secondary antibody solution containing 1:1000 dilution of goat anti-rabbit biotin (Abcam, #ab6720) and 1:1000 dilution of Alexa Fluor 568 donkey anti-mouse (Invitrogen, #A10037) overnight at 4 °C; and finally with AMCA solution containing 1:500 dilution of AMCA Avidin-D (Vectorlabs, #A-2008). All samples were mounted with Fluoromount™ aqueous mounting medium (Sigma Aldrich, #F4680). Images were acquired using inverted confocal Leica SP5 microscope and were processed with ImageJ software.[86]

2.4. Results

2.4.1. Microdevice characterisation

NeSUr8 microfluidic devices were successfully fabricated in the IBEC clean room. Imaging of SU-8 masters showed an alignment between layers (FIGURE 2-5-B) and properly defined features (FIGURE 2-5-A, C, D). Chambers and reservoirs showed the expected height (190-200 µm, FIGURE 2-5-G) and fabricated microchannels showed maximum height of 17 µm (FIGURE 2-5-H). Fluorescein test showed good fluidic connectivity of the device and good bonding of the PDMS replica to the glass without leakage outside microchannels (FIGURE 2-5-E, F). Finally, medium diffusion test showed that the phenol-red in the medium in *side-1* becomes more concentrated with time due to evaporation effects, and the diffusion in 72 h to *side-2* is less than 2% (FIGURE 2-5-I). In all biological experiments the medium was changed every 48 h, guaranteeing less than 2% diffusion.

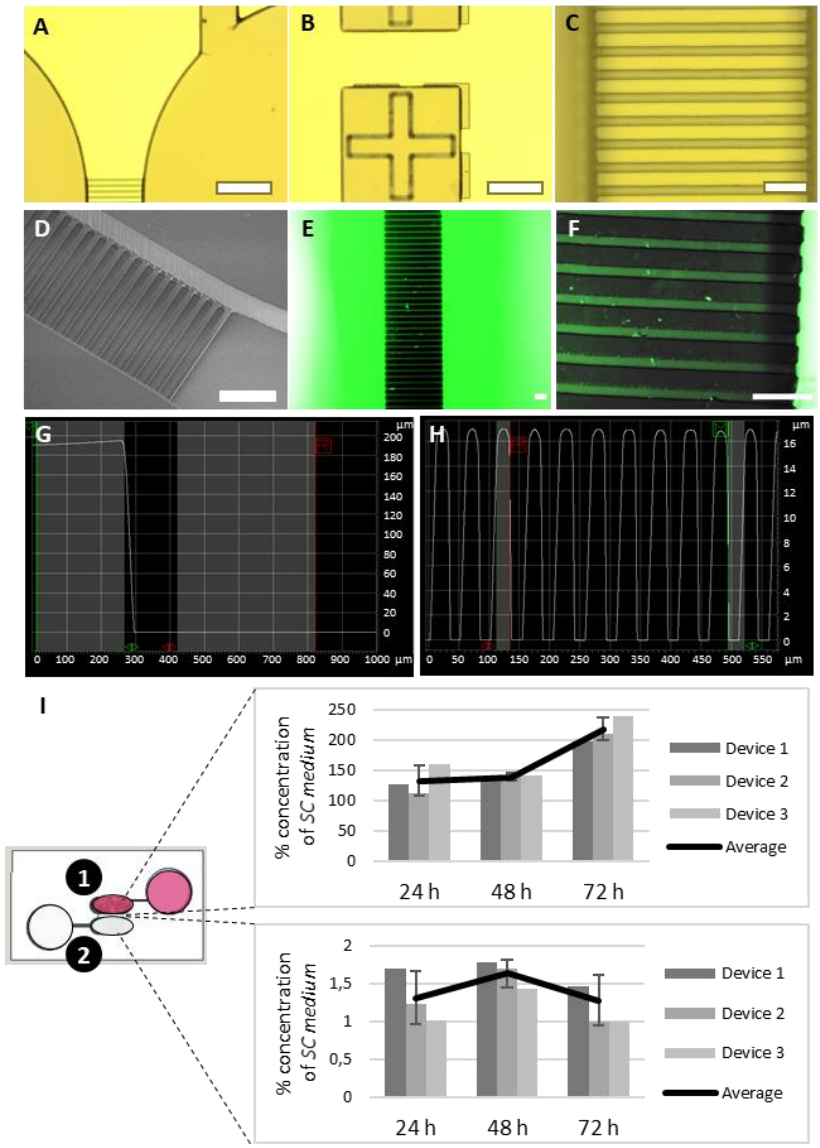

Figure 2-5. *NeSUr8 device characterisation. Optic microscopy imaging of NeSUr8-vB2.1 SU-8 masters (500 µm long microchannels) showing connection of chambers and microchannels (**A**, scale bar 500 µm), alignment motifs (**B**, scale bar 500 µm), and microchannels in detail (**C**, scale bar 100 µm). SEM characterisation of the SU8 master of NeSUr8-vB2.1 devices (**D**, scale bar 200 µm). Fluorescein test on NeSUr8-vB2.1 PDMS devices (**E** and **F**, scale bar 100 µm). Profilometer characterisation of the SU8 master measuring chambers **(G)** and microchannels **(H)**. Diffusion test performed on NeSUr8-vB2.2 (1 mm long microchannels) over 72 h showing the SC medium concentration percentage in side-1 and side-2 of the devices, with average and standard deviation for every three devices **(I)**.*

2.4.2. SC viability assay

Schwann cells were exposed to MN medium and DRG medium, assessing the effects on their viability. Propidium iodide viability test performed on SC showed that *MN medium* induced higher cell death in Schwann cells, as compared to its own *SC medium*, especially in the first 24 h (FIGURE 2-6). Results of the viability test performed in *DRG medium* showed that SC do not survive in DRG medium (FIGURE 2-7-B). But when culturing on DRG medium with different nutrients from the *SC medium*, it can be observed that they could survived when adding FBS (FIGURE 2-7-C).

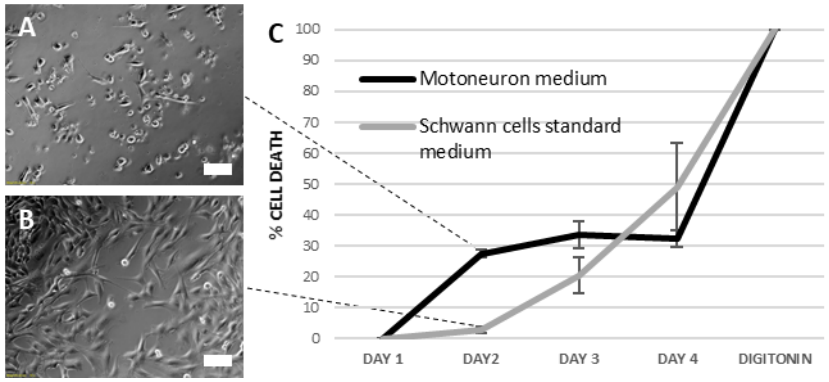

Figure 2-6. *Schwann cells (SC) viability assessment in motoneuron medium. SC cultured in MN medium die in 48 h* ***(A)****, compared to culturing them in SC medium* ***(B)*** *(scale bar 100 µm).* ***C)*** *Average and standard error of propidium iodide analysis over 4 days (n=3).*

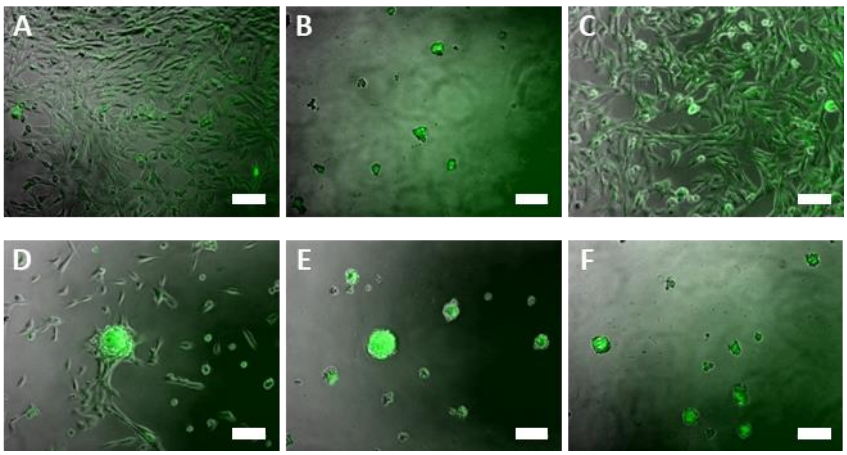

Figure 2-7. *Schwann cells viability test in DRG medium. SW10-GFP+ cells cultured in Schwann cell standard medium live* ***(A)****, but they die in DRG medium* ***(B)****. They only survive when adding 10% FBS to the DRG medium* ***(C)****, in contrast to the addition of 1% SC medium* ***(D)****, 1% sodium pyruvate* ***(E)****, or 4.5* $mg \cdot mL^{-1}$ *of glucose* ***(F)****. Scale bar 100 µm.*

2.4.3. Myelin induction

Several components were tested on Schwann cells to promote higher myelination values, as well as trying to control proliferation levels (see details of conditions tested in TABLE 2-6). The amount of MBP production was evaluated through western blot.

We could observed in the experiment that, among all base media tested, *SC medium* and *DRG medium* supplemented with FBS induced similar MBP production levels, whereas DRG-CM myelin levels were the smallest ones (FIGURE 2-8-B). The addition of AraC 1.5 µM induced Schwann cell death after 2 DIV (results not shown). The addition of 10% and 25% HS resulted in similar levels of MBP production, comparable with the ones obtained in the positive

control (FIGURE 2-8-B). This increase in MBP levels, as compared to same media without HS, was detected from 4 DIV (FIGURE 2-8-A).

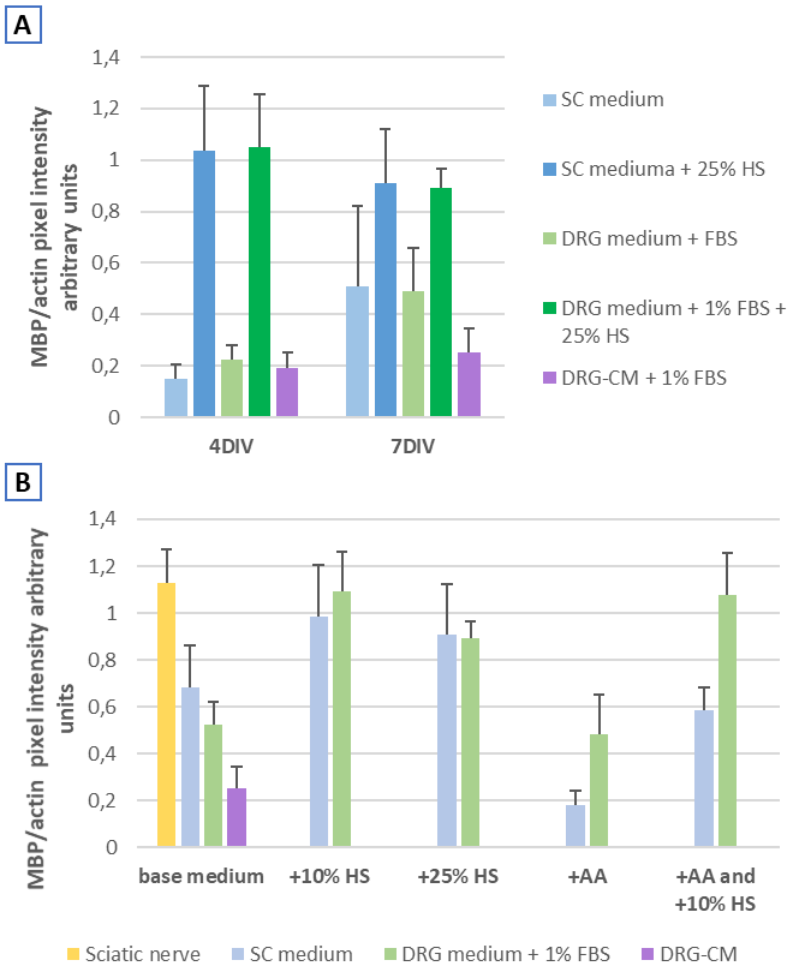

Figure 2-8. *Quantification of myelin produced by Schwann cells in different medium conditions. Average and standard error of myelin base protein (MBP) production normalised against actin production is represented.* ***A)*** *Myelin production after 4 and 7 DIV when exposing cells to different medium conditions (SC medium, DRG medium and DRG-CM) supplemented in some cases with 25% horse serum (HS).* ***B)*** *Myelin production after 7 DIV when exposing SC to different media (SC medium, DRG medium with 1% FBS, or DRG conditioned medium) without extra supplements (base medium), with 10% HS, with 25% HS, with ascorbic acid (AA), or with AA and 10% HS. Positive control measurements of a mouse sciatic nerve are included. Cells died in all conditions containing AraC in 2 DIV, impeding the quantification. Average and standard error are shown (n=3).*

The addition of AA had different effects when applied onto *SC medium* or *DRG medium* (FIGURE 2-8-B). In the case of *SC medium*, the addition of AA resulted in lower MBP levels than *SC medium* alone, that were only recovered to base medium levels when adding AA with 10% HS. In the case of *DRG medium* with FBS, the addition of AA did not induce a significant increase or decrease in myelin production.

2.4.4. Mimicking a myelinating PNS

Promyelinating medium (containing 25% HS) was utilised to study myelinating PNS in NeSUr8 devices (culturing MN or DRGn with SC) and to assess the ultrastructure of the afferent pathway of the PNS (seeding DRGn with SC on top of Aclar® surfaces, observed through TEM).

Regarding the studies of the afferent pathway of the PNS, we observed successful myelination of DRGn by SC seeded in *chamber-2* of NeSUr8 devices (FIGURE 2-9-B) and by endogenous Schwann cells (FIGURE 2-9-D and E). Myelin sheath formation was also noticed (FIGURE 2-9-C). In the ultrastructure observation with TEM, apposed membranes were detected, but classic myelin sheath formation was not seen (FIGURE 2-10).

Regarding the studies of the efferent pathway of the PNS, we faced some problems with the long-term culture of motoneurons. MN

needed around 12 DIV to cross to *chamber-2* (FIGURE 2-11-A) and died after 14 DIV (2 DIV coculture), not providing enough time to induce myelination under tested conditions. Furthermore, MN did not last alive for up to 19 DIV in tested conditions (FIGURE 2-11-D), and their death could have induced SC death (FIGURE 2-11-C). Endogenous myelin was observed in *chamber-1* (FIGURE 2-11-A) prior to the addition of SC.

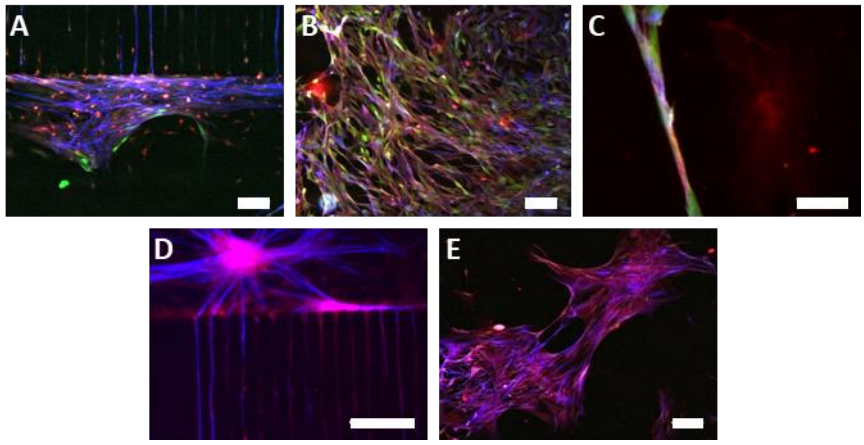

Figure 2-9. *Immunostaining images of afferent PNS-on-a-chip showing TUJ1 in blue, SW10-GFP+ Schwann cells in green and MBP in red.* ***A)*** *DRGn axons crossing microchannels to chamber-2 after 14 DIV (2 DIV coculture).* ***B)*** *Schwann cells proliferate and myelinate axons in chamber-2 after 19 DIV (7 DIV coculture).* ***C)*** *Myelin sheath formation in chamber-2 after 19 DIV (7 DIV coculture).* ***D)*** *DRGn cultured without SW10-GFP+ Schwann cells crossing microchannels from chamber-1 to chamber-2 after 19 DIV.* ***E)*** *Endogenous myelination is observed after 19 DIV. Scale bar is 100 µm for all pictures except* ***C****, that is 25 µm.*

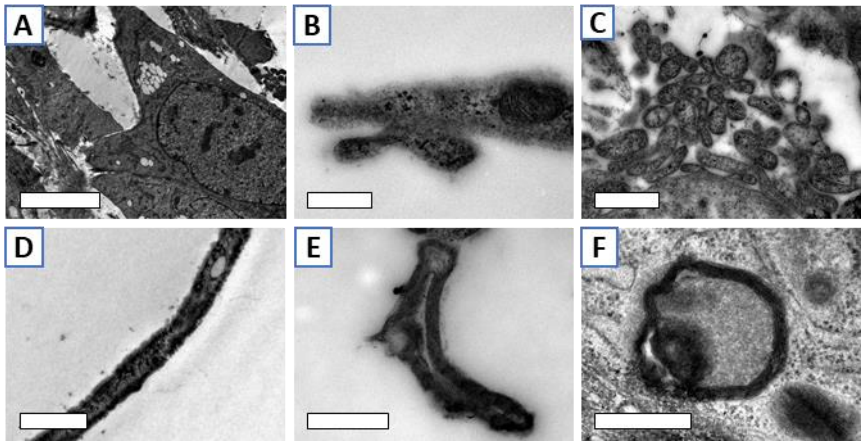

Figure 2-10. *TEM analysis results of the DRGn and SC coculture after 17 DIV (5 days of coculture).* ***A)*** *Neuron soma (scale bar 10 µm).* ***B)*** *Synaptic terminal (scale bar 500 nm).* ***C)*** *Transversal cut of axons or astrocytes (scale bar 1 µm).* ***D)*** *Longitudinal cut of an unmyelinated axon (scale bar 2 µm).* ***E)*** *Longitudinal cut of a myelinated axon (scale bar 5 µm).* ***F)*** *Apposed membranes (scale bar 500 nm).*

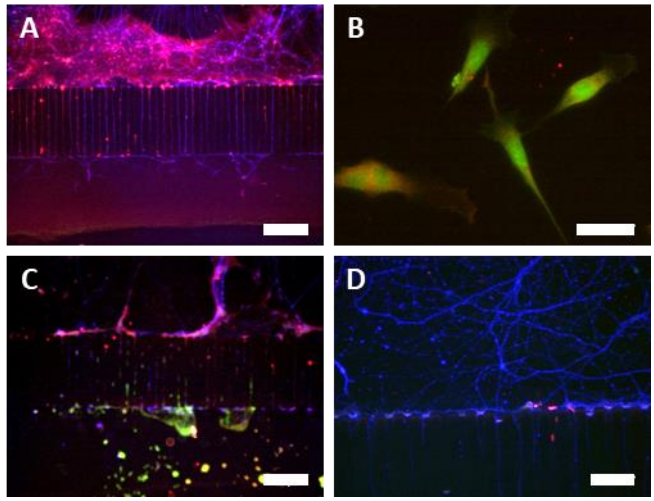

Figure 2-11. *Immunostaining images of efferent PNS-on-a-chip showing TUJ1 in blue, SW10-GFP+ Schwann cells in green and MBP in red.* ***A)*** *MN axons have just crossed microchannels from chamber-1 to chamber-2 after 14 DIV (2 DIV coculture).* ***B)*** *Schwann cells start to form myelin after 2 DIV coculture.* ***C)*** *MN and Schwann cells are death after 19 DIV (7 DIV coculture).* ***D)*** *MN cultured without SW10-GFP+ Schwann cells die after 19 DIV. Scale bar is 300 µm for pictures* ***A*** *and* ***C****, 25 µm for picture* ***B****, and 100 µm for picture* ***D****.*

2.4.5. 3D cell culture

To move to a 3D culture system, first the ECM viability was tested and seeding densities were optimised in Matrigel-based composites. Matrigel diluted in medium (75% or 50% dilution) demeaned during the required culture span (results not shown), proving not to be suitable for 3D cultures of any studied cell kind. Regarding the rest of the Matrigel-based composites (100% Matrigel and 1:1 dilution with collagen-I), different results were obtained for each cell type. SkM showed a viability higher than 80% in all ECM composites studied, although there were more variations among low cell-density samples (FIGURE 2-12-B).

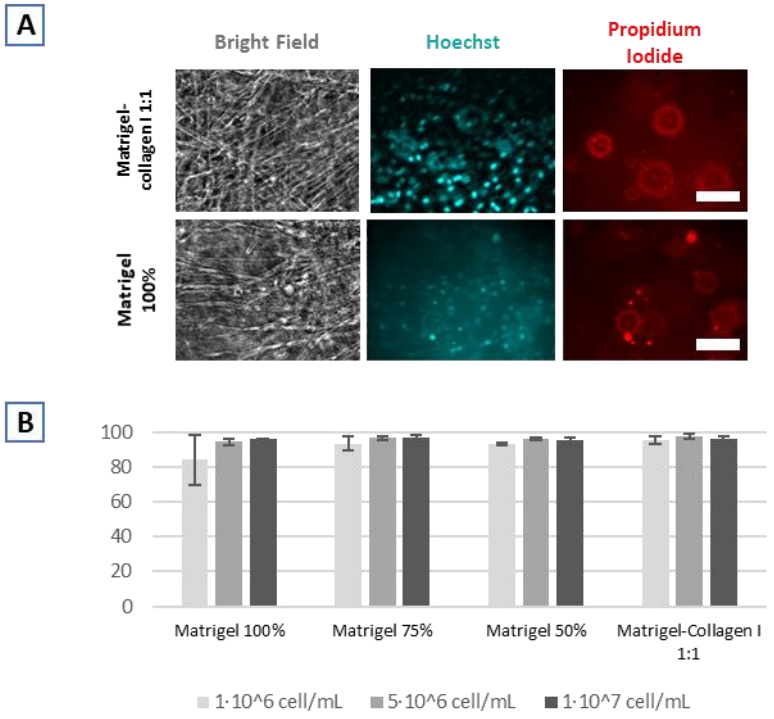

Figure 2-12. *Viability test of SkM cells at different seeding densities embedded in different Matrigel-based composites.* ***A)*** *Qualitative viability analysis of C2C12*

cells seeded at a density of $5 \cdot 10^6\ cell \cdot mL^{-1}$ *after 10 DIV, embedded in Matrigel and Matrigel-collagen I composites. The morphology of muscle fibres (phase contrast, grey), total cell nuclei (Hoechst, blue) and death cell nuclei (propidium iodide, red) is observed. Scale bar 100 µm.* ***B)*** *Quantitative viability percentage showing average and standard deviation of SkM cells seeded at initial densities of* $1 \cdot 10^6\ cell \cdot mL^{-1}$, $5 \cdot 10^6\ cell \cdot mL^{-1}$, $1 \cdot 10^7\ cell \cdot mL^{-1}$ *in different Matrigel-based composites after 10 DIV.*

SC showed high cell death levels in 100% Matrigel regardless of the seeding density (FIGURE 2-13), and showed lower levels of death when culturing them in Matrigel-collagen with DRGn or MN (FIGURE 2-14). Furthermore, SC initially seeded on top of neurons, were able to migrate towards DRGn and MN, ending up in the same Z plane with many endogenous myelinating glial cells (FIGURE 2-14).

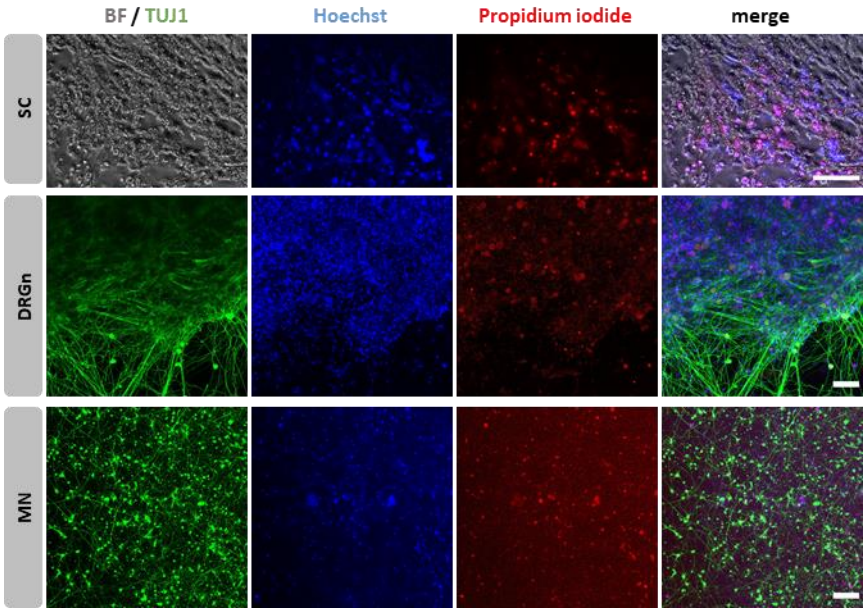

Figure 2-13. *Qualitative viability analysis of cells cultured in Matrigel 100%. Maximum Z proyection of 3D cutures of SC, DRGn and MNs showing Hoechst (blue), propidium iodide (red), Tuj1 (green) and morphology of SC (bright field). Images are taken at the experimental endpoint in cultures of* $5 \cdot 10^5\ cell \cdot mL^{-1}$ *for SC,* $2.5 \cdot 10^6\ cell \cdot mL^{-1}$ *for MN culture, and* $1 \cdot 10^6\ cell \cdot mL^{-1}$ *for DRGn. Scale bar 100 µm.*

DRGn presented high viability levels when culturing them in Matrigel 100% (**Figure 2-13**) and in Matrigel-collagen (**Figure 2-14**), although evaluated densities were too high.

MN showed much higher cell death when culturing them in Matrigel-collagen (FIGURE 2-14), compared to the viability obtained when culturing in Matrigel 100% (FIGURE 2-13), that resulted in 46.7% ± 7.09 standard deviation for the lowest density of MN tested in Matrigel.

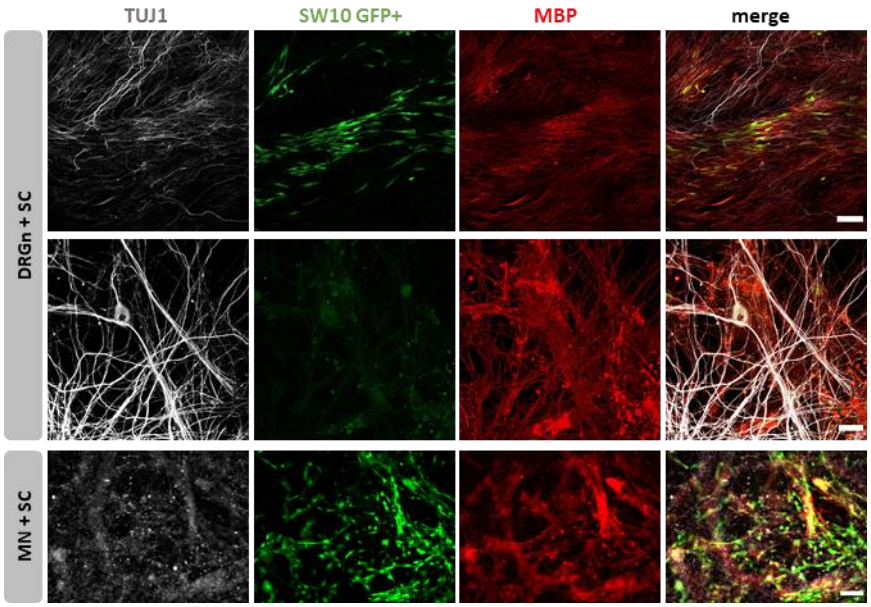

Figure 2-14. *Neural 3D culture in Matrigel-collagen I 1:1. Maximum Z proyection of 3D cutures of DRGn with SC afer 16 DIV (4 DIV of coculture) and MN with SC after 19 DIV (7 DIV of coculture). Tuj-1 (grey), myelin base protein (red), and GFP+ Schwann cells (green) are observed. Scale bars are from the top 100 µm, 20 µm and 100 µm.*

After optimising 3D culture conditions (composite and seeding densities), DRGn or MN were cultured with SkM in NeSUr8 devices, embedding cells in Matrigel 100%.

Results showed that both cell types could grow in Matrigel 100% (FIGURE 2-15). SkM showed differentiation with multinuclear fibres and MHC positive staining in most fibres (FIGURE 2-15-E). However, myocytes were probably not mature enough to detect any kind of functional interaction with neither type of neuron. MN and DRGn axons were able to reach *chamber-2*, but no morphology of synapses or spindles was observed with SkM cells. Apart from axons, some SkM fibres were also observed into the microchannels.

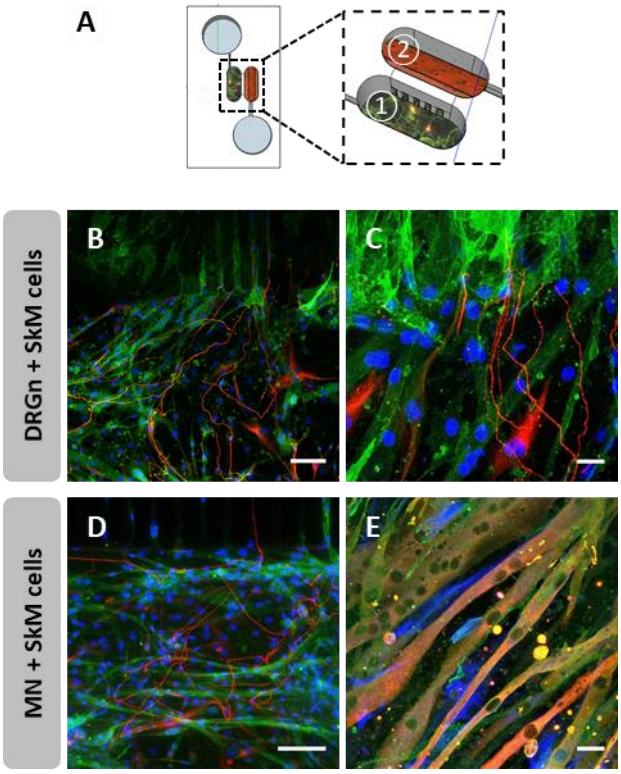

Figure 2-15. *Compartmentalised neuromuscular coculture with cells seeded embedded in Matrigel after 13 DIV of culture (9 DIV cocultured).* ***(A)*** *The device utilised has neural (indicated as ①) and muscular (indicated as ②) compartments (chamber-1 and chamber-2) connected through microchannels.* ***(B)*** *In the compartmentalised coculture of DRGn with SkM, axons of DRGn seeded in chamber-1 cross microchannels towards chamber-2 (scale bar 100µm),* ***(C)*** *where they reach myotubes (scale bar 25µm).* ***(D)*** *In the compartmentalised coculture of MN with SkM, axons of MN seeded in chamber-1 cross microchannels towards chamber-2 (scale bar 100µm),* ***(E)*** *where myotubes are formed (scale bar 25µm). The immunostaining for* ***B, C, D*** *shows: Hoechst (blue), Tuj1 (red), C2C12-YFP+ (green). The immunostaining for* ***E*** *shows: Tuj1 (blue), MHC (red), C2C12-YFP+ (green).*

2.5. Discussion

2.5.1. Compartmentalised microfluidic device

NeSUr8 device was designed and fabricated offering the opportunity to culture in 2D different cell types, connecting them through microchannels. It has proved to be an *in vitro* versatile culture platform, transparent, non-toxic, suitable for imaging, and cost-effective once the process is optimised. Compartmentalisation permits mimicking of two interconnected microenvironments, each supplied by its own medium. Neurons can be cultured in more physiological conditions — physically separated from Schwann cells or skeletal muscle cells, but connected through microchannels so that axons can travel through different compartments —, and exposed to different media with low diffusion. Oval shape of seeding chambers maximises cell exposure to microchannels, shortens the distance to be covered by axons, while the lack of corners facilitates medium change without accumulation of death cells in the corners. The addition of reservoirs limits shear stress applied on neurons during medium changes and assures medium supply without evaporation for the required time periods. The size of microchannels (15x15x1000 µm) facilitates the partial isolation of neural somas from cells seeded in *chamber-2*. Compartmentalised cultures showed that in few cases glia and even SkM cells go into the microchannels (FIGURE 2-9-A and FIGURE 2-15). To assure complete isolation, microchannels width and height should be smaller.

However, smaller microchannels reduce the probability of axons from finding the channel and crossing; and minimises the diffusion of trophic factors secreted from the cells in *chamber-2* that recruit axons to that side to make connections.

Additionally, the compartmentalisation of the device and the fluidic resistance diminishes the media diffusion from one chamber to the other (FIGURE 2-5-I), avoiding possible cell damage caused by undesired components in the medium, as shown that occurs for SC with *MN medium* in FIGURE 2-6 and *DRG medium* in FIGURE 2-7.

The PDMS moulding (including PDMS curing, punching, and bonding) is a largely manual process, and specially the punching step may cause differences from one replica to another. And although there is a height of 200 µm in areas close to microchannels not properly opened with the punch, cells tend to remain in the opened chamber. Therefore, the accuracy of punches made close to microchannels could determine the space neural axons have to go over before reaching *chamber-2*. This difficulties in manual processes suggest that a more automated process could be better. This is further studied with the fabrication of MINDS device in *Chapter 4*.

2.5.2. Myelin induction

The myelin production analysis performed on SC after exposing them to different media (FIGURE 2-8) showed that *DRG medium* with 1% FBS and 10% or 25% HS could be a suitable medium to promote myelination, providing minimum FBS required for SC (FIGURE 2-7) and reaching similar MBP levels to the ones obtained in a sciatic nerve. There is a controversy on this regards, as some studies have induced myelination with up to 40% HS in rat brain explants,[57] whereas others report that the use of 15% calf bovine serum inhibited myelination in rat primary DRG cultures,[88] and cultures containing 5% HS induce higher myelin sheath formation on primary mice Schwann cells compared to using 15% HS.[52] These differences could be due to the different kind of serum used, small variations in its composition among lots, and mostly due to the type of cell culture where myelination analysis was performed, being affected by the influence of neurons and other glial cells contained in primary cultures. Our results indicate that horse serum can induce myelination in tested conditions in SW10 Schwann cells cultured alone.

DRG-CM was expected to induce high levels of myelination in SC, as DRG neurons release in the medium trophic factors that could hypothetically induce the recruitment and myelination of SC. However, the lowest MBP levels were obtained with DRG-CM (FIGURE 2-8), probably caused by a shortage of nutrients in the

medium, previously consumed by DRG utilised to generate the DRG-CM.

Results also showed that AraC, suggested as an inhibitor to decrease proliferation, is indeed toxic for SC in a concentration of 1.5 µM (FIGURE 2-8), agreeing with the SC death obtained in *MN medium* (FIGURE 2-6).

Ascorbic acid antioxidant, was first described to induce myelination by Eldridge *et al.,*[56] and it has been later on reported to be essential for myelination using a dose of 50 $\mu g \cdot mL^{-1}$, or up to 100 $\mu g \cdot mL^{-1}$.[52–55] Podratz *et al* also reported that ascorbic acid together with antioxidants of B-27™ supplement onto N-2 medium could induce myelination in rat primary DRG cultures.[88] However here obtained results suggest other way. SC cultured in their own medium with AA experienced a decrease in MBP production, compared to base medium, that was restored when adding 10% HS (FIGURE 2-8-B). This decrease in MBP could be hypothetically related to the need of certain reactive oxygen species — blocked by the antioxidant ascorbic acid — to induce myelination, as it occurs in other regenerative processes.[89] In the case of SC cultured in *DRG medium* with FBS, there is no observable effect of ascorbic acid (FIGURE 2-8-B) probably because of the influence of B-27™, a neural-culture supplement known to support cell viability and growth, contained in *DRG medium*. B-27™ has been reported before to support myelination.[88] However, its composition is quite complex

(antioxidants, corticosterone, biotin, L-carnitine, D-galactose, retinyl acetate, ethanolamine and triiodo-1-thyrosine and N2 supplement components). The effect of B-27™ components should be further studied individually in normalised conditions in Schwann cells alone to find out the precise influence of antioxidants and other components of B-27™ in myelination process.

2.5.3. Mimicking a myelinating PNS

Mimicking the myelinating PNS on NeSUr8 devices represented a challenge on stablishing the coculture timepoint (once axons had reached *chamber-2*) and stablishing the time span to achieve myelination in *chamber-2* using a SC cell line with high proliferation ratios. AraC, reported to reduce proliferation of glial cells, had shown in other experiments to be toxic for SC in the concentration used (FIGURE 2-8 and FIGURE 2-6), needing to reduce the initial seeding density for the longest possible coculture time. A coculture time window of 7 DIV was successfully achieved once axons had reached *chamber-2*.

Within that time window, PNS-on-a-chip was successfully mimicked for the afferent pathway, obtaining myelination as well as formation of myelin sheaths (FIGURE 2-9). Although, apposed membranes were observed in TEM imaging of DRGn and SC cocultures, classical myelin sheath was not observed (FIGURE 2-10). Regarding the mimicking of PNS efferent pathway, long-term culture of MN

entailed complications (FIGURE 2-11), agreeing with results obtained by Gingras *et al.* where MN do not survive after 14 DIV when seeded alone.[55]

Several studies coculturing primary MN and primary Schwann cells achieve myelination and synapse formation in long term cultures.[2,54,55,90] Some studies that coculture primary DRGn and primary Schwann cells also report successful results.[2,3,52] Proper myelination of the efferent pathway requires long-term coculture of neurons and Schwann cells. However, in the experiment performed within the stablished time window, MN started dying after 14 DIV (2 DIV of coculture), making impossible to achieve proper myelination of the efferent pathway of the PNS. In our experiment, working with cell-lines together with primary cells within the defined time window, represented a challenge due to different proliferation rate as well as media requirements.

2.5.4. 3D cell culture

Moving to a 3D system to increase cell viability and for a more physiologically relevant mimicking, meant a requirement of a similar ECM composition for all cells involved (neurons, glia and muscle cells), as neurons have to go through all compartments and interact with all cells to reach the muscle in the compartmentalised microfluidic culture system. MN showed highest viability when culturing in 100% Matrigel (FIGURE 2-13); whereas DRGn seemed to

grow properly in Matrigel-collagen too. SkM cell viability was similar in all composites studied at high densities (FIGURE 2-12). However at lower densities, it was better with Matrigel-collagen, agreeing with previous studies.[84] SC showed high cell-death levels in Matrigel-based composites (FIGURE 2-13), being more viable Matrigel-collagen due to higher stiffness, as previously reported.[77]

Working with SC seemed to be a complication, as it has different proliferation rates, different medium requirements and different ECM compatibility, compared to neurons. Furthermore, myelinating endogenous Schwann cells can be obtained from the same dissection as primary neurons, being that enough to induce myelination with promyelinating medium. Therefore, we decided to prescind from exogenous SC cell line, taking profit of endogenous SC, and stablish Matrigel 100% as the composite compatible for the 3D cell culture of all essential cells utilised. Although its tumoral origin raise concerns in the scientific community for similar effects on cells seeded on them.[91]

We decided to build up a preliminary 3D mechanosensory-motor system embedding cells (MN, DRGn and SkM cells) in Matrigel and seeding them in NeSUr8 devices. Results showed that both cell types could grow in Matrigel 100%. However, Matrigel blocked some microchannels impeding proper medium flow and nutrient diffusion. MN and DRGn axons were able to reach *chamber-2*, but no morphology of synapses or spindles was observed with SkM cells

(FIGURE 2-15). This could be due to an insufficient maturation of SkM cells to form extrafusal muscle fibres (interacting with MN through a synapse) or difficulties of C2C12 cell line to form intrafusal muscle fibres (interacting with DRGn forming spindle-like structures). Higher maturation levels could be achieved by biochemical, optical, mechanical or electrical stimuli.

For instance, parallel experiments performed in the co-supervision of the master thesis of A. Esteban Tezanos,[83] we could observe the effect of different optical stimuli protocols on the maturation of same skeletal muscle cells embedded in Matrigel. In that project optical training was conducted applying 15 min of optical pulses every 24 h, for 9 days, starting after 2 DIV. Different protocols were applied: mercury lamp with green fluorescence filter (0.11 $W \cdot mm^{-2}$ potency lamp, 5 s pulses) and cyan LED 470 nm (0.18 $mW \cdot mm^{-2}$ potency lamp, 1 ms pulses). After 11 DIV, the contractility of myocytes was assessed under optical stimulation. Fluorescence images showed lowest maturation rate for control samples, not exposed to optical training, with the highest green-minus-red mean grey value of 4.09 (FIGURE 2-16-A). The ultrastructure analysis showed as well features related to lowest maturation in non-stimulated control samples, as compared to the ones with optical training (FIGURE 2-16-B). Finally, the contractility assessment showed significant differences between samples exposed to optical training and control ones. During the differentiation, no spontaneous contraction was observed in control samples (detected in the rest of

the samples), and at the final timepoint, no contraction was achieved, whereas samples exposed to optical training showed contraction frequencies of 1.22 and 2.07 Hz (FIGURE 2-16-C).

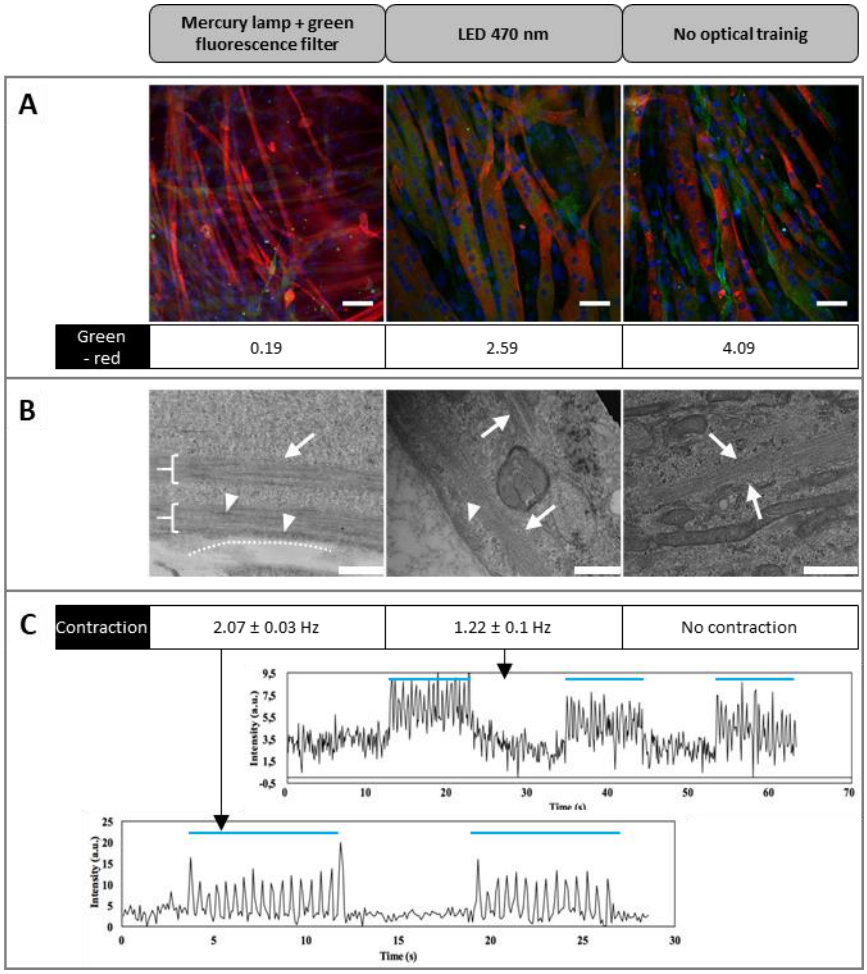

Figure 2-16. *Characterisation of the maturation of C2C12 ChR2+ YFP+ skeletal muscle cells exposed to optical training for 9 days (11 DIV), showing fluorescence imaging* ***(A)****, TEM imaging* ***(B)*** *and the contractility assessment* ***(C)*** *for three conditions: samples subjected to optical training with mercury lamp and green fluorescence filter, samples undergoing optical training with LED lamp at 470 nm, and control samples without optical training.* ***A)*** *Fluorescence imaging, showing nuclei (blue), MHC (red) and YFP of cells (green). Scale bars are 200 µm. Mean grey value quantification of the subtraction of red to green (all cells – differentiated cells = non differentiated cells) is shown for each condition.* ***B)*** *TEM imaging of cells*

cultured in Matrigel. Actin filaments are indicated with an arrow, z-bodies with a triangle, sarcomere-like structures with brackets and cell-membrane with a discontinuous line. Scalebars are from left to right: 1 µm, 100 nm and 500 nm. Actin filaments are observed in the cytosol; progressively migrating to locations close to the membrane in more mature samples; and the most mature samples show actin structures close to the membrane, z-bodies and sarcomere-like organisation ***C)*** *Contraction frequencies observed in the contractility assessment after 11 DIV. Optical stimulation pulses are represented with a blue line. Image adapted from Esteban Tezanos et al.*[83]

In another project performed in collaboration with the group of Prof. J.A. del Río,[82] myotube maturation, neuromuscular junction formation and the effect of optical stimuli on the regeneration of MN axons previously axotomised was evaluated. In this case, C2C12 ChR+ YFP+ cells maturation was achieved through chemical stimuli (a different composition of differentiation medium), obtaining patterned sarcomeric structures (FIGURE 2-17-A). These myotubes were also able to contract in response to electrical stimuli (3 cycles of 20 ms ON and 980 ms OFF of 10 V, 1 Hz pulses, applied for 10 seconds, followed by 10 seconds resting) or optical stimuli (470 nm light, 20-25 $mW \cdot cm^{-2}$ light intensity), avoiding only fatigue with pulsed light stimuli (5 ms pulses, 20 Hz pulse frequency) and obtaining contractions of around 1.13 Hz (FIGURE 2-17-B).

C2C12 ChR2+ YFP+ were cultured embedded in Matrigel in compartmentalised microdevices containing an axotomy microchannel, and after 5 DIV primary MN were added in the other compartment. In this case, contrary to results obtained in this chapter in FIGURE 2-15, muscle cells were seeded first and facilitated

axon regeneration and neuromuscular junction formation in 7-10 days of coculture (FIGURE 2-17-C). Then vacuum-assisted axotomy was performed and we assessed the effects of modulating muscular activity of denervated muscle fibres through optogenetics on axon regeneration. Results showed that increasing muscular activity after MN axotomy by optical stimulation, induced higher regeneration of axons (FIGURE 2-17-D) related to the release of leukemia inhibitory factor (LIF) and glial cell line-derived neurotrophic factor (GDNF) in a paracrine signalling fashion from muscle cells. This can explain why in this chapter in FIGURE 2-15, immature SkM cells could not form functional connections with MN. Further maturation prior to coculturing with neurons would be required to facilitate axon elongation, shorten coculture time length and obtain functional interactions.

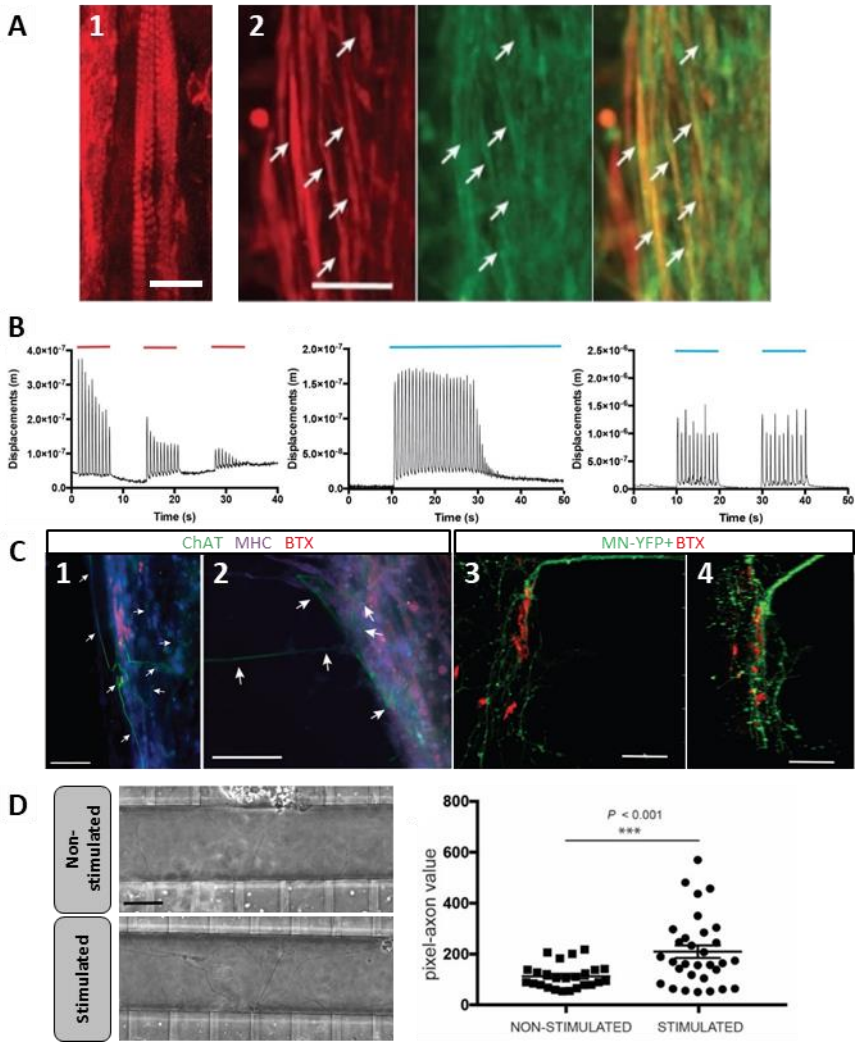

Figure 2-17. *Neuromuscular interaction with MN and C2C12 ChR2+ YFP+ cells.* ***A)*** *Fluorescence imaging of C2C12 ChR2+ YFP+ cells after 7 DIV, showing MHC (red), and ChR2+ YFP (green). Scalebars are 50 µm (1) and 25 µm (2).* ***B)*** *C2C12 ChR2+ YFP+ displacement measurements after pulsed electrical stimulation pulses (red line) or continuous or pulsed optical stimulation (blue line).* ***C)*** *Fluorescence imaging of neuromuscular interaction after 12-15 days of coculture showing MN (ChAT or YFP+), myocytes (MHC) and synapsis (BTX). Scalebars are: 200 mm (1,2), 70 mm (3), 30 mm (4).* ***D)*** *Quantification of axons present in the axotomy channel 48 h after the axotomy, in the presence or absence of optical stimulation applied on C2C12 ChR2+ differentiated myotubes. Scalebars are 50 µm. Each dot on the graph corresponds to the number of pixels occupied by a measured axon. Image adapted from Sala-Jarque et al.*[82]

2.6. Conclusions

This work stablishes the techniques for 2D and 3D neuromuscular cell culture model in a microfluidic device using mice primary cells and cell lines.

The NeSUr8 devices was successfully designed and fabricated. It has proved to be a versatile device, with minimal media diffusion for neural 2D cultures.

Myelination induction tests performed showed that *DRG medium* with 1% FBS, and 10% or 25% HS could be a suitable medium to promote myelination. HS acted as an enhancer of the myelination in tested conditions in SW10 Schwann cells cultured alone. Obtained results also suggest that B-27™ supplement could have an effect in myelination. The influence of each of its components should be further studied in Schwann cells cultured alone to elucidate the effect of certain antioxidants or other components in the myelin formation.

To study the PNS, a coculture time window for primary neurons and SC cell-line was successfully stablished, making possible a coculture of 7 DIV. Within that time window,the PNS afferent pathway with promyelinating medium was successfully recreated in NeSUr8 devices, obtaining myelin sheaths and apposed membranes. However, regarding efferent PNS experiments performed, long-term culture of primary MN entailed complications. Moving to a 3D

system increased MN viability and mimicked better physiological microenvironment.

Matrigel 100% worked successfully to create 3D cell cultures for most of the cells. Diluted Matrigel did not work for 3D cultures due to its degradability, but 100% Matrigel and Matrigel-collagen mixture showed high viability results for DRGn and SkM cells. MN showed their highest viability in 100% Matrigel. SC, on the other hand, showed high cell death ratios in all composites tested and therefore we decided to prescind them for the neuromuscular culture on NeSUr8 devices taking advantage of the endogenous Schwann cells obtained from primary neuronal cultures.

Neuromuscular afferent and efferent pathways were mimicked in NeSUr8 devices embedding in Matrigel 100% DRGn and SkM cells, and MN and SkM cells respectively, showing good compatibility among cells within the Matrigel. Although axons reached muscular chamber, no interaction was observed, due to an insufficient maturation of myocytes. Proper maturation and neuromuscular junction formation was successfully achieved in parallel projects performed in collaboration, exposing SkM cells to biochemical and optical stimuli.

The *in vitro model* presented in this chapter represents first steps towards a miniaturisation of a PNS motor unit on a chip. And it has served as a first proof of concept for the next steps in the

collaboration projects presented here, and coculturing MN, SN and SkM in the MINDS device (see *Chapter 4*).

2.7. Appendix

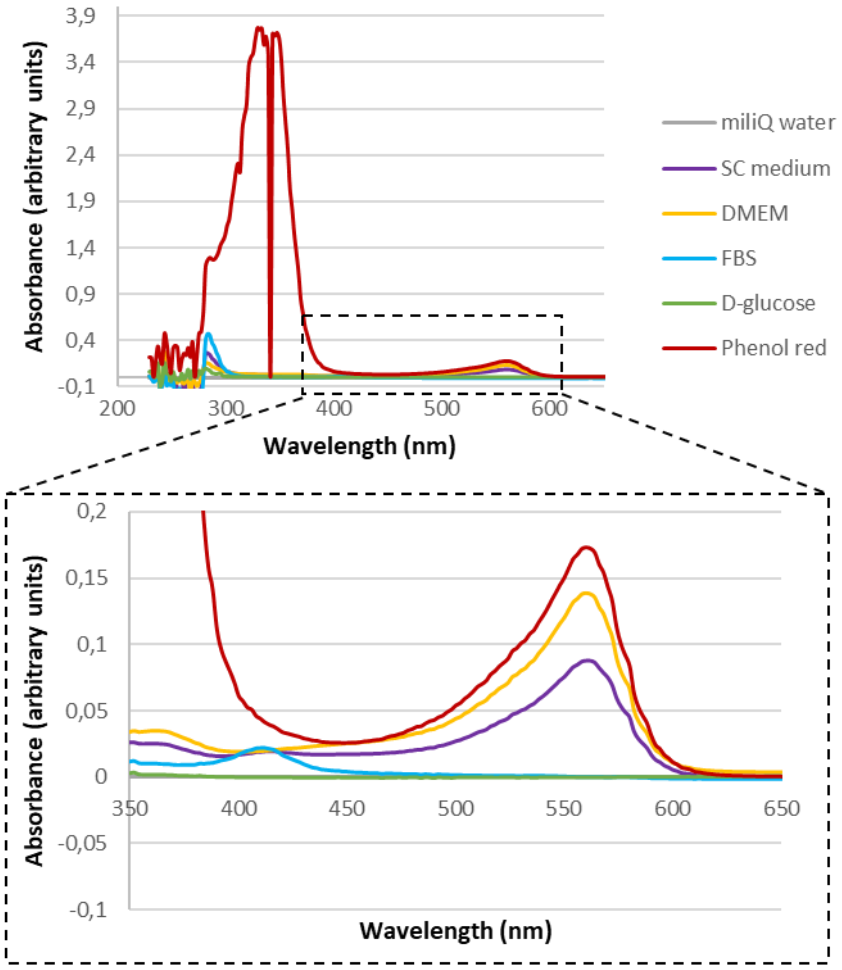

Figure 2-18. *Absorbance of medium components versus wavelength. The absorbance spectrum for supplemented medium (SC medium) and different medium components (D-glucose, FBS, phenol red, DMEM) and miliQ water. The augmented image of the spectrum shows a peak in all components containing phenol red (SC medium, DMEM and phenol red) at 560 nm. All components were measured in a 1:5 dilution. The average values (n=3) are normalised against miliQ water.*

Table 2-9. *Composition of radioimmunoprecipitation assay (RIPA) buffer and other stock solutions required to prepare it.*
N/A = not applicable; SDS = sodium dodecyl sulphate

Gel	Components	Final concentration	Commercial reference
SDS 10%	Sodium dodecyl sulfate	10% (wt/vol)	(Bio-Rad, #161-0301)
	Milli-Q water	N/A	N/A
Protease 100X	Complete mini (protease inhibitor cocktail tablets)	100X	(Roche, #11836153001)
	Milli-Q water	N/A	N/A
RIPA buffer	Tris base	10 mM	(Sigma Aldrich, #154563)
	Magnesium chloride	1 M	(PanReac, #131396.1210)
	Triton	1%	(Sigma Aldrich, #T8787)
	Protease 100X	1X	(from stock)
	SDS 10%	0.25%	(from stock)
	Milli-Q water	N/A	N/A

Table 2-10. *Western blot stock solutions.*
N/A = not applicable; wt/vol = weight/volume; SDS = sodium dodecyl sulphate; APS = ammonium persulfate.

WB stock solutions	Components	Final concentration	Commercial reference
Tris 1.5 M pH 8.8	Tris base	1.5 M	(Sigma Aldrich, #154563)
	Milli-Q water	N/A	N/A
	————————-Adjuts pH to 8.8————————-		
Tris 1 M pH 6.8	1 M Tris base	1 M	(Sigma Aldrich, #154563)
	Milli-Q water	N/A	N/A
	————————-Adjuts pH to 6.8————————-		
APS 10%	Ammonium persulfate	10% (wt/vol)	(Bio-Rad, #161-0700)
	Milli-Q water	N/A	N/A
Tris / Glycine 10X	Glycine	1.9 M	(Sigma Aldrich, #G7126)
	Tris base	0.25 M	(Sigma Aldrich, #154563)
	Milli-Q water	N/A	N/A
SDS 20%	Sodium dodecyl sulfate	20% (wt/vol)	(Bio-Rad, #161-0301)
	Milli-Q water	N/A	N/A
SDS 10%	Sodium dodecyl sulfate	10% (wt/vol)	(Bio-Rad, #161-0301)
	Milli-Q water	N/A	N/A
Laemmli 4X	Tris 1M pH 6.8	0.25 M	(from stock)
	SDS 20%	4%	(from stock)
	Glycerol	40%	(Sigma Aldrich, #G7757)
	Bromophenol blue	0.005% (wt/vol)	(Sigma Aldrich, #B5525)
	Milli-Q water	N/A	N/A

Table 2-11. *Composition of electrophoresis gels. The mixture is prepared under the fumehood in the order indicated. The mixture is prepared with Acrylamide 30% (Biorad, #161-0158), TEMED (Biorad, #161-0800) and stock solutions previously prepared (see* ***Table 2-10****).*

Gel	Components and final concentration	Amount for 2 gels
Resolving gel (bottom)	Milli-Q H2O	6.6 mL
	12% Acrylamide	8 mL
	Tris 1.5 M pH 8.8	5 mL
	SDS 10%	0.2 mL
	APS 10%	0.2 mL
	TEMED	8uL
Stacking gel (top)	Milli-Q H2O	5.5 mL
	5% Acrylamide	1.3 mL
	Tris 1M pH 6.8	1 mL
	SDS 10%	80 µL
	APS 10%	80 µL
	TEMED	8 µL

Table 2-12. *Western blot buffers. They are prepared utilising Western blot stock solutions (see* ***Table 2-10****).*
SDS = sodium dodecyl sulphate; N/A = not applicable.

Buffer	Components	Final concentration	Commercial reference
Loading buffer	Laemmli 4X	90%	(from stock)
	β-mercaptoethanol	10%	(Sigma Aldrich, #M6250)
Running buffer	Tris/Glycine 10X buffer	1X	(from stock)
	SDS 20%	0.1%	(from stock)
	Milli-Q water	N/A	N/A
Transfer buffer	Methanol	20%	(Sigma Aldrich, #179337)
	Milli-Q water	N/A	N/A
	Tris/Glycine 10X buffer	1X	(from stock)

Table 2-13. *Immunoblotting buffers.*
PBS = Dulbecco's Phosphate Buffered Saline; FBS = foetal bovine serum; HRP = horseradish peroxidase; N/A = not applicable

Buffer	Components	Final concentration	Commercial reference
TPBS	PBS	1X	(Gibco, #21600-010)
	Tween® 20	0.1%	(Sigma Aldrich, #P7949)
	Milli-Q water	N/A	N/A
Blocking solution	TPBS	N/A	(from stock)
	Skimmed milk powder	5% (wt/vol)	Sveltesse (Nestle) Leche desnatada en polvo rica en calcio
	FBS	2%	(Gibco, #26140079)
Secondary antibody solution	TPBS	N/A	(from stock)
	Skimmed milk powder	5% (wt/vol)	Sveltesse (Nestle) Leche desnatada en polvo rica en calcio
	FBS	1%	(Gibco, #26140079)
	Goat anti mouse HRP	1:3.000	(Millipore, #12-349)
	Protein ladder anti HRP	1:20.000	(Bio-Rad, #1610385)

2.8. References

1. Deenen, J. C. W., Horlings, C. G. C., Verschuuren, J. J. G. M., Verbeek, A. L. M. & Van Engelen, B. G. M. The epidemiology of neuromuscular disorders: a comprehensive overview of the literature. *J. Neuromuscul. Dis.* **2**, 73–85 (2015).
2. Vilmont, V., Cadot, B., Ouanounou, G. & Gomes, E. R. A system for studying mechanisms of neuromuscular junction development and maintenance. *Development* **143**, 2464–2477 (2016).
3. Hunter, G., Aghamaleky Sarvestany, A., Roche, S. L., Symes, R. C. & Gillingwater, T. H. SMN-dependent intrinsic defects in Schwann cells in mouse models of spinal muscular atrophy. *Hum. Mol. Genet.* **23**, 2235–2250 (2014).
4. Tang-Schomer, M. D. *et al.* Bioengineered functional brain-like cortical tissue. *Proc. Natl. Acad. Sci.* **111**, 13811–13816 (2014).
5. Morimoto, Y., Kato-Negishi, M., Onoe, H. & Takeuchi, S. Three-dimensional neuron–muscle constructs with neuromuscular junctions. *Biomaterials* **34**, 9413–9419 (2013).
6. Jablonka, S. *et al.* Distinct and overlapping alterations in motor and sensory neurons in a mouse model of spinal muscular atrophy. *Hum. Mol. Genet.* **15**, 511–518 (2006).
7. Lobsiger, C. S. & Cleveland, D. W. Glial cells as intrinsic components of non-cell-autonomous neurodegenerative disease. *Nat. Neurosci.* **10**, 1355–1360 (2007).
8. Scannell, J. W., Blanckley, A., Boldon, H. & Warrington, B. Diagnosing the decline in pharmaceutical R&D efficiency. *Nat. Rev. Drug Discov.* **11**, 191–200 (2012).
9. DiMasi, J. A., Grabowski, H. G. & Hansen, R. W. Innovation in the pharmaceutical industry: New estimates of R&D costs. *J. Health Econ.* **47**, 20–33 (2016).
10. Sackmann, E. K., Fulton, A. L. & Beebe, D. J. The present and future role of microfluidics in biomedical research. *Nature* **507**, 181–9 (2014).
11. Volpatti, L. R. & Yetisen, A. K. Commercialization of microfluidic devices. *Trends Biotechnol.* **32**, 347–350 (2014).
12. Bhatia, S. N. & Ingber, D. E. Microfluidic organs-on-chips. *Nat. Biotechnol.* **32**, 760–772 (2014).
13. Uzel, S. G. M., Pavesi, A. & Kamm, R. D. Microfabrication and microfluidics for muscle tissue models. *Prog. Biophys. Mol. Biol.* **115**, 279–293 (2014).

14. Sakar, M. S. *et al.* Formation and optogenetic control of engineered 3D skeletal muscle bioactuators. *Lab Chip* **12**, 4976–85 (2012).

15. Marsano, A. *et al.* Beating heart on a chip: a novel microfluidic platform to generate functional 3D cardiac microtissues. *Lab Chip* **16**, 599–610 (2016).

16. Truskey, G. A. Development and application of human skeletal muscle microphysiological systems. *Lab Chip* **18**, 3061–3073 (2018).

17. Lam, M. T., Huang, Y. C., Birla, R. K. & Takayama, S. Microfeature guided skeletal muscle tissue engineering for highly organized 3-dimensional free-standing constructs. *Biomaterials* **30**, 1150–1155 (2009).

18. Badiola-Mateos, M., Hervera, A., del Río, J. A. & Samitier, J. Challenges and future prospects on 3D in-vitro modeling of the neuromuscular circuit. *Front. Bioeng. Biotechnol.* **6**, 194 (2018).

19. Haase, K., Gillrie, M. R., Hajal, C. & Kamm, R. D. Pericytes contribute to dysfunction in a human 3D model of placental microvasculature through VEGF-Ang-Tie2 signaling. *Adv. Sci.* **6**, 1900878 (2019).

20. Nashimoto, Y. *et al.* Vascularized cancer on a chip: The effect of perfusion on growth and drug delivery of tumor spheroid. *Biomaterials* **229**, 119547 (2020).

21. Huh, D. *et al.* Reconstituting organ-level lung functions on a chip. *Science (80-.).* **328**, 1662–1668 (2010).

22. Benam, K. H. *et al.* Small airway-on-a-chip enables analysis of human lung inflammation and drug responses in vitro. *Nat. Methods* **13**, 151–157 (2016).

23. Wang, L. *et al.* A disease model of diabetic nephropathy in a glomerulus-on-a-chip microdevice. *Lab Chip* **17**, 1749–1760 (2017).

24. Musah, S. *et al.* Mature induced-pluripotent-stem-cell-derived human podocytes reconstitute kidney glomerular-capillary-wall function on a chip. *Nat. Biomed. Eng.* **1**, 0069 (2017).

25. Jang, K. J. *et al.* Human kidney proximal tubule-on-a-chip for drug transport and nephrotoxicity assessment. *Integr. Biol.* **5**, 1119–1129 (2013).

26. Xiao, S. *et al.* A microfluidic culture model of the human reproductive tract and 28-day menstrual cycle. *Nat. Commun.* **8**, 14584 (2017).

27. Kim, H. J., Huh, D., Hamilton, G. & Ingber, D. E. Human gut-on-a-chip inhabited by microbial flora that experiences intestinal peristalsis-like motions and flow. *Lab Chip* **12**, 2165–2174 (2012).

28. Lee, H. *et al.* Cell-printed 3D liver-on-a-chip possessing a liver microenvironment and biliary system. *Biofabrication* **11**, 025001 (2019).

29. Booth, R. & Kim, H. Characterization of a microfluidic in vitro model of the blood-brain barrier (μBBB). *Lab Chip* **12**, 1784–1792 (2012).

30. Adriani, G., Ma, D., Pavesi, A., Kamm, R. D. & Goh, E. L. K. A 3D neurovascular microfluidic model consisting of neurons, astrocytes and cerebral endothelial cells as a blood–brain barrier. *Lab Chip* **17**, 448–459 (2017).

31. Xu, H. *et al.* A dynamic in vivo-like organotypic blood-brain barrier model to probe metastatic brain tumors. *Sci. Rep.* **6**, 36670 (2016).

32. Maschmeyer, I. *et al.* A four-organ-chip for interconnected long-term co-culture of human intestine, liver, skin and kidney equivalents. *Lab Chip* **15**, 2688–2699 (2015).

33. Edington, C. D. *et al.* Interconnected microphysiological systems for quantitative biology and pharmacology studies. *Sci. Rep.* **8**, 4530 (2018).

34. Loskill, P., Marcus, S. G., Mathur, A., Reese, W. M. & Healy, K. E. μOrgano: A Lego®-like plug & play system for modular multi-organ-chips. *PLoS One* **10**, e0139587 (2015).

35. Sung, J. H. *et al.* Using physiologically-based pharmacokinetic-guided "body-on-a-chip" systems to predict mammalian response to drug and chemical exposure. *Exp. Biol. Med.* **239**, 1225–1239 (2014).

36. Zhang, W. *et al.* Elastomeric free-form blood vessels for interconnecting organs on chip systems. *Lab Chip* **16**, 1579–1586 (2016).

37. Park, J. W., Vahidi, B., Taylor, A. M., Rhee, S. W. & Jeon, N. L. Microfluidic culture platform for neuroscience research. *Nat. Protoc.* **1**, 2128–2136 (2006).

38. Masuda, S., Washizu, M. & Nanba, T. Novel method of cell fusion in field constriction area in fluid integration circuit. *IEEE Trans. Ind. Appl.* **25**, 732–737 (1989).

39. Ho, C. M. B., Ng, S. H., Li, K. H. H. & Yoon, Y. J. 3D printed microfluidics for biological applications. *Lab Chip* **15**, 3627–3637 (2015).

40. Melchels, F. P., Feijen, J. & Grijpma, D. W. A review on stereolithography and its applications in biomedical engineering. *Biomaterials* **31**, 6121–6130 (2010).

41. Whitesides, G. M., Ostuni, E., Takayama, S., Jiang, X. & Ingber, D. E. Soft lithography in biology and biochemistry. *Annu. Rev. Biomed. Eng.* **3**, 335–373 (2001).

42. Nave, K.-A. & Werner, H. B. Myelination of the nervous system: mechanisms and functions. *Annu. Rev. Cell Dev. Biol.* **30**, 503–533 (2014).

43. Jessen, K. R. & Mirsky, R. The repair Schwann cell and its function in regenerating nerves. *J. Physiol.* **594**, 3521–3531 (2016).

44. Arbour, D., Vande Velde, C. & Robitaille, R. New perspectives on amyotrophic lateral sclerosis: the role of glial cells at the neuromuscular junction. *J. Physiol.* **595**, 647–661 (2017).

45. Singh, T. & Vazquez, M. Time-dependent addition of neuronal and Schwann cells increase myotube viability and length in an in vitro tri-culture model of the neuromuscular junction. *Regen. Eng. Transl. Med.* **5**, 402–413 (2019).

46. Barik, A., Li, L., Sathyamurthy, A., Xiong, W. C. & Mei, L. Schwann cells in neuromuscular junction formation and maintenance. *J. Neurosci.* **36**, 9770–9781 (2016).

47. Chan, J. R. *et al.* NGF controls axonal receptivity to myelination by Schwann cells or oligodendrocytes. *Neuron* **43**, 183–191 (2004).

48. Schumacher, M. *et al.* Progesterone synthesis and myelin formation in peripheral nerves. *Brain Res. Rev.* **37**, 343–359 (2001).

49. Wanner, I. B. & Wood, P. M. N-cadherin mediates axon-aligned process growth and cell–cell interaction in rat Schwann cells. *J. Neurosci.* **22**, 4066–4079 (2002).

50. Feltri, M. L. *et al.* Conditional disruption of β1 integrin in Schwann cells impedes interactions with axons. *J. Cell Biol.* **156**, 199–210 (2002).

51. Kegel, L. *et al.* Functional phylogenetic analysis of LGI proteins identifies an interaction motif crucial for myelination. *Development* **141**, 1749–1756 (2014).

52. Päiväläinen, S. *et al.* Myelination in mouse dorsal root ganglion/Schwann cell cocultures. *Mol. Cell. Neurosci.* **37**, 568–578 (2008).

53. Stettner, M. *et al.* Promoting myelination in an in vitro mouse model of the peripheral nerve system: the effect of wine ingredients. *PLoS One* **8**, e66079 (2013).

54. Hyung, S. *et al.* Coculture of primary motor neurons and Schwann cells as a model for in vitro myelination. *Sci. Rep.* **5**, 15122 (2015).

55. Gingras, M., Beaulieu, M. M., Gagnon, V., Durham, H. D. & Berthod, F. In vitro study of axonal migration and myelination of motor neurons in a three-dimensional tissue-engineered model. *Glia* **56**, 354–364 (2008).

56. Eldridge, C. F., Bunge, M. B., Bunge, R. P. & Wood, P. M. Differentiation of axon-related Schwann cells in vitro. I. Ascorbic acid regulates basal lamina assembly and myelin formation. *J. Cell Biol.* **105**, 1023–1034 (1987).

57. Chida, N. & Shimizu, Y. Biosynthesis of myelin lipids of cultured nervous tissues - Incorporation of choline and CDP-choline into myelin phospholipids. *Tohoku J. Exp. Med.* **111**, 41–49 (1973).

58. Siddique, R. & Thakor, N. Investigation of nerve injury through

microfluidic devices. *J. R. Soc. Interface* **11**, 20130676 (2014).

59. Tong, Z. *et al.* A microfluidic neuronal platform for neuron axotomy and controlled regenerative studies. *RSC Adv.* **5**, 73457–73466 (2015).

60. Karimi, M. *et al.* Microfluidic systems for stem cell-based neural tissue engineering. *Lab Chip* **16**, 2551–2571 (2016).

61. Kerman, B. E. *et al.* In vitro myelin formation using embryonic stem cells. *Development* **142**, 2213–2225 (2015).

62. Johnson, B. N. *et al.* 3D printed nervous system on a chip. *Lab Chip* **16**, 1393–1400 (2016).

63. Uzel, S. G. M. *et al.* Microfluidic device for the formation of optically excitable, three-dimensional, compartmentalized motor units. *Sci. Adv.* **2**, e1501429 (2016).

64. Osaki, T., Uzel, S. G. M. & Kamm, R. D. On-chip 3D neuromuscular model for drug screening and precision medicine in neuromuscular disease. *Nat. Protoc.* **15**, 421–449 (2020).

65. LaPlaca, M. C., Vernekar, V. N., Shoemaker, J. T. & Cullen, D. K. Three-dimensional neuronal cultures. in *Methods in Bioengineering: 3D Tissue Engineering* (eds. Berthiaume, F. & Morgan, J. R.) 187–204 (Artech House Publishers, 2010).

66. Antoni, D., Burckel, H., Josset, E. & Noel, G. Three-dimensional cell culture: a breakthrough in vivo. *Int. J. Mol. Sci.* **16**, 5517–5527 (2015).

67. Baker, B. M. & Chen, C. S. Deconstructing the third dimension – how 3D culture microenvironments alter cellular cues. *J. Cell Sci.* **125**, 3015–3024 (2012).

68. Yamada, K. M. & Cukierman, E. Modeling tissue morphogenesis and cancer in 3D. *Cell* **130**, 601–610 (2007).

69. Ravi, M., Paramesh, V., Kaviya, S. R., Anuradha, E. & Solomon, F. D. P. 3D cell culture systems: advantages and applications. *J. Cell. Physiol.* **230**, 16–26 (2015).

70. Frantz, C., Stewart, K. M. & Weaver, V. M. The extracellular matrix at a glance. *J. Cell Sci.* **123**, 4195–4200 (2010).

71. Pampaloni, F., Reynaud, E. G. & Stelzer, E. H. K. The third dimension bridges the gap between cell culture and live tissue. *Nat. Rev. Mol. Cell Biol.* **8**, 839–845 (2007).

72. Murphy, A. R., Laslett, A., O'Brien, C. M. & Cameron, N. R. Scaffolds for 3D in vitro culture of neural lineage cells. *Acta Biomater.* **54**, 1–20 (2017).

73. Ruedinger, F., Lavrentieva, A., Blume, C., Pepelanova, I. & Scheper, T. Hydrogels for 3D mammalian cell culture: a starting guide for laboratory practice. *Appl. Microbiol. Biotechnol.* **99**, 623–636 (2015).

74. Lancaster, M. A. *et al.* Cerebral organoids model human brain development and microcephaly. *Nature* **501**, 373–379 (2013).

75. De Guzman, R. C., Loeb, J. A. & VandeVord, P. J. Electrospinning of Matrigel to deposit a basal lamina-like nanofiber surface. *J. Biomater. Sci. Polym. Ed.* **21**, 1081–1101 (2010).

76. Wells, M. R. *et al.* Gel matrix vehicles for growth factor application in nerve gap injuries repaired with tubes: a comparison of Biomatrix, collagen, and methylcellulose. *Exp. Neurol.* **146**, 395–402 (1997).

77. Dewitt, D. D., Kaszuba, S. N., Thompson, D. M. & Stegemann, J. P. Collagen I-Matrigel scaffolds for enhanced Schwann cell survival and control of three-dimensional cell morphology. *Tissue Eng. Part A* **15**, 2785–2793 (2009).

78. Tong, Z. *et al.* Engineering a functional neuro-muscular junction model in a chip. *RSC Adv.* **4**, 54788–54797 (2014).

79. Lopez-Martinez, M. J. *et al.* Multiple-internal-reflection poly(dimethylsiloxane) systems for on-line pH monitoring. in *14th International Conference on Miniaturized Systems for Chemistry and Life Sciences 2010, MicroTAS 2010* vol. 1 587–589 (2010).

80. Nagel, G. *et al.* Channelrhodopsin-2, a directly light-gated cation-selective membrane channel. *Proc. Natl. Acad. Sci.* **100**, 13940–13945 (2003).

81. Raman, R. *et al.* Optogenetic skeletal muscle-powered adaptive biological machines. *Proc. Natl. Acad. Sci.* **113**, 3497–3502 (2016).

82. Sala-Jarque, J. *et al.* Neuromuscular Activity Induces Paracrine Signaling and Triggers Axonal Regrowth after Injury in Microfluidic Lab-On-Chip Devices. *Cells* **9**, 302 (2020).

83. Esteban Tezanos, A., Badiola Mateos, M. & Samitier Martí, J. Maturation and characterisation of optically excitable skeletal muscle model in-vitro. (Universitat de Barcelona, 2018).

84. Esteban Tezanos, A., Badiola Mateos, M. & Samitier Martí, J. 3D bioprinted muscle on a chip. in *Libro de Actas. XXXV Congreso Anual de la Sociedad Española de Ingeniería Biomédica* (eds. Jané Campos, R., Aramendi Ecenarro, E., Irusta Zarandona, U. & Alonso González, E.) 395–398 (2017).

85. Vilches, S. *et al.* Domain-specific activation of death-associated intracellular signalling cascades by the cellular prion protein in neuroblastoma cells. *Mol. Neurobiol.* **53**, 4438–4448 (2016).

86. Rueden, C. T. *et al.* ImageJ2: ImageJ for the next generation of scientific image data. *BMC Bioinformatics* **18**, 529 (2017).

87. Gil, V. & Del Río, J. A. Analysis of axonal growth and cell migration in 3D hydrogel cultures of embryonic mouse CNS tissue. *Nat. Protoc.* **7**, 268–

280 (2012).

88. Podratz, J. L., Rodriguez, E. H. & Windebank, A. J. Antioxidants are necessary for myelination of dorsal root ganglion neurons, in vitro. *Glia* **45**, 54–58 (2004).

89. Hervera, A. *et al.* Reactive oxygen species regulate axonal regeneration through the release of exosomal NADPH oxidase 2 complexes into injured axons. *Nat. Cell Biol.* **20**, 307–319 (2018).

90. Haastert, K. *et al.* Rat embryonic motoneurons in long-term co-culture with Schwann cells—a system to investigate motoneuron diseases on a cellular level in vitro. *J. Neurosci. Methods* **142**, 275–284 (2005).

91. Hughes, C. S., Postovit, L. M. & Lajoie, G. A. Matrigel: A complex protein mixture required for optimal growth of cell culture. *Proteomics* **10**, 1886–1890 (2010).

Chapter 3

The relevance of proprioception in Amyotrophic Lateral Sclerosis

Summary

This chapter is focused on the study of proprioceptive sensory neurons (pSN) in sporadic amyotrophic lateral sclerosis (ALS).

Results obtained from the differentiation of human neural stem cells (hNSC) to sensory neurons (SN) suggest that: **i)** the expression of ETV1 and VGluT1, required to form functional connections, could be partially induced by cytokines and growth factors secreted by target cells; **ii)** CHIR99021 could induce an increase of spheroid size, remodelling the spheroid ECM, promote cell proliferation and axon regeneration; **iii)** ROCK inhibitor Y27632 could interfere not only with hNSC cell differentiation, but also with ALS genetic pathway; **iv)** basal levels of some pSN related genes (NTRK3, RUNX3 and DICER) are different and are regulated differently in ALS cells compared to healthy cells; **v)** ETV1, required to form functional feedback connection between pSN and motoneuron, is downregulated in some ALS samples and it could be involved in the development of the disease.

Studying all the components in the neuromuscular circuit and its failures in an ALS, such as the one presented here, could help to understand better the disease and discover new targets for therapies.

Contributions and acknowledgements

This work was achieved during my stay of 5.5 months at Massachusetts Institute of Technology (MIT) funded by Severo Ochoa Triple-I program for predoctoral researchers from IBEC and MISTI Global Seed Funds from La Caixa foundation and MISTI (MIT international science and technology initiatives). I performed the experiments in collaboration with some members from the Mechanobiology lab, at MIT: Dr. Tatsuya Osaki, who supported me, taught me some of the techniques employed, and collaborated in performing with me some of the experiments; and Prof. Roger Kamm, who supported me during my stay at MIT.

The work presented in this chapter is in preparation for a publication.

3.1. Introduction

3.1.1. Neuromuscular circuit and proprioception

Proprioception is the sense of relative spatial positioning of one's body and its movement or force executed on the environment.[1] Its functions are: **i)** body balance, stabilisation and protection of the body (e.g. compensating flexor and extensor muscle contraction or extension to find body balance and avoid falling on the bus); **ii)** audiovisual-motor coordination (e.g. utilise visual inputs to know how far you want to extend a limb); **iii)** coordination of rhythmic movements (e.g. walking); **iv)** control and refinement of motion through feedback to achieve better precision of movements (e.g. to acquire, refine or execute a motor skill, such as playing tennis); **v)** distance estimation and navigation in the absence of visual cues (e.g. being able to walk in the darkness), and **vi)** modulation of the magnitude and timing of limb-targeted impulses (e.g. to ensure a robust motor output whey throwing a ball).[2]

In the early 20th century, Charles Sherrington defined "proprioceptors" as the receptors within the body — generally located in muscles, joints and tendons — that respond to stress and strain, and detect stimuli that are traceable to actions of the organism itself.[3] Although the muscle spindle, the muscular proprioceptor organ, had been described many years earlier by Ruffini,[4] Sherrington demonstrated for the first time the influence

of sensory neurons innervating the muscle spindle on movement and posture control. He described the “reflex pathways” that convert proprioceptive feedback into motor output.[5]

Although the term “proprioception” could include visual and tactile feedback, among others, in this thesis, the term “proprioception” refers to the classical view of sensorimotor proprioception. Sensorimotor proprioceptive functions have a conscious and a subconscious components.[6] Somatosensory senses make possible to detect tactile inputs, pain, temperature and conscious proprioception, whilst unconscious proprioception is exclusively detected by neuromuscular senses. Conscious proprioception is the ability to detect voluntary muscle movement, and it includes kinesthesia (limb movement), joint position sense (limb position), and sense of tensile forces. Unconscious proprioception detects posture, joint stability, and feed-forward control (the modulation of a reflex), to control joints through reflexes and pre-program muscle stiffness in anticipation of motor actions. The cerebellum is the primary site where unconscious proprioception is generated; whereas the afferent signals from muscle spindles, Golgi tendon organs and cutaneous receptors are primary conscious proprioceptive receptors.[6] Muscle spindles, Golgi tendon organs and joint receptors are the sensorimotor proprioceptive organs known in humans.[2]

Cell bodies of proprioceptive neurons reside in dorsal root ganglia (DRG) — ganglia located alongside the spinal cord— together with other type of sensory neuron that detect pain, temperature, pressure, etc.[7] DRG neurons have pseudo-unipolar morphology and transmit an heterogenous pool of signals (temperature, pressure, pain, body position and movement) to the spinal cord.[7] DRG neurons differ in axon diameter, myelination degree, cell body size, peripheral targets and efferent terminals in the spinal cord.[8] Proprioceptive sensory neurons (pSN), or sensorimotor afferents, represent 7.5% of DRG neurons. They have myelinated axons of 6-20 µm diameter, form Aα and Aβ fibres, and have fast conduction velocity (30-120 m/s).[8] Sensorimotor proprioceptive afferents send information about muscle contraction status to the spinal cord, and include group Ia and group II muscle afferent fibres (that connect to intrafusal fibres in the muscle spindle), and group Ib muscle afferent fibres (that innervate the Golgi tendon organ), as shown in FIGURE 3-1. Group Ia and II afferents sense muscle fibre elongation through muscle-spindle, whereas group Ib afferents sense muscle contraction through Golgi tendon organ.

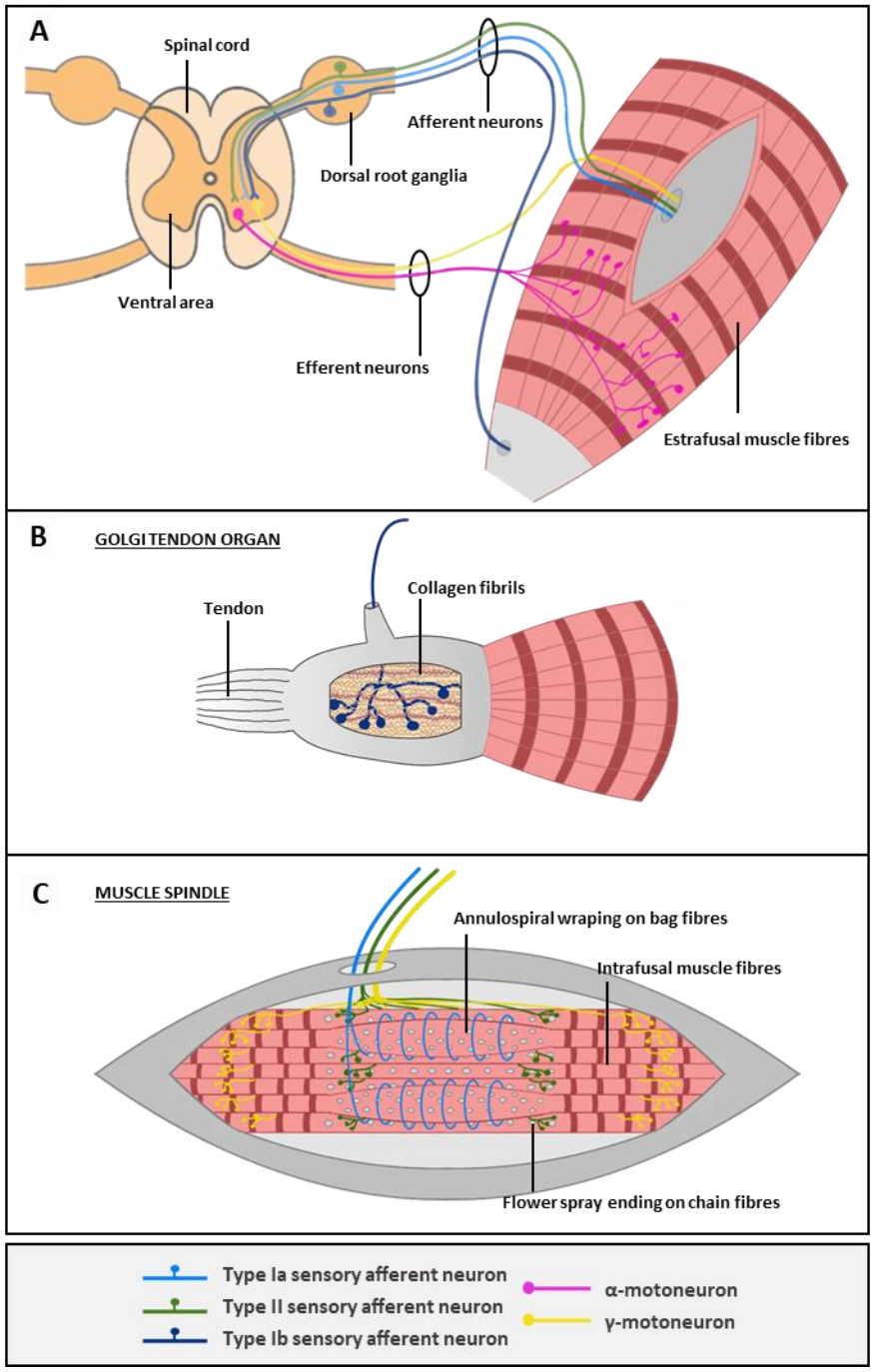

Figure 3-1. *Spinal neuromuscular circuit and proprioceptive receptors in the muscle.* ***A)*** *Efferent neurons in the muscle include the innervation of extrafusal muscle fibres by α-MN (pink), triggering the contraction, and the innervation of*

intrafusal muscle fibres by γ-MN (yellow), modulating the excitability input and the contractibility of the muscle-spindle. The somas of α-MN and γ-MN are located in the ventral area of spinal cord, and they extend long axons towards skeletal muscle. Afferent neurons in the muscle include types Ia (clear blue), II (green) and Ib (dark blue) afferents, that are in charge of proprioception through specialised organs: Golgi tendon organ (GTO) and muscle spindles. They sense muscle contraction and send the signal back to the spinal cord, passing through dorsal root ganglia, where their somas are located. ***B)*** *Golgi tendon organ, located at the joint between muscle fibres and tendons, is formed by encapsulated structures of collagen fibrils that compress when the muscle is contracted, innervating a single Ib afferent neuron.* ***C)*** *Muscle spindles, located inside extrafusal muscle fibres, are formed by encapsulated intrafusal muscle fibres (bag and chain fibres) connected to Ia and II afferent sensory endings. Type Ia sensory fibres form annulospiral wrappings and sense the rate of length change. Type II sensory fibres form flower-spray endings and sense relative muscle length. γ-motoneurons innervate polar regions of intrafusal muscle fibres and calibrate the sensitivity of muscle spindles, forming the fusimotor system.*

Golgi tendon organs are encapsulated structures of collagen fibres located at the interface between muscle fibres and tendons.[2] Each Golgi tendon organ is innervated by one single type Ib sensory afferent ending, wrapped around the collagen fibres, that are attached to individual muscle fibres. Type Ib sensory afferents are silent when the muscle is resting, and they increase firing rate when the muscle force or tension increases (e.g. during resisted movements).

Muscle spindles are located inside mammalian skeletal muscle, in muscle fascicles of perigpheral nerves and their function is to sense changes in muscle length of the specific muscle they supply. Their main components are intrafusal muscle fibre and sensorimotor proprioceptive afferents.[2,9–11] These components are surrounded by a capsule of connective tissue positioned in parallel to extrafusal fibres.

Intrafusal muscle fibres are specialised muscle fibres divided by a central noncontractile region — in which sarcomeres are almost completely replaced with clusters of nuclei — into two functionally separate contractile regions. There are three types of intrafusal muscle fibres: bag_1, bag_2 and chain fibres. Muscle spindles normally have around 2-3 bag fibres and around 5 chain fibres, being the last one quite variable number. Bag fibres have a cluster of nuclei in the equatorial side of the fibre, whereas chain fibres have aligned nuclei in the centre of the fibre. Intrafusal fibres are positioned parallel to extrafusal fibres (ordinary fibres or force-producing ones), so that any changes in their length is reflected in the length of the muscle spindle.

Sensorimotor afferents are proprioceptive sensory neurons of type Ia fibres and type II fibres. A single type Ia axon wraps around the central region of bag_1 and other intrafusal muscle fibres, forming a structure called annulospiral wrapping (ASW) or primary afferent ending. A variable number of type II axons contact with the bag_2 and chain intrafusal muscle fibres in areas adjacent to central region forming a structure called flower spray ending (FSE) or secondary afferent ending. Group Ia sensory neurons have static and dynamic sensitivity: they encode information about muscle length and the velocity of length change, being able to rapidly detect postural perturbations. Their firing rate is high when the muscle is at a longer length, but it is even higher when the muscle is being lengthened. Group II afferents have static sensitivity and little dynamic

sensitivity: they encode information about the static muscle length. Their firing rate is higher when the muscle is longer.

The process by which terminals of sensorimotor afferents detect information by stretch-sensitive mechanically gated ion channels and convert those mechanical stimuli into electrical activity is called the mechanotransduction. The information available so far on the mechanotransduction of the muscle spindle has been thoroughly reviewed by Bewick and Banks.[12] Briefly, it consists on the following sequence of events: **1)** in a resting muscle, synaptic-like vesicles, located in the sensory afferent terminal, go through an exocytosis of glutamate, activating phospholipase-D coupled metabotropic glutamate receptors; **2)** when muscle stretches, mechanosensory sodium channels and sodium voltage channels open, generating an influx of Na^{+} that depolarises the membrane and increases action potential firing; **3)** the action potential triggers the opening of P/Q type voltage dependent calcium channels, leading to an influx of Ca^{+2}; **4)** the resulting intracellular Ca^{+2} opens calcium activated potassium channels, producing an efflux of K^{+}, repolarising the membrane and moderating the firing rate; **5)** mechanosensory calcium channels open provoking an influx of Ca^{+2}; **6)** the increased intracellular calcium causes synaptic like vesicle exocytosis of glutamate, activating further phospholipase-D coupled metabotropic glutamate receptors; **7)** phospholipase-D activity increases maintaining the ability of the afferent ending to respond to subsequent muscle stretches.

The muscle spindle excitatory input is modulated by γ-motoneurons and β-motoneurons, that innervate the muscle spindle on the polar regions of intrafusal muscle fibres forming the fusimotor system.[11,13,14] The difference between them, is that γ-MN innervate exclusively intrafusal fibres, whereas β-MN innervate both intrafusal and extrafusal fibres. These neurons adjust the sensitivity of muscle spindles, and thus the gain of sensory afferents, by regulating the muscle spindle length shortening. Their activation shortens the polar regions of intrafusal fibres and stretches the central region, causing an increase in sensory afferent firing rate or predisposing sensory afferents to fire in response to stretch.

Sensorimotor proprioception is achieved by the integration of all these signals coming from the fusimotor system, the muscle spindle, Golgi tendon organ and joint receptors. The integration of afferent signals gives us conscious and unconscious awareness of muscle position and movement (muscle extension-flexion state) and makes possible to coordinate movements. Failures in any part of this circuit can hamper muscle movement, interfere with reflexes, and finally lead to sensorimotor diseases.

3.1.2. Amyotrophic lateral sclerosis, a sensorimotor disease

Sensory neuron diseases are known to be a group of peripheral nervous system (PNS) diseases, that include hereditary sensory and

autonomic neuropathies, pure posterior column ataxia, hereditary ataxias (e.g. Friedreich's ataxia), mitochondrial disorders, and other neuropathies such as Fabry's disease and Tangier's disease.[15] They are also involved in autism spectrum disorder.[16] Proprioceptive sensory neurons, have only recently been reported to play a relevant role in aging,[17,18] and some neuromuscular diseases (NMD): Friedreich's ataxia,[8] spinal muscular atrophy,[19–22] and amyotrophic lateral sclerosis.[23–27]

Amyotrophic lateral sclerosis (ALS) is a fatal idiopathic neuromuscular neurodegenerative disease that causes the progressive paralysis. It has approximately a worldwide mortality rate of 30.000 patients per year,[28] an incidence of 2-3 per 100.000 individuals in Europe,[29] and it is usually fatal within 2-5 years.[30] Despite the considerable efforts, its pathology is still poorly understood.[28] ALS cases are classified in two types: sporadic (sALS) and familiar (fALS). Most ALS cases are sporadic (sALS), but there is a prevalence of 10% in cases presenting common causative gene expression patterns and first-degree relatives who also have ALS (fALS). Both fALS and sALS have identical pathology, and even mutations usually found in fALS can be found in sALS too.[31] Some studies also suggest that it is possible that motoneuron degeneration occurring in sALS cases, covering 90% of total cases, is related to multiple mechanism.[32] The main genetic mutations known to be linked to ALS include: the hexanucleotide repeat expansion within the chromosome 9 open reading frame 72

(C9ORF72 gene), superoxide dismutase 1 (SOD1), TAR DNA-binding protein (TARDBP) and FUS RNA binding protein (FUS). Currently more than thirty genes have been related to fALS as well as to some sALS cases.[33–35] But ALS has a strong polygenic component and genetic pleiotropy (the production by a single gene of two or more apparently unrelated effects) with some other diseases and pathological traits.[36,37] A recent study performed by Broce *et al.* found 89 ALS risk loci across 21 chromosomes and 65 different pathological traits associated with ALS,[37] being many of them associated both to fALS and to sALS.

ALS is characterised by the progressive degeneration of both corticospinal or upper motoneurons (neurons that project from the cortex to the brainstem and spinal cord) and lower motoneurons (neurons that project from the brainstem or spinal cord to muscle).[29] Failure of upper motoneurons results in muscle stiffness and spasticity (increased tendon reflex activity and hypertonia combined with paralysis and altered skeletal muscle performance). Lower motoneuron failure results initially in excessive electrical irritability and fasciculations (brief spontaneous contraction affecting a small number of muscle fibres). Later on, it causes the loss of synaptic connectivity with muscles and atrophy of the muscles of the tongue, oropharynx, and limbs, affecting also at the late stages muscles from the bladder and eyes.[31] Its clinical manifestations include cognitive and behavioural impairment, dysphagia (difficulty or discomfort in swallowing), dysarthria

(difficult or unclear articulation of speech), respiratory insufficiency, muscle cramps, spasticity, muscle weakness and atrophy.[29] There is no currently any treatment, though first gene-specific individualised therapies for some genetic subtypes of ALS, with mutations in SOD1 and C9ORF72, are undergoing clinical trials.[38]

Although ALS has long been known as motor neuron disease, it is not just a motoneuron disease. Even within the MN pool, there are differences underestimated: α-MN forming the fast-fatigable motor units go first under degeneration, followed by fast fatigue resistant MN, whereas neighbouring slow α-MN, γ-MN and ocular MN remain resistant to degeneration.[25,39] The motoneuron degeneration comes together with neuro inflammatory processes driven by the proliferation of astroglia, microglia, and oligodendroglia.[40,41] Furthermore, recent studies have shown that proprioceptive sensory neurons are also impaired and go through degeneration.[23,24,26] In the stretch-reflex circuit, pSN sensory feedback modulates MN activity. The lack of Ia muscle spindle afferent inputs to spinal γ-MN has been suggested as a ALS disease resistance mechanism,[25,42] and the ablation of the spindle has even been related to a decrease in MN death in ALS,[25] relating muscle spindle afferents to ALS early triggers of MN degeneration.[43]

Proprioceptive sensory neuron degeneration, altered morphology, signal transmission and spindle malfunctions in ALS have been observed in ALS mice models ($SOD1^{\mathrm{G93A}}$, $TDP43^{\mathrm{A315T}}$ and

FUS^{P525L}), human stem cell derived neuromuscular models, and human ALS patients. Sábado *et al.* analysed DRG of an ALS mice model ($SOD1^{\mathrm{G93A}}$) and they found that DRG pSN accumulate misfolded SOD1 and suffer degeneration that involves the inflammatory recruitment of macrophagic cells.[27] Vaughan *et al.* performed a study of pSN in $SOD1^{\mathrm{G93A}}$ and $TDP43^{\mathrm{A315T}}$ mice ALS models and found alterations in Ia/II proprioceptive nerve endings in muscle spindles before the symptomatic phase of the disease.[23] In a later study performed by the same author, they found that $TDP43^{\mathrm{A315T}}$ sensory neurons have shorter and less complex neurites than the ones of controls or $SOD1^{\mathrm{G93A}}$ model, and are also more sensitive to vincristine (a microtubule inhibitor that causes axonal degeneration and induces cellular stress).[24] They suggest that MN and pSN may have similar molecular mechanisms involved in the failure, maintenance and repair occurring in ALS.[24] In a recent study performed by Lalancette-Hebert *et al.*,[25] they examined the spinal reflex circuit of ALS mice models ($SOD1^{\mathrm{G93A}}$, $TDP43^{\mathrm{A315T}}$ and FUS^{P525L}) and found that γ-MN are preserved at the end stage of the diseases, they are resistant to the toxicity mechanisms of ALS that causes degeneration of α-MN. They also found that proprioceptor feedback increases α-MN loss, and the elimination of γ-MN, decreasing stretch sensitivity of the spindle and pSN response, delays the stage of the disease.[25] Furthermore in a research performed by Seki *et al.*,[26] they examined postnatal abnormalities in the muscle spindle pSN and their electrical

excitability in $SOD1^{G93A}$ mice. They found *in vitro* evidence for stretch-reflex failure in the early disease process, and impaired and arrhythmic action potential burst discharge associated with Nav1.6 sodium channel deficiency, that could be responsible for initiating fasciculations in ALS.[26] On top of that, there are few clinical studies published in which they have found evidence of alterations in proprioception in ALS patients.[44,45]

Several advances have been made in ALS study models, both in mice models and human cell lines.[46,47] However, despite the recent evidences supporting the idea of an important role of pSN in early ALS development, most of the studies are still exclusively focused in the motoneuron and its connexion with skeletal muscle cells.

3.1.3. State of the art on proprioceptive sensory neuron differentiation and characterisation

Human neuromuscular circuit, together with ALS physiopathology, can be studied *in vitro* thanks to stem cell technologies. Induced pluripotent stem cells (iPSC) have widely been applied for disease-modelling, regenerative therapies and drug-screening for NMD.[48] They can be derived into neural stem cells, such as the ones utilised in this study, characterised by their ability to differentiate into central nervous system (CNS) and peripheral nervous system (PNS) cell lineages. Once neural stem cells (NSC) lose their self-renewal

ability and limit their proliferative ability, they differentiate into neural progenitors. Human neural progenitors (hNP) can give rise to all neural lineages involved in the neuromuscular circuit in response to several biochemical stimuli.

The protocol to differentiate hNSC directly into motoneurons (MN) has previously been stablished.[49] For mechanoreceptive and nociceptive sensory neurons, there are several differentiation protocols,[50] and several publications have suggested different approaches to obtain cell cultures enriched in all subtypes of sensory neurons, including some detecting pSN.[8,51–59] However, there is no validated protocol yet to differentiate specifically pSN and characterise or detect them. PNS neurons and glia are derivatives of neural crest cells. Therefore, differentiating hNSC into pSN involves going through the following intermediate steps: differentiating first hNSC into neural crest stem cells (NCSC),[60–62] then into PNS lineage, peripheral neurons, peripheral sensory neuron, to finally obtain pSN.

The protocol presented here to differentiate hNSC into pSN was adapted from Guo *et al.*[51] Several combinations of the established differentiation protocol were studied — increasing neurotrophin-3 concentration, adding CHIR99021 and/or Y-27632 —, to assess their differential effect on healthy and ALS sensory neurons. Neurotrophin-3 (NT-3) is expressed in muscles and limbs, implicated in target recognition and survival for MN,[63] and known to play an

important role in proprioceptive development.[64] Y27632, also known as RHO/ROCK pathway inhibitor, is known to promote neuronal differentiation of iPSC, neurogenesis and migration of neural stem cells, neurite outgrowth of sensory neurons *in vitro*, and enhance the regeneration of motor axons.[65] Low doses are known to mediate pro-nociceptive responses, whereas high doses reduce edemas.[65] CHIR99021, also known as glycogen synthase kinase 3 (GSK3) inhibitor, is a Wnt signalling pathway agonist. It promotes extracellular matrix (ECM) remodelling by inducing the expression of matrix metalloproteinases,[66] it can promote proliferation of hNP,[67] and axon regeneration in sensory neurons.[68] It also facilitates the differentiation towards neural crest cells, being reported by higher levels of p75 neurotrophin receptor (p75NTR) and whilst maintaining similar levels of HNK-1 to other protocols.[60] Furthermore, a specific type of ALS characterised by mutations in the spastic paraplegia gene 11, is known to have GSK3 pathway dysregulated in hNP, causing as a result motor neuron degeneration and peripheral sensorimotor neuropathies.[69] Modulating GSK3, it is possible to rescue mitotical activity of hNP.[69]

Although several efforts have been made in obtaining pSN from stem cells, the lack of consensus within the scientific community on sensory neuron classification and molecular markers, increases the difficulty to compare the results. There are inconsistencies in the literature that define gene expression profiles of sensory neuron DRG subpopulations and their classification.[53,54,70,71] The general

consensus agrees on at least the three types of peripheral sensory neurons — that can be further classified in more subtypes —, based on the type of tropomyosin receptor kinase (Trk) expressed: **i)** nociceptors (TrkA+): able to detect pain, itch and temperature changes; **ii)** mechanoreceptors (TrkB+ and in some cases TrkC+): able to detect mechanical stimuli (i.e. pressure) from dermal and epidermal regions; **iii)** proprioceptors or proprioceptive sensory neurons (pSN), (TrkC+): able to detect muscle position, balance and movement. Although several markers have been reported to be expressed in all pSN (i.e. TrkC, parvalbumin, ETV1 and RUNX3), pSN-specific unique molecular markers have yet to be identified. For that reason, this study includes a molecular analysis at two checkpoints of 17 genes and 3 housekeepers (GAPDH, β-actin, RPS18), summarised in TABLE 3-1. The genes analysed are related to the detection of NCSC (HNK-1+ and TUBB3+), pSN, and other cell populations potentially present in a pSN-enriched hNSC-derived cell culture, such as motoneurons (MNX1+), and astrocytes (GFAP+). To differentiate sensory neuron subtypes at the final endpoint, Trk markers were analysed (NTRK1, NTRK2, NTRK3) together with other markers expected to be expressed in pSN (POU4F1, PRPH, RUNX3, DICER, ETV1, SPP1, and VGluT1).

Table 3-1. *Genes analysed in the qPCR: gene name. encoding protein and function. The information for gene description is taken from the databases Genecards*[72] *and OMIM,*[73] *and other papers cited below.*

Gene	Encoding protein and function
GAPDH	Glyceraldehyde 3-phosphate dehydrogenase plays a role in cell glycolysis and nuclear functions. It is implicated in metabolic and non-metabolic functions, such as initiation of apoptosis or axoplasmic transport. It is frequently used as a housekeeper gene.
ACTB	β-actin, a human isoform of actin, is a highly preserved protein involved in cell structure, integrity and motility. It is frequently used as a housekeeper gene.
RPS18	Ribosomal protein S18 is a component of the 40S subunit of ribosomes, organelles that catalyse protein synthesis. It is frequently used as a housekeeper gene.
HNK1	Galactosylgalactosylxylosylprotein 3-β-glucuronosyltransferase 1 (B3GAT1) is an enzyme that in humans is encoded by the B3GAT1 gene, also known in immunology as HNK1 (human natural killer-1). It is involved in cell metabolism and expressed in NCSC.[62,74]
TUBB3	Class III β-tubulin is a microtubule element of the tubulin family, found almost exclusively in neurons and testis. It plays a role in DRG axon projection towards the spinal cord.[75]
PRPH	Peripherin is a type III intermediate filament protein expressed mainly in neurons of the PNS and motor neurons.[54] It is known to be upregulated in ALS.[76]
POU4F1	POU domain, class 4, transcription factor 1 (POU4F1) also known as brain-specific homeobox/POU domain protein 3A (BRN3A), is a protein highly expressed in the developing peripheral sensory nervous system (e.g. DRG). [51,54,77]
NTRK1	Tropomyosin receptor kinase A (TrkA), also known as neurotrophic tyrosine kinase receptor type 1 (NTRK1), is expressed in peptidergic and some nonpeptidergic nociceptive neurons, and binds to nerve growth factor (NGF).[53,71]
NTRK2	Tropomyosin receptor kinase B (TrkB), also known as neurotrophic tyrosine kinase receptor type 2 (NTRK2) is expressed in some mechanoreceptive type of sensory neurons and binds to brain-derived neurotrophic factor (BDNF).[53,71]
NTRK3	Tropomyosin receptor kinase C (TrkC), also known as neurotrophic tyrosine kinase receptor type 3 (NTRK3), is expressed in proprioceptive type of sensory neurons and some mechanoreceptive neurons.[71] It binds to neurotrophin-3 (NT-3), mediating neuronal differentiation and survival.[53,78]
RUNX3	Runt-related transcription factor 3 (Runx3) regulates survival and axonal projections of proprioceptive sensory neurons.[79] Runx3 has a different regulation in each subtype of TrkC+ neuron.[80]
DICER	Dicer is essential for maintenance rather than initiation of synaptic contacts in sensorimotor connections, and for processing micro RNAs (miRNAs). Selective impairment in sensory neurons causes sensory ataxia.[79,81]

ETV1	ETS variant 1 expression is induced by NT3-TrkC signalling and it is involved in proprioceptive axon projection regulation.[79,82] It is also needed for the survival and differentiation of pSN.[83] But it is also critical in the formation of functional connections between pSN and MN.[82]
SPP1	Secreted phosphoprotein 1 is important for cell-matrix interaction and immune functions, and is known to be expressed in pSN.[71] It is frequently present in the inflammatory environment of dystrophic and injured muscles.[71,84]
VGluT1	Vesicular glutamate transport 1 (VGluT1), also known as solute carrier family 17 member 7 (SLC17A7), transports glutamate to synaptic vesicles before exocytotic release. It is expressed in pSN at the site of innervation of intrafusal fibers.[85] But it is also detected at the synaptic contacts of interneurons coming from the spinal cord and descending cortical axons, being expressed in the spinal cord in the dorsal horn, intermediate gray and ventral horn, and in sensory DRG neurons.[23]
PVALB	Parvalbumin, although frequently used as a proprioceptive sensory neuron marker, is also expressed in other cells of the motor system, including but not limited to motoneurons and interneurons within the spinal cord and muscles. [81,82,86]
MBP	Myelin basic protein is the major constituent of the myelin sheath formed by oligodendrocytes, in the CNS, and Schwann cells, in the PNS. Both MN and pSN are myelinated cells.[71] Anormal levels of MBP are related with demyelinating diseases, multiple sclerosis and ALS. Myelin sheath ultrastructure is known to be disorganised in ALS.[87] Furthermore, oligodendrocyte maturation and MBP expression is known to be reduced in ALS,[88,89] and myelinating Schwann cells are known to be damaged in ALS and trigger inflammatory mechanisms in ALS peripheral nerves.[90,91]
GFAP	Glial fibrillary acidic protein is one of the major filament proteins of mature astrocytes. It is also present in Schwann cells under stress conditions and following nerve damage or denervation, and it has been found to be upregulated in the peripheral nerve Schwann cells in ALS.[92]
MNX1	Motor neuron and pancreas homebox 1, also known as homeobox HB9 (HLXB9), used for identification of MN, it is involved in neural stem cell differentiation pathway and lineage-specific markers.
TNFSF1B	Tumour necrosis factor receptor superfamily member 1B, also known as p75 tumour necrosis factor receptor (P75TNFR), mediates anti-apoptotic and inflammation signals, and it is related with ALS pathway as it is observed in higher expression levels in ALS patients.[93]

3.2. Specific objectives of the chapter

The aim of this chapter has been to obtain sensory neurons from hNSC, and analyse the role of proprioceptive sensory neurons in ALS. For that purpose, the specific objectives of the chapter have been:

- To optimise proprioceptive sensory neuron differentiation protocol from human neural stem cell, valid for healthy and ALS cells.
- To assess proprioceptive sensory neuron marker differences between healthy and ALS cells when exposed to different media conditions.

3.3. Materials and methods

3.3.1. Facilities

All experiments were performed at Mechanobiology lab (Biological Engineering department, Massachusetts Institute of Technology, Cambridge, U.S.) in a collaboration with Nanobioengineering lab (Institute of Bioengineering of Catalonia, Barcelona, Spain). Confocal microscopy imaging and flow cytometry was performed at the Koch Institute for Integrative Cancer Research (Massachusetts Institute of Technology, Cambridge, U.S.). cDNA synthesis, quantification and qPCR were performed using equipment kindly lent by Prof. Alan J. Grodzinsky's group (Biological Engineering department, Massachusetts Institute of Technology, Cambridge, U.S.). cDNA quantification was performed using equipment kindly lent by Prof. Eric Alm's group (Biological Engineering department, Massachusetts Institute of Technology, Cambridge, U.S.).

3.3.2. Experimental design

The experiments presented in this chapter include the progressive differentiation of proprioceptive sensory neurons (pSN) from human neural stem cells (hNSC) and the experiments performed to characterise them at each timepoint (TP), summarised in FIGURE 3-2. Healthy and ALS hNSC were maintained in proliferation until TP0, when cells were transferred to the desired platform (coated plates

for 2D culture or spheroid forming plates). hNSC proliferate until TP1, when the differentiation towards sensory neurons (SN) begins. For the characterisation different techniques were utilised at TP2 and TP3: bright field (BF) imaging, flow cytometry (FC) analysis, confocal laser scanning microscopy (CLSM) imaging, and quantitative polymerase chain reaction (qPCR).

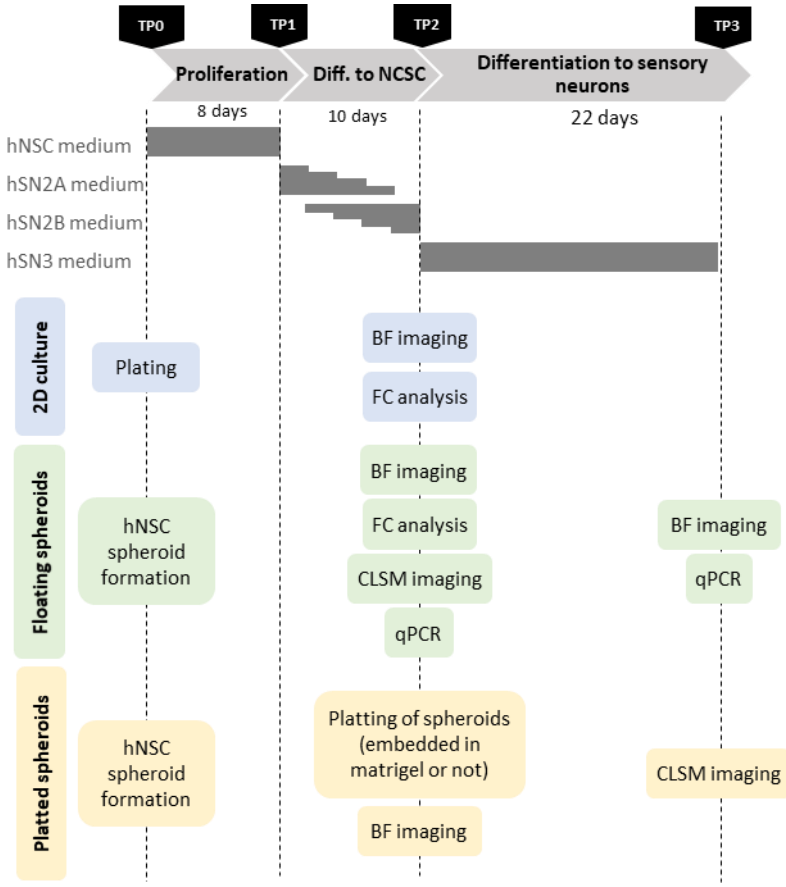

Figure 3-2. *Diagram of the SN differentiation process with each media utilised and stablished timepoints (TP), and experiments performed for the characterisation at each timepoint on 2D cultures, floating spheroids and platted spheroids.*

3.3.3. Maintenance of neural stem cells and formation of neurospheroids

The cells utilised were healthy human neural stem cells (hNSC) H9-derived (Gibco, #N7800100) and human ALS iPS-derived neural stem cells (iXCells Biotechnologies, #40HU-007), sporadic ALS hNSC line created from a mid-50s female patient with rapid onset and progression ALS, without any known mutations in TARDBP, SOD1 or C9ORF72. Both healthy and ALS hNSC were seeded onto Matrigel-coated surfaces prepared by making 1:30 dilution of Matrigel® hESC-Qualified Matrix (Corning, #354277) into Knockout™ DMEM/F-12 medium, also known as Dulbecco's Modified Eagle Medium/Nutrient Mixture F-12 (Gibco, #12660012) incubated for 1 h at room temperature. Cells were maintained in a CO_2 incubator at 37 °C and 95% humidity (Thermo Fisher Scientific) with *hNSC medium* (proliferation medium, see composition in TABLE 3-2) changing it every day after. Once the desired number of cells was reached, at TP0, cells were washed with sterile DPBS, also known as Dulbecco's Phosphate Buffered Saline (Lonza, #17-512F), detached with TrypLE™ express enzyme (Gibco, #12604021), counted with a haemocytometer and transferred in the desired density to ultra-low attachment PrimeSurface® 3D culture spheroid plates (S-Bio, #MS-9096MZ) to form neurospheroids or to seed onto Matrigel-coated glass bottom multiwell plates for 2D cell culture. The remaining cells were frozen into Stem-Cellbanker® solution for stock (AMSbio,

#11890). From this point onwards, cultured cells followed the required differentiation protocol.

Table 3-2. *Composition of hNSC proliferation medium, utilised before differentiation of neural cells.*
hNSC = human neural stem cell; FGF = fibroblast growth factor; EGF = epidermal growth factor.

Medium	Components and final concentration	Commercial reference
hNSC proliferation medium	Knockout™ DMEM/F-12	(Gibco, #12660012)
	1X final concentration of StemPro™ neural supplement	(Gibco, #A1050801)
	$2\ mM$ of GlutaMAX™ supplement	(Gibco, #35050061)
	$20\ ng \cdot ml^{-1}$ of FGF-basic (aminoacid 10-155) recombinant human protein	(Gibco, #PHG0024)
	$20\ ng \cdot ml^{-1}$ of EGF recombinant human protein	(Gibco, #PHG0314)

3.3.4. Differentiation of hNSC to proprioceptive sensory neurons

This section explains the pSN differentiation procedure starting at TP0 from the creation of hNSC spheroids or seeding hNSC in 2D in Matrigel coated surfaces, following the previously explained protocol (see SECTION 3.3.3). A diagram of this procedure summarised can be seen in FIGURE 3-2. The general differentiation protocol media composition is described in TABLE 3-3.

Table 3-3. *Composition of different cell culture media utilised during the differentiation of proprioceptive sensory neurons from human neural stem cells. NCSC = neural crest stem cell; NGF = nerve growth factor; GDNF = glial cell line-derived neurotrophic factor; BDNF = brain-derived neurotrophic factor; NT-3 = neurotrophin-3; 8-Br-cAMP = 8-Bromoadenosine-3',5'-cyclic monophosphate. (*) = only in some conditions. (**) = varying concentration for each protocol tried.*

Medium	Components and final concentration	Commercial reference
Medium hSN2A	Knockout™ DMEM/F-12	(Gibco, #12660012)
	1X final concentration of StemPro™ neural supplement	(Gibco, #A1050801)
	$2\ mM$ of GlutaMAX™ supplement	(Gibco, #35050061)
	$500\ ng \cdot ml^{-1}$ of recombinant human Noggin	(Goldbio, #1180-09-20)
	$10\ \mu M$ of SB431542	(StemCell Technologies, #72232)
	(*) $3\ \mu M$ of CHIR99021	(Caymanchem, #13122)
Medium hSN2B	Neurobasal™ Plus medium	(Gibco, #A3582901)
	1X final concentration of B-27™ Plus supplement	(Gibco, #A3582801)
	$10\ ng \cdot ml^{-1}$ of recombinant human BDNF	(R&D Systems, #248-BD-025)
	$10\ ng \cdot ml^{-1}$ of recombinant human GDNF	(R&D Systems, #212-GD-010)
	$10\ ng \cdot ml^{-1}$ of recombinant human NGF	(Axol Bioscience, #ax139789)
	$10\ ng \cdot ml^{-1}$ of human Wnt-1	(Axol Bioscience, #ax135565)
	$10\ ng \cdot ml^{-1}$ of human NT-3	(Axol Bioscience, #ax139811)
	$10\ \mu M$ of 8-Br-cAMP	(Axxora, #BLG-B007)
	$200\ \mu M$ of L-Ascorbic acid	(Sigma-Aldrich, #A4403)
	$500\ ng \cdot ml^{-1}$ of recombinant human Noggin	(Goldbio, # 1180-09-20)
	$10\ \mu M$ of SB431542	(StemCell Technologies, #72232)
	(*) $3\ \mu M$ of CHIR99021	(Caymanchem, #13122)
Medium hSN3	Neurobasal™ Plus medium	(Gibco, #A3582901)
	1X final concentration of B-27™ Plus supplement	(Gibco, #A3582801)
	$10\ ng \cdot ml^{-1}$ of recombinant human BDNF	(R&D Systems, #248-BD-025)
	$10\ ng \cdot ml^{-1}$ of recombinant human GDNF	(R&D Systems, #212-GD-010)
	$10\ ng \cdot ml^{-1}$ of recombinant human NGF	(Axol Bioscience, #ax139789)
	$10\ ng \cdot ml^{-1}$ of human Wnt-1	(Axol Bioscience, #ax135565)
	$10\ \mu M$ of 8-Br-cAMP	(Axxora, #BLG-B007)
	$200\ \mu M$ of L-Ascorbic acid	(Sigma-Aldrich, #A4403)
	(**) $10 - 50\ ng \cdot ml^{-1}$ of human NT-3	(Axol Bioscience, #ax139811)
	(*) $25\ \mu M$ of ROCK inhibitor Y27632	(R&D Systems, #1254)

To optimise the differentiation protocol, five different conditions were assessed (*protocols A-E*) summarised in TABLE 3-4. The initial medium assessed (*protocol A*) was adapted from a previous publication.[51] The increase of NT-3 concentration and addition of CHIR99021 and ROCK inhibitor Y27632 at different steps of the differentiation were assessed adapting the process (protocols B-E).

Table 3-4. *Overview of the main differences among the proprioceptive sensory neuron differentiation protocols performed.*
TP1 = timepoint 1; TP2 = timepoint 2; TP3 = timepoint 3; NT-3 = neurotrophin-3.

	pSN differentiation protocol				
	Protocol A	**Protocol B**	**Protocol C**	**Protocol D**	**Protocol E**
***Medium SN2A and SN2B* (TP1 to TP2)**	-	-	+ CHIR99021	+ CHIR99021	-
***Medium SN3* (TP2 to TP3)**	+ NT-3 $10\ ng \cdot ml^{-1}$	+ NT-3 $50\ ng \cdot ml^{-1}$	+ NT-3 $50\ ng \cdot ml^{-1}$	+ ROCK inhibitor Y27632 + NT-3 $50\ ng \cdot ml^{-1}$	+ ROCK inhibitor Y27632 + NT-3 $50\ ng \cdot ml^{-1}$

hNSC seeded at TP0 were kept with *hNSC medium* for 8 days (until TP1). During the 10 following days, to promote the beginning of the differentiation towards NCSC, the medium was progressively changed from *medium hSN2A* to *medium hSN2B*, changing its composition every two days (see compositions in TABLE 3-3). In other words, at TP1 cells were kept for two days with 100% *medium hSN2A*, then two days with 75% *medium hSN2A* and 25% *medium hSN2B*, then two days with 50% of each media, then two days with 25% *medium hSN2A* and 75% *medium hSN2B*, remaining finally for

two extra days with 100% *medium hSN2B*. During this progressive differentiation, in some experimental conditions CHIR99021 was freshly added on every change of medium. After the last two days with 100% *medium hSN2B*, at TP2, cells were changed to *medium hSN3* (see compositions in TABLE 3-3). During this step, in some experimental conditions ROCK inhibitor Y27632 was freshly added on every change of medium. This medium was kept until the endpoint of the experiment, for 22 days, changing it every day after.

3.3.5. Characterisation of differentiated sensory neurons

For the optimal characterisation and monitoring several techniques and experiments were performed at different timepoints of the differentiation process, summarised in TABLE 3-5.

3.3.5.1. Imaging of 2D SN cell-cultures

Healthy and ALS hNSC were cultured in Matrigel coated surfaces in 2D at a density of $57.000\ cells \cdot cm^{-2}$. At TP1 experimental samples followed the *SN differentiation protocol A*, whereas a control group was maintained with *hNSC medium* to see if the differentiation towards neurons was spontaneous. Cells were maintained in a CO_2 incubator at 37 °C and 95% humidity and the medium was changed every day after. Bright field images were taken every two days until TP2 using an inverted microscope for transmitted light (Zeiss, #Axiovert-200).

Table 3-5. *Overview of the characterisation techniques and experiments performed for each SN differentiation protocol, and the aim with each.*
TP1 = timepoint 1; TP2 = timepoint 2; TP3 = timepoint 3; BF = bright field; hNSC = human neural stem cells; CLSM = confocal laser scanning microscopy; FC = flow cytometry; qPCR = quantitative polymerase chain reaction.

		SN differentiation protocol					Objective
		A	B	C	D	E	
Characterisation test at TP2	BF imaging of differentiation of healthy and ALS hNSC in 2D cultures	**X**					Assess the spontaneity of differentiation.
	BF imaging quantification of floating spheroids	**X**					Assess their growth and optimise the initial seeding density.
	Quantification of BF imaging of healthy and ALS plated spheroid embedded in Matrigel		**X**	**X**	**X**	**X**	Compare results among differentiation protocols in healthy and ALS samples.
	CLSM imaging of floating spheroid	**X**	**X**	**X**	**X**	**X**	Detect the expression of certain markers at TP2.
	FC of 2D cell cultures and floating spheroids of different seeding densities (healthy and ALS)	**X**	**X**	**X**	**X**	**X**	
	qPCR	**X**					Assess proprioceptive sensory neuron marker differences through time
Characterisation test at TP3	CLSM imaging of plated spheroids	**X**					Detect the expression of certain markers at TP3.
	CLSM imaging of spheroids embedded in matrigel			**X**	**X**		
	qPCR	**X**	**X**	**X**	**X**	**X**	Assess proprioceptive sensory neuron marker differences between healthy and ALS cells when exposed to different media conditions
	BF imaging quantification of floating spheroids	**X**					Assess their growth and optimise the initial seeding density.

3.3.5.2. *Imaging of floating SN spheroids*

Cell culture, BF image collection and quantification

SN spheroids of different cell densities ($\rho_1 = 3.000\, cell \cdot spheroid^{-1}$; $\rho_2 = 4.500\, cell \cdot spheroid^{-1}$; $\rho_3 = 6.000\, cell \cdot spheroid^{-1}$) were made with ultra-low attachment PrimeSurface® 3D culture spheroid plates (S-Bio, #MS-9096MZ) as indicated in SECTION 3.3.3. The spheroids were cultured following *SN differentiation protocol A*, monitoring their diameter until TP3 through bright field (BF) imaging with an inverted microscope for transmitted light (Zeiss, #Axiovert-200). The maximum transversal area of spheroids was quantified with ImageJ software.[94] Mean and standard deviation of obtained result was quantified for n = 3 samples.

Spheroid immobilisation and immunostaining

At TP2, spheroids were washed with DPBS and then fixed and permeabilised with Cytofix/Cytoperm (BD Biosciences, #51-2090KZ) for 30 min. After a 3 min centrifugation at 1000 rpm, samples were washed in tubes with DPBS. To perform easier the immunostaining and imaging, spheroids were immobilised by embedding them in a collagen neutralised solution and placing them in glass bottom multiwell plates. The composite solution was prepared mixing 8 parts of collagen cell matrix type I-A (Wako Chemical, #631-00651), 1 part of $NaHCO_3$ 0.05 N (Sigma Aldrich, #S5761), and 1 part of balanced and concentrated Ham-F12 10X medium (Wako Chemical,

#630-29661), as previously described.[95] The collagen with spheroids was incubated for 10 min at 37 °C to enable the polymerisation.

For a later imaging, the immunostaining procedure was performed as follows, with all steps made at room temperature unless stated otherwise. Floating spheroids were washed three times with DPBS for 10 min, permeabilised with DPBS 0.1% triton (Sigma, #T9284) for 10 min, and incubated for 2 h with a blocking solution containing 1% bovine serum albumin (BSA, Sigma, #A9657) in DPBS. Samples were then washed three times with DPBS for 10 min, and incubated overnight at 4 °C with the primary antibody solution containing 0.1% triton, 1% BSA, 0.01% sodium azide (Sigma, #71289), and 1:500 dilution of mouse anti-TUJ1 antibody, also known as anti-beta III Tubulin (Abcam, #ab78078) in DPBS. The day after, primary antibody solution was removed, and samples were washed three times with DPBS for 10 min. Then samples were incubated for 2 h protected from light with a secondary antibody solution containing 0.1% triton, 1% BSA, 0.01% sodium azide, and 1:150 dilution of HNK1-FITC (Biolegend, #359603) in DPBS. From this moment, samples were kept protected from light throughout the whole procedure. After secondary antibody solution was removed, samples were washed three times with DPBS for 10 min. Then samples were incubated for 10 min with 14.3µM of DAPI (4',6-Diamidino-2-Phenylindole dihydrochloride, Invitrogen™, #D1306) in DPBS. Samples were washed with DPBS and mounted with Olympus scaleview solution (Olympus, #ScalView-A2 optics). Imaging was performed with a

confocal laser scanning microscope (Olympus, #FV1200) and images were processed afterwards with ImageJ software.[94]

3.3.5.3. Immunostaining of plated spheroids

For a later imaging, the immunostaining procedure was performed at room temperature unless stated otherwise. SN plated spheroids undergoing *SN differentiation protocol A* previously fixed were first washed with DPBS and permeabilised incubating with DPBS 0.1% triton for 10 min. Then cells were incubated for 2 h with a blocking solution containing 1% BSA in DPBS. Cells were then washed three times with DPBS, incubating 10 min per wash. After adding the primary antibody solution — 0.1% triton, 1% BSA, 0.01% sodium azide, 1:500 dilution of mouse anti-TUJ1 antibody (Abcam, #ab78078), 1:100 dilution of rabbit anti-Pou4f1 (Invitrogen, #PA5-41509) and 1 $\mu g \cdot mL^{-1}$ of goat anti-TrkC antibody (R&D Systems, #AF373) in DPBS — cells were incubated overnight at 4 °C. After aspirating the primary antibody solution, samples were washed three times with DPBS, incubating 10 min per wash. The secondary antibody solution incubation was performed in two steps. Samples were first incubated for 2 h protected from light with the secondary antibody solution-1 containing 0.1% triton, 1% BSA, 0.01% sodium azide, 1:500 dilution of donkey anti-goat Alexa Fluor 633 (Invitrogen, #A21082). From this moment, samples were kept protected from light throughout the whole process. Then the solution was removed, and samples were washed with DPBS three times, 10 min per

incubation. Samples were incubated afterwards for 2 h with a secondary antibody solution-2 containing 0.1% triton, 1% BSA, 0.01% sodium azide, 1:500 dilution of goat anti-mouse Alexa Fluor 488 (Invitrogen, #A11029), and 1:500 dilution of donkey anti-rabbit Alexa Fluor 555 (Invitrogen, #A21428) in DPBS. After secondary antibody solution was removed, samples were washed with DPBS three times, 10 min per incubation. Then samples were incubated for 10 min with DAPI solution (14.3µM in DPBS), washed with DPBS three times, 10 min per incubation, and mounted with Olympus scaleview solution. Samples were imaged with a confocal laser scanning microscope (Olympus, #FV1200) and images were processed afterwards with ImageJ software.[94]

3.3.5.4. Imaging of plated healthy and ALS SN spheroids embedded in Matrigel

The variation of several parameters of SN spheroids was assessed, comparing in this case the effect of *SN differentiation protocols B-E* in healthy and ALS samples in a 3D environment: spheroid core area, spheroid corona area and neurite length.

Cell culture and BF image collection

To that end, SN spheroids of the selected cell density ($\rho_3 = 6.000\ cell \cdot\ spheroid^{-1}$) were generated at TP0 as indicated in SECTION 3.3.3, starting from healthy or ALS hNSC.

Spheroids proliferated until TP1, when the differentiation began, and at TP2 (10 ddiff) spheroids were transferred to glass bottom 24 well plate embedded in 100 µL of ice-cold Matrigel per spheroid sample. After polymerising at 37 °C for 30 min, the corresponding differentiation medium was added to each sample. Bright field images were taken 24 h later using an inverted microscope (Zeiss, #Axiovert-200). The samples were maintained until TP3. Then samples were fixed in 4% paraformaldehyde solution and stored at 4 °C until the immunostaining was performed.

Image quantification

BF images were evaluated assessing spheroid core area, spheroid corona area and quantifying neurite length for every spheroid. The core area was considered as the area occupied by the central circular shape of the neurospheroid. The corona area was considered as the area occupied by the surrounding glia cells and neural projections. The average and standard deviation of neurite length quantification was plotted on a graph.

Immunostaining

The immunostaining was performed only in healthy spheroids following *SN differentiation protocol C* and *D* as described in SECTION 3.3.5.3.

3.3.5.5. Flow cytometry

At TP2, samples of healthy and ALS hNSC undergoing *SN differentiation protocol A* differentiated as 2D cultures ($57.000\ cells \cdot cm^{-2}$) and spheroids of different seeding densities ($\rho_1 = 3.000\ cell \cdot spheroid^{-1}$; $\rho_2 = 4.500\ cell \cdot spheroid^{-1}$; $\rho_3 = 6.000\ cell \cdot spheroid^{-1}$) were analysed to understand the influence of the seeding density and the spheroid on the initial differentiation, within the working range. A further analysis was performed onto healthy and ALS hNSC undergoing each of the other differentiation protocols (B-E) in the form of spheroids ($\rho_3 = 6.000\ cell \cdot spheroid^{-1}$) to assess the effects of each differentiation protocol onto the initial steps of the differentiation. In all cases, the analysis was performed looking for HNK1+ cells, a NCSC marker.

To that end, cells were washed with DPBS, and trypsinised incubating 5 min at 37 °C with TrypLE (Gibco, #12604021) in the case of 2D cultures or Accumax (Innovative Cell Technologies, #AM105) for spheroids. Then samples were placed in a washing buffer made of 5% foetal bovine serum (FBS) in DPBS. From this moment samples were kept in ice all the time. Cell suspensions were filtered and placed into flow cytometry tubes with 75 µm filters (Falcon, #352235). Then they were centrifuged for 4 min at 200 g and after aspirating the supernatant, the pellet was resuspended in 100 µL of washing buffer. The staining was performed incubating samples for

15 min with a solution of 1:100 dilution of P75-APC (Biolegen, #358405) and 1:200 dilution of HNK1-FITC (Biolegend, #359603) in washing buffer. Then samples were diluted 5 times in washing buffer to increase the sample volume and analysed in a BD™ LSR II flow cytometer. The data obtained were processed using Flowing Software version 2.5.1.[96]

3.3.5.6. Real time PCR for mRNA quantification

The mRNA of healthy SN spheroids following differentiation protocol A was quantified at all timepoints (TP1, TP2, TP3) to assess the relative evolution in gene expression. The mRNA of healthy and ALS spheroids following each differentiation protocol (B-E) was quantified at the final timepoint to find differences in gene expression in healthy and ALS samples and to assess the effect of each differentiation protocol. For that purpose, after doing cell lysis, RNA was isolated, converted to cDNA and then real time polymerase chain reaction or quantitative PCR (qPCR) was performed.

mRNA isolation and reverse transcription to cDNA

For each sample two spheroids were washed with sterile DPBS and incubated with 100 µL of Accumax (Innovative cell technologies, #AM105) for 5 min at 37 °C. The cell suspension was neutralised in 5 mL of DMEM supplemented with 10% FBS, and centrifuged for 4 min at 3.5 g. After aspirating the supernatant, samples were placed on ice. The mRNA was isolated using the manufacturer's protocol of RNeasy mini kit for RNA isolation (Qiagen, #74104), RNase free

water (Ambion, #AM9938), RNase spray for hands (Ambion, #AM9782), RNase free tubes and micropipette tips and keeping samples during the whole process in ice. Once the mRNA was obtained, reverse transcription was performed to obtain cDNA using SuperScript VILO cDNA Synthesis Kit (Invitrogen, #11754-050) and a thermocycler (Eppendorf, MasterCycler personal). Afterwards, the obtained cDNA was quantified using a nanodrop (Thermofisher, Nanodrop 200) to check for the purity and concentration of nucleic acids.

Real time PCR

Forward and reverse primer sequences of each gen of interest (summarised in TABLE 3-6) were chosen according to PrimerBank database,[97] checking for NCBI Gene ID, and purchased from IDT (Integrated DNA Technologies, Inc., U.S.). The cDNA samples were incubated with the mastermix and dye — TB Green® Premix Ex Taq™ II (Clontech Takara, #RR820L)—, RNase free water, and the forward and reverse primers for each gene of interest. Samples were loaded in optical 384 well plates (MicroAmp, #4309849) filling 3 wells for each target gene and sample. Then the plate with three technical replicates was covered with optical adhesive films (MicroAmp, #4311971), and centrifuged for 2 min at 2.000 rpm before reading the plates in a 7900HT Fast Real-Time PCR System (Applied Biosystems) performing for the amplification an initial step of 2 min at 50 °C, followed by 50 cycles of 5 s at 95 °C and 30 s at 60 °C, and

finishing with a dissociation stage of 15 s at 95 °C, 15 s at 60 °C and 15 s at 95 °C, to assure the specificity of qPCR quantification.

Table 3-6. *qPCR primers. Target gene name, with alternative names, Gene ID code and forward and reverse sequences (both 5'-3') are indicated. All gene sequences are for Homo sapiens.*

Target gene	Gene ID	Forward primer	Reverse primer sequence
GAPDH	2597	GGAGCGAGATCCCTCCAAAA	GGCTGTTGTCATACTTCTCATG
ACTB	60	CATGTACGTTGCTATCCAGGC	CTCCTTAATGTCACGCACGAT
RPS18	6222	GCGGCGGAAAATAGCCTTTG	GATCACACGTTCCACCTCATC
HNK1 (a.k.a. B3GAT1)	27087	CTCCTTCGAGAACTTGTCACC	GGGTCAGTGAAGCCCTTCTT
TUBB3	10381	GGCCAAGGGTCACTACACG	GCAGTCGCAGTTTTCACACTC
PRPH	5630	GCCTGGAACTAGAGCGCAAG	CCTCGCACGTTAGACTCTGG
POU4F1 (a.k.a. BRN3A)	5457	GGGCAAGAGCCATCCTTTCAA	CTGTTCATCGTGTGGTACGTG
NTRK1 (a.k.a. TrkA)	4914	AACCTCACCATCGTGAAGAGT	TGAAGGAGAGATTCAGGCGAC
NTRK2 (a.k.a. TrkB)	4915	TCGTGGCATTTCCGAGATTGG	TCGTCAGTTTGTTTCGGGTAAA
NTRK3 (a.k.a. NTRK3)	4916	ACGAGAGGGTGACAATGCTG	CCAGTGACTATCCAGTCCACA
RUNX3	864	AGGCAATGACGAGAACTACT	CGAAGGTCGTTGAACCTGG
DICER	23405	TGCTATGTCGCCTTGAATGTT	AATTTCTCGATAGGGGTGGTCT
ETV1 (a.k.a. ER81)	2115	TGGCAGTTTTTGGTAGCTCTT	CGGAGTGAACGGCTAAGTTTAT
SPP1 (a.k.a. OPN)	6696	CTCCATTGACTCGAACGACTC	CAGGTCTGCGAAACTTCTTAGA
VGluT1 (a.k.a. SLC17A7)	57030	CGACGACAGCCTTTTGTGGT	GCCGTAGACGTAGAAAACAGA
PVALB	5816	AAGAGTGCGGATGATGTGAA	GCCTTTTAGGATGAATCCCAGC
MBP	4155	CACGCAGGCAAACGAGAATT	CTGAGGTTGTCCGTGAAAGTT
GFAP	2670	CTGCGGCTCGATCAACTCA	TCCAGCGACTCAATCTTCCTC
MNX1 (a.k.a. Hb9)	3110	GATGCCCGACTTCAACTCCC	GCCGCGACAGGTACTTGTT
TNFRSF1B (a.k.a.	7133	CGGGCCAACATGCAAAAGTC	CAGATGCGGTTCTGTTCCC

Quantification of qPCR results

The obtained C_T values for each sample were analysed following the Livak method for relative quantification.[98,99] First, for each sample and gene read ($C_T(sample, gen)$) the average of the three technical

replicates was calculated. Then, the three housekeeping readings (ACTB, GAPDH, RPS18) were used as internal standard control to calculate the ΔC_T for each sample, gen and housekeeper, as indicated in the following equation:

$$\Delta C_T = C_T(sample, gen) - C_T(sample, housekeeper) \quad (3\text{-}1)$$

To perform relative quantification, the calibrator sample was set as *protocol A* TP1 for the analysis of healthy samples undergoing *SN differentiation protocol A* at different timepoints. Healthy and ALS samples undergoing all protocols at TP3, were analysed twice, stablishing both results from *protocol A* TP3 and results from *protocol A* TP1 as calibrators. Testing samples were compared against calibrator samples:

$$\Delta\Delta C_T = \Delta C_T(test) - \Delta C_T(calibrator) \quad (3\text{-}2)$$

Then the normalised expression ratio of the expression of each sample and gene against each housekeeper was calculated as follows:

$$Normalised\ expression\ ratio = log_2(2^{-\Delta\Delta C_T}) \quad (3\text{-}3)$$

Finally, the mean fold change was calculated performing the average of the normalised expression ratio for each gene and sample against each of the three housekeepers:

$$Mean\ fold\ change = average\ (Normalised\ expression\ ratio_{housekeeper}) \quad (3\text{-}4)$$

3.4. Results

3.4.1. Optimisation of SN seeding conditions

3.4.1.1. Differentiation in 2D

Healthy and ALS hNSC maintained with proliferation medium showed an over-proliferation of glial-like morphologies and no spontaneous differentiation, whereas both ALS and healthy hNSC undergoing first steps of *SN differentiation protocol A* showed neurite formation and neural rosette-like structures (radial arrangement of cells), as seen in FIGURE 3-3, especially for healthy cells. ALS cells at 8 ddiff look similar to healthy cells at 6 ddiff.

3.4.1.2. Spheroid size and seeding density

Spheroids undergoing *SN differentiation protocol A* showed little variation in size during the whole differentiation period (see FIGURE 3-4). At the beginning, 2 DIV after the spheroid was formed, spheroid transversal area was $0.08 \pm 0.02\ mm^2$, and after 26 ddiff, the size had increased up to $0.12 \pm 0.02\ mm^2$.

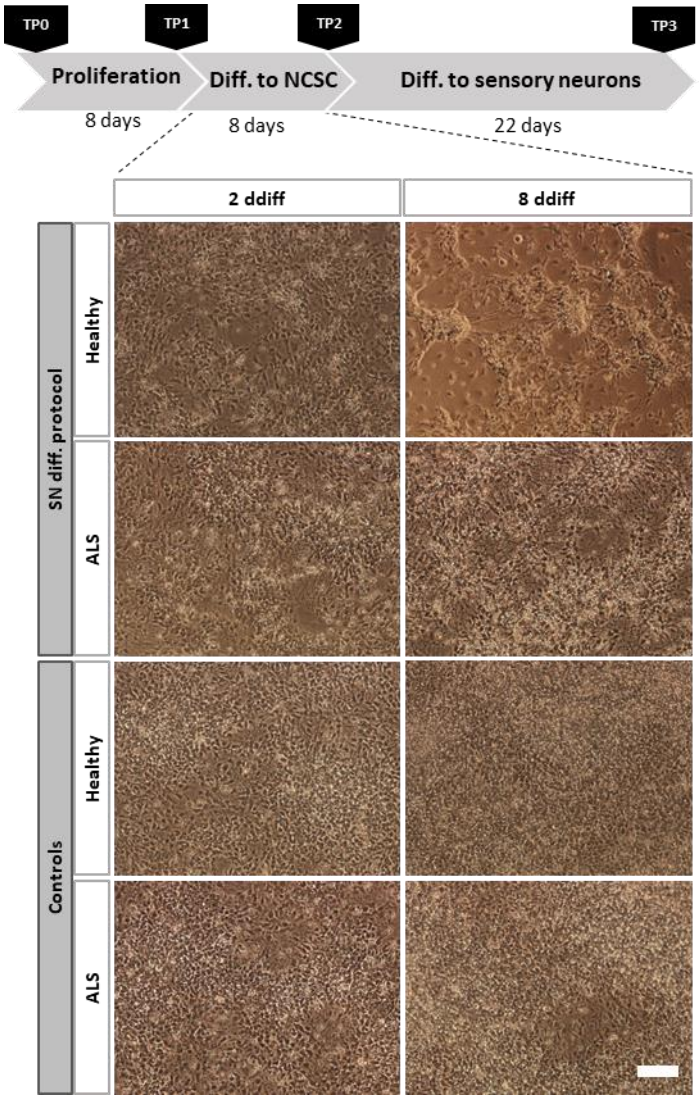

Figure 3-3. *hNSC differentiation to SN in 2D. Bright field images of healthy or ALS neural stem cells undergoing the second step of SN differentiation protocol A at 2 and 8 days of differentiation. As a control healthy and ALS cells were exposed to neural stem cell maintenance medium. Scale bar 100 µm.*

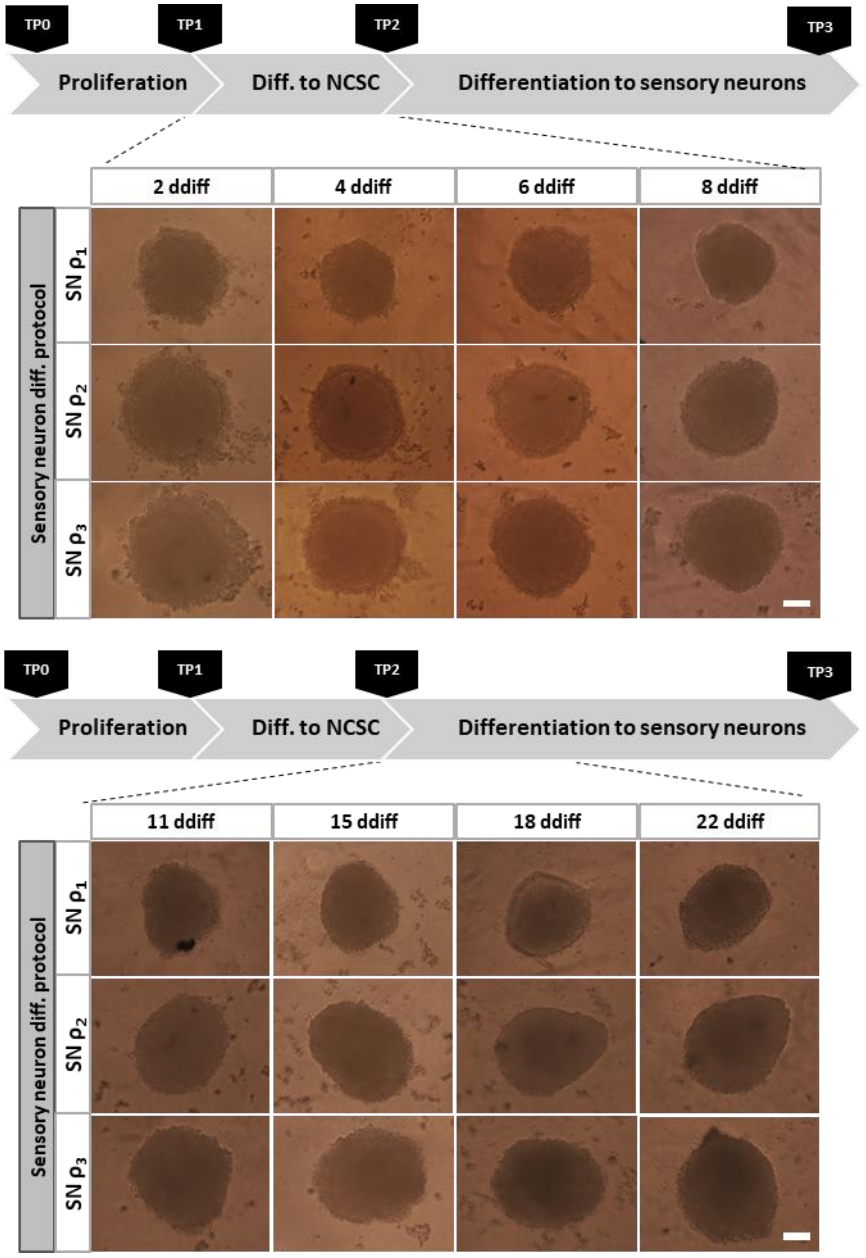

Figure 3-4. *Floating spheroid size variation analysis. Bright field images of the differentiation of hNSC to sensory neurons as spheroids following SN differentiation protocol A and seeding initially cells in three different densities (3.000, 4.500 and 6.000 $cell \cdot spheroid^{-1}$). Images taken at different days after differentiation started (ddiff). Scale bar 100 µm.*

3.4.2. Characterisation of SN differentiation protocols

3.4.2.1. Characterisation at TP2

The immunostaining and flow cytometry (FC) analysis performed onto floating spheroids of healthy and ALS cells undergoing SN differentiation through different protocols showed that all samples assessed express HNK1, both analysed through immunostaining and through FC, as seen in FIGURE 3-5. The representative image of immunostaining of floating spheroids shows that cells present in the spheroid are successfully expressing HNK1 and there is a little expression of TUJ1. Results from FC analysis showed that all samples analysed were HNK1 positive, regardless of being 2D culture, spheroids of different seeding densities, healthy or ALS samples undergoing different differentiation protocols. Samples undergoing differentiation protocols B-E showed higher percentage of HNK1- cells (see FIGURE 3-5-D and E).

At TP2 spheroids embedded in Matrigel for 24 h undergoing *SN differentiation protocols B-E*, did not show big differences between healthy and ALS samples (FIGURE 3-6). The biggest spheroid core and corona size were observed for protocol D, followed by protocol C samples, being in both cases similar for healthy and ALS samples (FIGURE 3-6-A). Neurite length analysis resulted in more consistent results between healthy and ALS samples for protocols C and D, and a higher variation in protocols B and E (FIGURE 3-6-B).

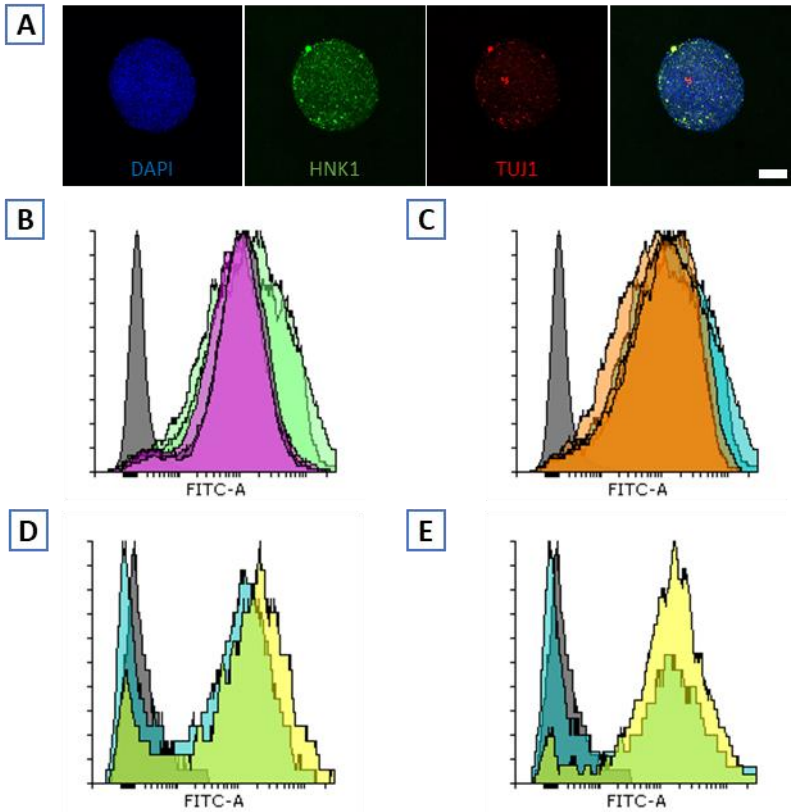

Figure 3-5. *Characterisation of spheroids undergoing SN differentiation protocols at TP2.* ***A)*** *Floating spheroid immunostaining at TP2. Maximum z-projection of fluorescence images obtained of the immunostaining of healthy samples undergoing SN differentiation protocol-A at TP2. DAPI is shown in blue, HNK1 in green, and TUJ1 in red. Scale bar 100µm.* ***B)*** *Flow cytometry analysis of HNK1 on 2D culture (green) and 3D spheroids of different densities (purple), all undergoing Protocol A.* ***C)*** *Flow cytometry analysis of HNK1 of 2D cultures of healthy (blue) and ALS (orange) samples, all undergoing Protocol A.* ***D)*** *Flow cytometry analysis of HNK1 of healthy spheroids undergoing protocols B and E (without CHIR99021, in blue), and healthy spheroids undergoing protocols C and D (with CHIR99021, in yellow).* ***E)*** *Flow cytometry analysis of HNK1 of ALS spheroids undergoing protocols B and E (without CHIR99021, in blue), and ALS spheroids undergoing protocols C and D (with CHIR99021, in yellow). In all FC graphs negative control of non-stained healthy samples is shown in grey.*

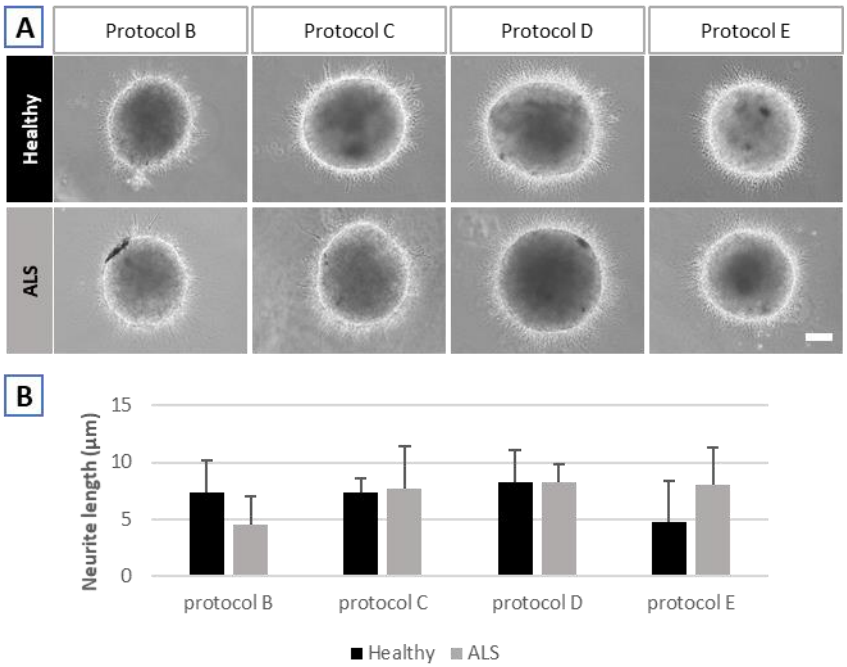

Figure 3-6. *Characterisation of spheroids undergoing SN differentiation protocols B-E, 1 DIV after plating them embedded in Matrigel at TP2.* ***A)*** *Bright field images of SN spheroids created from healthy and ALS hNSC. Scale bar 100 µm.* ***B)*** *Quantification of the neurite length observed in the corona area of spheroids, showing average and standard deviation (n=5).*

3.4.2.2. Characterisation at TP3

The immunostaining of hNSC derived SN spheroids embedded in Matrigel was performed in healthy samples of the two protocols that at TP2 seem to have more promising result and more consistent between healthy and ALS samples: *protocol C* and *D*. SN spheroid plated onto Matrigel coated surface undergoing *protocol A* was utilised as a comparison. Results showed that culturing spheroids embedded in Matrigel with protocols C and D induced higher neurite production and elongation, and apparently higher number of TrkC+ neurons (FIGURE 3-7).

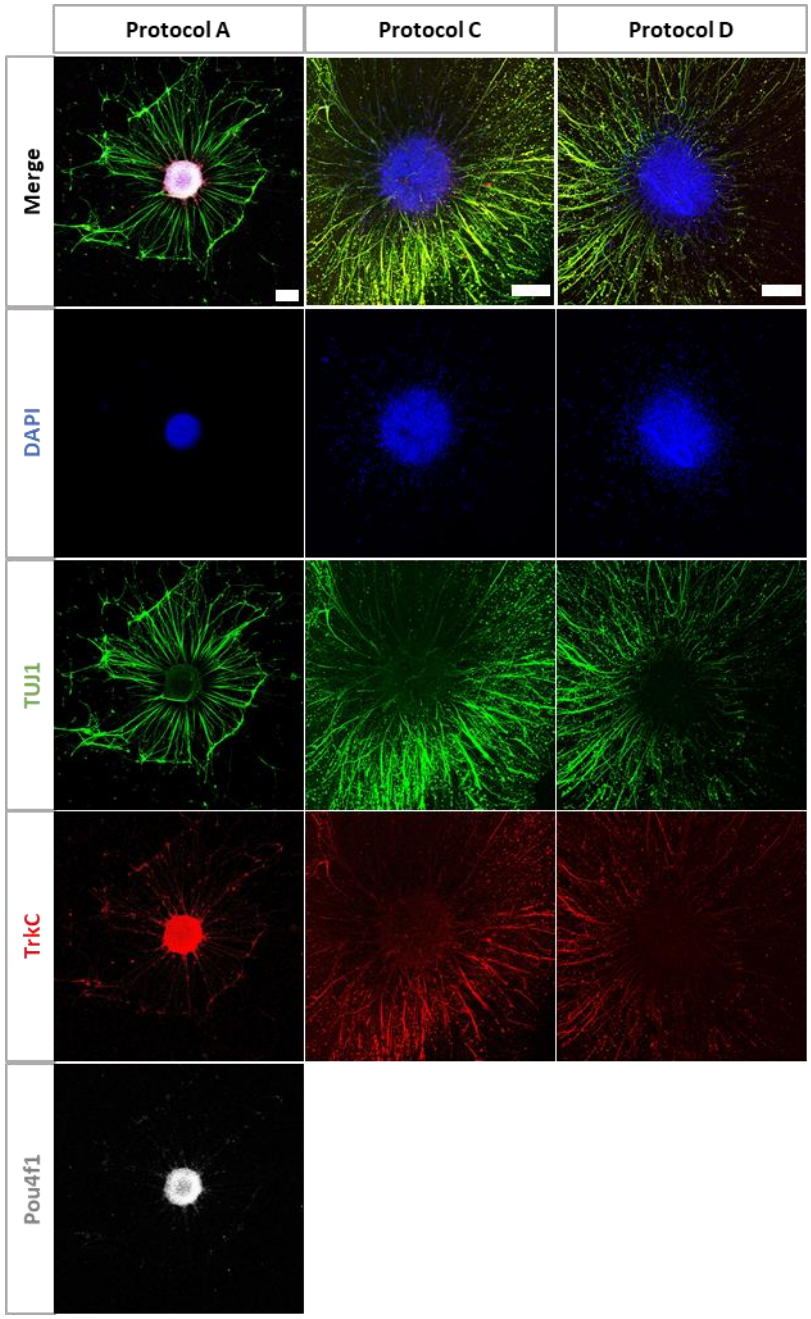

Figure 3-7. *Immunostaining of healthy hNSC differentiated to SN spheroids through different protocols. Samples undergoing protocol A are seeded onto coated surfaces, whereas samples undergoing protocols C and D are cultured embedded in Matrigel. Nuclei are stained in blue, TUJ1 in green, TrkC in red and*

Pou4f1 in grey. Images taken at TP3. Scale bar: 200 µm (protocol A), 100 µm (protocols C and D).

3.4.3. Gene expression throughout the differentiation process

The qPCR analysis performed on spheroids undergoing *SN differentiation protocol A* at different timepoints normalised against TP1 (FIGURE 3-8-A) showed that the expression of most of the genes increased at TP2, and most decreased at TP3. The analysis performed on healthy and ALS spheroids undergoing all differentiation protocols normalised against TP1 (FIGURE 3-8-B) revealed that the expression of most genes had also incremented from TP1, for most of the genes, except of NTRK1, MBP, ETV1 and DICER. Though in all cases the decrease of expression was close to zero. The expression of PVALB for healthy samples undergoing protocol E was impossible to read, it was out of the machine's scale probably due to too low expression. The analysis performed on healthy and ALS spheroids undergoing all differentiation protocols normalised against protocol A at TP3 (FIGURE 3-8-C) revealed in general quite different expression of healthy samples undergoing protocol E and ALS samples undergoing protocols D and E. The differences in expression are further analysed in the discussion.

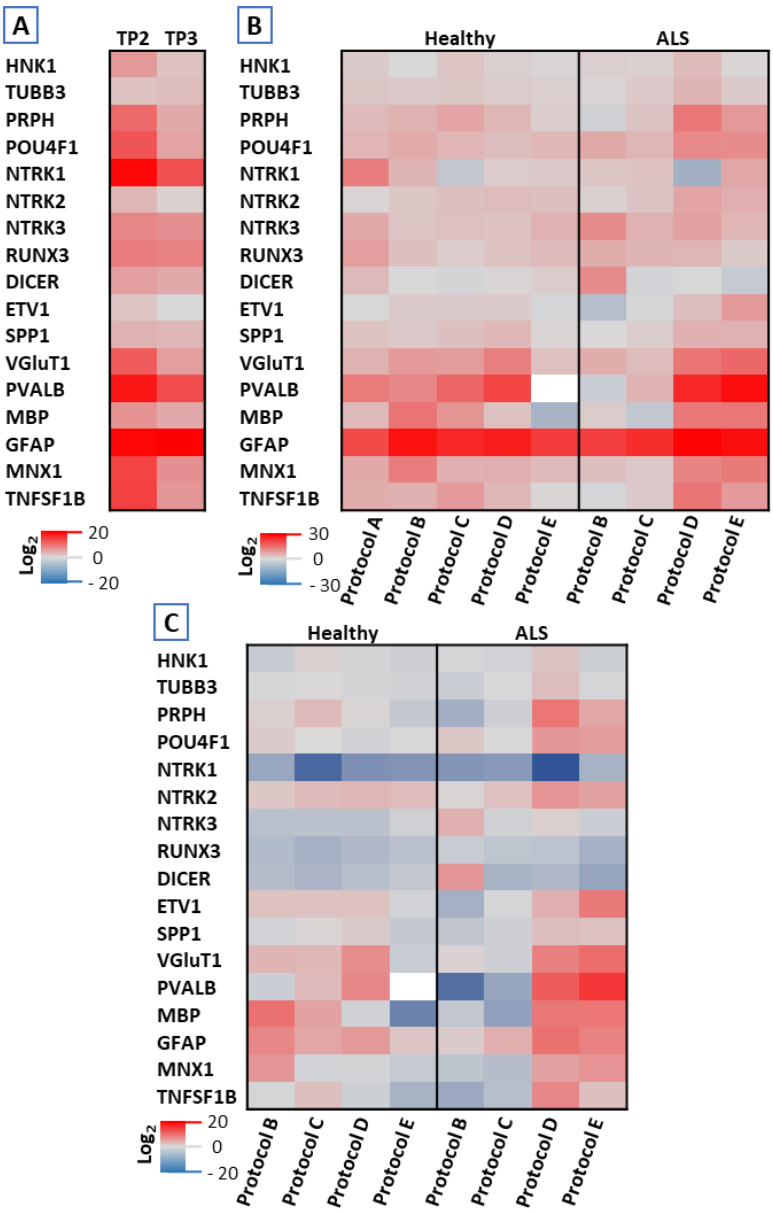

Figure 3-8. *qPCR analysis.* ***A)*** *mRNA quantification at TP2 and TP3 of healthy SN spheroids undergoing differentiation protocol A, normalised against mRNA expression at TP1.* ***B)*** *mRNA quantification at TP3 of healthy and ALS SN spheroids undergoing differentiation protocols A-E, normalised against mRNA expression of SN spheroids at TP1.* ***C)*** *mRNA quantification at TP3 of healthy and ALS SN spheroids undergoing differentiation protocols B-E, normalised against mRNA expression of SN spheroids undergoing differentiation protocol A at TP3.*

3.5. Discussion

3.5.1. Seeding conditions

3.5.1.1. Differentiation in 2D

The hNSC culture performed in 2D following *SN differentiation protocol A* (FIGURE 3-3) showed that neural differentiation from this cell type **is not spontaneous**, and the performed protocol was able to induce neural differentiation inducing rosette-like formation in both ALS and healthy cells. However, ALS cells seem to need longer time to reach similar differentiation levels compared to healthy cells.

3.5.1.2. Spheroid differentiation

The hNSC culture performed with healthy spheroids following *SN differentiation protocol A* revealed that during the differentiation process the spheroid transversal area barely augmented (FIGURE 3-4). This can be due to little cell proliferation, a compensation of the proliferation with high cell death, or a compensation of the proliferation with high cell loss caused by poor cohesion properties on the spheroid ECM. To check the last option, different protocols were assessed, including in some of them CHIR99021, a chemical compound known to induce ECM remodelling,[66] proliferation of hNP,[67] and SN axon regeneration.[68] For the rest of the experiments, the spheroid seeding density was established to the highest one

(6.000 $cell \cdot spheroid^{-1}$) to guarantee cell number and still within a spheroid size range that can be handled with a pipette.

3.5.2. Assessment of differences induced by each differentiation protocol

3.5.2.1. SN differentiation at TP2

Results from FC and floating spheroid immunostaining performed at TP2 (FIGURE 3-5) suggested an **adequate differentiation towards NCSC** with higher specificity with *Protocol A*, as all samples assessed through immunostaining and FC expressed HNK1, regardless of being 2D cultures, spheroids of different seeding densities, healthy or ALS samples. The analysis performed onto 2D cell cultures and spheroids of different seeding densities of healthy and ALS hNSC undergoing *SN differentiation protocol A,* to understand the influence of the seeding density and the spheroid on the initial differentiation, showed that they do not affect the differentiation towards HNK1+ cells. The analysis performed onto spheroids healthy and ALS hNSC undergoing the rest of differentiation protocols (B-E) to assess the effects of each differentiation protocol onto the initial steps of the differentiation showed that **all protocols were able to induce the formation of HNK1+ cells** at TP2 in healthy and ALS hNSC.

The BF image observation performed on spheroids of undergoing *protocols B-E* at TP2 (FIGURE 3-6) suggested that *protocol D* could induce the formation bigger spheroid core and corona size, followed by *protocol C* spheroids, both containing CHIR99021. And although neurite length was quite similar for all protocols, measurements were similar for ALS and healthy samples only on *protocols C* and *D*; whereas it resulted in long neurites for healthy spheroids undergoing *protocol B* and ALS spheroids undergoing *protocol E*, and much shorter neurites for their corresponding ALS and healthy samples. The addition of CHIR99021 into differentiation medium utilised in *protocols C* and *D*, promoted an **increase of spheroid size** as a result of ECM remodelling,[66] proliferation of hNP,[67] and SN axon regeneration.[68] The addition of ROCK inhibitor Y27632 in *protocols D* and *E*, resulted in **different effects in healthy and ALS samples** in the core and corona size, and in the neurite length observed.

3.5.2.2. SN characterisation at TP3

The differentiation of hNSC can generate any neural lineage. Although the aim was to obtain a pSN enriched culture, it is assumable that the cell population is almost impossible to be pure and actually, heterogeneous cell cultures are better at biomimicking a natural environment as cells provide their native support to each other. Moreover, TrkC+ cell population is known to be dynamic throughout the differentiation process,[53] and pSN subtypes have some variations in their genetic profile, such as RUNX3.[80] Therefore,

it is important to understand the cell population behind each condition and timepoint, and the effect of each condition onto healthy and ALS cells. For that purpose, in this section the results obtained from qPCR tests (FIGURE 3-8) are compared with immunostainings (FIGURE 3-7) and the information available on the genetic expression previously assessed (TABLE 3-1).

mRNA expression evolution in samples undergoing protocol A through time

The analysis performed on healthy SN spheroids following *SN differentiation protocol A* at TP1, TP2 and TP3, normalised against TP1 (FIGURE 3-8-A) indicates that the expression of all genes analysed increases at TP2 and some of them decreases at TP3. Results suggest that at TP2, there is an increase of NCSC population (HNK1+), that decreases at TP3. The neuron population (TUBB3+) is stable from TP2, and peripheral neurons (PRPH+), motoneurons (MNX1+), and sensory neurons (POU4F1+) reach their maximum expression levels at TP2, suggesting that **the peak of NCSC population (HNK1+) is earlier than TP2** and, at that moment, NCSC are already differentiated to certain level to the specific neural lineages. Surprisingly, motor system neuron population (PVALB+) remains almost the same, probably due to an **increase in interneuron population**, or other non-peripheral motor system neurons. Myelin levels (MBP+) are also decreased at TP3, probably linked to the decrease in motoneuron population (MNX1+) and small decrease in pSN population. Astrocyte population (GFAP+) remains constant

from TP2. The sensory neuron population (POU4F1+) is predominantly shifted to nociceptive SN (NTRK1+), with very little mechanoreceptive SN (NTRK2+) and some pSN (NTRK3+, RUNX3+, DICER+, SPP1+, ETV1+, VGluT1+). At TP3, all SN decrease slightly but the expression of ETV1 and VGluT1, reported to be related with pSN (see TABLE 3-1), decreases a lot. ETV1 expression is linked to NT3-TrkC signaling on pSN,[79,82] but it is also critical in the formation of functional connections between pSN and MN.[82] VGluT1 is expressed at the end terminals of pSN, at the synaptic contacts of interneurons and some other SN.[23] Both ETV1 and VGluT1 are indicators of functional connectivity, and their expression is decreased at TP3. As mRNA samples were extracted from floating spheroids, this could suggest that although neurons can express these markers at the beginning on their own, in a long term, neurons are not able to sustain the expression of proteins destined to form functional connections in the absence of the target tissue (e.g. the muscle). This could be a way of saving resources from neurons and, it could also be linked to the effect of cytokines and growth factors secreted in native conditions by innervated cells. Similar phenomena have been reported to occur in the neuromuscular junction formation, where the post-synaptic domain is first formed in the muscle and together with Schwann cells, they send signals to the motoneuron axon to form the synapse.[100,101] Results suggest that **the expression of ETV1 and VGluT1** required to form functional connections, could be to some length, induced by cytokines and growth factors

secreted by target cells. This highlights the relevance of a biomimicking environment to induce an adequate genetic expression.

Assessment of the effects of each medium composition onto healthy and ALS cell population

One of the things to highlight is outstanding variations for each medium condition onto gene panel expression among healthy and ALS cells. Normalising the expression of all samples against healthy ones, as performed in FIGURE 3-8-B and FIGURE 3-8-C, highlights the different genetic pattern of SN in ALS cells.

The **increment of NT-3** concentration on the medium in *SN differentiation protocol B* (FIGURE 3-8-C, protocol B) induced a drastic reduction in nociceptive sensory neurons (NTRK1+); an augment in myelinated MN (MBP+, MNX1+) and astrocytes in healthy cells and a decrease of both in ALS cells; a small decrease of some pSN markers (DICER, NTRK3 and RUNX3) in healthy cells, being the expression of NTRK3 and DICER augmented in ALS cells; a small increase in the expression of pSN functionality related markers (ETV1 and VGluT1) in healthy cells, in contrast to a decreased expression in ALS cells.

The addition of **CHIR99021** on the medium of *SN differentiation protocol C,* on top of the increment of NT-3 (FIGURE 3-8-C, protocol C), compared to *protocol B*, induced a further reduction of nociceptive SN (NTRK1+) in healthy cells, a small reduction of some

pSN markers (RUNX3 and DICER); an augment of PRPH and PVALB in healthy cells indicating possibly an increment of peripheral interneurons, together with their reduction in ALS cells; a reduction of myelinated MN (MNX1+, MBP+), being much higher reduction in ALS; and a reduction in astrocytes (GFAP+). ETV1 and VGluT1 levels did not vary in heathy cells, but they decreased in ALS cells.

The **addition of ROCK inhibitor Y27632** on *SN differentiation protocol E,* on top of the increment of NT-3 on the medium (FIGURE 3-8-C, protocol E), compared to *protocol B*, induced in healthy cells a drastic decrease of myelin (MBP+) probably related to the decrease of peripheral neurons (PRPH), the big decrease of MN (MNX1+) and the small decrease of sensory neurons (POU4F1+). The expression levels of astrocytes (GFAP+) and pSN functionality related markers (ETV1 and VGluT1) were also reduced. The effect of ROCK inhibitor Y27632 onto ALS cells could be observed in the same genes, in an opposite manner: the expression of PRPH, POU4F1, ETV1, VGluT1, MBP, GFAP and MNX1 was incremented. This suggests that **ROCK inhibitor Y27632 could interfere not only with hNSC cell differentiation, but also with ALS genetic pathway**.

The **addition of ROCK inhibitor Y27632** on *SN differentiation protocol D,* on top of the increment of NT-3 on the medium and the addition of CHIR99021 (FIGURE 3-8-C, protocol D), induced in healthy cells a similar effect as CHIR99021 alone (*protocol C*), whereas in ALS

cells it induced a similar effect as ROCK inhibitor Y27632 alone (*protocol E*).

To sum up, the results of healthy cells (FIGURE 3-8-B, healthy) suggest that ***protocol A*** generates a SN population highly enriched in nociceptive sensory neurons, and slightly less in pSN, being the protocol that **induces the highest production of pSN**, followed by *protocol E*. The protocol that induces smallest production of nociceptive SN is *protocol C*. In the rest of the cases, sensory neuron population was balanced or slightly more inclined to mechanoreceptive sensory neurons (NTRK2+). The results of ALS cells (FIGURE 3-8-B, ALS) suggest that ***protocol B*** **generates a SN population with highest enrichment in pSN**. *Protocol D* induces the smallest production of nociceptive sensory neurons, and *protocols C* and *E* a quite balanced population of sensory neurons. However, the *protocol A* could also improve these results in ALS cells. Further studies would be required to evaluate this. The different results obtained in healthy and ALS cells highlights the **importance of analysing and considering the different response of each cell type to external stimuli**, determining its differentiation onto different neural lineages.

Assessment of the expression of ALS markers

ALS is characterised by the altered regulation of some genes,[102] and among the ones analysed in this study, it is characterised by the upregulation of PRPH,[76] the downregulation of MBP,[88,89] the

upregulation of GFAP,[92] and the upregulation of TNFSF1B.[93] Nevertheless, DICER and SPP1 could also be involved in ALS. DICER is known to be downregulated in ataxia,[79,81] and SPP1 is known to be upregulated in inflammatory processes of dystrophic and injured muscles.[71,84]

Comparing those target gene expression at TP3 in ALS cells versus healthy cells (FIGURE 3-8-B), it is outstanding the effect of *protocols D* and *E*, both containing ROCK inhibitor Y27632, on inducing the upregulated expression of many genes, in some cases agreeing with ALS expression patterns. In both protocols *D* and *E*, peripherin and TNFSF1B levels are high, and DICER levels are low. However, comparing to healthy cells, SPP1 and GFAP expression was not upregulated.

When comparing ALS cells to healthy cells exposed to *protocol B* (FIGURE 3-8-B), we can see that basal ALS cells expression of ETV1, motor system cells (PVALB+), myelin (MBP), and motoneurons (MNX1+) is much lower. This suggests that despite following the same protocol, **ALS cells form a smaller population of myelinated MN that fails to form successful connections with pSN**, as observed by critically low levels of ETV1, even lower than healthy cells at TP1. **ETV1 could hypothetically be involved in the development of the disease, interfering with the motor feedback from pSN.** Studying the connection between pSN and MN in ALS cells would help elucidating the role of ETV1 and finding out if it could be a feasible

treatment target. The comparison of healthy and ALS cells exposed to *protocol B* shows, as well, an increase in NTRK3 and DICER in ALS cells, though without an increase in RUNX3 expression. RUNX3 is known to have a different regulation in each subtype of NTRK3+ neuron.[80] This suggest that **the pSN subtype population in ALS cells is quite different from the one of healthy cells**. Assessing and understanding the pSN subtypes present in healthy and ALS cells would help elucidating their role in the disease progression.

The effect of CHIR99021 alone onto cells, exposed to *protocol C*, compared to same samples exposed to *protocol B* (FIGURE 3-8-B), revealed as well genetic expression pattern differences in pSN related genes. Healthy cells maintained the expression levels, but in ALS cells NTRK3 and DICER levels reduced drastically, RUNX3 levels were maintained and ETV1 and PVALB levels were increased. These genes, together with MBP, were also affected differently in healthy and ALS cells exposed to ROCK inhibitor Y27632, in *protocols C* and *D*. Taking all of this together, results suggest that **pSN related gene basal levels are different and regulated differently in ALS cells compared to healthy cells**. And the assessed conditions interfere not only with the differentiation of hNSC, as expected, but also on ASL genetic profile in different way in healthy and ALS cells.

Protocols comparison from immunostainings experimental results

The immunostaining performed on SN spheroids (FIGURE 3-7) revealed that *SN differentiation protocol A* was able to induce certain number of pSN, expressing Pou4f1 in their soma and TrkC in the whole cell body, colocalising with TUJ1 expression. It also showed that **embedding spheroids in Matrigel facilitates their neurite production and elongation**, in comparison to plated spheroids. The results also suggested apparently that *SN differentiation protocols C* and *D* induce higher number of TrkC+ neurons comparing with *protocol A* (FIGURE 3-7). However, the qPCR performed onto healthy cells (FIGURE 3-8-B, healthy samples) suggested that the protocol able to induce higher number of pSN (TUBB3+, PVALB+, PRPH+, POU4F1+, NTRK3+, DICER+, RUNX3+, SPP1+, MBP+, ETV1+ and VGluT1+) was the *SN differentiation protocol A*. Therefore, the different results from immunostainings could be due to the effect of embedding cells in Matrigel (*protocols C* and *D*) versus not embedding them (*protocol A*). This suggesting that **embedding the cells in Matrigel could be promoting neuron survival and neurite extension**, and as a result, the number of neurons detected (Tuj1+) and pSN detected (TrkC+) is also higher.

3.6. Conclusions

Human neural stem cells were successfully differentiated to SN populations enriched in TrkC+ neurons, both healthy and ALS samples. The differentiation of hNSC to SN through several differentiation protocols showed that SN differentiation is not spontaneous and NCSC formation and HNK1 expression may not be affected by the conformation of spheroids versus 2D culture in healthy and ALS samples. The obtained results suggested as well that the expression of ETV1 and VGluT1, required to form functional connections, could be to some length induced by cytokines and growth factors secreted by target cells.

Evaluating each SN differentiation protocol, we could observe that CHIR99021 induced an increase of spheroid size, remodelling the spheroid ECM, promoting cell proliferation and axon regeneration. ROCK inhibitor Y27632 induced different effects in healthy and ALS samples in the core and corona size; in the neurite length observed; and opposite effects in the expression of some genetic markers assessed (PRPH, POU4F1, ETV1, VGluT1, MBP, GFAP and MNX1) in ALS cells, suggesting that ROCK inhibitor Y27632 could interfere not only with hNSC cell differentiation, but also with ALS genetic pathway. The different genetic expression patterns observed in ALS cells compared to healthy ones exposed to same conditions, suggest that ALS cells have lower basal levels or predisposition to form myelinated MN that successfully interact with pSN through ETV1,

and therefore ETV1 could hypothetically be involved in the development of the disease, interfering with the motor feedback from certain subtypes of pSN. Furthermore, obtained results suggest that the basal levels of some pSN related genes (NTRK3, RUNX3 and DICER) are different and are regulated differently in ALS cells compared to healthy cells. These genetic differences between healthy and ALS cells emphasise the importance of assessing basal neural populations behind each condition and timepoint in ALS, and evaluating the effect of each differentiation media on the neural differentiation and on the interferences with ALS genetic pathway to develop an ALS study model. The ALS has been considered for years a MN disease and only the role of proprioception in the disease progression has recently been reported in few publications.

All the SN differentiation protocols assessed induced small variations in the resulting neural population at TP3 and resulted in a heterogeneous neural population. Protocol A was the one inducing the formation of more TrkC+ SN. This pSN enriched heterogenous cell population is better at biomimicking the physiological environment, as different kind of cells provide support to each other. Understanding the pSN subtypes present in healthy and ALS cells would help elucidating their role in the disease progression.

3.7. References

1. Proske, U. & Gandevia, S. C. The proprioceptive senses: their roles in signaling body shape, body position and movement, and muscle force. *Physiol. Rev.* **92**, 1651–1697 (2012).
2. Tuthill, J. C. & Azim, E. Proprioception. *Curr. Biol.* **28**, R194–R203 (2018).
3. Sherrington, C. S. The integrative action of the nervous system. in *Yale University Mrs. Hepsa Ely Silliman memorial lectures* (ed. Sons, C. S.) 1–411 (Yale University Press, 1906).
4. Ruffini, A. On the minute anatomy of the neuromuscular spindles of the cat, and on their physiological significance. *J. Physiol.* **23**, 190–208 (1898).
5. Sherrington, C. S. Reflex inhibition as a factor in the co-ordination of movements and postures. *Q. J. Exp. Physiol.* **6**, 251–310 (1913).
6. Hagert, E. Proprioception of the wrist joint: a review of current concepts and possible implications on the rehabilitation of the wrist. *J. Hand Ther.* **23**, 2–17 (2010).
7. Lallemend, F. & Ernfors, P. Molecular interactions underlying the specification of sensory neurons. *Trends Neurosci.* **35**, 373–381 (2012).
8. Dionisi, C., Rai, M., Chazalon, M., Schiffmann, S. N. & Pandolfo, M. Induced pluripotent stem cell-derived primary proprioceptive neurons as Friedreich ataxia cell model. *bioRxiv* 829358 (2019) doi:10.1101/829358.
9. Banks, R. Muscle Spindles and Tendon Organs. in *Reference Module in Biomedical Sciences* 1–10 (Elsevier, 2018). doi:10.1016/B978-0-12-801238-3.99489-3.
10. Macefield, V. G. & Knellwolf, T. P. Functional properties of human muscle spindles. *J. Neurophysiol.* **120**, 452–467 (2018).
11. Taylor, J. L. Kinesthetic inputs. in *Neuroscience in the 21st Century* (ed. Pfaff, D. W.) 931–964 (Springer New York, 2013). doi:10.1007/978-1-4614-1997-6_31.
12. Bewick, G. S. & Banks, R. W. Mechanotransduction in the muscle spindle. *Pflügers Arch. - Eur. J. Physiol.* **467**, 175–190 (2015).
13. Pierrot-Deseilligny, E. & Burke, D. Fusimotor mechanisms, muscle spindles and their role in the control of movement. in *The Circuitry of the Human Spinal Cord* 110–137 (Cambridge University Press, 2012). doi:10.1017/CBO9781139026727.004.
14. Colón, A., Guo, X., Akanda, N., Cai, Y. & Hickman, J. J. Functional analysis of human intrafusal fiber innervation by human γ-motoneurons. *Sci. Rep.* **7**, 17202 (2017).

15. Sghirlanzoni, A., Pareyson, D. & Lauria, G. Sensory neuron diseases. *Lancet Neurol.* **4**, 349–361 (2005).

16. Orefice, L. L. *et al.* Peripheral mechanosensory neuron dysfunction underlies tactile and behavioral deficits in mouse models of ASDs. *Cell* **166**, 299–313 (2016).

17. Vaughan, S. K., Stanley, O. L. & Valdez, G. Impact of aging on proprioceptive sensory neurons and intrafusal muscle fibers in mice. *Journals Gerontol. Ser. A Biol. Sci. Med. Sci.* **72**, 771–779 (2016).

18. Van de Winckel, A. *et al.* Age-related decline of wrist position sense and its relationship to specific physical training. *Front. Hum. Neurosci.* **11**, 570 (2017).

19. Mentis, G. Z. *et al.* Early functional impairment of sensory-motor connectivity in a mouse model of spinal muscular atrophy. *Neuron* **69**, 453–467 (2011).

20. Gogliotti, R. G. *et al.* Motor neuron rescue in spinal muscular atrophy mice demonstrates that sensory-motor defects are a consequence, not a cause, of motor neuron dysfunction. *J. Neurosci.* **32**, 3818–3829 (2012).

21. Thirumalai, V. *et al.* Preservation of VGLUT1 synapses on ventral calbindin-immunoreactive interneurons and normal locomotor function in a mouse model of spinal muscular atrophy. *J. Neurophysiol.* **109**, 702–710 (2013).

22. Fletcher, E. V *et al.* Reduced sensory synaptic excitation impairs motor neuron function via Kv2.1 in spinal muscular atrophy. *Nat. Neurosci.* **20**, 905–916 (2017).

23. Vaughan, S. K., Kemp, Z., Hatzipetros, T., Vieira, F. & Valdez, G. Degeneration of proprioceptive sensory nerve endings in mice harboring amyotrophic lateral sclerosis-causing mutations. *J. Comp. Neurol.* **523**, 2477–2494 (2015).

24. Vaughan, S. K. *et al.* The ALS-inducing factors, TDP43A315T and SOD1G93A, directly affect and sensitize sensory neurons to stress. *Sci. Rep.* **8**, 16582 (2018).

25. Lalancette-Hebert, M., Sharma, A., Lyashchenko, A. K. & Shneider, N. A. Gamma motor neurons survive and exacerbate alpha motor neuron degeneration in ALS. *Proc. Natl. Acad. Sci.* **113**, E8316–E8325 (2016).

26. Seki, S. *et al.* Circuit-specific early impairment of proprioceptive sensory neurons in the SOD1 G93A mouse model for ALS. *J. Neurosci.* **39**, 8798–8815 (2019).

27. Sábado, J. *et al.* Accumulation of misfolded SOD1 in dorsal root ganglion degenerating proprioceptive sensory neurons of transgenic mice with amyotrophic lateral sclerosis. *Biomed Res. Int.* **2014**, 1–13 (2014).

28. Petrov, D., Mansfield, C., Moussy, A. & Hermine, O. ALS clinical trials review: 20 years of failure. Are we any closer to registering a new treatment? *Front. Aging Neurosci.* **9**, 68 (2017).

29. Hardiman, O. *et al.* Amyotrophic lateral sclerosis. *Nat. Rev. Dis. Prim.* **3**, 17071 (2017).

30. Van den Berg, L. H. Therapy of amyotrophic lateral sclerosis remains a challenge. *Lancet Neurol.* **13**, 1062–1063 (2014).

31. Brown, R. H. & Al-Chalabi, A. Amyotrophic lateral sclerosis. *N. Engl. J. Med.* **377**, 162–172 (2017).

32. Valko, K. & Ciesla, L. Amyotrophic lateral sclerosis. in *Progress in Medicinal Chemistry* vol. 58 63–117 (Elsevier B.V., 2019).

33. Mathis, S., Goizet, C., Soulages, A., Vallat, J.-M. & Masson, G. Le. Genetics of amyotrophic lateral sclerosis: A review. *J. Neurol. Sci.* **399**, 217–226 (2019).

34. ALSoD - Amyotrophic Lateral Sclerosis online Database. https://alsod.ac.uk/.

35. Wroe, R., Wai-Ling Butler, A., Andersen, P. M., Powell, J. F. & Al-Chalabi, A. ALSOD: The Amyotrophic Lateral Sclerosis Online Database. *Amyotroph. Lateral Scler.* **9**, 249–250 (2008).

36. Brenner, D. & Weishaupt, J. H. Update on amyotrophic lateral sclerosis genetics. *Curr. Opin. Neurol.* **32**, 735–739 (2019).

37. Broce, I. J. *et al.* Partitioning the genetic architecture of amyotrophic lateral sclerosis. *bioRxiv* 505693 (2019) doi:10.1101/505693.

38. Biogen exercises option with Ionis to develop and commercialize investigational treatment BIIB067 for a subtype of familial amyotrophic lateral sclerosis (ALS) based on positive phase 1 data - Biogen. Biogen. https://investors.biogen.com/news-releases/news-release-details/biogen-exercises-option-ionis-develop-and-commercialize (2018).

39. Hegedus, J., Putman, C. T., Tyreman, N. & Gordon, T. Preferential motor unit loss in the SOD1 G93A transgenic mouse model of amyotrophic lateral sclerosis. *J. Physiol.* **586**, 3337–3351 (2008).

40. Van Rheenen, W. *et al.* Genome-wide association analyses identify new risk variants and the genetic architecture of amyotrophic lateral sclerosis. *Nat. Genet.* **48**, 1043–1048 (2016).

41. Ferraiuolo, L. *et al.* Oligodendrocytes contribute to motor neuron death in ALS via SOD1-dependent mechanism. *Proc. Natl. Acad. Sci.* **113**, E6496–E6505 (2016).

42. Keller, E. L. & Robinson, D. A. Absence of a stretch reflex in extraocular

muscles of the monkey. *J. Neurophysiol.* **34**, 908–919 (1971).

43. Held, A. *et al.* Circuit dysfunction in SOD1-ALS model first detected in sensory feedback prior to motor neuron degeneration is alleviated by BMP signaling. *J. Neurosci.* **39**, 2347–2364 (2019).

44. Simon, N. G. *et al.* Segmental motoneuronal dysfunction is a feature of amyotrophic lateral sclerosis. *Clin. Neurophysiol.* **126**, 828–836 (2015).

45. Sangari, S. *et al.* Impairment of sensory-motor integration at spinal level in amyotrophic lateral sclerosis. *Clin. Neurophysiol.* **127**, 1968–1977 (2016).

46. Myszczynska, M. & Ferraiuolo, L. New in vitro models to study amyotrophic lateral sclerosis. *Brain Pathol.* **26**, 258–265 (2016).

47. Lutz, C. Mouse models of ALS: Past, present and future. *Brain Res.* **1693**, 1–10 (2018).

48. Selvaraj, S. & Perlingeiro, R. C. R. Induced pluripotent stem cells for neuromuscular diseases: potential for disease modeling, drug screening, and regenerative medicine. in *Reference Module in Biomedical Sciences* (eds. McQueen, C. A. et al.) 471–481 (Elsevier, 2018). doi:10.1016/B978-0-12-801238-3.65504-6.

49. Jha, B. S., Rao, M. & Malik, N. Motor neuron differentiation from pluripotent stem cells and other intermediate proliferative precursors that can be discriminated by lineage specific reporters. *Stem Cell Rev. Reports* **11**, 194–204 (2015).

50. Viventi, S. & Dottori, M. Modelling the dorsal root ganglia using human pluripotent stem cells: A platform to study peripheral neuropathies. *Int. J. Biochem. Cell Biol.* **100**, 61–68 (2018).

51. Guo, X., Spradling, S., Stancescu, M., Lambert, S. & Hickman, J. J. Derivation of sensory neurons and neural crest stem cells from human neural progenitor hNP1. *Biomaterials* **34**, 4418–4427 (2013).

52. Blanchard, J. W. *et al.* Selective conversion of fibroblasts into peripheral sensory neurons. *Nat. Neurosci.* **18**, 25–35 (2015).

53. Alshawaf, A. J. *et al.* Phenotypic and functional characterization of peripheral sensory neurons derived from human embryonic stem cells. *Sci. Rep.* **8**, 603 (2018).

54. Guimarães, M. Z. P. *et al.* Generation of iPSC-derived human peripheral sensory neurons releasing substance P elicited by TRPV1 agonists. *Front. Mol. Neurosci.* **11**, 277 (2018).

55. Lee, K. S. *et al.* Human sensory neurons derived from induced pluripotent stem cells support Varicella-Zoster virus infection. *PLoS One* **7**, e53010 (2012).

56. Boisvert, E. M. *et al.* The specification and maturation of nociceptive neurons from human embryonic stem cells. *Sci. Rep.* **5**, 16821 (2015).

57. Denham, M. *et al.* Multipotent caudal neural progenitors derived from human pluripotent stem cells that give rise to lineages of the central and peripheral nervous system. *Stem Cells* **33**, 1759–1770 (2015).

58. Hoelting, L. *et al.* Stem cell-derived immature human dorsal root ganglia neurons to identify peripheral neurotoxicants. *Stem Cells Transl. Med.* **5**, 476–487 (2016).

59. Guo, X. *et al.* Tissue engineering the mechanosensory circuit of the stretch reflex arc with human stem cells: Sensory neuron innervation of intrafusal muscle fibers. *Biomaterials* **122**, 179–187 (2017).

60. Umehara, Y. *et al.* Robust induction of neural crest cells to derive peripheral sensory neurons from human induced pluripotent stem cells. *Sci. Rep.* **10**, 4360 (2020).

61. Butler, S. J. & Bronner, M. E. From classical to current: Analyzing peripheral nervous system and spinal cord lineage and fate. *Dev. Biol.* **398**, 135–146 (2015).

62. Menendez, L. *et al.* Directed differentiation of human pluripotent cells to neural crest stem cells. *Nat. Protoc.* **8**, 203–212 (2013).

63. Gingras, M., Beaulieu, M. M., Gagnon, V., Durham, H. D. & Berthod, F. In vitro study of axonal migration and myelination of motor neurons in a three-dimensional tissue-engineered model. *Glia* **56**, 354–364 (2008).

64. Taylor, M. D., Holdeman, A. S., Weltmer, S. G., Ryals, J. M. & Wright, D. E. Modulation of muscle spindle innervation by neurotrophin-3 following nerve injury. *Exp. Neurol.* **191**, 211–222 (2005).

65. Kalpachidou, T., Spiecker, L., Kress, M. & Quarta, S. Rho GTPases in the physiology and pathophysiology of peripheral sensory neurons. *Cells* **8**, 591 (2019).

66. Wu, B., Crampton, S. P. & Hughes, C. C. W. Wnt signaling induces matrix metalloproteinase expression and regulates T cell transmigration. *Immunity* **26**, 227–239 (2007).

67. Esfandiari, F. *et al.* Glycogen synthase kinase-3 inhibition promotes proliferation and neuronal differentiation of human-induced pluripotent stem cell-derived neural progenitors. *Stem Cells Dev.* **21**, 3233–3243 (2012).

68. Gizak, A., Duda, P., Pielka, E., McCubrey, J. A. & Rakus, D. GSK3 and miRNA in neural tissue: From brain development to neurodegenerative diseases. *Biochim. Biophys. Acta - Mol. Cell Res.* **1867**, 118696 (2020).

69. Mishra, H. K. *et al.* GSK3ß-dependent dysregulation of neurodevelopment in SPG11-patient induced pluripotent stem cell model. *Ann. Neurol.* **79**,

826–840 (2016).

70. Li, C. L. *et al.* Somatosensory neuron types identified by high-coverage single-cell RNA-sequencing and functional heterogeneity. *Cell Res.* **26**, 83–102 (2016).

71. Usoskin, D. *et al.* Unbiased classification of sensory neuron types by large-scale single-cell RNA sequencing. *Nat. Neurosci.* **18**, 145–153 (2015).

72. Weizmann Institute of Science. GeneCards - The human gene database. https://www.genecards.org/ (2020).

73. Johns Hopkins University. OMIM - Online Mendelian Inheritance in Man. An online catalog of human genes and genetic disorders. https://omim.org/ (2020).

74. Menendez, L., Yatskievych, T. A., Antin, P. B. & Dalton, S. Wnt signaling and a Smad pathway blockade direct the differentiation of human pluripotent stem cells to multipotent neural crest cells. *Proc. Natl. Acad. Sci.* **108**, 19240–19245 (2011).

75. Shao, Q., Yang, T., Huang, H., Alarmanazi, F. & Liu, G. Uncoupling of UNC5C with polymerized TUBB3 in microtubules mediates Netrin-1 repulsion. *J. Neurosci.* **37**, 5620–5633 (2017).

76. Oberstadt, M., Claßen, J., Arendt, T. & Holzer, M. TDP-43 and cytoskeletal proteins in ALS. *Mol. Neurobiol.* **55**, 3143–3151 (2018).

77. Greenwood, A. L., Turner, E. E. & Anderson, D. J. Identification of dividing, determined sensory neuron precursors in the mammalian neural crest. *Development* **126**, 3545–3559 (1999).

78. Klein, R. *et al.* Disruption of the neurotrophin-3 receptor gene trkC eliminates la muscle afferents and results in abnormal movements. *Nature* **368**, 249–251 (1994).

79. Imai, F. & Yoshida, Y. Molecular mechanisms underlying monosynaptic sensory-motor circuit development in the spinal cord. *Dev. Dyn.* **247**, 581–587 (2018).

80. Appel, E. *et al.* An ensemble of regulatory elements controls Runx3 spatiotemporal expression in subsets of dorsal root ganglia proprioceptive neurons. *Genes Dev.* **30**, 2607–2622 (2016).

81. O'Toole, S. M. *et al.* Dicer maintains the identity and function of proprioceptive sensory neurons. *J. Neurophysiol.* **117**, 1057–1069 (2017).

82. Arber, S., Ladle, D. R., Lin, J. H., Frank, E. & Jessell, T. M. ETS gene Er81 controls the formation of functional connections between group Ia sensory afferents and motor neurons. *Cell* **101**, 485–498 (2000).

83. De Nooij, J. C., Doobar, S. & Jessell, T. M. Etv1 inactivation reveals proprioceptor subclasses that reflect the level of NT3 expression in muscle

targets. *Neuron* **77**, 1055–1068 (2013).

84. Uaesoontrachoon, K. *et al.* Osteopontin and skeletal muscle myoblasts: Association with muscle regeneration and regulation of myoblast function in vitro. *Int. J. Biochem. Cell Biol.* **40**, 2303–2314 (2008).

85. Wu, S. X. *et al.* Vesicular glutamate transporter immunoreactivity in the central and peripheral endings of muscle-spindle afferents. *Brain Res.* **1011**, 247–251 (2004).

86. Honda, C. N. Differential distribution of calbindin-D28k and parvalbumin in somatic and visceral sensory neurons. *Neuroscience* **68**, 883–892 (1995).

87. Kim, S. *et al.* Myelin degeneration induced by mutant superoxide dismutase 1 accumulation promotes amyotrophic lateral sclerosis. *Glia* **67**, 1910–1921 (2019).

88. Kang, S. H. *et al.* Degeneration and impaired regeneration of gray matter oligodendrocytes in amyotrophic lateral sclerosis. *Nat. Neurosci.* **16**, 571–579 (2013).

89. Philips, T. *et al.* Oligodendrocyte dysfunction in the pathogenesis of amyotrophic lateral sclerosis. *Brain* **136**, 471–482 (2013).

90. Trias, E. *et al.* Schwann cells orchestrate peripheral nerve inflammation through the expression of CSF1, IL-34, and SCF in amyotrophic lateral sclerosis. *Glia* **68**, 1165–1181 (2020).

91. Arbour, D., Vande Velde, C. & Robitaille, R. New perspectives on amyotrophic lateral sclerosis: the role of glial cells at the neuromuscular junction. *J. Physiol.* **595**, 647–661 (2017).

92. Keller, A. F., Gravel, M. & Kriz, J. Live imaging of amyotrophic lateral sclerosis pathogenesis: Disease onset is characterized by marked induction of GFAP in Schwann cells. *Glia* **57**, 1130–1142 (2009).

93. Poloni, M. *et al.* Circulating levels of tumour necrosis factor-α and its soluble receptors are increased in the blood of patients with amyotrophic lateral sclerosis. *Neurosci. Lett.* **287**, 211–214 (2000).

94. Rueden, C. T. *et al.* ImageJ2: ImageJ for the next generation of scientific image data. *BMC Bioinformatics* **18**, 529 (2017).

95. Osaki, T., Uzel, S. G. M. & Kamm, R. D. On-chip 3D neuromuscular model for drug screening and precision medicine in neuromuscular disease. *Nat. Protoc.* **15**, 421–449 (2020).

96. Cell Imaging Core & Turku Centre for Biotechnology. Flowing Software. http://flowingsoftware.btk.fi/ (2013).

97. The Massachusetts General Hospital. PrimerBank - PCR primers for gene expression detection and quantification.

https://pga.mgh.harvard.edu/primerbank/index.html (2006).

98. Livak, K. J. & Schmittgen, T. D. Analysis of Relative Gene Expression Data Using Real-Time Quantitative PCR and the 2−ΔΔCT Method. *Methods* **25**, 402–408 (2001).

99. Wong, M. L. & Medrano, J. F. Real-time PCR for mRNA quantitation. *Biotechniques* **39**, 75–85 (2005).

100. Darabid, H., Perez-Gonzalez, A. P. & Robitaille, R. Neuromuscular synaptogenesis: coordinating partners with multiple functions. *Nat. Rev. Neurosci.* **15**, 703–718 (2014).

101. Legay, C. & Mei, L. Moving forward with the neuromuscular junction. *J. Neurochem.* **142**, 59–63 (2017).

102. Kanehisa Laboratories. KEGG (Kyoto Encyclopedia of Genes and Genomes) pathway: amyotrophic lateral sclerosis (ALS) - Homo sapiens (human). https://www.kegg.jp/kegg-bin/show_pathway?hsa05014+7133 (2019).

Chapter 4

Human neuromuscular circuit on a chip

Summary

This chapter is focused on the development of a physiological human neuromuscular circuit on a microfluidic device, integrating motor and sensory pathways in a 3D culture. To that end, human neural stem cells (hNSC) were differentiated to sensory neurons (SN) and motoneurons (MN), and they were cultured with human skeletal myocytes (hSkMc) in the Xona commercial microfluidic devices in 2D, and in the developed MINDS devices in 3D (compartmentalised devices suitable for the culture of three cell types interconnected in series).

The compartmentalised coculture of SN and hSkMc performed shows for the first time the formation of synaptic bouton like structures in the contact points of TrkC+ neurons wrapping around skeletal muscle fibres, in structures similar to annulospiral wrapping. The compartmentalised coculture of SN, hSkMc and MN performed is the first time reported until now in which SN have been seeded together with hSkMc and MN, in 3D, in a microfluidic device, using human cells.

This chapter shows the first steps towards a future 3D physiological spinal neuromuscular circuit on a chip for neuromuscular diseases studies.

Contributions and acknowledgements

This work was achieved during my stay of 5.5 months at Massachusetts Institute of Technology (MIT) funded by Severo Ochoa Triple-I program for predoctoral researchers from IBEC and MISTI Global Seed Funds from La Caixa foundation and MISTI (MIT international science and technology initiatives). I performed the experiments in collaboration with some members from the Mechanobiology lab, at MIT: Dr. Tatsuya Osaki, who supported me, taught me some of the cellular biology techniques employed, and collaborated in performing with me some of the experiments; and Prof. Roger Kamm, who supported me during my stay at MIT. The utilisation of MINDS devices was only possible due to the collaboration with PhD student Roberto Paoli and senior postdoc researcher Dr. Maria José López, from Nanobioengineering group at IBEC, who collaborated in the design, and utilisation protocol of the devices. 3D printed masters for MINDS device were fabricated by PhD student Roberto Paoli, as part of his thesis "Cell culture interfaces for different organ-on-chip applications: from photolithography to rapid-prototyping techniques with sensor embedding".[1]

The work presented in this chapter is in preparation for a publication.

4.1. Introduction: sensory neuromuscular studies *in vitro*

The neuromuscular motor pathway has been thoroughly studied for years,[2] but when looking at the sensory afferent pathway, it is remarkable the small literature of experiments performing *in vitro* coculture of sensory neurons with skeletal muscle cells.[3–6] Most of the publications utilise mouse or rat tissue preparations as sample of study. Although they do not accurately mimic human conditions, they have helped elucidating the role of several molecules on the proprioception and the spindle: the expression of low affinity epithelial sodium channel (ENaCs) and acid-sensing ion channel (ASIC2) in sensory afferent terminals;[7] the need of ETS transcription factor Etv1 for pSN survival and differentiation;[8] the role of PlexinD1 and Sema3E on monosynaptic sensory-motor connectivity specificity;[9] the expression of Whirlin PDZ-scaffold protein in pSN sensory endings and its role facilitating sensory firing;[10] the expression of Piezo2 (a mechanically activated non-selective cation channel) in sensory ending of pSN connecting muscle spindle and Golgi tendon organ;[11] the different regulation of Runx3 in each subtype of TrkC+ neurons;[12] the role of ASIC3 in dynamic mechanosensitivity in pSN;[13] the function of Dicer in the survival of pSN;[14] and the existing genetic correlation between proprioceptors and the muscle-type innervated by each pSN.[15] Furthermore animal studies have served to study the ultrastructure of γ-MN connecting

muscle spindle;[16] to collect data of electrical recordings of sensory afferents in response to stretch;[17] to determine the role of proprioceptive input in determining the rhythmic discharge of respiratory pacemakers;[18] and to perform a quantitative analysis of proprioceptive receptors, proprioceptive afferents, and observe their morphology and diameter.[19] They have even provided invaluable information about proprioception in aging,[20,21] and some neuromuscular diseases (NMD): Friedreich's ataxia,[22] spinal muscular atrophy,[23–26] and amyotrophic lateral sclerosis (as described in *Chapter 3*).[27–31]

Nevertheless, the benefit offered by rodent models is limited as they do not carry human genetic background. *In vitro* cultures enable a more human research and they can be adapted to human conditions by means of iPSCs. Though, culturing *in vitro* isolated pSN with skeletal muscle (SkM) cells seems quite a challenge and using human stem cells even higher challenge. As described in the previous chapter, the protocol for differentiating pSN is not quite clear yet, and only recently there has been published an intrafusal and extrafusal muscle fibres differentiation protocol.[32] The few studies coculturing sensory neurons with skeletal muscle cells *in vitro* published during the last decade are summarised in TABLE 4-1. They all perform 2D cell culture of a healthy sensory afferent circuit and, only Guo *et al.* use human cells. So far, there are no publications of the proprioceptive pathway *in vitro* performing 3D cell culture,

integrating it with the motor pathway, or culturing cells into microfluidic compartmentalised devices.

Table 4-1. *Summary of the publications studying the sensory afferent pathway in vitro in the last decade. The cells utilised and highlighted results are described for each publication reference.*

Sample of study	Highlights	Ref.
Rat primary sensory neurons cocultured with rat primary myocytes	Immunofluorescence analysis revealed the presence of annulospiral wrapping (ASW) and flower spray ending (FSE), together with the expression in sensory terminals of the stretch sensitive sodium channel BNaC1 and the membrane support protein PICK1. Calcium currents imaging after stretching an intrafusal muscle fibre through microelectromechanical systems, cantilever deflection, detected the presence of physiologically relevant sensory endings.	Rumsey *et al.*, 2010[3]
Rat dissociated DRG cells cocultured with rat primary skeletal muscle cells	Observation through immunofluorescence, phase contrast imaging and scanning electron microscopy (SEM) of the interrelation and contacts formed between sensory neurons and skeletal muscle cells.	Liu *et al.*, 2011[4]
Human neural progenitors derived sensory neurons cocultured with human skeletal muscle stem cells derived intrafusal fibres	They observed bag and chain intrafusal fibre morphologies through phase contrast imaging and FSE and ASW morphologies through immunofluorescence imaging. Patch-clamp electrophysiological recordings suggest that human intrafusal muscle fibres have a repetitive firing rate, in contrast to human extrafusal fibres.	Guo *et al.*, 2017[5]
Rat DRG explants cocultured with skeletal muscle cells dissociated from rat limb	NRG-1β treatment promoted neuronal migration from the DRG explants and neurite outgrowth. This modulation, correlated with GAP-43 expression, could be linked to intrafusal muscle fibre formation.	Qiao *et al.*, 2018[6]

4.2. Specific objectives of the chapter

The aim of this chapter was to integrate the knowledge acquired in *Chapters 2 and 3*, and stablish the basis to create a human neuromuscular circuit on a microfluidic device in 3D culture. For that purpose, the specific objectives of the chapter were:

- To differentiate neural stem cells to motoneurons and proprioceptive sensory neurons independently and assess their morphological differences.
- To differentiate human skeletal myoblast to myocytes.
- To perform compartmentalised coculture of proprioceptive sensory neurons and skeletal muscle in 2D, adapting commercial Xona microfluidic devices.
- To design and fabricate a compartmentalised device suitable for the 3D culture of motoneurons, skeletal myocytes and sensory neurons embedded in a hydrogel.
- To perform compartmentalised coculture of proprioceptive sensory neurons, skeletal muscle and motoneurons in 3D, embedding cells in Matrigel and seeding them in MINDS devices.

4.3. Materials and methods

4.3.1. Facilities

All experiments were performed at Mechanobiology lab (Biological Engineering department, Massachusetts Institute of Technology, Cambridge, U.S.) in a collaboration with Nanobioengineering lab (Institute of Bioengineering of Catalonia, Barcelona, Spain). Some of the microfluidic devices utilised ("MINDS" devices) were previously fabricated in the Nanobioengineering lab (Institute of Bioengineering of Catalonia, Barcelona, Spain). Confocal microscopy imaging and flow cytometry was performed at the Koch Institute for Integrative Cancer Research (Massachusetts Institute of Technology, Cambridge, U.S.).

4.3.2. Experimental design

The experiments presented in this chapter stablish the basis for a 2D and 3D human neuromuscular complete circuit on microfluidic devices employing motoneurons, proprioceptive sensory neurons and skeletal myocytes. The timepoints (TP) for each protocol were established according to the experimental requirements of proprioceptive sensory neuron differentiation timeline, previously stablished in *Chapter 3*. A diagram of the timepoints and a summary of the steps can be seen in FIGURE 4-1.

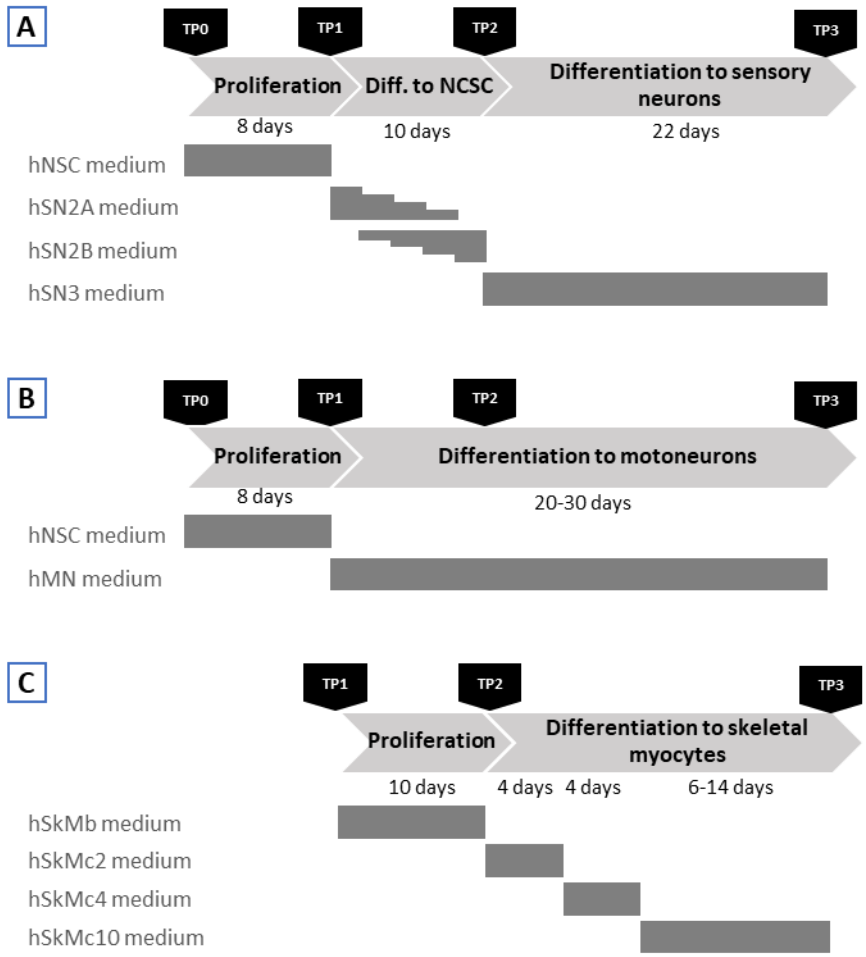

Figure 4-1. *Diagram of the events, media utilised and timepoints (TP) for each cell type utilised in this chapter.* ***A)*** *Proliferation of human neural stem cells and differentiation to neural crest stem cells first and later to sensory neurons, using four different media compositions.* ***B)*** *Proliferation of human neural stem cells and differentiation to motoneurons using two media compositions.* ***C)*** *Proliferation of human skeletal myoblasts and differentiation to skeletal myocytes using four different media compositions.*

Human neural stem cells (hNSC) were maintained in proliferation until TP0, when cells were transferred to the desired platform (coated plates for 2D culture or spheroid forming plates). hNSC proliferate until TP1, when the differentiation towards motoneurons (MN) or sensory neurons (SN) begins. For coculture purposes, TP1 is also the timepoint to start proliferating skeletal muscle (SkM) cells in the microdevice. MN and SN spheroids were transferred to compartmentalised microdevices for 2D or 3D coculture purposes at TP2, and they were maintained in coculture until TP3.

The cell culture protocol for MN had been previously described,[33] and for SkM cells it was adapted from previous publications.[34–36] The proprioceptive sensory neuron differentiation protocol was taken from the ones developed in *Chapter 3*. Then the compartmentalised cocultures were performed in microdevices in 2D and in 3D utilising two of the selected protocols.

4.3.3. Maintenance of neural stem cells and formation of neurospheroids

Matrigel-coated petri dishes were first prepared by making 1:30 dilution of Matrigel® hESC-Qualified Matrix (Corning, #354277) into Knockout™ DMEM/F-12 medium (Gibco, #12660012), and incubating for 1 h at room temperature. Then healthy hNSC H9-derived (Gibco, #N7800100) were seeded and incubated

proliferating until reaching confluency. At TP0, once cells had proliferated enough, cells were washed with DPBS (Lonza, #17-512F), detached with TrypLE™ express enzyme (Gibco, #12604021), counted and seeded in ultra-low attachment PrimeSurface® 3D culture spheroid plates (S-Bio, #MS-9096MZ) to form neurospheroids. Three different seeding densities were assessed ($\rho_1 = 3.000\ cell \cdot spheroid^{-1}$; $\rho_2 = 4.500\ cell \cdot spheroid^{-1}$; $\rho_3 = 6.000\ cell \cdot spheroid^{-1}$).

During the proliferation in Matrigel-coated surfaces or as spheroids, hNSC were maintained in a CO_2 incubator at 37 °C and 95% humidity with *hNSC medium* (proliferation medium, see composition in CHAPTER 3, TABLE 3-2) changing every day after. Then hNSC followed the required differentiation protocol (to motoneurons or proprioceptive sensory neurons).

4.3.4. Differentiation of hNSC

4.3.4.1. Differentiation of hNSC to proprioceptive sensory neurons

The differentiation of proprioceptive sensory neurons (pSN), stablished in the previous chapter, started from the creation of hNSC spheroids at TP0, following the previously explained protocol (see SECTION 4.3.3). A diagram of this procedure summarised can be seen in FIGURE 4-1-A. For the following experiments, *SN*

differentiation protocol A and C (see CHAPTER 3, SECTION 3.3.4) were utilised.

4.3.4.2. Differentiation of hNSC to motoneurons

This section explains the motoneuron (MN) differentiation procedure starting from the creation of hNSC spheroids at TP0, following the previously explained protocol (see SECTION 4.3.3). A diagram of this procedure summarised can be seen in FIGURE 4-1-B and utilised media can be seen in TABLE 4-2.

Table 4-2. *Composition of the medium utilised to differentiate human neural stem cells into motoneurons.*
hNSC = human neural stem cell; hESC = human embryonic stem cell; BSA = bovine serum albumin; Shh = Sonic Hedgehog; E.coli = Escherichia coli; FGF = fibroblast growth factor; BDNF = brain-derived neurotrophic factor; GDNF = glial cell line-derived neurotrophic factor.

Medium	Components and final concentration	Commercial reference
hMN medium	DMEM/F-12, GlutaMAX™ supplement	(Gibco, #10565-018)
	1X final concentration of StemPro® hESC Supplement	(Gibco, #A10006-01)
	2% BSA	(Gibco, #A10008-01)
	$200\ ng \cdot ml^{-1}$ of recombinant human Shh	(Peprotech, #100-45)
	$50\ \mu M$ of retinoic acid	(Sigma-Aldrich, #R2625)
	$10\ ng \cdot ml^{-1}$ of recombinant human, murine, rat Activin A (*E.coli* derived)	(Peprotech, #120-14E)
	$8\ ng \cdot ml^{-1}$ of recombinant human FGF basic (154 aminoacids)	(Peprotech, #100-18B)
	$10\ ng \cdot ml^{-1}$ of human recombinant BDNF, animal component free	(StemCell Technologies, #78133)
	$10\ ng \cdot ml^{-1}$ of recombinant human GDNF	(R&D Systems, #212-GD-010)

The MN differentiation protocol was taken from a previous publication.[33,35] Briefly, hNSC spheroids were generated at TP0 as indicated in SECTION 4.3.3. The spheroids were maintained in a CO_2

incubator at 37 °C and 95% humidity with *hNSC medium*, changing it every day after. At TP1, the medium was replaced with *hMN medium* (see composition in TABLE 4-2) to induce motoneuron differentiation and maturation. This medium was maintained until the endpoint of the experiment at TP3 (i.e. 30 days for comparison with SN), changing it every day after.

4.3.5. Characterisation of differentiated hNSC and comparison between SN and MN spheroids

Several morphological features of spheroids undergoing *MN differentiation protocol* and *SN differentiation protocol A* were assessed and compared with each other.

4.3.5.1. Bright field imaging of floating spheroids

MN and SN spheroids of same cell densities ($\rho_1 = 3.000\ cell \cdot spheroid^{-1}$; $\rho_2 = 4.500\ cell \cdot spheroid^{-1}$; $\rho_3 = 6.000\ cell \cdot spheroid^{-1}$) following *MN differentiation protocol* or *SN differentiation protocol A* were analysed. The spheroids diameter was monitored through bright field imaging until TP3 using an inverted microscope for transmitted light (Zeiss, #Axiovert-200). The maximum transversal area of spheroids was quantified with ImageJ software.[37] Mean and standard deviation of obtained result was quantified for n = 3 samples. Results obtained for MN and SN spheroids were compared.

4.3.5.2. Imaging of plated spheroids

Several parameters of spheroid morphology following *SN differentiation protocol A* and *MN differentiation protocol* were assessed in plated spheroids through bright field (BF) imaging: core and corona area increment, migration and neural projection diameter. Spheroids were also characterised through immunostaining and confocal imaging.

Cell culture and BF image collection

hNSC spheroids of an initial cell density of $6.000\ cell \cdot\ spheroid^{-1}$ were cultured, inducing their differentiation to SN or MN from TP1 and transferring them to Matrigel coated plates at TP2. To perform the plating, after aspirating the Matrigel solution, two SN or MN spheroids with up to 300 µL of the required medium were placed in the middle of each coated well, handling them with wide orifice tips (VWR, #736-0205). Samples were incubated for approximately 4 h to let spheroids adhere to the bottom of the plate. Then additional 200 µL of medium were gently added. Spheroids were maintained in a CO_2 incubator at 37 °C and the medium was changed every day after until TP3. Bright field images were taken every 3-4 days, at the same timepoints for MN and SN spheroids, using an inverted microscope (Zeiss, #Axiovert-200). Images were quantified from 15 days after differentiation (ddiff) using ImageJ software.[37]

BF image quantification

The increment percentage of the core area (considered as the area occupied by the central circular shape of the neurospheroid) and the corona area (considered as the area occupied by the surrounding glia cells and neural projections) were quantified for every spheroid at each timepoint (TP_x) normalised against the area at 15 ddiff, as shown in the following equation. Average (n = 2) and standard error for each core area measurement were calculated and plotted on a graph.

$$\%\ Area\ increment = \frac{area\ at\ TP_x}{area\ at\ 15\ ddiff} \cdot 100 \qquad (4\text{-}1)$$

The spheroid approximation percentage (considered as the inter-spheroid distance shortening) was calculated measuring the distance between the centre of spheroid cores at each timepoint (TP_x) and normalising it against the initial measured distance at 15 ddiff as shown in the following equation.

$$\%\ Approximation = 100 - \left(\frac{interspheroid\ distance\ at\ TP_x}{interspheroid\ distance\ at\ 15\ ddiff.} \cdot 100\right) \qquad (4\text{-}2)$$

Finally, the diameter of neural projections in the area next to the core was measured. Average (n = 5) and standard deviation were calculated and plotted on a graph.

Immunostaining

Plated spheroids were maintained in culture until TP3, when samples were fixed incubating them with a 4% paraformaldehyde solution for 30 min at room temperature. Then samples were

washed three times with DPBS and stored at 4 °C until the immunostaining was performed.

Spheroids were first washed with DPBS and permeabilised incubating with DPBS 0.1% triton for 10 min. Then samples were incubated with a blocking solution containing 1% bovine serum albumin (BSA, Sigma, #A9657) in DPBS for 2 h. Spheroids were then washed three times with DPBS, incubating 10 min per wash, and incubated with the primary antibody solution overnight at 4 °C. For MN spheroids, the primary antibody solution was: 0.1% triton, 1% BSA, 0.01% sodium azide, 1:200 dilution of rabbit anti-ChAT antibody, also known as anti-choline acetyltransferase antibody (Abcam, #ab78078), and 1:500 dilution of mouse anti-TUJ1 antibody (Abcam, #ab78078) in DPBS. For SN spheroids, the primary antibody solution utilised consisted in: 0.1% triton, 1% BSA, 0.01% sodium azide, 1:500 dilution of mouse anti-TUJ1 antibody (Abcam, #ab78078), 1:100 dilution of rabbit anti-Pou4f1 (Invitrogen, #PA5-41509) and $1\ \mu g \cdot mL^{-1}$ of goat anti-TrkC antibody (R&D Systems, #AF373) in DPBS.

After the incubation with the primary antibody solution overnight samples were washed three times with DPBS, incubating 10 min per wash. Then spheroids were incubated with the secondary antibody and from this moment, samples were kept protected from light throughout the whole process. For that purpose, MN spheroids were incubated for 2 h at room temperature with a solution

containing: 0.1% triton, 1% BSA, 0.01% sodium azide, 1:500 dilution of goat anti-rabbit Alexa Fluor 488 (Invitrogen, #A-11034), and 1:500 dilution of goat anti-mouse Alexa Fluor 647 (Invitrogen, #A-21235) in DPBS. In the case of SN spheroids, the incubation with the secondary antibody was performed in two steps. SN spheroids were first incubated for 2 h protected from light with the secondary antibody solution-1 containing 0.1% triton, 1% BSA, 0.01% sodium azide, 1:500 dilution of donkey anti-goat Alexa Fluor 633 (Invitrogen, #A21082). Then the solution was removed, and samples were washed with DPBS three times, 10 min per incubation. SN spheroids were incubated afterwards for 2 h with a secondary antibody solution-2 containing: 0.1% triton, 1% BSA, 0.01% sodium azide, 1:500 dilution of goat anti-mouse Alexa Fluor 488 (Invitrogen, #A11029), and 1:500 dilution of donkey anti-rabbit Alexa Fluor 555 (Invitrogen, #A21428) in DPBS.

After the incubation with the secondary antibody was finished, samples were washed with DPBS three times, 10 min per incubation. Then samples were incubated for 10 min with 14.3µM of DAPI (4',6-Diamidino-2-Phenylindole dihydrochloride, Invitrogen™, #D1306) in DPBS, washed with DPBS three times, 10 min per incubation, and mounted with Olympus scaleview solution (Olympus, #ScalView-A2 optics). Samples were imaged with a confocal laser scanning microscope (Olympus, #FV1200) and images were processed afterwards with ImageJ software.[37]

4.3.6. Differentiation of skeletal myoblasts to myocytes

4.3.6.1. Cell culture procedures

Healthy iCell® skeletal myoblasts (Cellular Dynamics International - Fujifilm, U.S.) were seeded onto Matrigel-coated surfaces. Human skeletal myoblasts (hSkMb) were maintained in a CO_2 incubator at 37 °C and 95% humidity with *hSkMb medium* (proliferation medium, see composition in TABLE 4-3) changing it every day after. Cells were kept proliferating for 6-10 days before reaching subconfluency. At that point they either started *SkM differentiation protocol* or were subcultured.

To perform a passage cells were washed with sterile DPBS (Lonza, #17-512F), detached with TrypLE™ express enzyme (Gibco, #12604021), counted with a haemocytometer and seeded in the desired density into a Matrigel coated surface or frozen in Stem-Cellbanker® solution (AMSbio, #11890).

The *SkM differentiation protocol* was adapted from a previous publication.[34–36] A diagram of this procedure summarised can be seen in FIGURE 4-1-C. Briefly, to induce differentiation to human skeletal myocytes (hSkMc), once hSkMb had reached subconfluency, cells were incubated with *hSkMc2 medium* for 4 days *in vitro* (DIV), then with *hSkMc4 medium* for 4 DIV, and finally with *hSkMc10 medium* up to the endpoint of the experiment at TP3, changing the medium every day after. In this way, the serum

percentage in the medium was progressively increased as indicated in the composition of each media in TABLE 4-3.

Table 4-3. *Composition of the media utilised to maintain and differentiate human skeletal myoblasts into myocytes.*
hSkMb = human skeletal myoblasts; hSkMc = human skeletal myocytes; hEGF = human epidermal growth factor; FBS = foetal bovine serum; IGF-I = insulin like growth factor type I.

Medium	Components and final concentration	Commercial reference
hSkMb proliferation medium	SKBM™-2 Skeletal Muscle Cell Growth Basal Medium-2	(Lonza, #CC-3246)
	hEGF	(Lonza, #CC-3244)
	Dexamethasone	(Lonza, #CC-3244)
	L-glutamine	(Lonza, #CC-3244)
	FBS	(Lonza, #CC-3244)
	Gentamicin / Amphotericin-B	(Lonza, #CC-3244)
hSkMc2 differentiation medium	DMEM, high glucose, pyruvate	(Gibco, #11995-065)
	2% horse serum	(Gibco, #16050130)
	1% penicillin streptomycin	(Gibco, #15140122)
	$10\ ng \cdot ml^{-1}$ hEGF	(Gibco, #PHG0311)
	$50\ ng \cdot ml^{-1}$ LONG® R3 IGF-I human	(Sigma Aldrich, #I1271)
hSkMc4 differentiation medium	DMEM, high glucose, pyruvate	(Gibco, #11995-065)
	4% horse serum	(Gibco, #16050130)
	1% penicillin streptomycin	(Gibco, #15140122)
	$10\ ng \cdot ml^{-1}$ hEGF	(Gibco, #PHG0311)
	$50\ ng \cdot ml^{-1}$ LONG® R3 IGF-I human	(Sigma Aldrich, #I1271)
hSkMc10 differentiation medium	DMEM, high glucose, pyruvate	(Gibco, #11995-065)
	4% horse serum	(Gibco, #16050130)
	1% penicillin streptomycin	(Gibco, #15140122)
	$10\ ng \cdot ml^{-1}$ hEGF	(Gibco, #PHG0311)
	$50\ ng \cdot ml^{-1}$ LONG® R3 IGF-I human	(Sigma Aldrich, #I1271)

4.3.6.2. *Characterisation of differentiated myocytes*

Bright field images were taken at different timepoints to monitor the proliferation and differentiation. For a later imaging, at TP3 cells were fixed in 4% paraformaldehyde and stained following the immunostaining procedure described for MN spheroids in SECTION 4.3.5.2, varying in this case the composition of the incubating solutions: **i)** primary antibody solution: 0.1% triton, 1% BSA, 0.01% sodium azide, 1:100 dilution of rabbit anti-MHC antibody, also known as anti-slow skeletal myosin heavy chain antibody (Abcam, #ab173366), and 1:200 dilution of mouse anti-sarcomeric α-actinin antibody (Abcam, #ab9465) in DPBS; **ii)** secondary antibody solution: 0.1% triton, 1% BSA, 0.01% sodium azide, 1:500 dilution of goat anti-mouse Alexa Fluor 488 (Invitrogen, #A-11029), and 1:500 dilution of goat anti-rabbit Alexa Fluor 555 (Invitrogen, #A-21428) in DPBS; and **iii)** 14.3µM of DAPI in DPBS. Samples were prepared for confocal laser scanning microscopy imaging using Olympus scaleview solution.

4.3.7. Compartmentalised coculture

The compartmentalised coculture was performed in Xona microfluidic culture devices and MINDS devices as summarised in FIGURE 4-2.

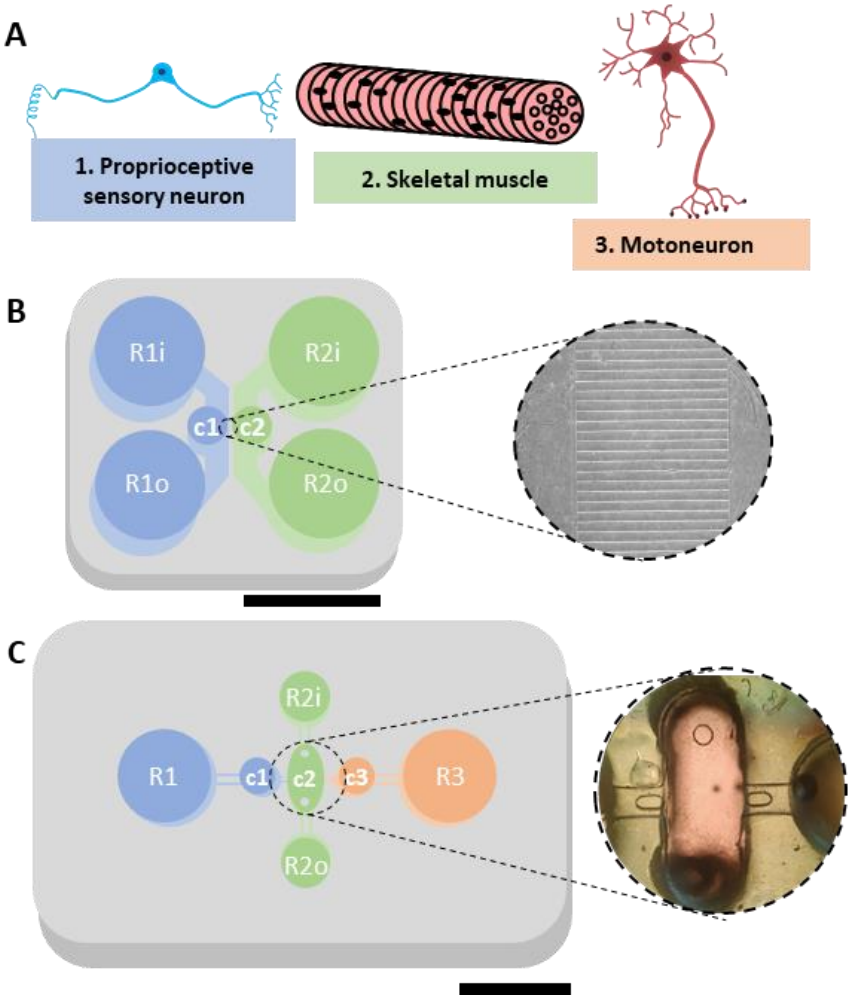

Figure 4-2. *Layout of the compartmentalised devices and cells utilised.* ***A)*** *Graphical summary of the cells utilised.* ***B)*** *Xona microfluidcs SND900 device with a perforation in the left side (c1) for direct seeding of the SN spheroid and a perforation in the right side (c2) for the seeding of SkM; inlet and outlet reservoirs with medium for SN (R1i, R1o) and inlet and outlet reservoirs with medium for hSkM (R2i, R2o). Augmented bright field image of the intersection formed by microchannels.* ***C)*** *MINDS device layout: SN are seeded on the left (c1) supplied by medium in the reservoir (R1), SkM in the middle area containing two posts (c2) supplied by medium in two reservoirs (R2i, R2o) and MN on the right (c3) supplied by medium in the reservoir (R3). Augmented bright field image of the middle compartment (c2) and its connection through fluid retention posts to the side compartments. Scale bars are 1 cm.*

4.3.7.1. 2D culture in Xona microfluidic devices

Preparation of Xona microfluidic devices

For the compartmentalised coculture in 2D, Xona microfluidics commercial devices with microchannels of 900 µm (length), 10 µm (width), 5 µm (height) and spaced apart 50 µm (Xonamicrofluidics, #SND900, U.S.) were utilised.

To prepare the devices, first of all, a 2 mm perforation was made in the SN seeding side with a punch (Miltex Instruments, #33-31, U.S.), and a 3 mm perforation in the SkM seeding side with another punch (Miltex Instruments, #33-32, U.S.), as shown in FIGURE 4-2-B for chambers c1 and c2 respectively. Then, the glasses (Fisher scientific, #12-542-C, U.S.) and the Xona polydimethylsiloxane (PDMS) devices were cleaned sonicating in 100% ethanol for 15 min, drying with nitrogen gas stream and dehydrating in a drying oven at 60 °C for at least 30 min (Binder, #FD-23). Finally, glasses were permanently bonded to the PDMS pieces exposing both to 1 min under high frequency oxygen plasma (Harrick plasma, #PDC-001) at 700 mTorr, then putting both pieces together and sealing them with at least 30 min dehydration in the oven at 60 °C. At this point, devices could be stored for the beginning of the experiment.

Device assembly and cell culture in Xona devices

To perform the cell culture of SN spheroids following *differentiation protocol A* with hSkMc, previously prepared devices were activated, sterilised, and coated before seeding cells in them. First the glass

and PDMS surfaces were activated applying 5 min of medium frequency oxygen plasma, adding right after sterile de-ionised water. At this point devices were transferred to the hood, where they were sterilised through 15 min of UV radiation, and rinsed with sterile water.

After aspirating all the water, the coating was performed from the inlet and outlet reservoirs (indicated in FIGURE 4-2-B as R1i, R1o, R2i, R2o), adding 200 µL of Matrigel® hESC-Qualified Matrix 1:30 in Knockout™ DMEM/F-12 medium in R1i and R2i, and after letting volumes equilibrate, adding extra 150 µL in R1o and R2o, to avoid in this way microbubbles inside the channels. The coating was performed by incubating devices for 1 h at room temperature.

Once devices were coated, the coating solution was aspirated and they were filled with *hSkMb medium* in the same way: putting 200 µL on R1i and R2i, letting volumes balance, and putting 200 µL on R1o and R2o. Then, previously trypsinised SkM cells were counted and, for each device, approximately 40.000 cells were resuspended in 10 µL of *hSkMb medium* and injected slowly in the seeding port (the perforated 3 mm hole indicated as *2* in the right side of FIGURE 4-2-B). SkM cells were maintained proliferating, changing the medium every day after until TP2. The medium was always changed aspirating the old one and adding the new one from the reservoirs to diminish as much as possible the shear stress onto cells.

At TP2 SkM cells were changed to *hSkMc2 medium*, changing it on only on the SkM side reservoirs (R2i and R2o). The SN side of the device was washed with DPBS before adding *hSN3 medium* (200 µL on R1i and, after volumes were balanced, 200 µL on R1o). Then, for each device, one SN spheroid was gently handled and inserted in the SN seeding port (the perforated 2 mm hole indicated as *1* in the left side of FIGURE 4-2-B), letting the spheroid precipitate to the bottom. The medium for each compartment was changed every day after. SN were kept with *hSN3 medium* until the endpoint of the experiment. SkM were changed after 4 DIV to *hSkMc4 medium*, and 4 DIV later to *hSkMc10 medium*, maintaining the last one until the endpoint of the experiment.

Characterisation through immunostaining

At TP3 devices were fixed with a 4% paraformaldehyde solution for 30 min. After washing the samples with DPBS, the immunostaining was performed as described in SECTION 4.3.5.2 to detect proprioceptive sensory neurons, or as described in SECTION 4.3.6.2 to detect myocytes, or with combinations of the previously mentioned antibodies to see their interaction. In some cases, samples were incubated with 0.1 µM of rhodamine phalloidin (Cytoskeleton, #PHDR1) in DPBS for 10 min as well. Imaging was performed with a confocal laser scanning microscope (Olympus, #FV1200) and images were processed afterwards with ImageJ software.[37]

4.3.7.2. 3D culture in MINDS microfluidic devices

Fabrication and design of MINDS microfluidic device layers

A 3D multi-layered compartmentalised device for neuromuscular coculture, named "MINDS device", was designed with 3 different chambers and 4 media reservoirs interconnected on different levels by microchannels. The MINDS device was formed by three PDMS layers assembled together, as shown in FIGURE 4-3. The bottom layer (indicated as L1 in the FIGURE 4-3) limits the diffusion between compartments and its elongated configuration with micro-posts facilitates SkM differentiation and fibre alignment. The middle layer, L2, has microchannels connected to reservoirs facilitate the diffusion between reservoirs and each cell compartment, while limiting the shear stress of media changes. The dimensions of reservoirs in the top layer, L3, guarantee the availability of medium for 48 h. The thickness of each master determines the thickness of the PDMS layers obtained.

MINDS device masters fabrication was performed in collaboration with PhD student Roberto Paoli, as part of his thesis.[1] Briefly, the master was designed in Autodesk Inventor®. The designs of the three separated masters for PDMS replica moulding were exported to Standard Tessellation Language (STL) file format and printed in Medicalprint® resin (Detax GmbH & Co. KG) with a customised stereolithography 3D printer (Ilios HD custom kit, Ilios3D).

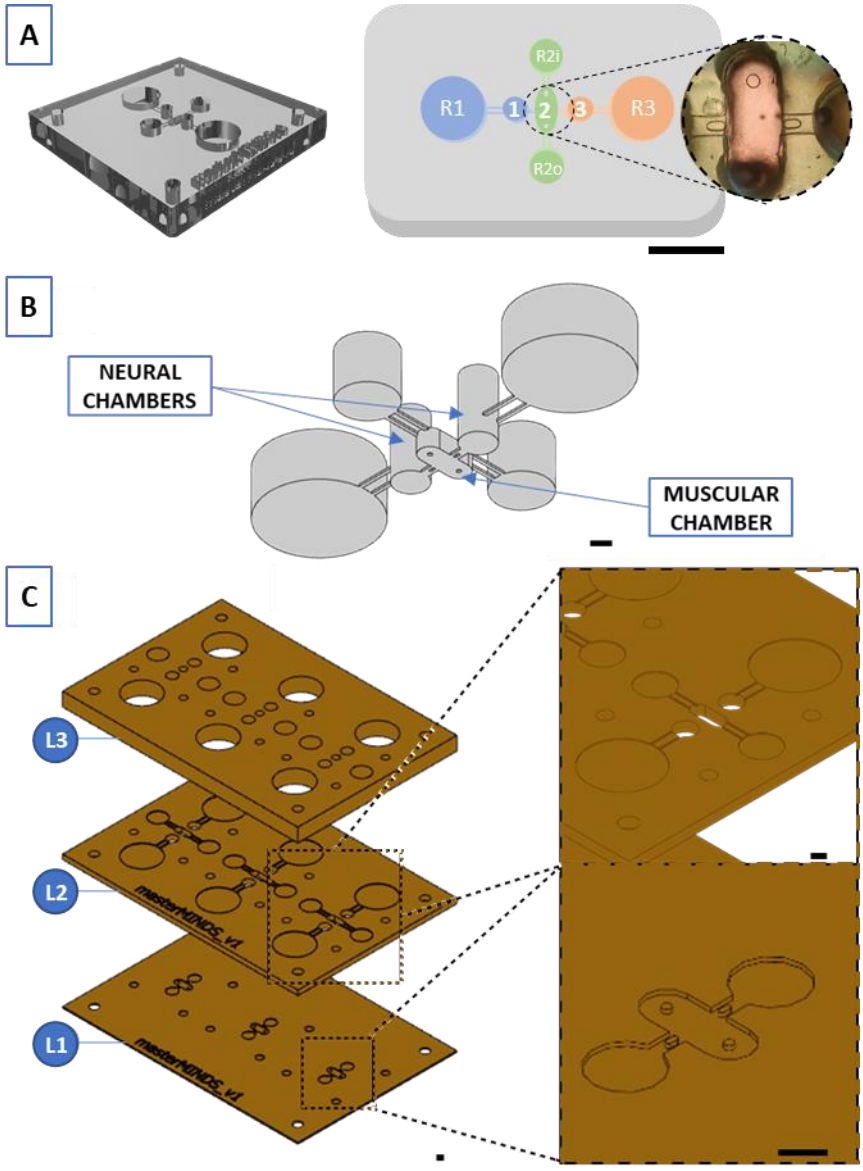

Figure 4-3. *MINDS device design.* ***A)*** *Diagram of the device with all layers assembled and indicating each area of the device. Scale bar 1 cm.* ***B)*** *Fluidic 3D structure (interior of the channels). Each chamber is connected to media reservoirs through microchannels located at an upper level. Scale bar 2 mm.* ***C)*** *Exploded view of three layers of masters utilised to form three replicas of the device after assembling all layers (L1, L2, L3). L1 includes the interconnection of the channels and PDMS posts; L2 contains the interconnection between each chamber and its media reservoir; L3 contains extra height for the media reservoirs. Scale bar 2 mm.*

The 3D printing process was performed under vacuum and under yellow light to avoid exposure of the resin, under the following printing parameters: 50 µm of resolution in Z; 30 pulse width modulation of the LED lamp; 5 burn-in layers; 6 s of burn-in exposure; 0.75 s of normal exposure; and 0.125 $mm \cdot s^{-1}$ of Z speed. 3D printing process of each layer took 20, 45 and 100 min for L1, L2 and L3 layers respectively. Each layer motifs were printed onto a 50 x 75 mm standard glass slides. Printed substrates were then washed in isopropanol (IPA, Sigma Aldrich, #278475), and after detaching from the glass substrate, they were sonicated twice in IPA for 3 min each time, and dried using N_2 gas stream. The post-curation of printed substrates was performed by exposing them for 30 min on each side to UV fluorescent light (bandwidth 300-400 nm, peak wavelength 365 nm).

These stereolithography 3D printed substrates were utilised as masters for PDMS soft lithography. Obtaining flat PDMS layers was of vital importance to be able to bond one layer to another. Because of that, the 3D printed masters were designed with a frame of the desired PDMS height, and for the PDMS curation, a lid was placed on top of the frame to control the height and assure that the obtained PDMS was flat. Curing the PDMS against a glass slide was not a suitable solution, as the thin layers could not cure due to the lack of oxygen permeability of glasses. Instead, we used Petri dish lids, that are popularly known to be gas-permeable materials. Controlled thickness of PDMS replica moulding and flat PDMS layers

were obtained by pouring degassed 10:1 mixture of PDMS (Dow Chemical, SYLGARD™ 184 Silicone Elastomer Kit) on the masters and curing it against a Petri dish bottom sandwiched between neodymium magnets (see FIGURE 4-4).

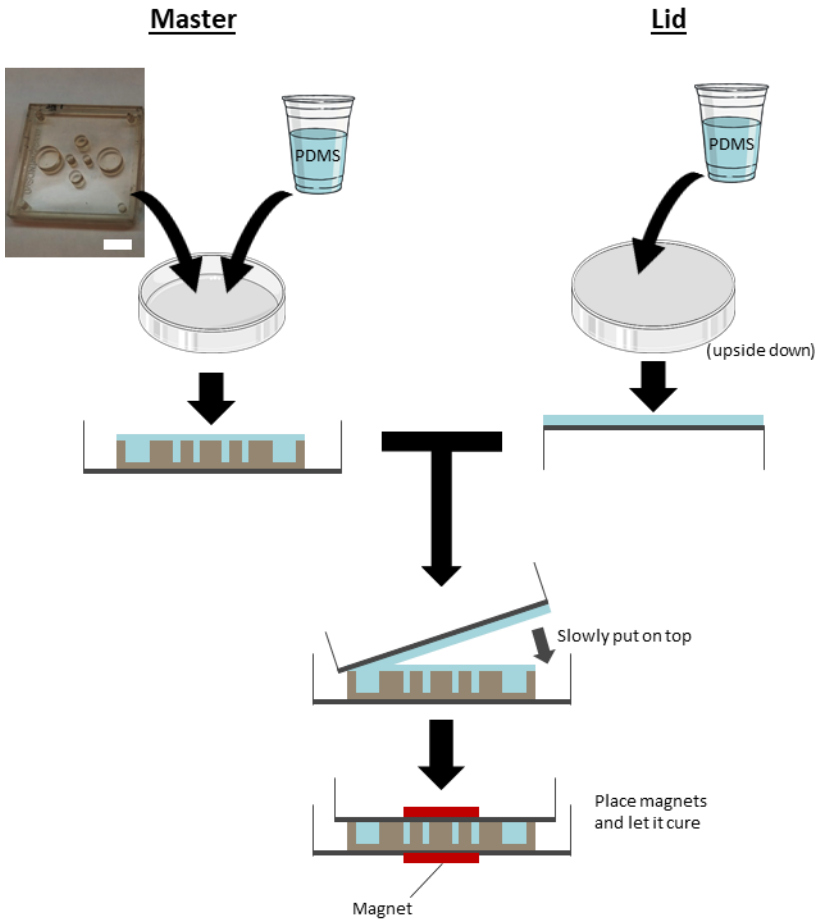

Figure 4-4. *MINDS device PDMS soft lithography with controlled PDMS layer height. Degassed PDMS was poured onto the master (example of L3) and onto the bottom of a Petri dish. After degassing them again, the Petri dish was placed on top of the master in contact with it. In case of need, magnets were placed to make sure the Petri dish at the top was always in contact with the master while curing the PDMS.*

Briefly, Petri dish bottom on one side, and 3D printed master on another side, were covered in degassed PDMS. Then, Petri dishes were placed as a lid in the area in contact with the master, displacing slowly the bubbles in the interface with the degassed PDMS of the master. Finally, a neodymium magnet (Lovimag, #DISC10P) was placed on top of the Petri dish lid, and another under the Petri dish holding the master, to secure the PDMS height and immobilise the system. The PDMS was cured overnight in the oven at 60 °C.

Once PDMS was cured, the PDMS layers were prepared by demoulding them from the master carefully. The sides of each PDMS layer were cut with a mini razor scraper (Titan Tools, #12031) and 0.22 mm razor blades (VWR, #55411-050). The PDMS cured in compartments and reservoirs was removed in the cases needed using sterile disposable biopsy punches of different diameters: 2 mm (Miltex, #33-31), 3 mm (Miltex, #33-32), 4 mm (Miltex, #33-34), 8 mm (Miltex, #33-37).

As the 3D printed masters are quite fragile, additional auxiliary masters were fabricated in Smooth cast® 320 (Smooth-on) as shown in FIGURE 4-5.

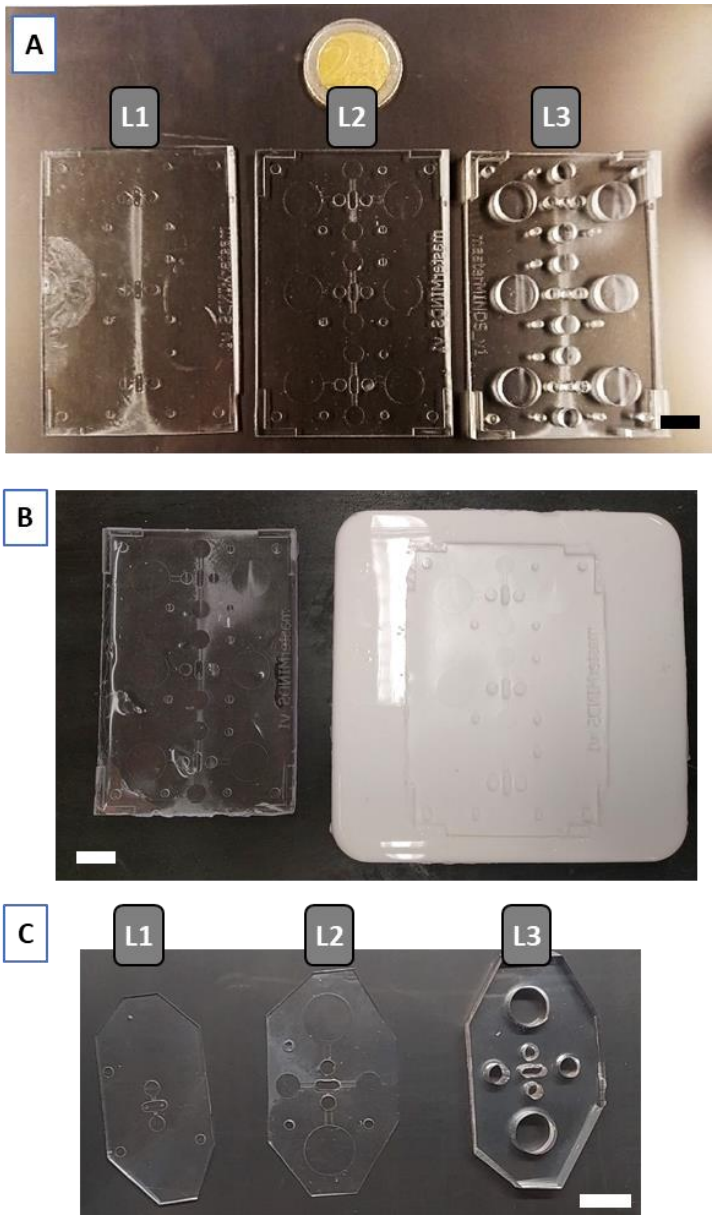

Figure 4-5. *MINDS device fabrication.* ***A)*** *3D printed masters to obtain three replicas of each layer (L1, L2, L3).* ***B)*** *Masters for the middle layer (L2), fabricated with stereolithography 3D printing (left) and casting (right).* ***C)*** *Replicated PDMS layers cut for one device, before assembling. Scale bar in all cases is 1 cm.*

Briefly, each component of the kit was first weighted and degassed separately. Then, both solutions were slowly mixed by pouring one onto the other, obtaining a mix with yellowish colour. This mixture was gently stirred without making bubbles until the solution changed to transparent. Then it was poured onto a demoulded PDMS layer attached to a Petri dish previously covered in PDMS and polymerised. The casting was performed at room temperature overnight on a flat surface. Once cured, the colour changed to white and the new casted master was demoulded from the Petri dish. This master was then ready to use in the same way as the 3D printed master.

Assembly of MINDS microfluidic devices

All three PDMS layers of each device were cleaned sonicating for 15 min in 100% ethanol, dried with nitrogen gas stream and dehydrated in an oven at 60 °C for at least 30 min. To perform the bonding, all three layers were exposed to 1 min of high frequency oxygen plasma (Harrick plasma, #PDC-001) at 700 mTorr. Then layers were aligned sequentially under the magnifying glass or using the customised aligner. To simplify alignment procedure and align up to 3 devices at a time, an aligner helper was designed in Autodesk Inventor®, and fabricated laser cutting 6 mm thickness poly(methyl methacrylate) (PMMA). Its aligning mechanism consisted in 2 mm and 2.5 mm stainless stell pins coinciding with same diameter holes replicated in the PDMS from masters. After aligning the pins, the

thin layer of PDMS was brought into contact with the previous layer through a manual vertical displacement mechanism (see FIGURE 4-6).

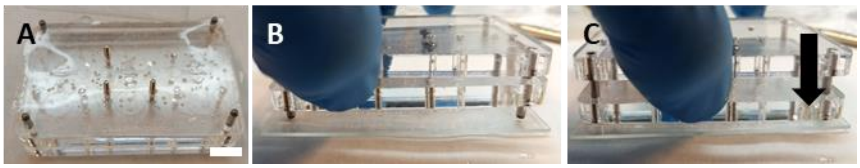

Figure 4-6. *PDMS aligning helper.* ***A)*** *A PDMS layer (L1) aligned with the stainless-steel pins. Scale bar 1 cm.* ***B)*** *An aligned PDMS layer (L1) is flipped on top of another PDMS layer (L2), using the pins to align.* ***C)*** *The PMMA with L1 adhered aligned slides down bringing both L1 and L2 surfaces into contact without misalignment.*

The bonding was performed sequentially between the L3 (placed with the posts facing up) and the L2 (placed with the microchannels facing up), and then, those two to the L1. The bonding was sealed exposing the sandwich of three layers to at least 30 min dehydration in the oven at 60 °C. At this point, devices were stored for the beginning of the experiment.

Fluidic characterisation of MINDS devices

To test the fluidic connectivity of the devices once assembled, previously prepared devices (not to use for cell culture) were activated with 5 min of medium frequency oxygen plasma and filled with sterile water. Then, some devices were filled with water with blue ink diluted. To test the diffusion, some other devices were first filled with water, and after aspirating it, they were filled with Matrigel using same amount and procedure as for the cell culture. Then different inks diluted in sterile water were added in each compartment from reservoirs R1, R2i and R3; with and without

previous activation with oxygen plasma; and with and without polymerised Matrigel inside cell culturing chambers. Images were taken 5 min after filling the device or 24 h later.

Cell culture in MINDS devices

To perform the cell culture (initially of SkM cells at TP1 and later of SN spheroids following *differentiation protocol C* and MN spheroids at TP2), previously prepared devices were activated, sterilised and coated before seeding cells in them. Same as with Xona devices (SECTION 4.3.7.1), the devices were activated with 5 min of medium frequency oxygen plasma, filled with water, sterilised with UV radiation for 15 min and rinsed with sterile water.

At TP1, SkM cells previously trypsinised were embedded in a density of $2 \cdot 10^6\ cell \cdot mL^{-1}$ in ice-cold Matrigel, by resuspending them first in *hSkMb medium*, and then in 10 times more of Matrigel® hESC-Qualified Matrix. The mixture of SkM cells and Matrigel was kept on ice until seeding them in the devices. For each device, first 4 µL of Matrigel without cells was injected in the SN and MN seeding ports (indicated as *1* and *3* in FIGURE 4-2-C), and then 9 µL of the mixture of Matrigel with SkM cells were slowly injected in the SkM seeding port (the elongated perforation in the middle with two posts at the bottom indicated as *2* in FIGURE 4-2-C), extending the composite with cells from the top post to the bottom one. In all cases, when adding the Matrigel in the seeding port, the injection was done directly slowly at the bottom of the device to avoid the

composite from going into the microchannels connecting with the reservoirs. After polymerising the Matrigel at 37 °C for 30 min, *hSkMb medium* was added in all reservoirs (indicated in FIGURE 4-2-C as R1, R2i, R2o, R3): 250 µL in R1, 70 µL in R2i, 70 µL in R2o, 250 µL in R3. SkM cells were maintained proliferating changing the medium every day after until TP2. The medium was always changed aspirating old medium and adding new medium from the reservoirs.

At TP2, after aspirating the medium from all reservoirs and washing R1 and R3 with DPBS, for each device one SN spheroid was embedded in 5 µL of ice-cold Matrigel, and inserted in the SN seeding port (indicated as *1* in the FIGURE 4-2-C), and one MN spheroid was embedded in 5 µL of ice-cold Matrigel and inserted in the MN seeding port (indicated as *3* in the FIGURE 4-2-C). After polymerising the Matrigel for 30 min at 37 °C, the following media were added to the reservoirs: 250 µL of *hSN3 medium* in R1, 70 µL of *hSkMc2 medium* in R2i, 70 µL of *hSkMc2 medium* in R2o, 250 µL of *hMN medium* in R3. The medium for each compartment was changed every day after. SN were kept with *hSN3 medium* and MN with *hMN medium* until the endpoint of the experiment. However, SkM cells were changed after 4 DIV to *hSkMc4 medium*, and 4 DIV later to *hSkMc10 medium*, maintaining the last one until the endpoint of the experiment.

Characterisation through immunostaining

At TP3 devices were fixed with a 4% paraformaldehyde solution for 30 min and washed with DPBS. The immunostaining was performed as described in SECTION 4.3.5.2 to detect proprioceptive sensory neurons and motoneurons, or as described in SECTION 4.3.6.2 to detect myocytes, or with combinations of the previously mentioned antibodies to see their interaction. Imaging was performed with a confocal laser scanning microscope (Olympus, #FV1200) and images were processed afterwards with ImageJ software.[37]

4.4. Results

4.4.1. Differentiation of hNSC to motoneurons and comparison with sensory neurons

4.4.1.1. Differentiation of MN and SN as floating spheroids

The transversal area quantification performed in spheroids undergoing *SN differentiation protocol A* and MN differentiation, showed that the size of floating SN spheroids remains the same during their differentiation whereas MN size augments up to four times (see FIGURE 4-7).

4.4.1.2. Differentiation of MN and SN as plated spheroids

The BF images taken in plated spheroids undergoing *SN differentiation protocol A* and MN differentiation, showed a clear augment of glia in the periphery of MN spheroids, contrary to SN spheroids, and migration of SN spheroids (FIGURE 4-8-A). The quantification performed showed that once spheroids are plated at TP2 (8 ddiff), there is no significant variation in the core area increment percentage. However, the corona keeps growing over time both in MN and SN spheroids (FIGURE 4-8-B). The spheroid migration analysis showed an spheroid approximation trend. In these samples SN spheroids were able to approximate to each other covering up to the 30% of the initial distance separating both spheroids in 14 days, fusing both coronas at 15 ddiff. MN spheroids did not show any migration trend and their inter-spheroid distance

was only affected by the spheroid core growth (FIGURE 4-8-C). In regards to neurite diameter analysis, results showed that SN neurites seem to aggregate to form thicker neural processes, resulting in much higher diameters than MN neurites, though with a wider range of diameter variation (FIGURE 4-8-D).

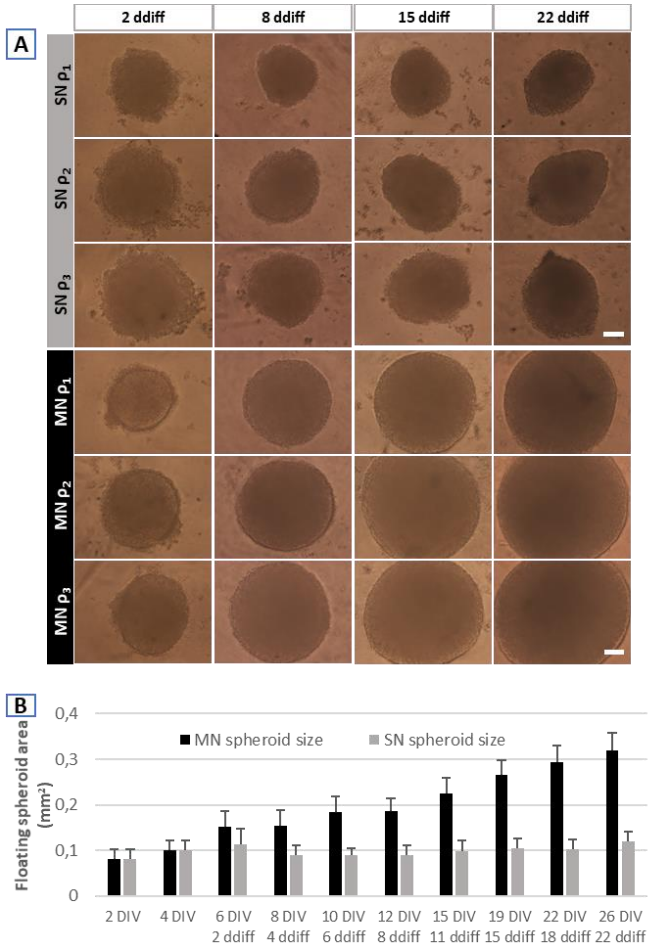

Figure 4-7. *Floating spheroid size variation analysis seeding initially cells in three different densities (3.000, 4.500 and 6.000* $cell \cdot spheroid^{-1}$*).* ***A)*** *Bright field images of the differentiation of hNSC to sensory neurons through differentiation protocol A or differentiation to MN. Images taken at different days after differentiation started (ddiff). Scale bar 100 µm.* ***B)*** *Quantification of the spheroid size at different timepoints. Average size and standard deviation of the three seeding densities.*

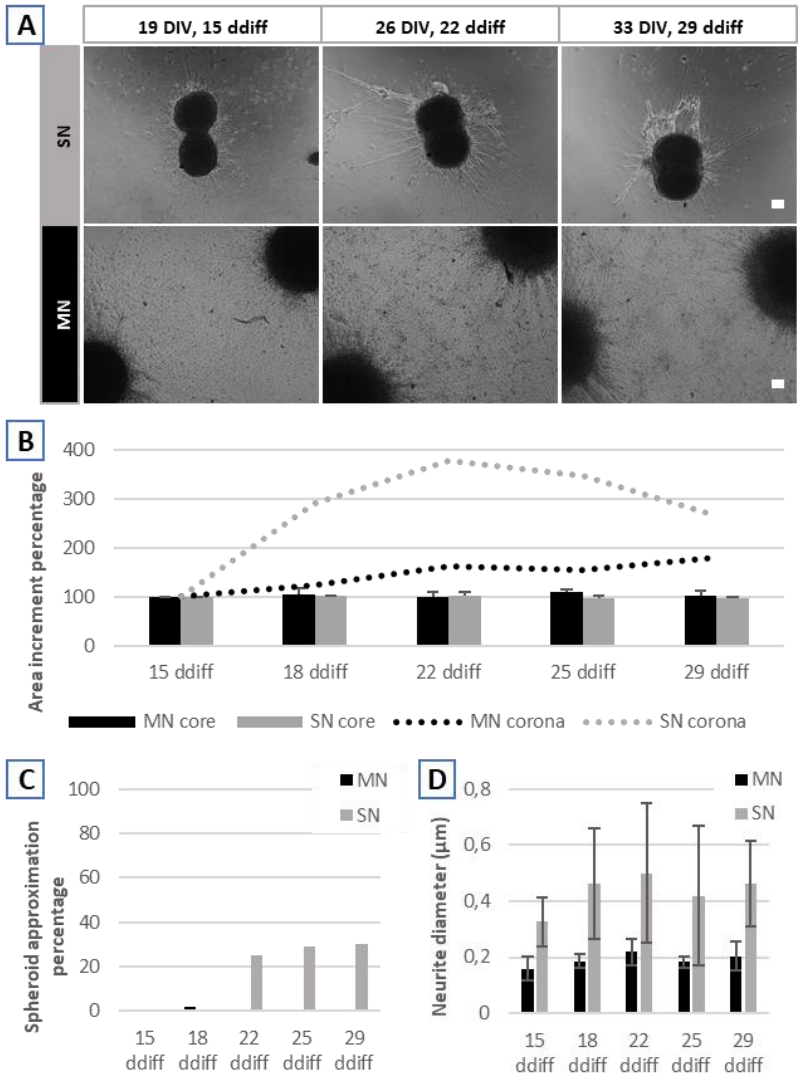

Figure 4-8. *Differentiation of healthy hNSC as plated spheroids.* ***A)*** *BF images of the differentiation of hNSC to SN through differentiation protocol A or to MN. Images taken at different timepoints. Scale bar 100 µm.* ***B)*** *Quantification of core and corona area increment percentage at different timepoints normalised against their size at 15 ddiff. Average and standard error are shown (n=2).* ***C)*** *Spheroid migration percentage trend normalised against the centre-to-centre inter-spheroid distance shortening percentage since 15 ddiff.* ***D)*** *Neurite diameter average and standard deviation calculated next to the core of SN and MN spheroids at different timepoints (n=5).*

The immunostaining images taken in plated spheroids undergoing *SN differentiation protocol A* (FIGURE 4-9, sensory neurons), showed few glial cells in the corona of the spheroid (stained with DAPI), high sensory neuron signal in the outside of the spheroid core (stained with Pou4f1), low number of neurites (stained with Tuj1) and low specificity in the differentiation towards pSN (low TrkC signal in the axons of the spheroid corona). Furthermore, when two spheroids were seeded together, they fused and formed a bigger one.

The immunostaining images taken in plated spheroids undergoing *MN differentiation protocol* (FIGURE 4-9, motoneurons), showed lots of glial cells in the corona of the spheroid (stained with DAPI) and high specificity in the differentiation protocol (high ChAT signal). Contrary to SN spheroids, when two MN spheroids were seeded together, they did not migrate and instead they made stronger connexions and thicker axons.

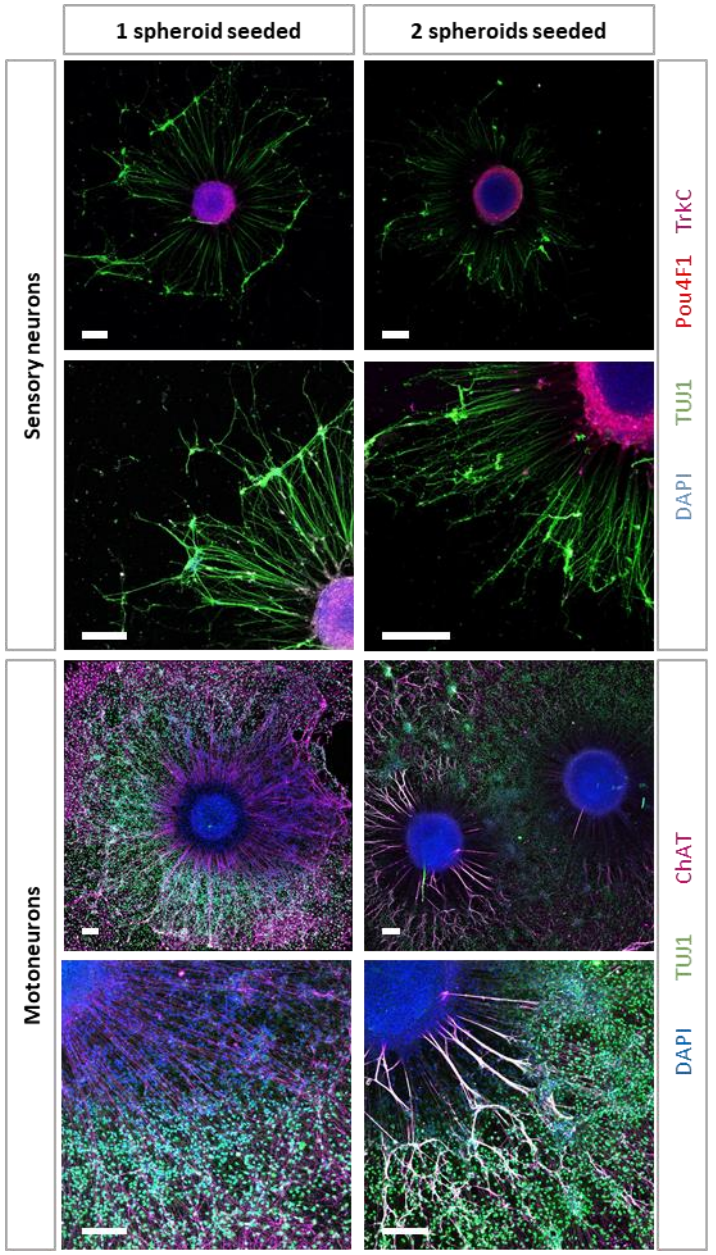

Figure 4-9. *SN and MN spheroids plated onto Matrigel coated surfaces at TP2. Images taken at TP3. SN spheroids differentiated with SN protocol A have nuclei stained in blue, TUJ1 in green, Pou4F1 in red and TrkC in magenta. MN spheroids have nuclei stained in blue, TUJ1 in green, and ChAT in magenta. Scale bars are 200 µm.*

4.4.2. Differentiation of skeletal myoblasts to myocytes

Skeletal myoblasts proliferated with fusiform morphology and required at least 12 ddiff to form skeletal myocytes, with elongated and aligned myofiber morphology (see FIGURE 4-10). The hSkMc expressed after 26 ddiff α-actinin, without showing its typical staining of actin bands in the sarcomere, and MHC, showing the striated distribution of myofibers in the sarcomere.

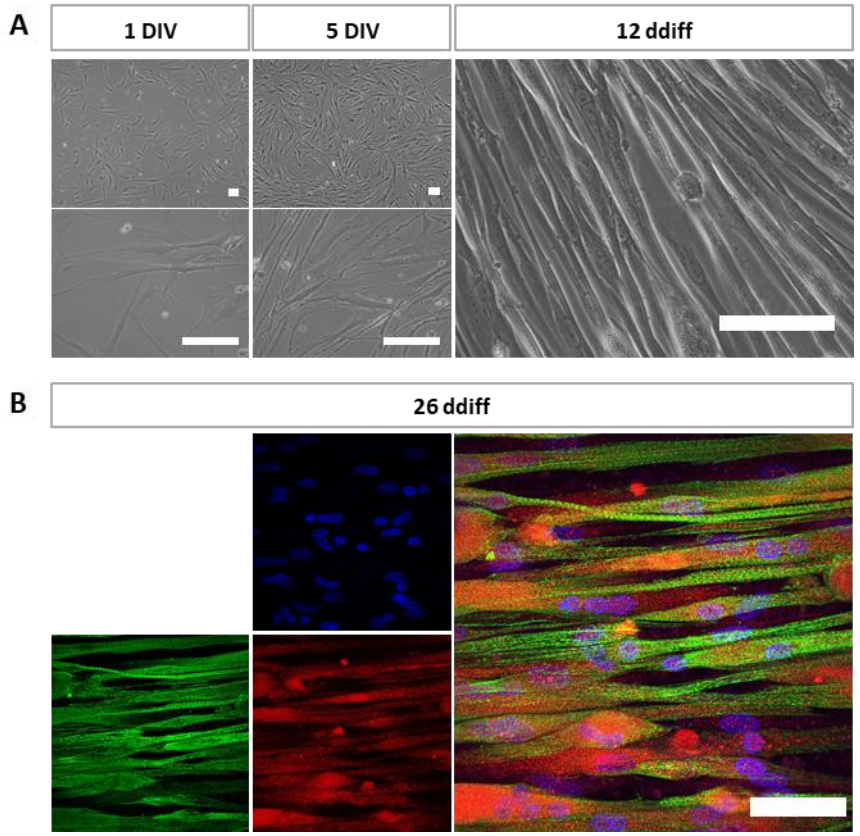

Figure 4-10. *Proliferation of human skeletal myoblasts and differentiation into myocytes.* ***A)*** *BF images show cell confluency and morphology during the proliferation after 1 DIV, after 5 DIV, and after 12 ddiff. Scale bars 100 µm.* ***B)*** *Immunostaining of skeletal myocytes at TP3, after 26 ddiff. Nuclei are stained in blue, MHC in green and α-actinin in red. Scale bar 25 µm.*

4.4.3. Compartmentalised coculture

4.4.3.1. Compartmentalised coculture of SN and SkM in Xona devices

The compartmentalised coculture of SN spheroids with hSkMc in Xona microfluidic devices, showed that SN spheroids (FIGURE 4-11-A) were able to extend their neurite projections throughout the whole neural compartment of the device (FIGURE 4-11-C), expressing few TrkC+ axons colocalising with Tuj1. The hSkMc with random alignment in the first steps of the differentiation (FIGURE 4-11-B) acquired aligned structure of their multinuclear fibres (FIGURE 4-11-D). However, hSkMc fibres were not completely differentiated as MHC and α-actinin did not show the typical striated sarcomeric organisation. Both TrkC+ and TrkC- axons were found interacting with SkM fibres, and in some cases, wrapping around them (FIGURE 4-12 and FIGURE 4-13).

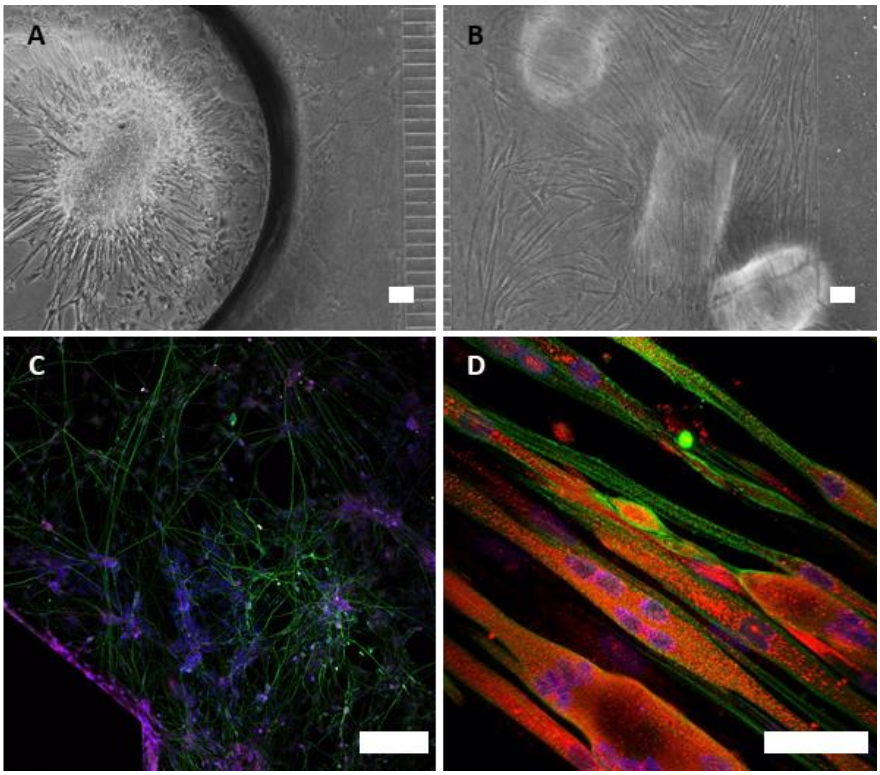

Figure 4-11. *Compartmentalised coculture of SN spheroids undergoing differentiation protocol A and SkM in xona microfluidic devices.* ***A)*** *Bright field image of SN compartment with the spheroid seeded in the hole near microchannels at TP3.* ***B)*** *Bright field image of SkM compartment at TP2 + 12 DIV.* ***C)*** *Immunostaining of the SN compartment at TP3 showing nuclei in blue, TUJ1 in green, and TrkC in magenta.* ***D)*** *Immunostaining of the SkM compartment at TP3, showing nuclei in blue, MHC in green and α-actinin in red. Scale bar is 100 µm.*

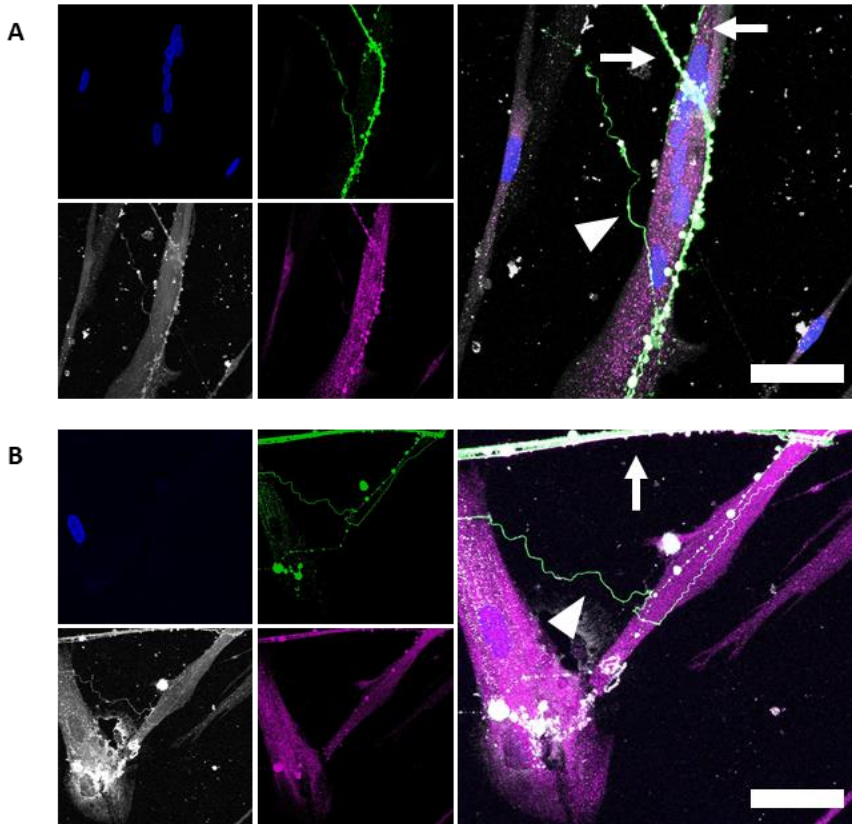

Figure 4-12. *Immunostainig of the interaction between SkM fibres and SN neurites in the SkM compartment at TP3, showing nuclei in blue, TUJ1 in green, phalloidin in grey and TrkC in magenta. Scale bars are 25 µm.* ***A)*** *Interaction between a TkC+ axon (arrow) and a TrkC- axon (triangle) with a multinuclear muscle fibre.* ***B)*** *Interaction of a TrkC+ axon (arrow) and one TrkC- axon (triangle) with another muscle fibre.*

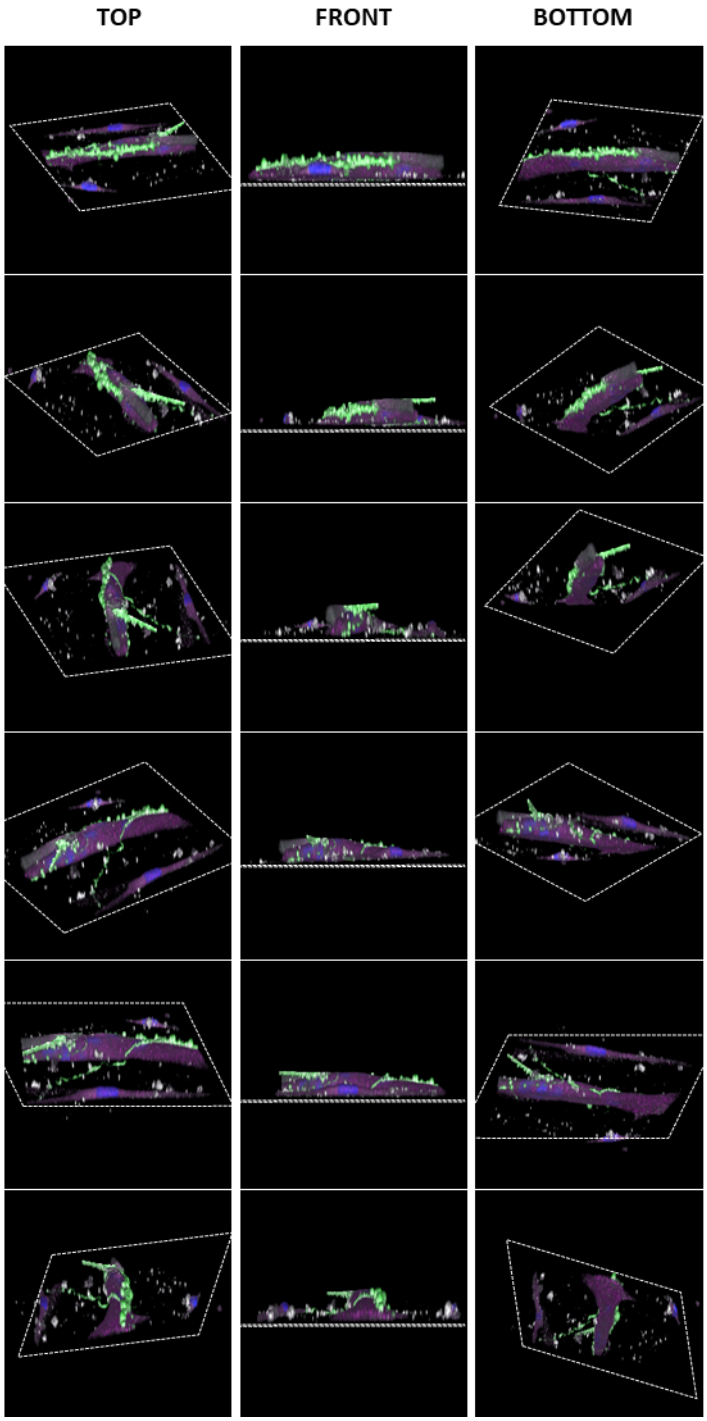
TOP
FRONT
BOTTOM

Figure 4-13. *3D view rotation of the immunostainig of SkM fibres and SN neurites interaction shown in* ***Figure 4-12-A****. Nuclei are shown in blue, TUJ1 in green, phalloidin in grey and TrkC in magenta. For each rotation angle images show the perspective from the top, front and bottom.*

4.4.3.2. MINDS devices: characterisation and compartmentalised coculture of SN, SkM and SN

MINDS device masters were successfully fabricated and replicated in PDMS and assembled. Devices filled with diluted blue ink showed good connection among compartments, lack of leakage and ease of the procedure of changing medium from the reservoirs (FIGURE 4-14-A). The test performed filling the device with and without previous activation with plasma showed that it was necessary to activate it previously to be able to fill the device and obtain the desired fluidic communication among compartments (FIGURE 4-14-B). The test performed activating the device, then filling the cell-seeding chambers with diluted Matrigel, polymerising it, and filling with diluted ink the reservoirs (similarly as the procedure to be performed with cells), showed that the Matrigel and compartmentalisation can limit diffusion among compartments (FIGURE 4-14-C and FIGURE 4-14-D). Once three cell types were cultured, different media colours could be appreciated in the reservoirs and compartments corresponding to each cell type (FIGURE 4-14-E).

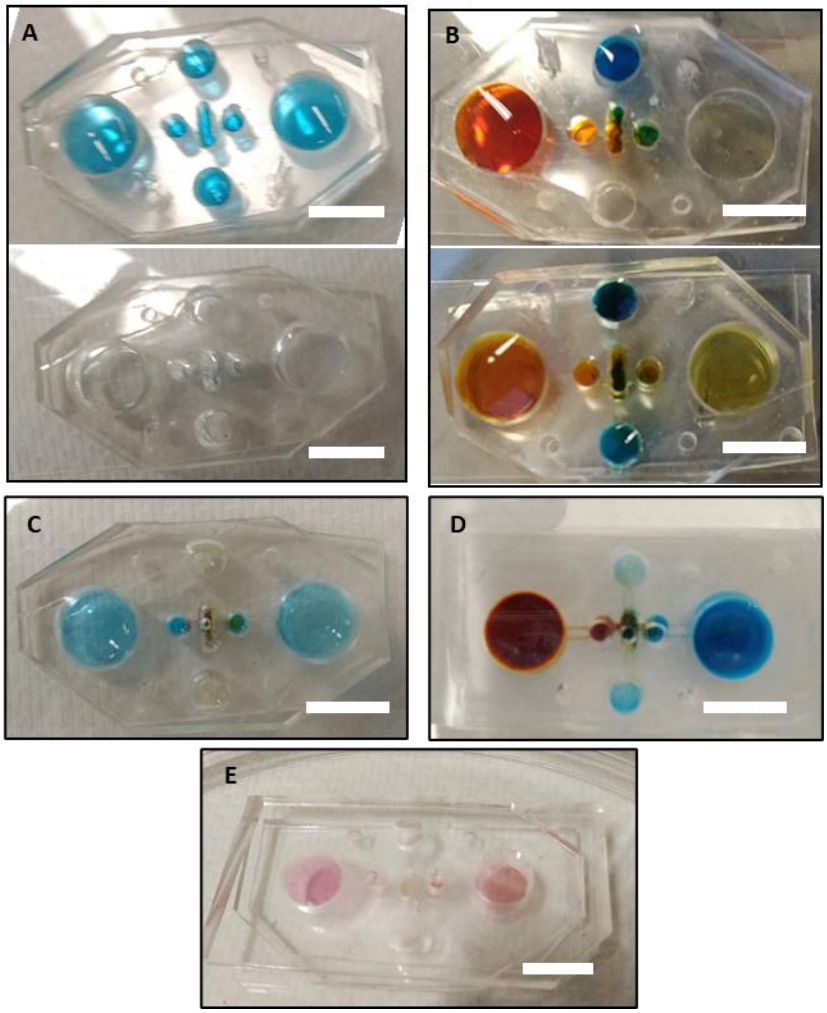

Figure 4-14. *Fluidic tests on assembled MINDS devices.* ***A)*** *The device filled with PBS and blue ink right after activation from all reservoirs, and after aspirating all the solution from the reservoirs that facilitates changing all the medium.* ***B)*** *The device filled with inks from reservoirs (orange in R1, blue in R2i, PBS in R2o and PBS in R3), without previous plasma activation (top) and right after plasma activation (bottom).* ***C)*** *The device filled with red ink and Matrigel in chamber 2 right after plasma activation, and after its gelation, filled with PBS containing blue ink in R1 and R3, and with PBS in R2i and R2o.* ***D)*** *The device filled with Matrigel in all chambers right after plasma activation, and after its gelation, filled with PBS containing red ink in R1, PBS containing blue ink in R3 and PBS alone in R2i and R2o. Image taken after 24 h.* ***E)*** *A device with triple culture ongoing (from left to right: MN, SkM, SN) showing different culture media colours 24 h after changing the media in R1; R2o and R2i; and R3. Scale bar for all pictures is 1 cm.*

Regarding the 3D culture performed in MINDS devices with healthy hNSC derived pSN in chamber 1, hSkMc in chamber 2, and healthy hNSC derived MN in chamber 3, the imaging performed onto immunostained samples on different areas of the device showed that TrkC+ axons are able to cross to the centre chamber reaching SkM fibres (FIGURE 4-15-B, indicated with triangles). SkM cells are aligned but MHC and α-actinin staining are not striated (FIGURE 4-15-C). Axons from MN compartment, TrkC-, cross easily to the medium compartment reaching SkM cells (FIGURE 4-15-D, indicated with a triangle).

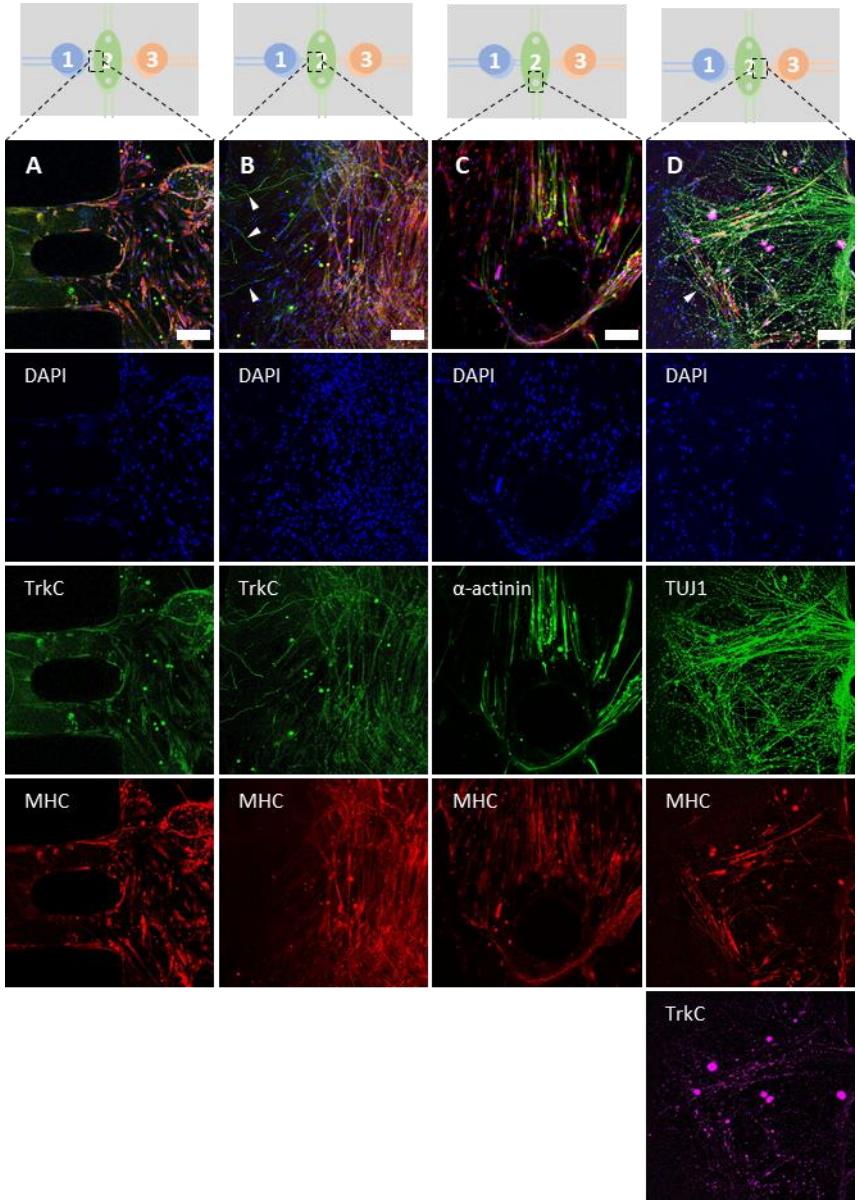

Figure 4-15. *Immunostaining of MN-SkM-SN coculture in 3D in MINDS devices at TP3 indicating the area of MINDS device where the picture is taken. SN are seeded in the compartment 1, SkM in the compartment 2, and MN in the compartment 3. SN arriving at SkM compartment (**A** and **B**) have DAPI is stained in blue, MHC in red and TrkC in green. SkM compartment with only hSkMc (**C**) shows DAPI stained in blue, α-actinin in green and MHC in red. MN arriving at SkM compartment (**D**) have DAPI stained in blue, TUJ1 in green, MHC in red and TrkC in magenta. Scale bar 100 µm.*

4.5. Discussion

4.5.1. Differentiation of SN versus MN

The differentiation of hNSC to MN spheroids has previously been stablished,[33,35] showing through imaging techniques the expression of stemness and motoneuron differentiation markers (Nestin, Olig2, Sox1, Tuj1, MAP2) in 2D cultures,[33] and neural differentiation markers (HB9, Tuj1, islet1, ChAT, F-actin) in spheroid form.[35] However, there are no stablished protocols to differentiate hNSC to SN and there are no publications using SN spheroids to our knowledge. Taking advantage of the protocols defined in the previous chapter to differentiate hNSC to SN spheroids, for the first time we have been able to compare MN and SN spheroids differentiated from the same hNSC cell source.

The analysis performed on images taken on floating spheroids (FIGURE 4-7) and plated spheroids (FIGURE 4-8 and FIGURE 4-9), shows that there is a lot of peripheral glia proliferation in MN spheroids. This can be observed in floating spheroids as an augment of the transversal area up to four times, and in plated spheroids as an increment of the glial cells in the corona of the spheroid, remaining the core area the same. In contrast, there are almost no glial cells in the corona area of plated SN spheroids, and the core size remains the same both floating and plated. The corona area of plated MN spheroids increases progressively, related to the proliferation of glial cells. However, in the case of SN, it increases exponentially as

the axons thicken and aggregate. Once spheroids are plated, the core stops growing in MN and SN spheroids. This suggests that **neural proliferation ends up before plating the spheroids**, with the differentiation, but glial proliferation keeps going in MN spheroids. Finally, the migration trend and fusion of two SN spheroids suggests that, **SN spheroids generated with *protocol* A could have poor cohesion properties on the spheroid ECM** or **that SN spheroids could detect the presence of another cluster of SN** (a nearby spheroid), and migrate towards it to form a bigger cluster of all kind of peripheral SN, as in physiological DRG.

4.5.2. Compartmentalised coculture in 2D in Xona devices

The study of neuromuscular interactions seeding MN and SkM in compartmentalised devices is well known.[2] However, there is little literature on *in vitro* coculture of sensory neurons with skeletal muscle cells,[3–6] and no publications seeding them in compartmentalised microfluidic culture systems.

The compartmentalised coculture in Xona microfluidic devices (FIGURE 4-11, FIGURE 4-12 and FIGURE 4-13) showed that **SN spheroids were able to extend neurites within the SN compartment and cross to the SkM compartment**. However, as expected from the results obtained in the previous chapter, the differentiation protocol utilised originated a diverse population of SN, guaranteeing a small

percentage TrkC+ sensory neurons among them. Regarding SkM cells, results suggest that **muscle fibres were not completely differentiated**. They formed aligned structures, in some cases with similar morphologies to bag fibres, but α-actinin, phalloidin and MHC staining did not show in the SkM a uniform striated distribution of myofibers in the sarcomere (FIGURE 4-10-B and FIGURE 4-11-D). The induction of differentiation of hSkMb into hSkMc can be affected not only by the components of the medium. The initial cell confluency and ability to proliferate determines the formation of multinuclear muscle fibres, as cells need to fuse their cytoplasm. And in the case of a coculture, the differentiation could also be influenced by the lack of electrical, optical or mechanical stimuli, or insufficient biochemical stimuli, as discussed in *Chapter 2* for the use of optical stimulation performed in parallel projects.[38,39] Furthermore, the differentiation of SkM and SN neurite extension could be influenced by paracrine signalling between them, and therefore, also by the coculture window of time, as reported for MN in a parallel work performed in collaboration, discussed in *Chapter 2*.[38] In our study, cells were cocultured at TP2 (after 10 days of proliferation and differentiation for SkM cells, and 10 days of differentiation for neural spheroids, before inducing their final differentiation to SN). Previous publications have shown that placing together fully differentiated SkM cells (after 14 days of culture) and with fully differentiated MN spheroids for a coculture period of 14 days results as well in functional interactions.[36]

However, previous studies coculturing SN and SkM have suggested that it is preferable to induce a partial differentiation before placing both cells together, as certain factors released by SN (such as neuregulin) could play a role in initiating downstream differentiation of intrafusal muscle fibres and spindles.[5]

The interaction between SN and SkM cells in *in vitro* cultures has only been analysed through imaging techniques in few cases,[3,5,6] summarised in FIGURE 4-16. Rumsey *et al.* have reported the formation of ASW and FSE using rat primary neurons and rat primary myocytes with chain fibre or nuclear fibre morphologies respectively.[3] Guo *et al.* observed FSE and ASW formation between human neural progenitors derived to sensory neurons and human skeletal muscle stem cells derived to intrafusal fibres.[5] And Qiao *et al.* have published immunostaining images of the interaction of rat primary DRG neurons (in some cases TrkC positive) with rat primary skeletal muscle cells.[6] So far, results obtained here represent a first report in the interaction between TrkC positive neurons and skeletal muscle cells, both from human origin, cultured *in vitro*, in compartmentalised microfluidic devices, and the first 3D reconstruction of their interaction.

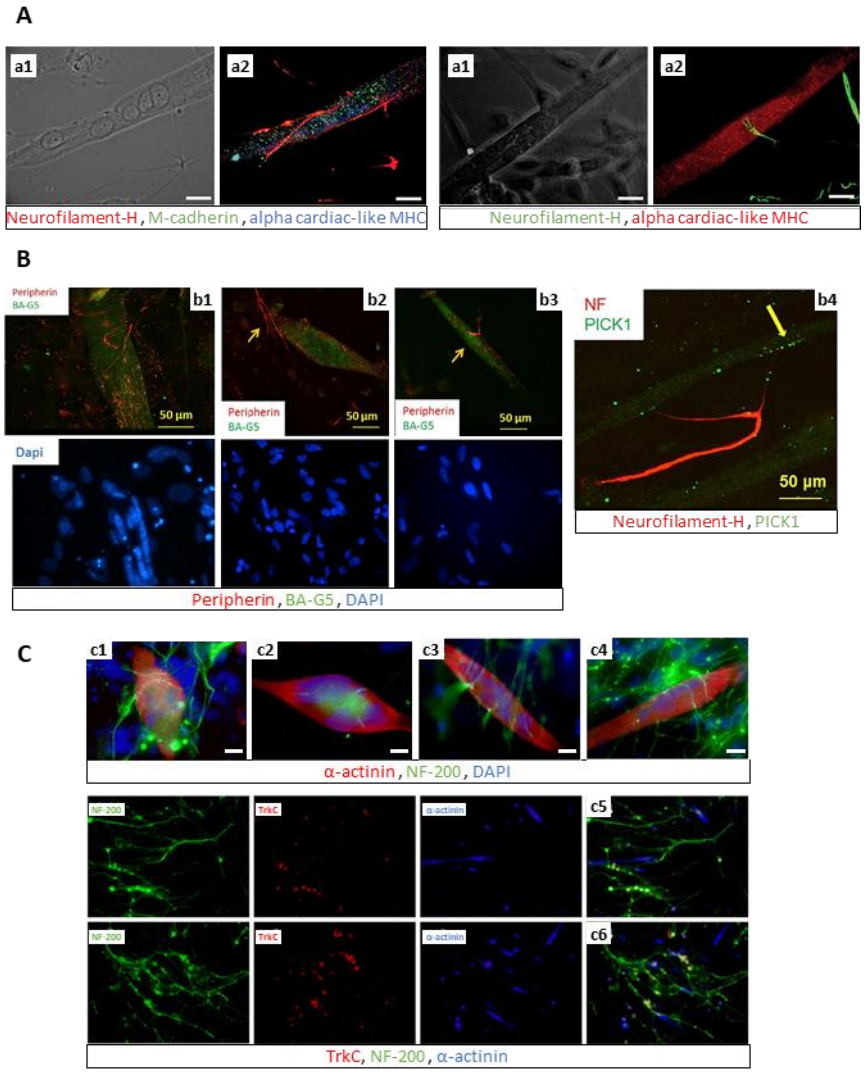

Figure 4-16. *Summary of the state-of-the art on SN-SkM interaction analysis through imaging techniques.* ***A)*** *Coculture of rat primary neurons and rat primary myocytes showing the formation of an ASW with chain fibres (**a1, a2**) and FSE morphologies with bag fibres (**a3, a4**). Scale bars are 50 µm. Images reproduced with permission from Rumsey et al.[2]* ***B)*** *Coculture of human sensory neurons derived from neural progenitors and human intrafusal fibres derived from skeletal muscle stem cells, showing the formation of ASW (**b1, b2**) and FSE (**b3**), and an image of the co-localization of PICK1 expression on the myofiber at the neural terminal ending site (**b4**). Terminal sites or interaction points are pointed by arrows. Images are reproduced with permission from Guo et al.[4]* ***C)*** *Coculture of rat primary DRG neurons with rat primary skeletal muscle cells , showing the*

*interaction between SN and intrafusal nuclear bag fibres (**c1, c2**), SN and intrafusal nuclear chain fibres (**c3, c4**), and TrkC positive SN and SkM (**c5, c6**). Scale bar is 20 µm (**c1-c4**) or 50 µm (**c1-c6**). Images are reproduced from Qiao et al.*[6]

In the results obtained here, some of the axons that reached a muscle fibre in SkM compartment (FIGURE 4-12) were TUJ1+ and TrkC+. Contrary to the publication of Qiao *et al.*[6] (see FIGURE 4-16-C5 AND C6), SkM fibres also expressed TrkC, as expected for human tissues.[40,41] In FIGURE 4-12-A and FIGURE 4-13, it seems that the axon at the top (TrkC+), wraps around the SkM fibre. This **suggest the formation of an ASW**. There is a controversy about this topic, as it has been reported that human primary terminals do not have that structure.[42] However, the *in vitro* studies performed by Guo *et al*.[5] coculturing sensory neurons and intrafusal muscle fibres from human origin, they observed that sensory terminals form structures with a similar morphology to ASW (see FIGURE 4-16-B1 AND B2). The image presented here supports the formation of ASW in human structures *in vitro*. Furthermore, the **TrkC+ axons interacting with SkM formed in the contact a synaptic bouton-like structure** —stained Tuj1+ and TrkC+ —, that TrkC- axons did not form in contact points with SkM fibres. Similar structures have been imaged by Qiao *et al.*[6] in SN terminals of rat primary DRG neurons connecting with intrafusal bag fibres (see FIGURE 4-16-C1), without assessing the type of SN or recreating the 3D structure. To our knowledge, **this kind of structures have not been found before in *in vitro* cultures of human SN with SkM**. However, further characterisation would be required

to confirm the specific type of TrkC positive neurons and SkM fibres present there, both through immunostaining and assessing the functionality.[43,44]

4.5.3. Compartmentalised coculture in 3D in MINDS devices

The coculture of hNSC derived SN following *protocol C*, hSkMc and MN in MINDS microfluidic devices (FIGURE 4-15) showed that the three type of cells seeded could coinhabit in the stablished conditions (ECM composition and low diffusion from the medium neighbouring compartments). Stablishing a coculture time window for three different kind of cells undergoing proliferation, differentiation and in some cases apoptosis processes after long-term cultures, is challenge, especially in 3D cultures, where differentiation timings tend to slow down. Results suggest that hSkMc did not differentiate completely, probably due to the low cell density that should be incremented for the future. However, the device design facilitated their alignment, even in non-differentiated muscle fibres. Axons from both SN and MN chambers were able to successfully reach the SkM compartment. Further characterisation with other immunostaining markers would be required to detect the specific type of neuron and the interaction with SkM fibres.

Neuromuscular compartmentalised cocultures have only been studied in 3D for MN-SkM connection,[34–36] achieving more mature

SkM structures. To our knowledge, this is the first time in which TrkC+ SN have been cultured *in vitro* in 3D, integrating it with the motor pathway, and inside a microfluidic compartmentalised device. Due to the high cell density required to create 3D cell cultures and maintain them alive, from imaging point of view, it was still easier to observe close interactions in 2D cultures, as reported for Xona devices (FIGURE 4-12 and FIGURE 4-13). However, the 3D culture has offered the advantage of recreating more physiological conditions. Further studies should be required to test the precise differences between differentiation rates and availability to create functional interactions in 2D and 3D triculture models.

To sum up, these results present a **proof of concept for compartmentalised neuromuscular tricultures and for the feasibility to use the MINDS device**. This compartmentalised culture system offers the possibility to test the interaction of cells present in three microenvironments (i.e. the muscle, the spinal cord and DRG), connecting axons from one to another.

4.6. Conclusions

This work stablishes the basis to create a human neuromuscular circuit on a microfluidic device in 3D culture and analyses the development of some innovative personalised medicine tools for its study, including human stem cells and microfluidic devices.

Human neural stem cells were successfully differentiated to motoneurons and TrkC+ populations of sensory neurons as described in previous chapter. The characterisation techniques performed to compare SN spheroids with the popularly known MN spheroids suggest that under the evaluated conditions: **1)** neural proliferation of MN and SN spheroids could stop before plating the spheroids at TP2, but glial cells continue proliferating afterwards only in the MN spheroid corona; **2)** embedding SN spheroids in Matrigel could promote neuron survival and neurite formation and extension; and **3)** SN spheroids could detect the presence of a nearby spheroid and migrate towards it to form a bigger cluster of all kind of peripheral SN, as in DRG.

Human skeletal myoblasts were differentiated to myocytes presenting typical markers of differentiated multinucleated fibres, although sarcomere-like structures were not achieved.

SN spheroids enriched in TrkC+ neurons were successfully cultured together with hSkMc in Xona commercial devices, leading to the formation of ASW-like structures, even in conditions in which SkM

cells were not fully differentiated. In the contact points between TrkC+ axons wrapping around SkM fibres, synaptic bouton-like structures were observed, that to our knowledge, have not been reported before in human *in vitro* cultures. Further studies would be required to evaluate those structures, characterise the cells and assess the functionality of the connection.

A multilayer PDMS device, named MINDS, suitable for 3D culture of three neuromuscular cell types embedded in Matrigel was successfully designed and fabricated. The tests performed to evaluate fluidic connection, leakage, and the device filling protocol with Matrigel and media showed that it is a feasible device that can be used for 3D cell culture containing cells embedded in Matrigel and enough medium supply with small diffusion among compartments.

Finally, TrkC+ enriched SN, SkM and MN were successfully cocultured in MINDS devices These results also show a proof of concept for the feasible use of MINDS devices seeding three cell types. This is the first time reported until now in which SN have been seeded together with hSkMc and MN, in 3D, in a microfluidic device, using human cells. The use of the here presented compartmentalised microfluidic culture systems, together with the differentiation techniques performed, present a **personalised medicine tool** for studies of the spinal neuromuscular circuit in healthy conditions and in different diseases. This offers a possibility

for studying the neuromuscular circuit (its formation, development, regulation, maintenance and repair), and to apply that knowledge onto NMD, such as ALS, serving as a platform to test drugs.

The compartmentalised culture performed in different microfluidic devices demonstrates the suitability of those platforms for the study of spinal neuromuscular circuit in more physiological conditions. Identifying and characterising neuromuscular circuit failures in a NMD physiological study model, such as the ones presented here, could help discovering new therapies. The findings exposed in this chapter represent the first steps towards a future 3D physiological spinal neuromuscular study model on a chip.

4.7. References

1. Paoli, R., Homs Corbera, A. & Samitier Martí, J. Cell culture interfaces for different organ-on-chip applications: from photolithography to rapid-prototyping techniques with sensor embedding. (Universitat de Barcelona; Institut de Bioenginyeria de Catalunya, 2019).
2. Badiola-Mateos, M., Hervera, A., del Río, J. A. & Samitier, J. Challenges and future prospects on 3D in-vitro modeling of the neuromuscular circuit. *Front. Bioeng. Biotechnol.* **6**, 194 (2018).
3. Rumsey, J. W., Das, M., Bhalkikar, A., Stancescu, M. & Hickman, J. J. Tissue engineering the mechanosensory circuit of the stretch reflex arc: Sensory neuron innervation of intrafusal muscle fibers. *Biomaterials* **31**, 8218–8227 (2010).
4. Liu, H. *et al.* Formation of neuromuscular junction-like structure between primary sensory terminals and skeletal muscle cells in vitro. *Anat. Rec. Adv. Integr. Anat. Evol. Biol.* **294**, 472–478 (2011).
5. Guo, X. *et al.* Tissue engineering the mechanosensory circuit of the stretch reflex arc with human stem cells: Sensory neuron innervation of intrafusal muscle fibers. *Biomaterials* **122**, 179–187 (2017).
6. Qiao, Y., Cong, M., Li, J., Li, H. & Li, Z. The effects of neuregulin-1β on intrafusal muscle fiber formation in neuromuscular coculture of dorsal root ganglion explants and skeletal muscle cells. *Skelet. Muscle* **8**, 29 (2018).
7. Simon, A., Shenton, F., Hunter, I., Banks, R. W. & Bewick, G. S. Amiloride-sensitive channels are a major contributor to mechanotransduction in mammalian muscle spindles. *J. Physiol.* **588**, 171–185 (2010).
8. De Nooij, J. C., Doobar, S. & Jessell, T. M. Etv1 inactivation reveals proprioceptor subclasses that reflect the level of NT3 expression in muscle targets. *Neuron* **77**, 1055–1068 (2013).
9. Fukuhara, K. *et al.* Specificity of monosynaptic sensory-motor connections imposed by repellent Sema3E-PlexinD1 signaling. *Cell Rep.* **5**, 748–758 (2013).
10. de Nooij, J. C. *et al.* The PDZ-domain protein Whirlin facilitates mechanosensory signaling in mammalian proprioceptors. *J. Neurosci.* **35**, 3073–3084 (2015).
11. Woo, S. H. *et al.* Piezo2 is the principal mechanotransduction channel for proprioception. *Nat. Neurosci.* **18**, 1756–1762 (2015).
12. Appel, E. *et al.* An ensemble of regulatory elements controls Runx3 spatiotemporal expression in subsets of dorsal root ganglia

proprioceptive neurons. *Genes Dev.* **30**, 2607–2622 (2016).

13. Lin, S.-H. *et al.* Evidence for the involvement of ASIC3 in sensory mechanotransduction in proprioceptors. *Nat. Commun.* **7**, 11460 (2016).

14. O'Toole, S. M. *et al.* Dicer maintains the identity and function of proprioceptive sensory neurons. *J. Neurophysiol.* **117**, 1057–1069 (2017).

15. Poliak, S., Norovich, A. L., Yamagata, M., Sanes, J. R. & Jessell, T. M. Muscle-type Identity of Proprioceptors Specified by Spatially Restricted Signals from Limb Mesenchyme. *Cell* **164**, 512–525 (2016).

16. Paik, S. K. *et al.* γ-Aminobutyric acid-, glycine-, and glutamate-immunopositive boutons on mesencephalic trigeminal neurons that innervate jaw-closing muscle spindles in the rat: Ultrastructure and development. *J. Comp. Neurol.* **520**, 3414–3427 (2012).

17. Franco, J. A., Kloefkorn, H. E., Hochman, S. & Wilkinson, K. A. An in vitro adult mouse muscle-nerve preparation for studying the firing properties of muscle afferents. *J. Vis. Exp.* e51948 (2014) doi:10.3791/51948.

18. Formenti, A. & Zocchi, L. Error signals as powerful stimuli for the operant conditioning-like process of the fictive respiratory output in a brainstem–spinal cord preparation from rats. *Behav. Brain Res.* **272**, 8–15 (2014).

19. Sonner, M. J., Walters, M. C. & Ladle, D. R. Analysis of proprioceptive sensory innervation of the mouse soleus: a whole-mount muscle approach. *PLoS One* **12**, e0170751 (2017).

20. Vaughan, S. K., Stanley, O. L. & Valdez, G. Impact of aging on proprioceptive sensory neurons and intrafusal muscle fibers in mice. *Journals Gerontol. Ser. A Biol. Sci. Med. Sci.* **72**, 771–779 (2016).

21. Van de Winckel, A. *et al.* Age-related decline of wrist position sense and its relationship to specific physical training. *Front. Hum. Neurosci.* **11**, 570 (2017).

22. Dionisi, C., Rai, M., Chazalon, M., Schiffmann, S. N. & Pandolfo, M. Induced pluripotent stem cell-derived primary proprioceptive neurons as Friedreich ataxia cell model. *bioRxiv* 829358 (2019) doi:10.1101/829358.

23. Mentis, G. Z. *et al.* Early functional impairment of sensory-motor connectivity in a mouse model of spinal muscular atrophy. *Neuron* **69**, 453–467 (2011).

24. Gogliotti, R. G. *et al.* Motor neuron rescue in spinal muscular atrophy mice demonstrates that sensory-motor defects are a consequence, not a cause, of motor neuron dysfunction. *J. Neurosci.* **32**, 3818–3829 (2012).

25. Thirumalai, V. *et al.* Preservation of VGLUT1 synapses on ventral calbindin-immunoreactive interneurons and normal locomotor function in a mouse model of spinal muscular atrophy. *J. Neurophysiol.* **109**, 702–710 (2013).

26. Fletcher, E. V *et al.* Reduced sensory synaptic excitation impairs motor neuron function via Kv2.1 in spinal muscular atrophy. *Nat. Neurosci.* **20**, 905–916 (2017).

27. Vaughan, S. K., Kemp, Z., Hatzipetros, T., Vieira, F. & Valdez, G. Degeneration of proprioceptive sensory nerve endings in mice harboring amyotrophic lateral sclerosis-causing mutations. *J. Comp. Neurol.* **523**, 2477–2494 (2015).

28. Vaughan, S. K. *et al.* The ALS-inducing factors, TDP43A315T and SOD1G93A, directly affect and sensitize sensory neurons to stress. *Sci. Rep.* **8**, 16582 (2018).

29. Lalancette-Hebert, M., Sharma, A., Lyashchenko, A. K. & Shneider, N. A. Gamma motor neurons survive and exacerbate alpha motor neuron degeneration in ALS. *Proc. Natl. Acad. Sci.* **113**, E8316–E8325 (2016).

30. Seki, S. *et al.* Circuit-specific early impairment of proprioceptive sensory neurons in the SOD1 G93A mouse model for ALS. *J. Neurosci.* **39**, 8798–8815 (2019).

31. Sábado, J. *et al.* Accumulation of misfolded SOD1 in dorsal root ganglion degenerating proprioceptive sensory neurons of transgenic mice with amyotrophic lateral sclerosis. *Biomed Res. Int.* **2014**, 1–13 (2014).

32. Colón, A., Badu-Mensah, A., Guo, X., Goswami, A. & Hickman, J. J. Differentiation of intrafusal fibers from human induced pluripotent stem cells. *ACS Chem. Neurosci.* **11**, 1085–1092 (2020).

33. Jha, B. S., Rao, M. & Malik, N. Motor neuron differentiation from pluripotent stem cells and other intermediate proliferative precursors that can be discriminated by lineage specific reporters. *Stem Cell Rev. Reports* **11**, 194–204 (2015).

34. Uzel, S. G. M. *et al.* Microfluidic device for the formation of optically excitable, three-dimensional, compartmentalized motor units. *Sci. Adv.* **2**, e1501429 (2016).

35. Osaki, T., Uzel, S. G. M. & Kamm, R. D. Microphysiological 3D model of amyotrophic lateral sclerosis (ALS) from human iPS-derived muscle cells and optogenetic motor neurons. *Sci. Adv.* **4**, eaat5847 (2018).

36. Osaki, T., Uzel, S. G. M. & Kamm, R. D. On-chip 3D neuromuscular model for drug screening and precision medicine in neuromuscular disease. *Nat. Protoc.* **15**, 421–449 (2020).

37. Rueden, C. T. *et al.* ImageJ2: ImageJ for the next generation of scientific image data. *BMC Bioinformatics* **18**, 529 (2017).

38. Sala-Jarque, J. *et al.* Neuromuscular Activity Induces Paracrine Signaling and Triggers Axonal Regrowth after Injury in Microfluidic Lab-On-Chip Devices. *Cells* **9**, 302 (2020).

39. Esteban Tezanos, A., Badiola Mateos, M. & Samitier Martí, J. Maturation and characterisation of optically excitable skeletal muscle model in-vitro. (Universitat de Barcelona, 2018).

40. Shibayama, E. & Koizumi, H. Cellular localization of the Trk neurotrophin receptor family in human non-neuronal tissues. *Am. J. Pathol.* **148**, 1807–18 (1996).

41. Shelton, D. *et al.* Human trks: molecular cloning, tissue distribution, and expression of extracellular domain immunoadhesins. *J. Neurosci.* **15**, 477–491 (1995).

42. Macefield, V. G. & Knellwolf, T. P. Functional properties of human muscle spindles. *J. Neurophysiol.* **120**, 452–467 (2018).

43. Alshawaf, A. J. *et al.* Phenotypic and functional characterization of peripheral sensory neurons derived from human embryonic stem cells. *Sci. Rep.* **8**, 603 (2018).

44. Viventi, S. & Dottori, M. Modelling the dorsal root ganglia using human pluripotent stem cells: A platform to study peripheral neuropathies. *Int. J. Biochem. Cell Biol.* **100**, 61–68 (2018).

Chapter 5

Blood-brain barrier on a chip: monitoring barrier integrity

Summary

This chapter is focused on the study of the blood-brain barrier (BBB). Here its structure is studied, and a simplified version of its functional unit is mimicked in a novel microfluidic platform integrating electrodes for barrier monitorisation analysis. The aim of this work was to assess a new healthy BBB-like microfluidic platform combined with a label-free, non-invasive and real-time barrier monitoring method based on electrical impedance spectroscopy (EIS). Endothelial cells and pericytes were cultured on opposite sides of the membrane embedded in the microfluidic device. Once the barrier was formed, hyperosmotic transient BBB opening was induced with mannitol. EIS-based monitoring was able to detect barrier formation, opening and its regeneration after the treatment, correlating with results obtained from immunostainings. The model and measurement technique presented here pave the way for elucidating the phenomena ongoing on the BBB.

Published content, contributions and acknowledgements

This work is an adaptation of the following paper:

In-vitro real-time monitoring of the blood-brain barrier integrity by machine learning algorithms of on-chip multiple point impedance spectroscopy

M. Badiola-Mateos,‡[ab] D. Di Giuseppe,‡[ef] R. Paoli,‡[ab] M. J. López,[ab] A. Mencanttini,[ef] J. Samitier,[abcd] E. Martinelli[ef]

[a] Nanobioengineering group, Institute for Bioengineering of Catalonia (IBEC)
Barcelona Institute of Science and Technology (BIST), Barcelona, Spain
[b] Department of Electronics and Biomedical Engineering, University of Barcelona, Barcelona, Spain
[c] Centro de Investigación Biomédica en Red en Bioingeniería, Biomateriales y Nanomedicina (CIBER-BBN), Madrid, Spain
d Institute of Nanoscience and Nanotechnology, Universitat de Barcelona (UB), Barcelona, Spain
[e] Department of Electronic Engineering, University of Rome Tor Vergata, Rome, Italy
[f] Interdisciplinary Center for Advanced Studies on Lab-on-Chip and Organ-on-chip applications (IC-LOC), University of Rome Tor Vergata, Rome, Italy
‡ These authors contributed equally to this work.

In preparation for ACS Sensors, September 2020

This work was done in collaboration with Roberto Paoli, PhD student from Nanobioengineering group at IBEC, who designed the microfluidic device and the flowing set-up, fabricated the device and performed the experiments; with Davide Di Giuseppe and his supervisor Prof. Eugenio Martinelli, from Sensors group of Rome Tor Vergata University, who collaborated in the device fabrication, electrode design, impedance spectroscopy, and video analysis; and with Dr. Maria José López, senior researcher from Nanobioengineering group at IBEC, who provided daily supervision on the project, and a hand when needed through the whole experiment. I, myself, collaborated on the cell culture processes, biological application design, and immunostainings.

5.1. Introduction

5.1.1. The blood-brain barrier

The blood-brain barrier (BBB), the most studied blood-neural barrier, is localised at the central nervous system (CNS) brain microvessels. It is a physical, metabolic and transport dynamic barrier constituted by a single layer of non-fenestrated endothelial cells (EC), surrounded by a basal membrane, and perivascular cells (pericytes or smooth muscle in the case of larger vessels, the end-feet of astrocytes, microglia and neurons), that collectively form the neurovascular unit (NVU),[1] see FIGURE 5-1. Surrounding the BBB, macrophages, and other immune cells interact with the BBB regulating its permeability through inter- or intra-cellular signalling, forming together the extended NVU.[2] The BBB is responsible for mediating brain supply of nutrients, waste efflux and inhibiting paracellular diffusion, forcing the transport of each kind of molecule through different transcellular mechanisms, as previously reviewed.[1] In this way it protects the CNS from: toxins, ion fluctuations (that would otherwise affect synaptic and axonal signalling), interferences with neurotransmitters released in the peripheral nervous system, inflammatory reactions, and flow of macromolecules.[3]

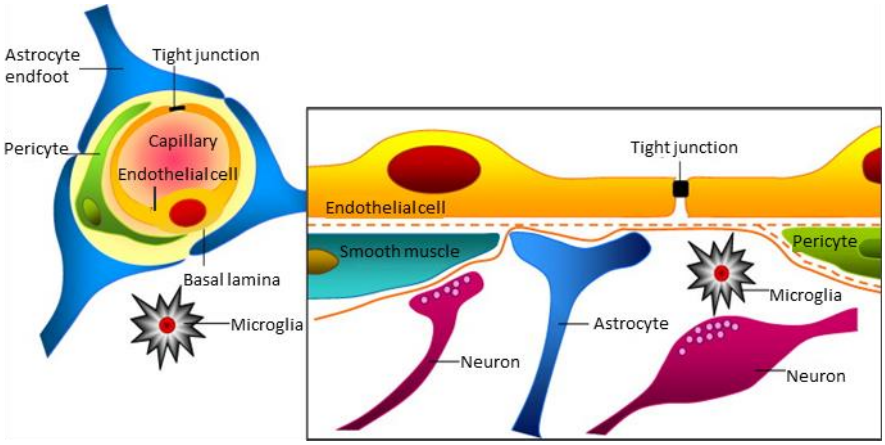

Figure 5-1. *Structure of a healthy NVU: a single layer of non-fenestrated endothelial cells (EC), surrounded by a basal membrane (discontinuous orange line), and perivascular cells (pericytes or smooth muscle in the case of larger vessels, the end-feet of astrocytes, microglia and neurons). Brain endothelial cells and pericytes are enclosed by and contribute to the local basement membrane, that forms a particular perivascular extracellular matrix. End-feet of astrocytes are in contact with the external basement membrane. Microglia and axonal projections are located in the peripheral neural tissue. All together, they contribute on forming TJ and AJ (not included in the picture) sealing the aqueous paracellular diffusion pathway. Image reproduced with permission from Abbott et al, 2010.*[1]

This is only possible due to its junctional complexes: tight junctions (TJ), adherens junctions (AJ) and gap junctions.[4,5] These complexes are intertwined nets of proteins that have a role in controlling the passage of substances. Gap junctions are essential for intercellular communication.[6,7] TJ can finely regulate barrier permeability by sealing the membrane and forming dynamic size- or charge-selective channels.[8,9] However, barrier integrity and dynamics are regulated by both TJ and AJ.[10,11] In brain EC, the major transmembrane AJ protein is vascular endothelial cadherin (VE-cadherin).[12] VE-cadherin based AJ are regulated by zonula occludens 1 (ZO-1), one of the most relevant components of the TJ, essential for the endothelial barrier formation.[13]

To understand the effect of dysfunctional BBB in some diseases, it is first necessary to modulate barrier tightness in *in vitro* models and to be able to efficiently monitor it. Opening the BBB for drug delivery to the CNS — for cancer or neurological disease treatment —, or closing it in pathologies involving BBB dysfunction and leakiness — such as stroke, ALS, Alzheimer or multiple sclerosis, among others reviewed elsewhere[1,4] —, is still a challenge. Barrier tightening studies mostly focus on molecular approaches, using several compounds to promote the sealing (such as dexamethasone, calcium channel blockers, brain hypothermia, pan-caspase inhibitors or VEGF), as previously summarised.[14] In contrast, barrier opening studies use two main approaches to enhance the CNS drug delivery: the transient BBB opening (BBBO)[15] and molecular modifications.[5,16,17] One of the main problems on targeting CNS drug delivery through molecular modifications, is the possible interaction among the numerous pathways involved in inducing junction complex changes. Although great advances have recently been made on elucidating the potential TJ regulation mechanisms,[5] little is known yet about predominant and downstream pathways. In contrast with molecular modification techniques, BBBO can be used to deliver small or large weight compounds of different nature to the CNS and is not affected by predominant or downstream molecular pathways involved in junctional complex changes. The intraarterial infusion of hyperosmotic agents, such as mannitol, is currently the gold standard technique to promote BBBO to enhance

drug delivery to the nervous system, such as for CNS chemotherapy.[18,19] *In vivo* trials of BBBO with mannitol have reported to be successful for 75% of patients, with 40 min BBBO time and less than 8 h recovery time.[19] Mannitol induces the following cascade of events recently reviewed by Linville *et al.:*[20] **1)** first of all, it induces an osmolarity driven fluid movement in EC, originating their shrinkage, increasing tensile forces on TJ; **2)** the weakest TJ between adjacent cells fail first, generating transient focal leaks (subcellular randomly distributed disruptions in the endothelium of 1-2 μm); **3)** paracellular permeability increases almost instantaneously, not altering the transcellular permeability or the global TJ network (ZO-1 expression remains intact within about 125 μm from the focal leak); **4)** microvessel diameter decreases and EC present vacuolation in a dose-dependent manner; **5)** EC apoptosis and lost occurs in a dose-dependent manner, probably as a result of vacuolation;[21] **6)** BBBO is reversed and the barrier function is re-stablished in a period of time inversely proportional to the dose; **7)** accumulated hyperosmotic stress can cause inconsistent barrier function up to 48h after the mannitol application. The BBBO occurs as a result of the magnitude of cell density, cells shrinkage and TJ strength. This means that low density of cells, fragile TJ and high cell shrinkage will always result in a BBBO and their magnitude will define recovery time. Therefore, the effects of mannitol BBBO treatment will always vary for each tissue condition (physiological and pathological), microvessel dimension

and treatment dose. But it is reasonable to conclude that it is a technique with a great potential still to be explored in detail.

5.1.2. BBB-on-a-chip: state of the art

Although great progress has been made in the last years in the BBB field, there is a big gap of knowledge to overcome before being able to understand events undergoing when the barrier opens in different diseases and to find treatments for them. This gap of knowledge is partially due to current technologies for BBB research. Currently used *in vitro* study models mimicking cellular barriers include: **i)** parallel artificial membrane permeability assays (PAMPA); **ii)** organoids; **iii)** cell-based Transwell assays; and **iv)** microfluidic devices and organ-on-chip systems.[22,23] BBB-like microfluidic devices can mimic a biological barrier by the compartmentalization created with: semipermeable synthetic[24,25] or organic[26] membranes, microchannels or micropillars,[27–29] gel-liquid interfaces,[30] tubules and vessels embedded within an extracellular matrix,[31] or *de novo* generated vessels through vasculogenesis and sprouting.[32] These devices offer several advantages: they can include shear-stress,[33,34] they can mimic 2D[28,35] or 3D[30,33,36] environments, they can be adapted for high-throughput,[37] connected to other microfluidic devices mimicking the brain parenchyma,[33] and they can integrate electrodes for performing electrical measurements on the biological microenvironment.[38,39]

BBB-like devices of microfluidic devices usually follow four main approaches: sandwich design, parallel design, 3D tubular design and vasculogenesis design.[23]

Most microfluidic devices mimicking the BBB are fabricated through photolithography and soft-lithography techniques. Poly-dimethylsiloxane (PDMS) is by far the gold standard material used in polymer microfluidics because of material elasticity, gas permeability, good optical transmissivity and other several unique advantages.[40] Nonetheless, PDMS still has some known limitations (i.e. media evaporation, absorption of hydrophobic molecules, non-scalability of the process, etc.).[41] Other materials such as polystyrene (PS) and cyclic olefin polymers (COP) are recently emerging as an alternative. COP has some interesting properties for biological experiments: lower absorption levels of hydrophobic drug molecules,[42] biologically inert,[43] not immunogenic,[44,45] high transparency in the visible and near ultraviolet regions of the spectrum,[43] and low autofluorescence.[46] Furthermore, it can be manufactured through rapid prototyping technique based on laser cutting.[47] It facilitates the fabrication of multi-layer devices by cutting through sheets of hard polymers the desired geometries and bonding all the layers with solvent-assisted bonding,[47,48] ultraviolet-ozone surface treatment[49] or transfer tape.[50] This rapid prototyping process offers some advantages: **1)** fast fabrication (i.e.: a complete microfluidic device can be cut and assembled in less than 10 min);

2) scalable process; **3)** ease of design variations and adjustments; **4)** it is cost-effective since it does not require cleanroom facilities.

5.1.3. Membrane integrity analysis

To fully understand the function of the BBB and the processes ongoing in pathological conditions such as ALS, the junctional properties have to be assessed in relation to the barrier integrity as result of a tested condition. They can be evaluated at different levels with several techniques reviewed by Keep *et al.* :[5] **1)** ultrastructural analysis of changes in TJ structure with electron microscopy; **2)** junction protein expression analysis with western blot; **3)** protein-protein interaction analysis with immunoprecipitation; **4)** protein localization assessment with immunostaining, two-photon microscopy, fluorescence resonance energy transfer, or fluorescence recovery after photobleaching; and **5)** mRNA expression analysis through qPCR. Quantifying the permeability of a barrier is essential to evaluate the effects of a compound (e.g. a vasodilator or vasoconstrictor drug), to test the ability of a compound to cross the barrier (e.g. nanoparticles for glioblastoma treatment[51]), and to monitor the progression of membrane integrity and functionality during a disease (e.g. elucidating the evolution of BBB structure and functionality in ALS under bone marrow-derived endothelial progenitor cells treatment[52]).

There are two gold standard techniques to quantify the membrane integrity: quantification of the diffusion of different tracers and trans-epithelial electrical resistance (TEER) measurements. Tracer diffusion permeability assays measure the diffusion of a known tagged compound from a donor to a receiver compartment and facilitate determining size- and charge-selectivity of the membrane.[53] This known compounds (sucrose, dextran, inulin, lucifer yellow, etc.) are radioisotope, fluorescent molecule or biochemically tagged. Although it is low-cost and it helps assessing transepithelial transport in both directions, this method has three main drawbacks: the tracers have to be carefully chosen not to interfere with the BBB function or the experiment; each tracer provides discrete limited information about the specific tracer-related membrane pore size and charge instead of global membrane integrity; and it is a single timepoint analysis. On the other hand, TEER measurement can quantify the net movement of ions across the barrier and it can be performed in real-time without damaging cells.[54] It is based on measuring the ohmic resistance applying direct current (DC) voltage to a pair of electrodes separated by the cellular barrier and reading the resulting current. However, when performing TEER on biological samples, since DC stimuli can damage the cells, an alternate current (AC) is applied in a frequency range of 10 – 100 Hz. The obtained barrier resistance is typically normalised against the measured area and expressed in $\Omega \cdot cm^2$. However, this technique has a big limitation: a complex biological process, such as

BBB permeability variations, is resumed in a single numeric value that depends on the electrode properties and positioning. To overcome these limitations, the approach proposed in this work to assess BBB integrity *in vitro* relies on electrical impedance spectroscopy (EIS) measurements and machine-learning algorithms. This label-free and non-invasive technique provides a multivariate representation of multifrequency TEER, by applying AC excitation voltages. The use of EIS has been exploited to enlarge the capability provided by TEER to a wider range of frequencies for maximizing the amount of information that can be acquired from the electric measurements reducing the damage caused to cells by DC applied on TEER and the complications of placing the electrodes on opposite sides of a membrane.

5.2. Specific objectives of the chapter

The global aim of this chapter was to create a microfluidic healthy BBB mimicking system, modulate barrier integrity and monitor it through a methodology that could easily be translated for ALS-BBB integrity studies in order to elucidate the ongoing events during disease evolution. For that purpose, the specific objectives of the chapter have been:

- To adapt a two-compartment microfluidic device for a blood-brain barrier on a chip *in vitro* model.
- To mimic a simplified healthy BBB model, coculturing endothelial cells and pericytes on the fabricated compartmentalised microdevice
- To promote BBB formation, disruption after hyperosmotic treatment and recovery.
- To design a system to analyse barrier integrity assembled in the microfluidic device.
- To assess barrier status at different timepoints correlating results obtained through immunostaining with barrier integrity measurement techniques (with dyes and EIS).

5.3. Materials and methods

5.3.1. Facilities

All cell-culture experiments were performed at Nanobioengineering lab, Institute of Bioengineering of Catalonia (IBEC), Barcelona, Spain. Confocal microscopy imaging was performed at the Advanced Microscopy Facilities of Institute for Research in Biomedicine (IRB), Barcelona, Spain. Fluorimetry analysis was performed at Parc Cientific de Barcelona (PCB) common facilities. The electrodes for the devices were fabricated in the MicroFabSpace and Microscopy Characterization Facility, unit 7 of ICTS (Infraestructuras Científicas y Técnicas Singulares) NANOBIOSIS from CIBER-BBN at IBEC. Laser cutting was performed at the Electronic Engineering department, Università degli Studi di Roma "Tor Vergata", Rome, Italy. Devices were finally assembled at Instituto di Fotonica e Nanotecnologie - Consiglio Nazionale delle Ricerche (IFN-CNR), Rome, Italy.

5.3.2. Experimental design

The following experiments aimed to mimic the BBB formation (co-culturing two different kind of cells), its disruption after administering D-Mannitol, and monitorisation of the barrier opening and regeneration through EIS and immunostaining. For that purpose, EC and pericytes were cultured in different experimental conditions (with or without mannitol; cocultured or alone) and

platforms (µBBB device, with or without electrodes for imaging purposes or in Petri dishes), as described in TABLE 5-1.

Table 5-1. *Experimental conditions overview. Petri dish monocultures were used as a control to compare with the events observed in µBBB devices. EC = endothelial cell; DIV = days in vitro; DoC = day of confluency; N/A = not applicable.*

Platform		Sample	Cells	Events			Purpose
				DoC	DoC+2	DoC+3	
µBBB devices	electrodes	**µBBB-treated**	EC + Pericyte	2 DIV	Mannitol	Fixation	Monitoring of the barrier through EIS
	no electrodes	**µBBB-treated**	EC + pericyte	3 DIV	Mannitol	Fixation	Imaging of the barrier 24 h after mannitol
		µBBB-control	EC + pericyte	3 DIV	Fixation	N/A	Imaging of the barrier before mannitol
		µBBB-EC-only	EC + empty channel	3 DIV	Mannitol	Fixation	Imaging of the barrier 24 h after mannitol without pericytes
Petri dish monocultures	EC	**EC-Petri-NoTreat**	EC	2 DIV	N/A	Fixation	Imaging EC before mannitol
		EC-Petri-0h	EC	2 DIV	Mannitol + Fixation	N/A	Imaging EC 0 h after mannitol
		EC-Petri-24h	EC	2 DIV	Mannitol	Fixation	Imaging EC 24 h after mannitol
	Pericytes	**PC-Petri-NoTreat**	Pericyte	2 DIV	N/A	Fixation	Imaging pericytes before mannitol
		PC-Petri-0h	Pericyte	2 DIV	Mannitol + Fixation	N/A	Imaging pericytes 0 h after mannitol
		PC-Petri-24h	Pericyte	2 DIV	Mannitol	Fixation	Imaging pericytes 24 h after mannitol

The timepoints of representative events (seeding, mannitol, fixation) are normalised against the timepoint when confluency was reached (DoC, day of confluence) on the microdevices, as there were variations in the effective seeding density observed. This was a measure to assure that mannitol treatment was applied on confluent monolayers, in equivalent conditions.

5.3.3. Microdevice fabrication

The microfluidic device, named "µBBB device", is formed of a porous polycarbonate membrane of 1 µm pore size and 10 µm thickness (Whatman® Cyclopore® polycarbonate and polyester membranes, Sigma-Aldrich #WHA70914710, U.S.) sandwiched between two networks of 4 parallel microfluidic channels (2 mm width, 180 µm height, 20 mm length) made of COP (180 µm thickness sheets), as shown in FIGURE 5-2. The two microchannel networks are placed perpendicularly, forming 16 intersections (surface area: $4\,mm^2$ each) on a single device. Each intersection forms a structure as shown in FIGURE 5-3 with two pairs of interdigitated electrodes, located respectively on the top of the upper channel and on the bottom of the lower channel with the membrane in between.

The device was designed in Autodesk Inventor®. Both COP sheets (Zeonor® #1420R, Zeon Corporation, Japan), adhesive transfer tape sheets (3M™ #467MP, U.S.) and double sided biocompatible pressure sensitive adhesive sheets (ARSeal® 8026, Adhesive

Research Inc., U.S.) were cut to the custom design using a Trotec Speedy 100 (Trotec Laser Inc., Austria) laser cutter system.

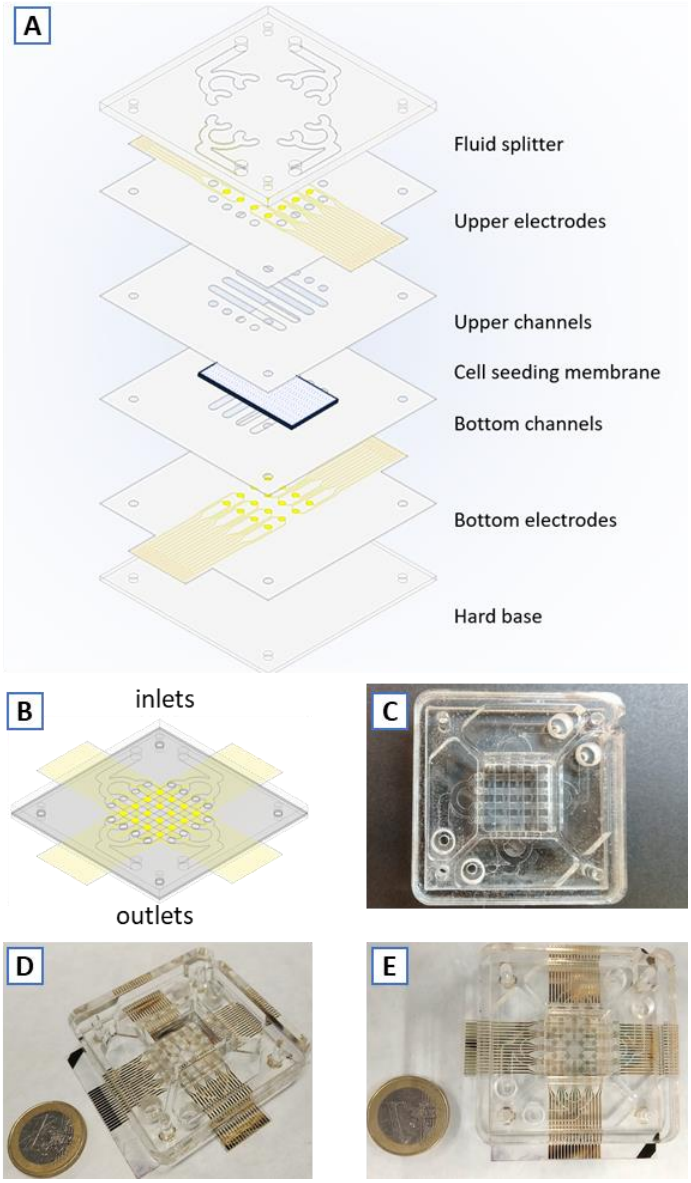

Figure 5-2. *µBBB device design.* ***A)*** *Exploded diagram of the device layout with integrated electrodes in opposite sides of the cell seeding membrane. Upper electrodes are under the COP layer but are shown on top for visual clarity.* ***B)*** *Diagram of the device with all the layers assembled.* ***C)*** *Picture of the device without electrodes.* ***D and E)*** *Picture of the device with integrated electrodes.*

Gold electrodes were fabricated on top of the corresponding COP layer. Briefly, after sputtering the substrates with 100 nm of gold, a 2 µm thick layer of AZ® 5214-E photoresist (Microchemicals GmbH, Germany) was spun on the substrate (2000 rpm, 30 seconds) and baked at 95 °C on a hotplate. Substrate was aligned with a chrome mask with the desired features, exposed with UV light (Energy of $200\ mJ \cdot cm^{-2}$) and developed for 30 seconds using 1:4 dilution of AZ® 400K Developer (Microchemicals GmbH, Germany) in milli-Q water. Gold was wet etched using TFA etchant (Transene Co Inc., U.S.) for 40 seconds. Finally, photoresist was removed by washing in AZ® 100 (Microchemicals GmbH, Germany) for 60 seconds.

The layers were assembled using a custom-made aluminium aligner. The assembly of the device started with the bottom half of the device, aligning first the COP and double-sided biocompatible pressure sensitive adhesive sheets, and then for top half layers, using a hydraulic press at 120 bar for 30 seconds. The polycarbonate membrane was manually cut to size, carefully positioned in contact with the channels before aligning and assembling with the previous stacks (FIGURE 5-2). Finally, PMMA layers forming medium reservoirs on top of the device were added with the 467MP transfer tape and pressed sequentially to obtain the complete device. The poly-methyl-meta-acrilate (PMMA) layer served as well as an interface to connect with the microfluidic set up: disposable syringes using 23G flat needles, Tygon tubing and ¼-28 UNF fluidic connectors.

5.3.4. Cell culture

The cell culture of experimental samples described in TABLE 5-1 was done as follows:

5.3.4.1. Cell culture on Petri dishes

For the culture of EC, glass bottom Petri dishes (Nunc™ #150682, Thermo Fisher Scientific, U.S.) were coated with collagen type-I solution from rat tail (5% v/v in PBS, 1h at 37 °C) (Sigma-Aldrich #C3867, U.S.). Human brain endothelial cells, hCMEC/D3 cell line (#SCC066) were seeded at a density of $50.000\ cell \cdot cm^{-2}$ in EC medium: EndoGRO MV complete culture medium (#SCME004) supplemented with 1 ng/mL basic fibroblast growth factor (bFGF, #GF003-AF) and 1% penicillin-streptomycin (P/S, Gibco® #15140-122, U.S.). Cells and all the media components were purchased from Merck Millipore (U.S.) unless stated otherwise.

For the culture of pericytes, glass bottom Petri dishes were coated with gelatine from porcine skin ($2\ mg \cdot mL^{-1}$, 15 min, 37 °C) (Sigma Aldrich #G1890, U.S.). Bovine pericytes were kindly donated by Prof. Ernest Giralt from Design, Synthesis and Structure of Peptides and Proteins group, at Institute for Research in Biomedicine (IRB Barcelona). They were seeded at a density of $36.000\ cell \cdot cm^{-2}$ in pericyte medium: Dulbecco's Modified Eagle Medium (DMEM, Gibco® #41965039, Thermo Fisher Scientific, U.S.), supplemented

with 20% calf serum (Sigma-Aldrich #C8056, U.S.), 1 ng/mL bFGF and 1% P/S.

In both cases, cells were kept in culture for a total of 5 days, changing the medium daily. After 4 DIV (DoC+2), some samples were treated with D-Mannitol (0.3 M, 45 min, 37 °C) (Sigma-Aldrich #M9647, U.S.), based on previous publications.[55] Afterwards samples were washed and changed back to their supplemented culture medium.

At the endpoint for each condition, samples were fixed in 4% paraformaldehyde (PFA, Sigma Aldrich #P6148, U.S.) for 30 min at room temperature, then washed with phosphate buffer saline (PBS, Gibco® #21600-010, Thermo Fisher Scientific, U.S.) and kept in PBS with 0.02% of sodium azide (Sigma-Aldrich #71290, U.S.) for a better preservation.

5.3.4.2. Cell culture on µBBB devices

The previously described cell seeding protocol from Petri dishes was adapted to microdevices through the steps described below. In all cases channels and inlet reservoirs were filled, and negative pressure driven flowrate of -50 µL/min was applied using a PHD 2000 Syringe Pump (Harvard Apparatus, U.S.).

Microdevice sterilisation: Top and bottom channels were sterilised perfusing 70% ethanol, then dried using N_2 gas stream.

Microdevice activation: Previously dried microdevices were exposed in the ultraviolet/ozone cleaner (BioForce Nanoscience, U.S.) for 20 min, after which both channels were filled inside the cell culture hood with sterile PBS (2 $mg \cdot mL^{-1}$, 15 min, 37 °C).

Microdevice coating: Lower channels were functionalised with collagen solution (1:20, 1 h, 37 °C) and upper channels were functionalised with a gelatine solution (2 $mg \cdot mL^{-1}$, 15 min, 37 °C).

Cell culture: Both EC and pericytes were seeded sequentially in the devices, as shown in FIGURE 5-3. A cell suspension of hCMEC/D3 cells in EC medium was inserted at the bottom channel ($2.8 \cdot 10^6\ cells \cdot mL^{-1}$) and left incubating for at least 2 h flipped upside-down to promote cell-adhesion onto the membrane. Then a cell suspension of pericytes in pericyte medium was inserted at the upper channel ($2 \cdot 10^6\ cells \cdot mL^{-1}$), except for the µBBB-EC-only devices, in which the top channel was filled with EC medium. Devices were incubated in a humidified CO_2 incubator at 37 °C, with reservoirs filled of corresponding media and covered with a lid, changing the media every day. At DoC+2, some samples were treated with D-Mannitol (0.3M, 45 min, 37 °C), and then washed and changed back to their supplemented culture medium.

Cell fixation: At the endpoint for each condition, samples were fixed in 4% PFA for 30 min at room temperature, then washed with PBS and kept in PBS with 0.02% of sodium azide.

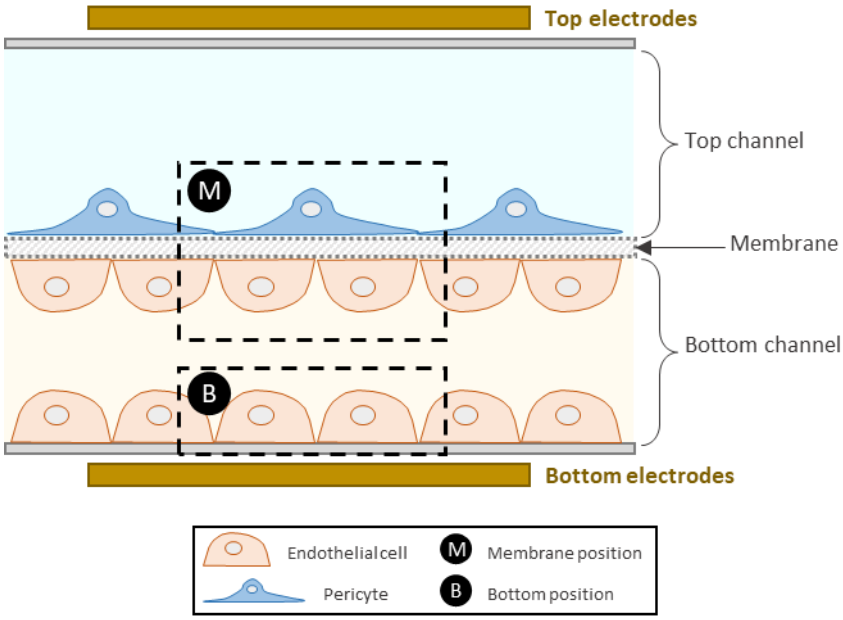

Figure 5-3. *Functional structure of each intersection and EIS measurement position on the "µBBB device". Endothelial cells are seeded in the bottom channel in contact with the bottom of the device and with the polycarbonate membrane, while pericytes are seeded on the bottom of the upper channel in contact with the polycarbonate membrane. Both membrane-position and bottom-position are analysed for imaging purposes. Each channel is covered with the culture medium required for each cell type. A pair of interdigitated electrodes are located on the top of the upper channel and the bottom of the lower channel to perform impedance spectroscopy measurements.*

5.3.5. Immunostaining

Immunostaining was performed in Petri dishes and µBBB devices without electrodes. For microfluidic devices, solutions were applied filling the inlet and using a negative pressure driven flow of $-50\ \mu L \cdot min^{-1}$ with a PHD 2000 Syringe Pump. All steps were performed at room temperature, unless stated otherwise. All Invitrogen™ and

Gibco® products mentioned below were purchased from Thermo Fisher Scientific (U.S.).

On the first day of the immunostaining, samples were washed with PBS, and then permeabilised with PBS with 0.1% Triton (Sigma-Aldrich #T8787, U.S.). Then they were incubated for 2 h at room temperature with a blocking solution: PBS with 0.1% Triton and 10% foetal bovine serum (FBS, Gibco® #26140079). Samples were washed with PBS-Triton solution and then incubated with the "primary antibody solution" — PBS with 0.1% Triton, 5% FBS, 0.01% sodium azide and 1:1000 dilution of rabbit polyclonal anti-VE-cadherin antibody (Abcam #ab33168, UK) — overnight at 4 °C.

On the following day, samples were washed with PBS-Triton and then incubated with the "secondary antibody solution A" — PBS with 0.1% Triton, 5% FBS, 0.01% sodium azide and 1:1000 dilution of goat anti-rabbit secondary antibody conjugated to Alexa Fluor 568 (Invitrogen™ #A-11036) — for 1 h at room temperature. From this moment onwards samples were kept protected from the light. Samples were then washed with PBS-Triton and incubated with the "secondary antibody solution B" — PBS with 0.1% Triton, 5% FBS, 0.01% sodium azide and 1:100 dilution of ZO-1 monoclonal antibody conjugated to Alexa Fluor 488 (Invitrogen™ #339188) — for 3 h at room temperature. Samples were then washed with PBS and incubated for 10 min with a solution of 32.4 µM of Hoechst 33342 (Invitrogen™ #H3570). Samples were then washed with PBS-azide

solution and prepared for imaging. In the case of petri dishes, after washing cells were covered with Fluoromount aqueous mounting medium (Sigma-Aldrich #F4680, U.S.). Images were acquired using inverted confocal Leica SP5 microscope.

5.3.6. Lucifer yellow permeability test

Lucifer yellow (LY) permeability test was performed on µBBB-treated devices to assess the permeability variations in response to barrier formation and mannitol treatment. All solutions were warmed at 37 °C and centrifuged at 500 g for 2 min to diminish microbubbles before introducing into microdevices. All solutions were applied filling the inlet and using a negative pressure driven flow of $-50\ \mu L \cdot min^{-1}$ with a PHD 2000 Syringe Pump. Samples stayed during the whole process inside the incubator at 37 °C. The test was performed at the following timepoints every 24 h: DoC, DoC+1, DoC+2 before mannitol treatment, DoC+2 right after finishing mannitol treatment, and DoC+3.

On each timepoint the inlet corresponding to the top channel (with pericytes) was filled with PBS, and the inlet corresponding to the bottom channel (with EC mimicking a microvessel) was filled with a solution of 20 µM of lucifer yellow CH dilithium salt (Sigma-Aldrich #L0259, U.S.) in PBS, as previously reported.[56,57] A small remaining volume of the solutions prepared of PBS and PBS with LY to insert in the inlet was stored at 4 °C protected from light for a later analysis

to calibrate the measures of each day (stock inlet top and stock inlet bottom). Then a total of 1 mL of each solution was pumped in the top and bottom channels, keeping samples constantly protected from light. An initial volume corresponding to the volume of each channel was first discarded to purge the channels and then the solutions obtained from the outlet at each timepoint were kept at 4 °C protected from light for a later analysis. Devices were washed with the medium corresponding to each channel and left back incubating.

The obtained solutions were measured filling Corning® dark 96 well plates (Sigma-Aldrich #CLS3694, U.S.) and reading the fluorescence in a Synergy H1 Hybrid Multi-Mode Reader (Biotek®, U.S.) with Gen5 software (Biotek®, U.S.). Samples were read using excitation wavelength of 428 nm and emission wavelength of 540 nm. The fluorescence value obtained at the bottom channel (where the LY was inserted) was normalised as indicated in the following equation to compensate the possible photobleaching occurring along the different timepoints of the experiment:

$$\%\ LY\ recovery = \frac{outlet\ bottom\ channel}{stock\ inlet\ top + stock\ inlet\ bottom} \cdot 100 \qquad (5\text{-}1)$$

Average (n = 3) and standard deviation for each measurement were calculated and plotted on a graph.

5.3.7. Electrical impedance spectroscopy and multivariate data analysis

The µBBB devices with electrodes were kept during the culture inside a H301 microscope incubator (Okolab, Italy) at 37 °C, 95% humidity, 5% CO_2, and 10% O_2 with electrical connections secured in a custom incubator adapter. EIS measurements were performed daily after media changed and after stabilising the temperature. EIS measurements were performed using an Agilent 4294A precision impedance analyser (Agilent Technologies, U.S.). After selecting 6 channels intersection over 16 available on the device, measurements were performed using a 3-terminals plus guard configuration. For each location, 100 spectra were acquired every 24 h using a custom MATLAB interface. Each spectrum was acquired in a frequency range between 100 Hz and 10 MHz. The acquired dataset consisted of 3000 total measurements by 300 spectral line features matrix.

The acquired EIS measurements were divided in two distinct datasets, one for the impedance modulus data and the other for the phase. Each of them consisted of 3000 total measurements by 300 spectral-line features matrix. The impedance modulus $|Z|(f)$ was defined as:

$$|Z|(f) = \sqrt{R(f)^2 + X(f)^2} \qquad (5\text{-}2)$$

where R is the resistance and X is the reactance at given frequency f. To evaluate the measurements repeatability, the fluctuation among measurements was calculated as:

$$Fluctuation(f)[\%] = \frac{\sigma_{|Z|}(f)}{\mu_{|Z|}(f)} * 100 \qquad (5\text{-}3)$$

where $\sigma_{|Z|}(f)$and $\mu_{|Z|}(f)$ are respectively the standard deviation and the mean value of the spectrum at given frequency across all the measurements done at a specific timepoint and in a specific intersection of the device.

To obtain a reliable classification model, a preliminary analysis was first conducted for both impedance modulus and phase datasets, creating an LDA (Linear Discriminant Analysis) model. The model was trained and tested with datasets of more than 1000 measurements corresponding to different locations in the device. Data analysis was performed in MATLAB r2019a environment (MathWorks, U.S.) using a classification toolbox provided by Milano Chemometrics.[58] To better understand the misclassification issues of the impedance spectrum dataset, a forward sequential feature selection (SFS) was performed. LDA classification model was improved after the SFS obtaining several possible combinations for each model considering only the selected features and removing all the outliers in the selected band due to high fluctuation measurements. The improved models were trained and tested again and compared with the immunostaining results.

5.4. Results

5.4.1. Analysis of junctional complexes

The effect of mannitol onto EC and pericytes independently (seeded on Petri dishes) was first analysed (FIGURE 5-4 and FIGURE 5-5). EC monoculture in a Petri dish presented high levels of ZO-1 expression throughout the cytoplasm (FIGURE 5-4-A, GREEN). The exposure of cells to mannitol 0.3 M led to an abrupt apoptosis (FIGURE 5-4-B, BLUE) and mostly nuclear localization of the ZO-1 (FIGURE 5-4-B, GREEN), although the confluency and cytoplasm expression of ZO-1 were recovered 24 h later (FIGURE 5-4-C, GREEN and BLUE). VE-cadherin expression, however, initially strong presented in the periphery of cells (FIGURE 5-4-A, RED), was severely affected with the treatment (FIGURE 5-4-B, RED) and barely recovered after (FIGURE 5-4-C, RED).

Pericytes monoculture in a Petri dish presented high levels of ZO-1 expression, located in the cytoplasm and cell-membrane (FIGURE 5-5-A, GREEN). When cells were exposed to mannitol, ZO-1 signal decreased slightly and, as a result of apoptosis, some pores appeared on the monolayer (FIGURE 5-5-B, GREEN). TJ signal was restored normally 24 h after the mannitol damage, being present even in the membrane (FIGURE 5-5-C, GREEN). However, the VE-cadherin signal, showed from the very beginning weak junctions (FIGURE 5-5-A, RED), and it was severely damaged with the treatment, being reduced to nuclear localisation (FIGURE 5-5-B, RED), and it was not restored afterwards, it almost vanished (FIGURE 5-5-C, RED).

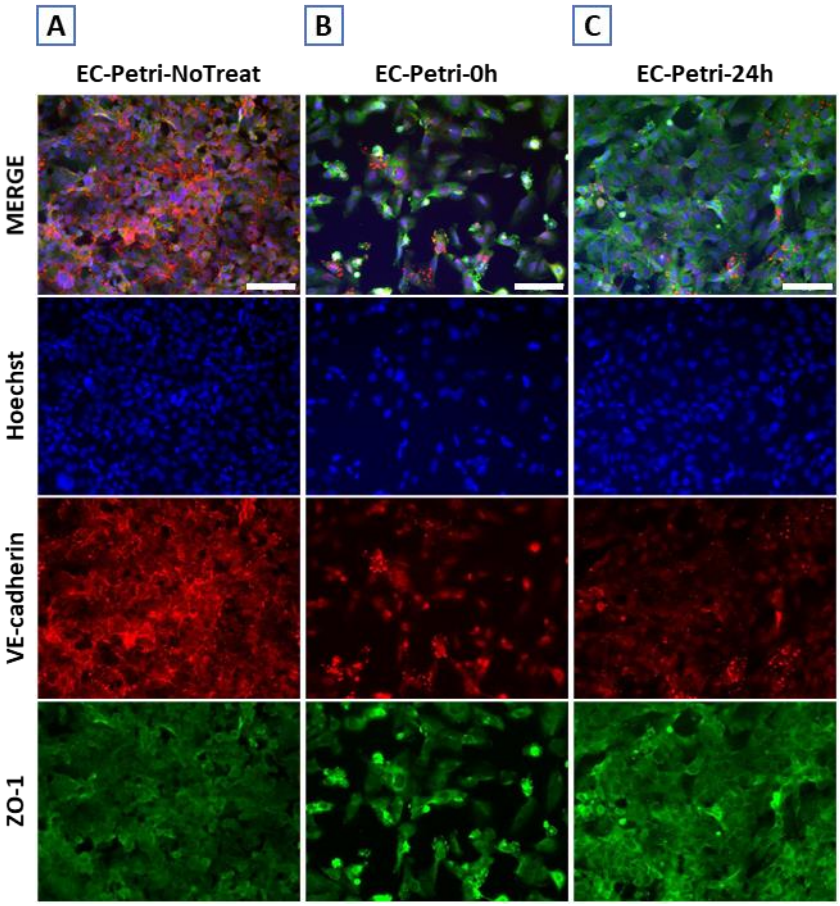

Figure 5-4. *Immunostaining of EC cultured on a Petri dish. ZO-1 tight junctions are stained in green. VE-cadherin adherens junctions are stained in red. Nuclei are stained in blue.* ***A)*** *"EC-Petri-NoTreat" samples show barrier integrity of controls non exposed to mannitol.* ***B)*** *"EC-Petri-0h" samples show barrier damages right after mannitol treatment.* ***C)*** *"EC-Petri-24h" show barrier recovery 24 h after the treatment. Scale bar 100 µm.*

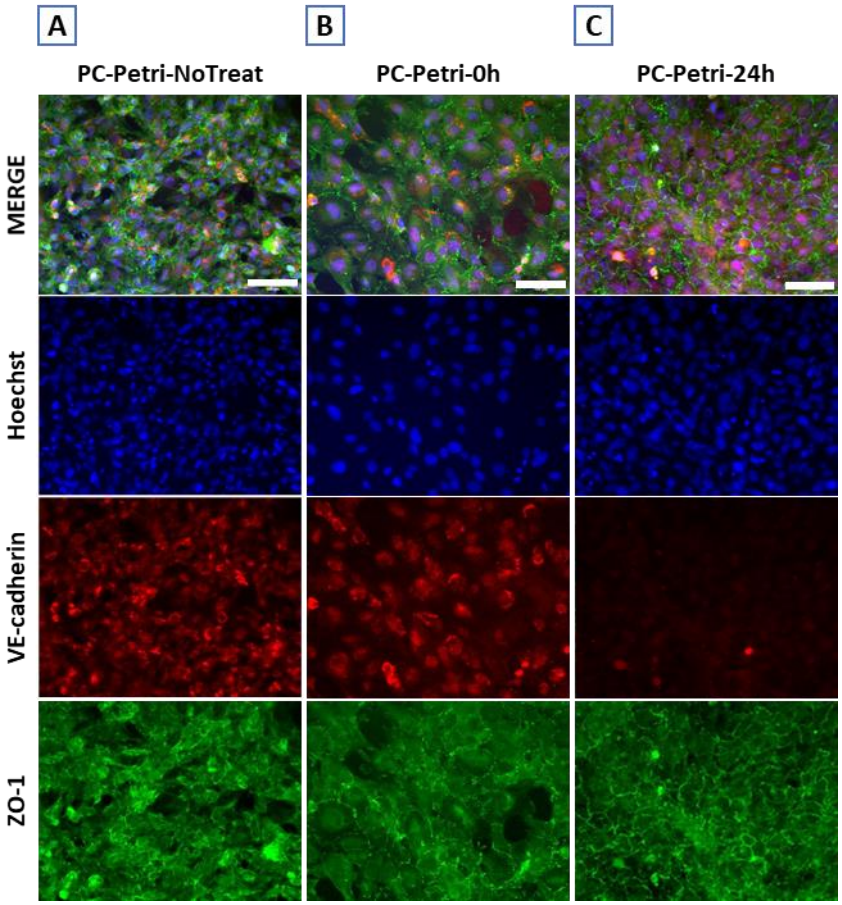

Figure 5-5. *Immunostaining of pericytes cultured on a Petri dish. ZO-1 tight junctions are stained in green. VE-cadherin adherens junctions are stained in red. Nuclei are stained in blue.* ***A)*** *"PC-Petri-NoTreat" samples show barrier integrity of controls non exposed to mannitol.* ***B)*** *"PC-Petri-0h" samples show barrier damages right after mannitol treatment.* ***C)*** *"PC-Petri-24h" samples show barrier recovery 24 h after the treatment. Scale bar 100 µm.*

Then, to make a simplified model of the BBB, µBBB devices were tested. Initially only endothelial cells (EC) were cultured on the bottom channel ("µBBB-EC-only"), as shown in FIGURE 5-6, and later on both cell types (EC and pericytes) were cultured on opposite sides of the membrane separating the upper and lower microchannels, as shown in FIGURE 5-7. Cells were exposed to shear stress through

media change every 24 h. The experiment timepoints were normalised in reference to the moment when around 90% of cell coverage was reached (DoC, day of confluency). Two days after reaching the confluency (DoC+2), experimental devices ("µBBB-treated") and devices with only EC seeded in the bottom-channel ("µBBB-EC-only") were exposed to mannitol and fixed 24 h later (DoC+3), while control devices ("µBBB-controls") were fixed for immunostaining without being treated (DoC+2). The effect of mannitol and co-culture with pericytes was analysed on the obtained results.

Results from the membrane of µBBB-EC-only (FIGURE 5-6) showed high levels of damage, apoptosis and barrier disruption when EC were cultured alone and exposed to mannitol.

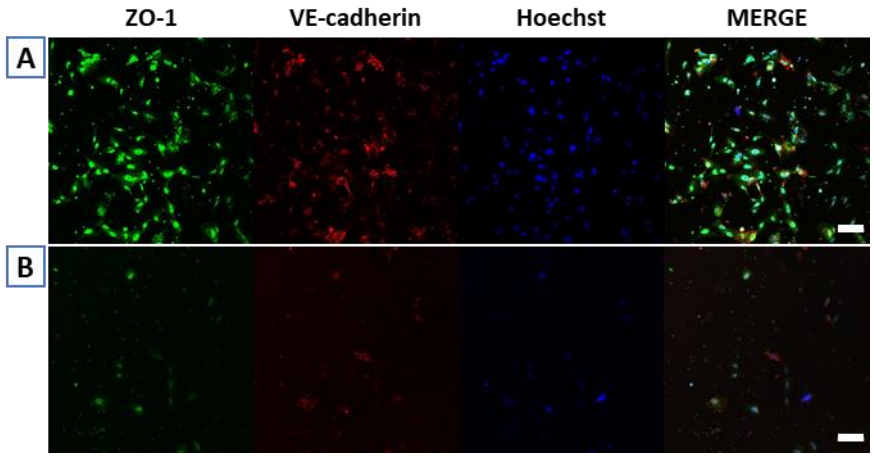

Figure 5-6. *Immunostaining results of µBBB-EC-only, 24 h after mannitol treatment. ZO-1 tight junctions are stained in green. VE-cadherin adherens junctions are stained in red. Nuclei are stained in blue.* ***A)*** *Z-projection of images taken at the bottom-position.* ***B)*** *Z-projection of images taken at the membrane-position. Scale bar 100 µm.*

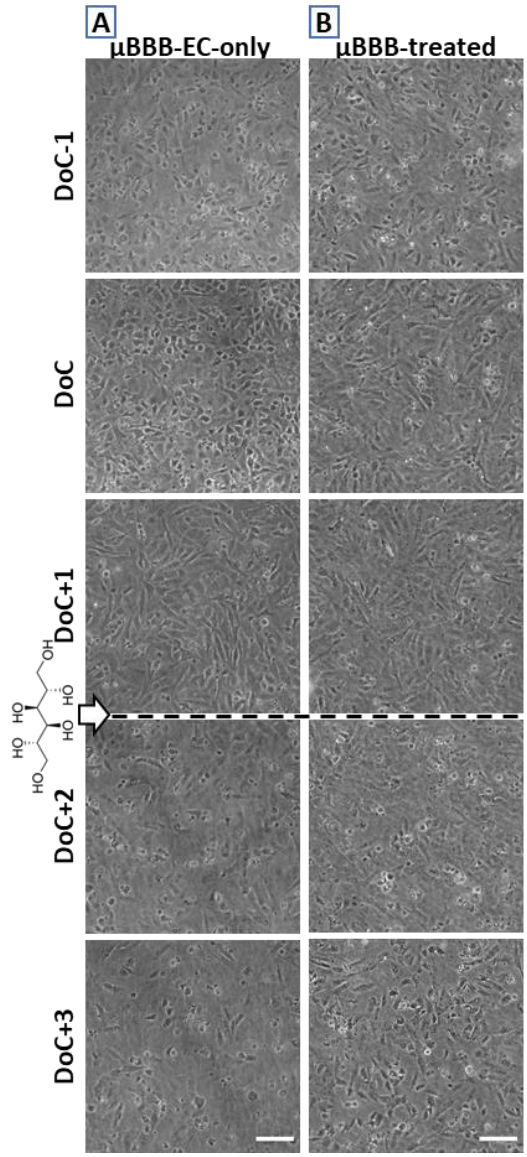

Figure 5-7. *Bright field live imaging of the bottom-position of µBBB-treated* ***(A)*** *and µBBB-EC-only devices* ***(B)*** *at different timepoints, including before and after the confluency is reached (DoC). The moment when mannitol treatment was applied (2 days after confluency was reached, DoC+2) is represented with the dashed line. µBBB-EC-only treated device (EC seeded at the bottom channel and top channel empty) shows higher cell death after mannitol treatment at DoC+3. µBBB-treated device (EC seeded at the bottom channel and pericytes at the top channel) shows better recovery at DoC+3. Scale bar 100 µm.*

The evolution of EC at the bottom-position and their response to mannitol treatment, when cultured alone (µBBB-EC-only) or with pericytes at the other side of the membrane (µBBB-treated), can be observed in FIGURE 5-7. Bright field images taken at each timepoint at the bottom-position of µBBB-EC-only and µBBB-treated devices showed less damage after mannitol treatment on EC cultured with pericytes (FIGURE 5-7).

The µBBB devices with both cell types cultured were utilised to compare the expression of relevant TJ and AJ markers related to confluency when samples were not treated (FIGURE 5-8), and when they were treated with mannitol and left for 24 h recovery (FIGURE 5-9).

At the bottom-position of the non-treated devices, where EC were not in close contact with pericytes, ZO-1 signal was detected in the cytoplasm and VE-cadherin in the cell periphery (FIGURE 5-8-C,D), similar to its corresponding monoculture of EC in Petri dish (FIGURE 5-4-A). But after mannitol treatment and 24 h recovery at the bottom-position, ZO-1 expression was reduced to cytoplasmatic and nuclear localization, and VE-cadherin was severely affected, related with the high apoptosis levels (as observed with the nuclear staining) (FIGURE 5-9-C,D), similar to the damage observed in the corresponding EC monoculture in Petri dish 0 h after treatment (FIGURE 5-4-B). However, Petri dish EC monocultures presented

higher cell confluency from the beginning and better recovery after hyperosmotic damage (FIGURE 5-4-C).

At the membrane-position of the non-treated devices, where both EC and pericytes were interacting at each side of the membrane, cells presented low confluency, together with a predominant nuclear staining of ZO-1 and some small areas with a membrane localisation, and almost absent expression of VE-cadherin (FIGURE 5-8-A,B). In this case, the corresponding Petri dish pericyte monocultures, presented much higher confluency from the beginning, and higher and stronger ZO-1 and VE-cadherin signal (FIGURE 5-5-A). After mannitol treatment in the devices and 24 h recovery, ZO-1 signal decreased slightly and remained exclusively with a nuclear and cytoplasmic localisation, whereas VE-cadherin staining remained the same, almost absent (FIGURE 5-9-A,B). Similarly, its corresponding controls presented almost no VE-cadherin signal after the treatment, though confluency and ZO-1 levels were much higher and presented a better recovery (FIGURE 5-5-C).

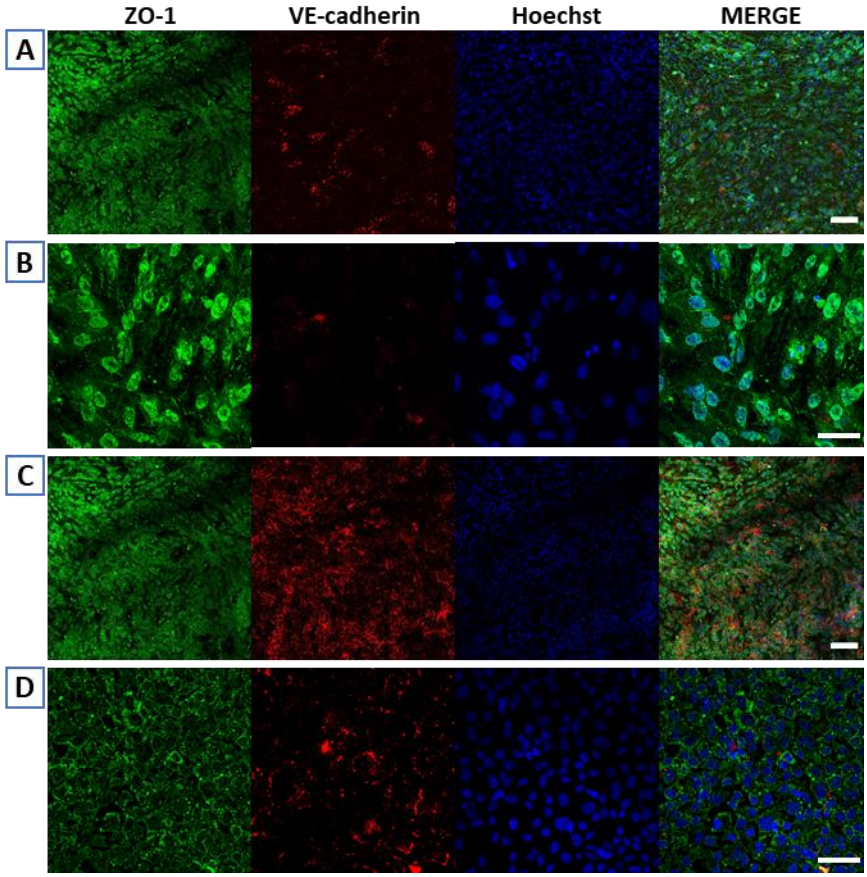

***Figure 5-8**. Immunostaining of µBBB-control devices (non-treated, DoC+2). Confocal microscopy images show Z-projection of the membrane-position **(A, B)** and bottom-position **(C, D)**, in agreement with the description of **Figure 5-3**. ZO-1 tight junctions are stained in green. VE-cadherin adherens junctions are stained in red. Nuclei are stained in blue. Scale bar is 100 µm for **A** and **B**, and 50 µm for **B** and **D**.*

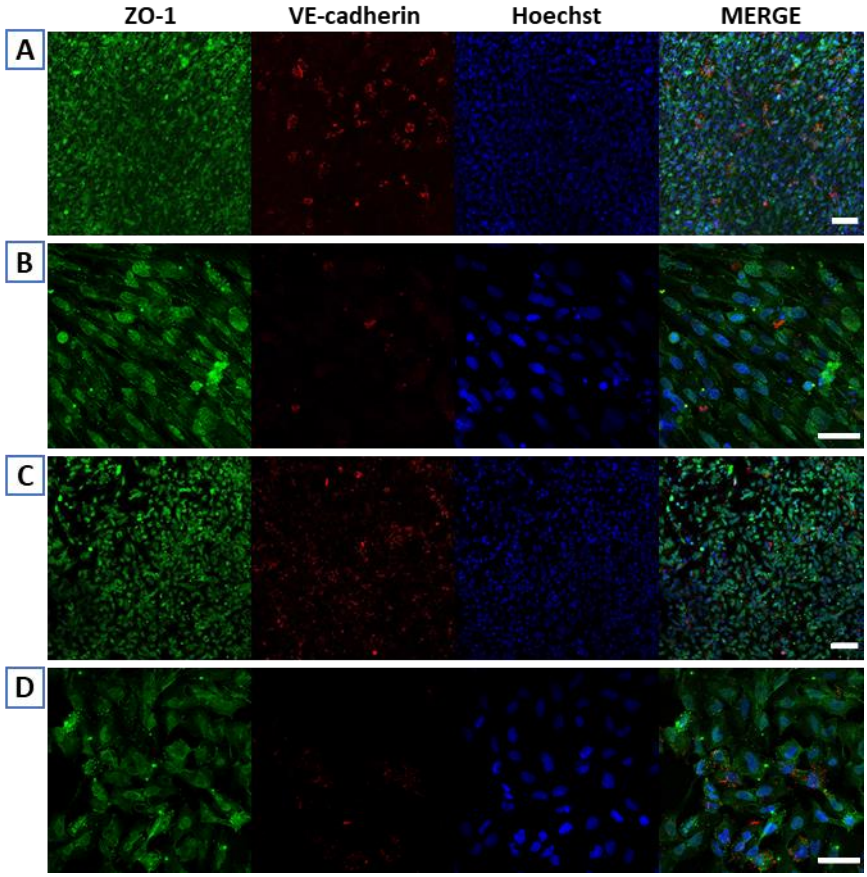

Figure 5-9. *Immunostaining of µBBB-treated devices (24h after the exposure to mannitol treatment, DoC+3). Confocal microscopy images show Z-projection of the membrane-position* ***(A, B)*** *and bottom-position* ***(C, D)****, in agreement with the description of* ***Figure 5-3****. ZO-1 tight junctions are stained in green. VE-cadherin adherens junctions are stained in red. Nuclei are stained in blue. Scale bar is 100 µm for* ***A*** *and* ***B****, and 50 µm for* ***B*** *and* ***D****.*

5.4.2. Monitoring the barrier integrity through lucifer yellow permeability test and EIS

Barrier integrity and permeability were assessed through both lucifer yellow permeability test and EIS.

Lucifer yellow permeability test was performed in µBBB-treated devices inserting LY solution at the microvessel mimicking channel (the bottom channel), and analysing the variations of recovered percentage at each timepoint (FIGURE 5-10). Results showed in the first timepoint (DoC) that 59.62% of inserted LY was recovered in the outlet, though with a standard deviation (SD) of a 10.45%. In the second timepoint (DoC+1, 24 h later), the barrier permeability remained constant, recovering as well 58.60% of inserted LY, though with a smaller SD. The barrier matured and started forming TJ and AJ, diffusing less to the other channel, obtaining 87.09% of recovery at DoC+2 just before the hyperosmotic treatment was applied. Right after mannitol treatment was applied at DoC+2, the barrier was damaged and LY recovery decreased down to 66.34%. After 24 h, the LY recovery increased again up to 85.06%, indicating some barrier regeneration.

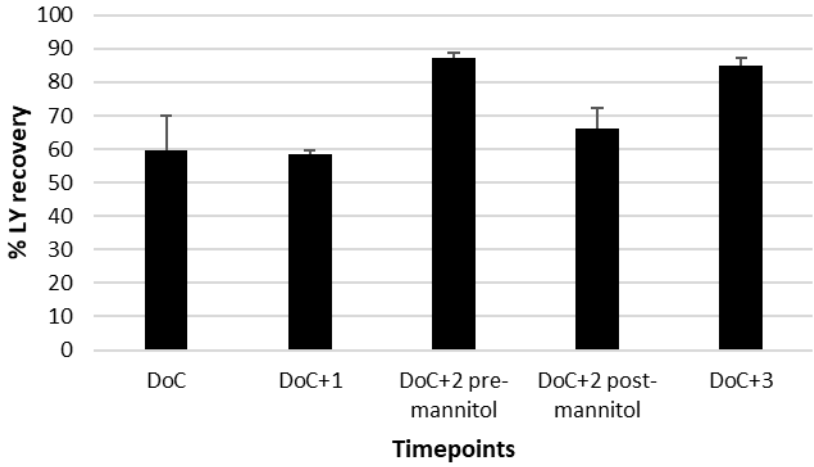

Figure 5-10. *Lucifer yellow recovery percentage in the outlet of the bottom channel (where it had been inserted) for each timepoint. Average and standard deviation are shown (n=3).*

EIS measurements — done in collaboration with PhD students Roberto Paoli and Davide Di Giuseppe as stated in the introduction —, were performed across the µBBB device membrane in six different intersections every 24 h during 5 days after cell seeding. Each intersection was considered a different sample under same experimental conditions since there were small variations among positions in terms of the cell number, tolerance on the alignment of the electrodes, etc. The measurements performed from DoC-1 to DoC+3, resulted in a dataset of 3000 measurements.

The impedance spectrum was measured across a defined frequency range, either through the impedance modulus or phase, for each intersection and timepoint. Typical impedance spectrum at a specific location for each timepoint for these experiments is shown in FIGURE 5-11. Fluctuation analysis showed a good impedance

measurement repeatability with maximum fluctuation across the whole dataset of 2.5%.

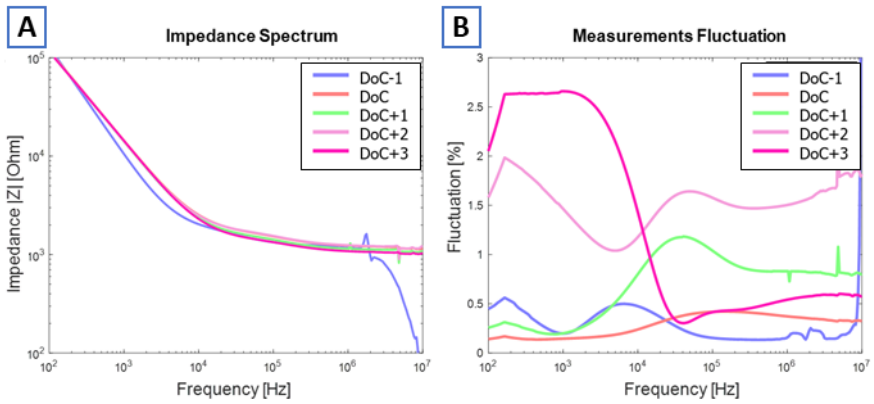

Figure 5-11. *Typical EIS spectra across different timepoints where each coloured line represents a different experimental timepoint in the same intersection (from DoC-1 to DoC+3).* ***A)*** *Impedance modulus spectra across all timepoints of a single location of µBBB device.* ***B)*** *Fluctuation of measurements across all timepoints of a single location.*

LDA classification model was created with the goal of recognising barrier status, and therefore each class corresponds to specific timepoint. The model resulted in 100% accuracy in training and testing. It showed a clear distinction among the acquired measurements on each intersection of the device, being more evident for the class DoC-1, as shown in FIGURE 5-12.

The forward sequential feature selection (SFS) performed afterwards for at least 100 repetitions, did not select any features in lower frequency band, it only selected the 10 kHz - 10 MHz band. High fluctuations were found in the 8-10 MHz range. After removing the outliers due to fluctuations and considering the features selected with the SFS, LDA model was improved obtaining several

possible combinations for each model. This led to new LDA classification model, obtaining in average of the possible combinations: **90%** accuracy in testing the impedance modulus dataset, and **96%** accuracy in testing the phase dataset.

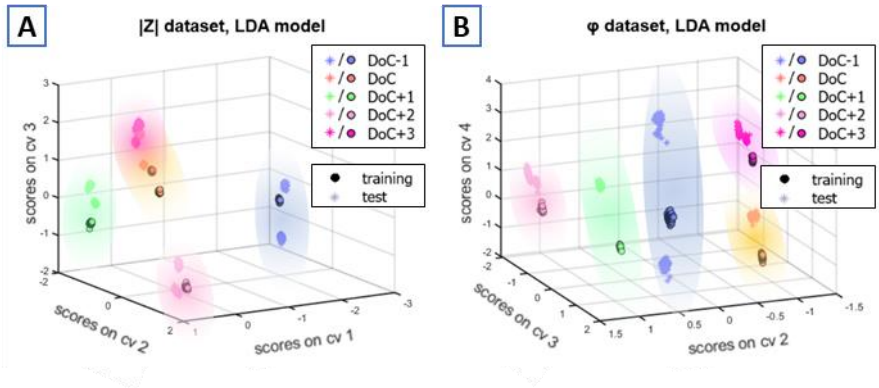

Figure 5-12. *Classification models created with EIS data acquired between timepoints DoC-1 and DoC+3.* ***A)*** *LDA model based on impedance modulus data. Clear separation between measurements acquired on different positions is visible on all classes, particularly on class DoC-1.* ***B)*** *LDA model based on impedance phase data.*

This resulting model, such as the example from FIGURE 5-13, was able to separate measurements from different timepoints with an accuracy of 100% in testing. It could separate all the classes corresponding to different timepoints — although the separability between the class DoC and DoC+3 was much lower with respect to the other classes—, and therefore it could attribute to each class a biological meaning.

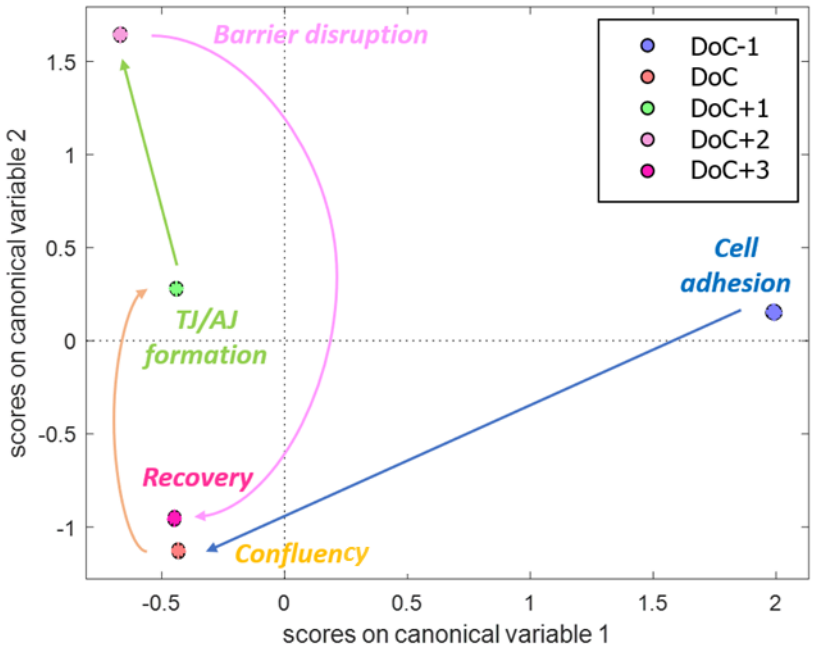

Figure 5-13. *Improved LDA model based on impedance modulus with the selected set of features. Score plot on canonical variables 1 and 2. Each biological phenomenon occurring at a different timepoint (DoC-1 to DoC+3) is clearly separated in the space.*

5.5. Discussion

In this section immunostaining results, EIS results and the correlation between them is discussed, paying special attention to barrier integrity in relation to some model intrinsic factors: barrier maturity, cell density, maturity, pericytes, media components and the effect of mannitol.

Monoculture controls performed on Petri dishes showed higher formation of AJ in EC (FIGURE 5-4-A), while TJ were more defined in pericytes (FIGURE 5-5-A,C), and confluency levels were higher than in µBBB-controls (FIGURE 5-8). Petri dish controls showed as well higher recovery of both junctional complexes and cell-confluency after the treatment (FIGURE 5-4-C and FIGURE 5-5-C) than treated microdevices (FIGURE 5-9). These results may be related to the **effective seeding density in microdevices**. It is known that the barrier integrity, is highly affected by the seeding density of EC.[59] The more confluent the cells are, the more likely they form a mature and stronger barrier, expressing higher levels of junctional proteins, and needing higher mannitol doses to cause disruption. Mature barriers are more predisposed to recover from a damage. And although proportional volumetric densities are correctly calculated, seeding of the devices is still one of the most delicate steps of the experimental procedure when working with cells and microfluidics devices.

Another reason to possibly explain the difference in results among Petri dish controls and microfluidic devices, both before and after the treatment, can be the availability of certain growth factors on the medium. Basic fibroblast growth factor (bFGF), present among other components in the hCMEC/D3 medium used here, is known to upregulate TJ proteins.[60] It can also be beneficial on recovering from the accumulated hyperosmotic stress in the BBB. It promotes cell growth, increase in density and microvessel recovery.[20] Furthermore, it can protect the BBB before hyperosmotic BBBO presumably altering the distribution of TJ strengths, increasing barrier integrity and making necessary higher doses of mannitol.[20] In the experiments here presented, hCMEC/D3 cells were cultured with medium with bFGF. However, while EC on Petri dishes were cultured with the standard corresponding volume of medium (2 mL for each 9.6 cm^2 well, approximately 208.3 $\mu L \cdot cm^{-2}$) and changed every 24 h, the immediate volume available on each microchannel (approximately 18 $\mu L \cdot cm^{-2}$) was much lower. This means that despite the diffusion of nutrients from the reservoir, a lower **immediate availability of bFGF** on microchannel with EC could be playing a relevant role on diminishing its proliferation and vessel maturation, as compared to Petri dishes static culture. Therefore, when analysing the BBBO, it should be considered not only the effect of mannitol and the implicit protection from bFGF, but also the immediate availability of bFGF in a closed microfluidic system.

To diminish this effect, the medium should be changed more frequently, or cells should be cultured with constant flow.

ZO-1 staining observed in samples varied from nuclear (FIGURE 5-4-B and FIGURE 5-9-C,D), to cytoplasmatic (FIGURE 5-8-C,D) and cell-membrane (FIGURE 5-5-A,C) locations within the cell. In all cases, pericytes presented more clear and peripheral staining than the EC cell line employed. Previous reports suggested that ZO-1 localization in the cell is related to the maturity and extent of cell-cell contacts,[61] being a nuclear localization at sub-confluency states representative of non-fully mature barriers, cytoplasmic less immature, and peripheral plasma-membrane localisation an indicator of a mature barrier.[61]

VE-cadherin staining observed in samples varied from nuclear (FIGURE 5-4-B, FIGURE 5-5-B), to peripheral or cell-membrane locations (FIGURE 5-8-C,D and FIGURE 5-4-A) and after mannitol treatment resulted in a negative almost absent signal (FIGURE 5-9 and FIGURE 5-5-C). In all cases, stable VE-cadherin networks were easier to form in EC than in pericytes. Previous reports suggest that the cadherin-catenin complex are responsible for modulating barrier function and cell permeability: weakening of junctional complexes results in the activation of intracellular mechanisms to increase cell permeability conditioning the degradation and nuclear signalling of some other junctional complex proteins, previously associated with VE-cadherin to form AJ.[62]

For the barrier formation and maturation, it was previously suggested that both AJ and TJ complex proteins have to interact during the barrier development.[10,13] Stable AJ, VE-cadherin in particular, are required for the EC survival, blood vessel assembly, stabilization and formation of TJ.[10] But at the same time, ZO-1 is essential for the VE-cadherin complex formation.[13] Therefore, based on the images obtained, the results presented here suggest that the biological barrier created on the membrane-position of µBBB-controls was not fully mature, whereas the EC monolayer at the bottom-position was slightly more mature, presenting higher and more peripheral expression of VE-cadherin and ZO-1 (FIGURE 5-8-C,D, RED and GREEN). When µBBB devices were exposed to the treatment, the observed damage (FIGURE 5-9) was much higher than the one observed in the Petri dish controls (FIGURE 5-4 and FIGURE 5-5). These results suggest as well that one of the reasons that conditions biological barrier recovery from a hyperosmotic treatment is its **initial maturity state**.

The EC cell line utilised (hCMEC/D3) is the most extensively characterised human brain EC cell-line. However, it has been reported to be less tight than primary cultured cells and probably deficient in some TJ proteins, enzymes and transport systems.[63] This cell-line can express many TJ and AJ junctional markers, as previously analysed by Weksler *et al.,*[64] but its TEER levels are among the lowest obtained with different cell-lines.[59] Furthermore, it has been reported not to be a good model to study the

permeability of cerebral clearance (brain-to-blood directional permeability).[65] Brain microvascular endothelial cell-line (hBMEC) seems to be a more promising alternative for future experiments, able to form a membrane with lowest paracellular permeability and highest integrity.[59]

After exposing μBBB devices to mannitol treatment, higher cell viability and recovery were observed on the membrane-position (FIGURE 5-9-A,B), compared to samples or areas with only EC (FIGURE 5-9-C,D, FIGURE 5-7 and FIGURE 5-6). Although the barrier formed was not fully mature in the membrane or at the bottom of the device, these results suggest an active role of the pericytes in the integrity of the BBB and in the recovery from a hyperosmotic BBBO. The results are coherent with previous publications which evidenced **the critical role of pericytes** in the development, maintenance, and regulation of BBB.[66,67] Pericytes are not essential for the tightness of the BBB (e.g. they are not essential to induce TJ complex protein expression), but they are vital to avoid leakiness on the BBB (e.g. they inhibit transcytosis).[68,69] They have previously been reported to play an essential role on the BBB regulating the transcytosis of EC, the integrity (as measured through TEER), the synthesis of basal membrane compounds (that contribute to the membrane tightness), the expression of efflux pumps, the inhibition of immune cell trafficking and the permeation of agents that promote vascular permeability.[70]

The **application of mannitol** (concentration, incubation time, and previous formation of the monolayer *in vitro*) to promote a BBBO in a previously formed microvessel is not yet under an established protocol. Previous studies have shown that a monolayer of hCMEC/D3 cells is able to form a barrier in 2-4 DIV.[24,59,71] In these experiments the BBBO was induced 2 days after EC reached the confluency (DoC+2) by applying a 0.3 M mannitol dose onto microvessel-mimicking channel for 45 min, based on previous publications applying it onto a 7 days old endothelial cell monolayer cultured onto a collagen microvessel.[55] Higher incubation times of the dose used are known to have more difficulties on recovering the barrier function, requiring up to 4 days to restore the barrier integrity levels of the timepoint when the treatment was applied.[55] Recent studies utilising much higher doses (1.4 M) for a shorter time on a 2 days old confluent monolayer of brain microvascular endothelial cells cultured onto a collagen microvessel, have also observed detachment of cells as a result of mannitol treatment.[20] Further studies should require an optimisation of the dosing related to the effect in real time at different timepoints and to elucidate its effect on 2D monolayers versus cells embedded in a collagen microvessel protecting them to some length from environmental alterations.

Barrier integrity assessment performed through lucifer yellow dye (FIGURE 5-10) showed an augment in the LY percentage recovery related with a decrease in the diffusion between DoC+1 and DoC+2,

that could be related with the formation of TJ and AJ. When mannitol treatment was applied, a decrease in the LY recovery was observed, that could indicate that more LY had passed to the other channel. Following the treatment, the barrier went under some regeneration, increasing again the LY recovery at DoC+3. Although this test provides some complementary information about barrier status in each timepoint, it is not able to detect significant differences between the first two timepoints and it does not provide much information. Furthermore, it can cause some stress on cell when submitting them to a flow of PBS and LY. And finally the result of this kind of test can be somehow biased as the collected LY in the outlet depends not only on the diffusion to the other channel and the integrity of the biological membrane, but also on the retention of LY by cells death or their debris collected in the output and by the polycarbonate membrane of the device itself.

The study presented here shows an alternative novel method to monitor barrier integrity that can lead to optimise the required dose to promote BBBO. The initial LDA model designed to process EIS acquired data, presented an accuracy of 80% in testing due to misclassifications of the samples belonging to classes DoC and DoC+3. This model was able to distinguish very small differences in the microenvironment among the intersections of the same µBBB device, as shown clearly in FIGURE 5-12 for the class DoC-1. The model was improved through SFS, obtaining several possible combinations for each model considering only the selected features

in the 10 kHz – 10 MHz band, and removing the outliers in the 8 MHz – 10 MHz range. The EIS combined with the improved LDA model resulted in a very sensitive measurement technique with an accuracy of 100% in testing.

In the first timepoint of the experiment (DoC-1), cell confluency was very low cells hadn't had enough time neither to generate a supporting extracellular matrix, nor to interact so much with neighbouring cells (FIGURE 5-7-B, DOC-1). Therefore, they appeared in the LDA model as an isolated class (FIGURE 5-13, DOC-1). Once the confluence was reached, the classification changed drastically (FIGURE 5-13, DOC). The barrier matured progressively, starting to form junctional complexes (TJ and AJ), detected as a slight separation in the classification plot (FIGURE 5-13, DOC+1; FIGURE 5-7-B, DOC+1; FIGURE 5-8). Once the mannitol was administered on the cells, they went under a process of shrinking, vacuolation and apoptosis caused by mannitol treatment that ended up opening the barrier. This was detected in the LDA model as an isolated cluster in the plot, very distant from the rest (FIGURE 5-13, DOC+2). After the treatment, cells started proliferating and re-constructing the barrier, going under a process of barrier recovery. The obtained barrier integrity level was similar to the one observed at DoC, with high confluency of cells, although junctional complexes were not formed and therefore the barrier was still permeable (FIGURE 5-7-A, DOC and DOC+3; FIGURE 5-9). These was coherent with results obtained from LDA model, that showed similarities in the

classification between these two timepoints (FIGURE 5-13, DOC and DOC+3).

Then, this model could potentially be used to easily test the effect of some compounds on the membrane integrity at real time, such as cholesterol as previously suggested by Shigetomi *et al.,*[11] or other systems or drugs employed to induce BBBO. It could even be used to modulate the drug dose needed to promote BBBO of certain kind of blood vessels, adapting the here used device to different size microchannels for each type of blood vessel. This work presents an approach of a simplified version of a healthy BBB, that could be translated to mimic diseased or other healthy biological barriers, such as blood-cerebrospinal fluid barrier, blood-spinal cord barrier, etc.

5.6. Conclusions

This work presents a simplified model of a healthy BBB on a microfluidic device and its permeability monitoring through integrated electrodes.

The sandwich compartmentalised microfluidic device, with an embedded porous membrane, was successfully adapted for mimicking a simplified BBB. To that end, EC and pericytes were cultured inside the µBBB devices. At DoC+1, an initial formation of AJ and TJ were observed.

The effect of mannitol hyperosmotic treatment onto barrier disruption and its subsequent short-time recovery were successfully monitored. Administering mannitol resulted in an impairment of the barrier, affecting cells confluency and formation of junctional complexes. The results suggest that BBB recovery after mannitol treatment is a result of: i) the presence of pericytes; ii) the immediate availability of bFGF during the culture and after the BBBO; iii) the effective seeding density in microdevices and initial confluency of the cultures; iv) the initial maturity of the cultures on the moment of mannitol treatment; v) the applied dose and timing of mannitol; and vi) the EC cell-line chosen.

EIS measurements, together with LDA classification model improved through SFS resulted in a successful and accurate technique to perform real-time non-invasive monitoring of the complex

processes ongoing on the barrier. The results obtained with the developed technique correlated with the ones obtained from immunostaining. It was possible to distinguish through a multivariate representation the following phenomena occurring at different timepoints: non-confluent cells (DoC-1), confluent monolayer (DoC), beginning of barrier sealing and junctional complexes formation (DoC+1), barrier opening after mannitol treatment (DoC+2), and its recovery (DoC+3) that confirm with immunostainings that the barrier was not yet fully recovered and sealed with mature TJ and AJ.

The model and measurement technique presented here can easily be translated to mimic the BBB or the blood-spinal cord barrier of a neurovascular pathology, such as ALS, using patient derived iPSC differentiated to EC and pericytes. Being able to monitor the phenomena ongoing on these biological barriers would help in a future to elucidate the implications of neurovascular damages on ALS. Furthermore, this device could be integrated with brain or neuromuscular system mimicking device through microfluidic connections, making possible to study the big picture.

5.7. References

1. Abbott, N. J., Patabendige, A. A. K., Dolman, D. E. M., Yusof, S. R. & Begley, D. J. Structure and function of the blood–brain barrier. *Neurobiol. Dis.* **37**, 13–25 (2010).
2. Neuwelt, E. A. *et al.* Engaging neuroscience to advance translational research in brain barrier biology. *Nat. Rev. Neurosci.* **12**, 169–182 (2011).
3. Abbott, N. J. Blood–brain barrier structure and function and the challenges for CNS drug delivery. *J. Inherit. Metab. Dis.* **36**, 437–449 (2013).
4. Stamatovic, S. M., Johnson, A. M., Keep, R. F. & Andjelkovic, A. V. Junctional proteins of the blood-brain barrier: New insights into function and dysfunction. *Tissue Barriers* **4**, e1154641 (2016).
5. Keep, R. F. *et al.* Brain endothelial cell junctions after cerebral hemorrhage: changes, mechanisms and therapeutic targets. *J. Cereb. Blood Flow Metab.* **38**, 1255–1275 (2018).
6. Bader, A. *et al.* Adenosine receptors regulate gap junction coupling of the human cerebral microvascular endothelial cells hCMEC/D3 by Ca 2+ influx through cyclic nucleotide-gated channels. *J. Physiol.* **595**, 2497–2517 (2017).
7. Meşe, G., Richard, G. & White, T. W. Gap Junctions: Basic Structure and Function. *J. Invest. Dermatol.* **127**, 2516–2524 (2007).
8. Anderson, J. M. & Van Itallie, C. M. Physiology and Function of the Tight Junction. *Cold Spring Harb. Perspect. Biol.* **1**, a002584–a002584 (2009).
9. Steed, E., Balda, M. S. & Matter, K. Dynamics and functions of tight junctions. *Trends Cell Biol.* **20**, 142–149 (2010).
10. Tietz, S. & Engelhardt, B. Brain barriers: Crosstalk between complex tight junctions and adherens junctions. *J. Cell Biol.* **209**, 493–506 (2015).
11. Shigetomi, K., Ono, Y., Inai, T. & Ikenouchi, J. Adherens junctions influence tight junction formation via changes in membrane lipid composition. *J. Cell Biol.* **217**, 2373–2381 (2018).
12. Li, W., Chen, Z., Chin, I., Chen, Z. & Dai, H. The Role of VE-cadherin in Blood-brain Barrier Integrity Under Central Nervous System Pathological Conditions. *Curr. Neuropharmacol.* **16**, 1375–1384 (2018).
13. Tornavaca, O. *et al.* ZO-1 controls endothelial adherens junctions, cell–cell tension, angiogenesis, and barrier formation. *J. Cell Biol.* **208**, 821–838 (2015).
14. Abbott, N. J., Rönnbäck, L. & Hansson, E. Astrocyte–endothelial

interactions at the blood–brain barrier. *Nat. Rev. Neurosci.* **7**, 41–53 (2006).

15. Chen, R., Zhao, X. & Hu, K. Physically open BBB. in *Brain Targeted Drug Delivery System* 197–217 (Elsevier, 2019). doi:10.1016/B978-0-12-814001-7.00009-3.

16. Mehta, D. & Malik, A. B. Signaling mechanisms regulating endothelial permeability. *Physiol. Rev.* **86**, 279–367 (2006).

17. Chow, B. W. & Gu, C. The molecular constituents of the blood–brain barrier. *Trends Neurosci.* **38**, 598–608 (2015).

18. Rapoport, S. I. Advances in osmotic opening of the blood-brain barrier to enhance CNS chemotherapy. *Expert Opin. Investig. Drugs* **10**, 1809–1818 (2001).

19. Siegal, T. *et al.* In vivo assessment of the window of barrier opening after osmotic blood—brain barrier disruption in humans. *J. Neurosurg.* **92**, 599–605 (2000).

20. Linville, R. M. *et al.* Modeling hyperosmotic blood–brain barrier opening within human tissue-engineered in vitro brain microvessels. *J. Cereb. Blood Flow Metab.* **40**, 1517–1532 (2020).

21. Shubin, A. V, Demidyuk, I. V, Komissarov, A. A., Rafieva, L. M. & Kostrov, S. V. Cytoplasmic vacuolization in cell death and survival. *Oncotarget* **7**, 55863–55889 (2016).

22. Yeste, J., Illa, X., Alvarez, M. & Villa, R. Engineering and monitoring cellular barrier models. *J. Biol. Eng.* **12**, 18 (2018).

23. Oddo, A. *et al.* Advances in microfluidic blood–brain barrier (BBB) models. *Trends Biotechnol.* **37**, 1295–1314 (2019).

24. Griep, L. M. *et al.* BBB on chip: microfluidic platform to mechanically and biochemically modulate blood-brain barrier function. *Biomed. Microdevices* **15**, 145–150 (2013).

25. Booth, R. & Kim, H. Characterization of a microfluidic in vitro model of the blood-brain barrier (μBBB). *Lab Chip* **12**, 1784 (2012).

26. Abhyankar, V. V., Wu, M., Koh, C.-Y. & Hatch, A. V. A reversibly sealed, easy access, modular (SEAM) microfluidic architecture to establish in vitro tissue interfaces. *PLoS One* **11**, e0156341 (2016).

27. Deosarkar, S. P. *et al.* A novel dynamic neonatal blood-brain barrier on a chip. *PLoS One* **10**, e0142725 (2015).

28. Prabhakarpandian, B. *et al.* SyM-BBB: a microfluidic blood brain barrier model. *Lab Chip* **13**, 1093–1101 (2013).

29. Yeste, J. *et al.* A compartmentalized microfluidic chip with crisscross microgrooves and electrophysiological electrodes for modeling the

blood–retinal barrier. *Lab Chip* **18**, 95–105 (2018).

30. Adriani, G., Ma, D., Pavesi, A., Kamm, R. D. & Goh, E. L. K. A 3D neurovascular microfluidic model consisting of neurons, astrocytes and cerebral endothelial cells as a blood–brain barrier. *Lab Chip* **17**, 448–459 (2017).

31. Kim, S., Lee, H., Chung, M. & Jeon, N. L. Engineering of functional, perfusable 3D microvascular networks on a chip. *Lab Chip* **13**, 1489–1500 (2013).

32. Yamamoto, K. *et al.* Construction of continuous capillary networks stabilized by pericyte-like perivascular cells. *Tissue Eng. Part A* **25**, 499–510 (2019).

33. Maoz, B. M. *et al.* A linked organ-on-chip model of the human neurovascular unit reveals the metabolic coupling of endothelial and neuronal cells. *Nat. Biotechnol.* **36**, 865–874 (2018).

34. Cucullo, L., Hossain, M., Puvenna, V., Marchi, N. & Janigro, D. The role of shear stress in Blood-Brain Barrier endothelial physiology. *BMC Neurosci.* **12**, 1–15 (2011).

35. Achyuta, A. K. H. *et al.* A modular approach to create a neurovascular unit-on-a-chip. *Lab Chip* **13**, 542–553 (2013).

36. Shin, Y. *et al.* Blood–brain barrier dysfunction in a 3D in vitro model of Alzheimer's disease. *Adv. Sci.* **6**, 1900962 (2019).

37. Xu, H. *et al.* A dynamic in vivo-like organotypic blood-brain barrier model to probe metastatic brain tumors. *Sci. Rep.* **6**, 36670 (2016).

38. Jeong, S. *et al.* A three-dimensional arrayed microfluidic blood–brain barrier model with integrated electrical sensor array. *IEEE Trans. Biomed. Eng.* **65**, 431–439 (2018).

39. Maoz, B. M. *et al.* Organs-on-Chips with combined multi-electrode array and transepithelial electrical resistance measurement capabilities. *Lab Chip* **17**, 2294–2302 (2017).

40. Tsao, C.-W. Polymer microfluidics: simple, low-cost fabrication process bridging academic lab research to commercialized production. *Micromachines* **7**, 225 (2016).

41. Berthier, E., Young, E. W. K. & Beebe, D. Engineers are from PDMS-land, Biologists are from Polystyrenia. *Lab Chip* **12**, 1224–1237 (2012).

42. Su, X. *et al.* Microfluidic cell culture and its application in high-throughput drug screening. *J. Biomol. Screen.* **16**, 101–111 (2011).

43. Nunes, P. S., Ohlsson, P. D., Ordeig, O. & Kutter, J. P. Cyclic olefin polymers: emerging materials for lab-on-a-chip applications. *Microfluid. Nanofluidics* **9**, 145–161 (2010).

44. Bonfield, T. L., Colton, E. & Anderson, J. M. Plasma protein adsorbed biomedical polymers: Activation of human monocytes and induction of interleukin 1. *J. Biomed. Mater. Res.* **23**, 535–548 (1989).

45. Niles, W. D. & Coassin, P. J. Cyclic olefin polymers: innovative materials for high-density multiwell plates. *Assay Drug Dev. Technol.* **6**, 577–590 (2008).

46. Piruska, A. *et al.* The autofluorescence of plastic materials and chips measured under laser irradiation. *Lab Chip* **5**, 1348 (2005).

47. Liga, A., Morton, J. A. S. & Kersaudy-Kerhoas, M. Safe and cost-effective rapid-prototyping of multilayer PMMA microfluidic devices. *Microfluid. Nanofluidics* **20**, 164 (2016).

48. Mohammed, M. I., Zainal Alam, M. N. H., Kouzani, A. & Gibson, I. Fabrication of microfluidic devices: improvement of surface quality of CO2 laser machined poly(methylmethacrylate) polymer. *J. Micromechanics Microengineering* **27**, 015021 (2017).

49. Tsao, C. W., Hromada, L., Liu, J., Kumar, P. & DeVoe, D. L. Low temperature bonding of PMMA and COC microfluidic substrates using UV/ozone surface treatment. *Lab Chip* **7**, 499–505 (2007).

50. Nath, P. *et al.* Rapid prototyping of robust and versatile microfluidic components using adhesive transfer tapes. *Lab Chip* **10**, 2286–2291 (2010).

51. Liu, L. *et al.* Photoacoustic therapy for precise eradication of glioblastoma with a tumor site blood-brain barrier permeability upregulating nanoparticle. *Adv. Funct. Mater.* **29**, 1808601 (2019).

52. Garbuzova-Davis, S. *et al.* Phenotypic characteristics of human bone marrow-derived endothelial progenitor cells in vitro support cell effectiveness for repair of the blood-spinal cord barrier in ALS. *Brain Res.* **1724**, 146428 (2019).

53. Saunders, N. R., Dziegielewska, K. M., Møllgård, K. & Habgood, M. D. Markers for blood-brain barrier integrity: how appropriate is Evans blue in the twenty-first century and what are the alternatives? *Front. Neurosci.* **9**, 1–16 (2015).

54. Srinivasan, B. *et al.* TEER measurement techniques for in vitro barrier model systems. *J. Lab. Autom.* **20**, 107–126 (2015).

55. Kim, J. A. *et al.* Collagen-based brain microvasculature model in vitro using three-dimensional printed template. *Biomicrofluidics* **9**, 024115 (2015).

56. Prades, R. *et al.* Delivery of gold nanoparticles to the brain by conjugation with a peptide that recognizes the transferrin receptor. *Biomaterials* **33**, 7194–7205 (2012).

57. Cecchelli, R. *et al.* A stable and reproducible human blood-brain barrier

model derived from hematopoietic stem cells. *PLoS One* **9**, e99733 (2014).

58. Ballabio, D. A MATLAB toolbox for Principal Component Analysis and unsupervised exploration of data structure. *Chemom. Intell. Lab. Syst.* **149**, 1–9 (2015).

59. Eigenmann, D. E. *et al.* Comparative study of four immortalized human brain capillary endothelial cell lines, hCMEC/D3, hBMEC, TY10, and BB19, and optimization of culture conditions, for an in vitro blood–brain barrier model for drug permeability studies. *Fluids Barriers CNS* **10**, 33 (2013).

60. Wang, Z. G. *et al.* bFGF protects against blood-brain barrier damage through junction protein regulation via PI3K-Akt-Rac1 pathway following traumatic brain injury. *Mol. Neurobiol.* **53**, 7298–7311 (2016).

61. Gottardi, C. J., Arpin, M., Fanning, A. S. & Louvard, D. The junction-associated protein, zonula occludens-1, localizes to the nucleus before the maturation and during the remodeling of cell-cell contacts. *Proc. Natl. Acad. Sci.* **93**, 10779–10784 (1996).

62. Giannotta, M., Trani, M. & Dejana, E. VE-Cadherin and endothelial adherens junctions: active guardians of vascular integrity. *Dev. Cell* **26**, 441–454 (2013).

63. Wilhelm, I., Fazakas, C. & Krizbai, I. A. In vitro models of the blood-brain barrier. *Acta Neurobiol. Exp. (Wars).* **71**, 113–28 (2011).

64. Weksler, B. B. *et al.* Blood-brain barrier-specific properties of a human adult brain endothelial cell line. *FASEB J.* **19**, 1872–1874 (2005).

65. Biemans, E. A. L. M., Jäkel, L., de Waal, R. M. W., Kuiperij, H. B. & Verbeek, M. M. Limitations of the hCMEC/D3 cell line as a model for Aβ clearance by the human blood-brain barrier. *J. Neurosci. Res.* **95**, 1513–1522 (2017).

66. Lai, C.-H. & Kuo, K.-H. The critical component to establish in vitro BBB model: Pericyte. *Brain Res. Rev.* **50**, 258–265 (2005).

67. Blanchette, M. & Daneman, R. Formation and maintenance of the BBB. *Mech. Dev.* **138**, 8–16 (2015).

68. Armulik, A. *et al.* Pericytes regulate the blood–brain barrier. *Nature* **468**, 557–561 (2010).

69. Daneman, R., Zhou, L., Kebede, A. A. & Barres, B. A. Pericytes are required for blood–brain barrier integrity during embryogenesis. *Nature* **468**, 562–566 (2010).

70. Moura, R. P., Almeida, A. & Sarmento, B. The role of non-endothelial cells on the penetration of nanoparticles through the blood brain barrier. *Prog. Neurobiol.* **159**, 39–49 (2017).

71. Walter, F. R. *et al.* A versatile lab-on-a-chip tool for modeling biological barriers. *Sensors Actuators B Chem.* **222**, 1209–1219 (2016).

General conclusions

Different cμFCS have been designed and fabricated to study the neuromuscular context *in vitro*, creating physiologically relevant models. Several cell culture techniques and cell sources have been used, moving from mice to human cells, from 2D cultures to 3D, from primary cells to hiPSC, and analysing both healthy and diseased cells.

Cell-culture techniques for mice primary cells and cell lines were optimised utilising the designed and fabricated compartmentalised microfluidic culture systems (PDMS devices with two compartments connected through microchannels and each connected to different reservoirs to supply the specific cell medium). Myelination, proprioceptive sensory neurons and vascularisation were identified as key components of the neuromuscular circuit, known to be affected in some NMD, such as ALS. Myelination and sensory neurons were included in both, the peripheral nervous system and neuromuscular mice models. Moving to a 3D system with Matrigel rendered an increase on neural viability and mimicked better physiological microenvironment.

Shifting onto human models, we first established the protocol to obtain proprioceptive sensory neurons (pSN) from human neural stem cells. This resulted in a heterogeneous neural population enriched in TrkC+ sensory neurons (a typical marker of pSN). Our hypothesis of a relevant role of pSN in ALS development was evaluated throughout the differentiation process induced with different medium components. Differentiation experiments in healthy and ALS cells showed that a medium component (ROCK inhibitor Y27632) could interfere not only with neural stem cell differentiation, but also with ALS genetic pathway. Besides, ALS samples showed altered pSN related genes' expression and regulation, together with lower ETV1 levels

(required for a functional connection between pSN and motoneurons). This supports the hypothesis of the strong involvement of pSN in ALS pathology.

Human motoneuron (MN) and skeletal muscle (SkM) differentiation procedures were stablished to create the full human model. A first sensorimotor model was created culturing human pSN with human SkM in two-compartment PDMS commercial microfluidic devices. This showed for the first time the formation of synaptic bouton like structures in the contact points of an annulospiral wrapping. MN and SN spheroids morphological comparison was conducted to incorporate the motor unit. Results showed that glia stopped proliferating with the induction of sensory neuron differentiation in SN spheroids, contrary to MN spheroids, and that SN spheroids can migrate towards another SN spheroid fusing into a bigger cluster of sensory neurons.

A new multilayer PDMS device was designed and fabricated to integrate sensorial and motor neuromuscular pathways. This device included three interconnected microenvironments cultured in 3D, each supplied by the specific medium required by the cell. These three compartments were separated by microposts instead of microchannels, enabling in this way 3D cell culture on them. Human SN, MN and SkM units were cultured together in these devices, setting the first steps towards 3D physiological neuromuscular circuit on a chip for neuromuscular disease studies.

Finally, vascularisation, identified as another key actor of certain neuromuscular diseases, was studied. The blood-brain barrier and the monitorisation of its permeability were evaluated through different

methods. A new label-free, non-invasive and real-time barrier monitoring method based on electrical impedance spectroscopy was developed.

The global aim of this thesis was to study the neuromuscular context through compartmentalised microfluidic culture systems and to create relevant *in vitro* models. The cell culture performed in different microfluidic devices enabled neuromuscular and neurological studies in more physiological conditions. This thesis has introduced new *in vitro* culturing systems including several cell-culturing techniques, integrating relevant components of the neuromuscular context. And it has developed for the first time a 3D physiological neuromuscular circuit model on a chip for NMD studies, paving the way for future studies in the neuromuscular field.